Novel Experimental Methodology for the Investigation of Recrystallisation during Industrial Hot Forging of Inconel 718

Nicola Stefani

Thesis Submitted for the degree of Doctor of Engineering

Department of Design, Manufacture and Engineering Management
University of Strathclyde, Glasgow UK

2020

This page is left intentionally blank

Declaration of Authenticity and Author's Rights

‘This thesis is the result of the author’s original research. It has been composed by the author and has not been previously submitted for examination which has led to the award of a degree.’

'The copyright of this thesis belongs to the author under the terms of the United Kingdom Copyright Acts as qualified by University of Strathclyde Regulation 3.50. Due acknowledgement must always be made of the use of any material contained in, or derived from, this thesis.’

Signed: Nicola Stefani

Date: 01/06/2020

Acknowledgements

Firstly, I would like to express my sincere gratitude to my supervisors Prof. Paul Blackwell and Dr. Olga Bylya for the continuous support during my studies, for their patience, motivation, and knowledge. Special gratitude goes to Dr. Bylya for being a close mentor throughout my studies.

Besides my supervisors, I would like to thank the rest of my research team: Dr. Aleksey Reshetov and Bhaskaran Krishnamurthy for their insightful comments and encouragement.

My sincere thanks also goes to Dr. Dorothy Evans, Jaqueline Schramm, Kornelia Kondziolka and all of the AFRC staff who gave guidance and access to the laboratory and research facilities. Without their precious support it would not have been possible to conduct this research.

Abstract

One of the current research challenges in the aerospace sector is the prediction of microstructural changes during the processing of Nickel Superalloys such as Inconel 718. From the literature it emerges that the vast majority of microstructural modelling attempts, focused on the prediction of microstructural transformations and first of all recrystallization, are based on uniaxial tests. The question about the sufficiency of this data for full understanding of this phenomenon, as well as the range of applicability of available microstructural models for industrial forging processes remains open. The main reason for that is the complexity of the thermo-mechanical history and, related to this, the combination of operative microstructural mechanisms. An original methodology using forging trials, based on industrial practices, coupled with a tailored data processing procedure has been designed to link microstructural transformations to thermo-mechanical histories. This provides the ability to investigate the recrystallization (RX) phenomena from a different perspective compared to the available literature. Besides that, data obtained with this methodology gives the ability to benchmark, calibrate and validate existing microstructural models in an industrial setting. Experimental work presented in the research detailed herein was specifically planned to perform a systematic investigation of the processes with increasing level of complexity: uniaxial laboratory tests, quasi-constant strain rate forging of double truncated cones (DTC) on a hydraulic press, DTC forging on a screw press (high strain rates) and complex geometry disc forging on the screw press. As part of the proposed methodology, the notion of the zero recrystallization boundary was introduced; experimentally constructed and studied. This helped to analyse the onset of RX and its correlation with the various loading histories. The results obtained have allowed advanced calibration of JMAK-type models and generated an understanding of the range of their applicability. It was found that the range of validity for JMAK models is limited to a specific strain rate and temperature domain and the main reason for unsatisfactory predictions is the overlapping of a few recrystallization mechanisms (e.g. continuous dynamic, discontinuous dynamic and post-dynamic recrystallisation). Unfortunately, decomposition (splitting) of these mechanisms is not trivial. The use of the commercial modelling software DIGIMU® as a tool for validation of possible microstructural hypothesis and for interpretation of experimental results is explored. As a part of industrial implementation, the proposed methodology was also used for benchmarking of standard JMAK models embedded in commercial FE software as used by several industrial companies. Lastly, a framework for a new microstructure modelling approach based on the above observations is proposed and a direction for further research outlined.

Contents

List of Figures

Chapter 1

Chapter 2

Chapter 3

Chapter 4

Chapter 5

Chapter 6

Chapter 7

List of Tables

List of Abbreviations

The following table describes the meaning of various abbreviations, acronyms and symbols used throughout the thesis.

AFRC	Advanced Forming Research Centre
CRX	Continuous Recrystallisation
DDRX	Discontinuous Dynamic Recrystallisation
DTC	Double-Truncated Cone
DRX	Dynamic Recrystallisation
EBSD	Electron backscatter diffraction
GAM	Grain Average Misorientation
GBA	Grain Boundary Area
GG	Grain Growth
GOS	Grain Orientation Spread
HP	Hydraulic Press
IN718	Inconel 718
KAM	Kernel Average Misorientation
MDRX	Meta-dynamic Recrystallisation
PDRX	Post-Dynamic Recrystallisation
RX	Recrystallisation
SEM	Scanning Electron Microscope
SP	Screw Press
TT	Tensile Test
ZB	Zero Boundary

List of Symbols

ε	Strain
$\dot{\varepsilon}$	Strain Rate
t	Time
T	Temperature
ρ	Dislocation Density
σ	Stress
W	Plastic Work/Strain Energy

Chapter 1

Introduction

1.1 General Background

In the aerospace sector new challenges in near-net shape industrial forging require a high level of reliability of modelling prediction, with particular regards to microstructure. There are two main motivations behind this:

1. Improvement in rheology description: The main data used in the phenomenological elasto-plastic models is normally obtained from uniaxial laboratory tests conducted under constant temperature and strain rate. The requirement for uniformity in the stress-strain state in the specimen (necessary for data processing) normally leads to significant limitations on the level of strain that it is possible to generate. Extrapolation and interpolation of the experimental data for complex loading histories may result in inaccuracies. The prediction of microstructure evolution and embedding the obtained information into a constitutive model gives an opportunity to resolve this problem.
2. Property prediction: The final operational properties of the forged parts significantly depend on the obtained material microstructure. In many processes, for example, disk forging, a specific microstructure can be a necessary requirement along with the geometry of the part. Some types of microstructures can be obtained by heat treatments, while the development of others has to be addressed through the total chain of manufacturing operations. Through-process FE modelling of the microstructural evolution can play a vital role in the optimisation of such manufacturing technologies.

The reasons, logic and mechanisms of microstructural transformations can be significantly different in different alloys. This research is devoted to nickel superalloys and, in particular, Inconel 718 (IN718) will be used for this study. Nickel-based superalloys are widely used in the aerospace sector for components such as disks in gas turbines. Predicting the material behaviour and microstructure evolution during industrial hot forging of these components is a challenging task. Indeed, industrial hot forging is characterised by a complex history of loading (i.e. a wide-range of changes of strain rate and temperature can occur during the process) and multiple operations, each of which may lead to various microstructural changes. The state of the material, and therefore its behaviour, changes during such processing. However, material data for process modelling often remains the same for each process. This results in modelling inaccuracies (e.g. wrong material flow predictions, loading errors). Moreover, the final property of forged components depend on the final obtained microstructure. For this reason, it is necessary to take into account the microstructural changes and their effect with a microstructural model which can be used throughout the processing chain of the alloy. Existing modelling approaches are mainly based on uniaxial laboratory tests which do not resemble industrial hot forgings conditions. The question about the sufficiency of this data for full understanding of microstructural evolution as well as the range of applicability of available microstructural models for industrial forging processes remains open.

1.2 Industrial Relevance

The following work was carried out at the Advanced Forming Research Centre (AFRC) in a collaborative effort between the AFRC and the Department of Design, Manufacture and Engineering Management, both part of the University of Strathclyde. The AFRC is one of seven centres within the High Value Manufacturing Catapult across the UK, it is a globally-recognised centre of excellence in innovative manufacturing technologies, R&D, and metal forming and forging research. This project was in line with AFRC core research areas sponsored by its Tier one members:

- *Rolls-Royce* is a global provider of integrated power systems predominantly used in aerospace, marine, energy and off-highway applications. One of the world's largest producers of aero engines and the second largest provider of defence aero engines in the world.
- *Boeing* is the world's leading aerospace company and the largest manufacturer of commercial jetliners and military aircraft.
- *TIMET* is the leading supplier of mill and melted titanium products supplying nearly one-fifth of the world's demand
- *Aubert & Duval* is a world-leading producer developing, melting and hot processing (open and closed die forging and rolling, casting or powder metallurgy) special steels, super-alloys, aluminium alloys and titanium alloys.
- *Bifrangi* are world leading manufacturers of closed die forgings and finished machining of large crankshafts offering a fully integrated service from initial design to supply of the finished product.

- *Spirit AeroSystems* is global leader in aero-structure manufacturing. The company applies emerging technologies to the design, assembly and integration of components and structures for the world's premier aerospace programs.

1.3 Research Question and Objectives

The capabilities of the AFRC offer the chance to perform industrial scale forging for the investigation of microstructural evolution of IN718. However, the use of industrial data is not straight forward and it is necessary to develop a methodology to successfully use it. From this it raises the overall research question of this thesis:

- *How can industrial-type forgings be used to investigate microstructural evolution of IN718?*

The development and implementation of the methodology proposed will enable the achievement of the following objectives:

- ✓ Assess the current microstructural prediction capabilities for industrial forging of IN718.
- ✓ Investigate the difference in the kinetics of recrystallisation between classic experiments and industrial forgings of IN718, and how these can be used to formulate microstructural models.
- ✓ Suggest improvements on current microstructural prediction capabilities of microstructural evolution in Inconel 718.

1.4 Contribution to Knowledge and Thesis Structure

The main contribution to knowledge of this work is the development and implementation of a novel systematised approach based on Industrial-type hot forging which links the full thermo-mechanical histories of the process to microstructural aspects.

Thanks to this approach it was possible to:

- Perform a systematised investigation on industrial-type forgings.
- Define a novel calibration methodology for microstructural models based on industrial-scale forging trials.
- Specify applicability limits for phenomenological JMAK models available in FE software.

- Develop the concept of the Zero Boundary and generate a new set of observations on the recrystallisation phenomena in IN718.
- Give recommendations on the modelling of the recrystallisation phenomena and suggest a novel modelling framework.
- Highlight further research directions based on multi-scale modelling through the use of DIGIMU® software and develop a series of tools to assist in this approach.

The thesis consists of eight main chapters and a series of appendices. In Appendix 1 are collected some enlarged microstructural pictures used in the thesis' figures. In the rest of the appendices are contained the information relevant to the specific chapters two to five. Apart from the present, the concluding chapter and the appendices, the structure of this document is shown in Fig.1.1.

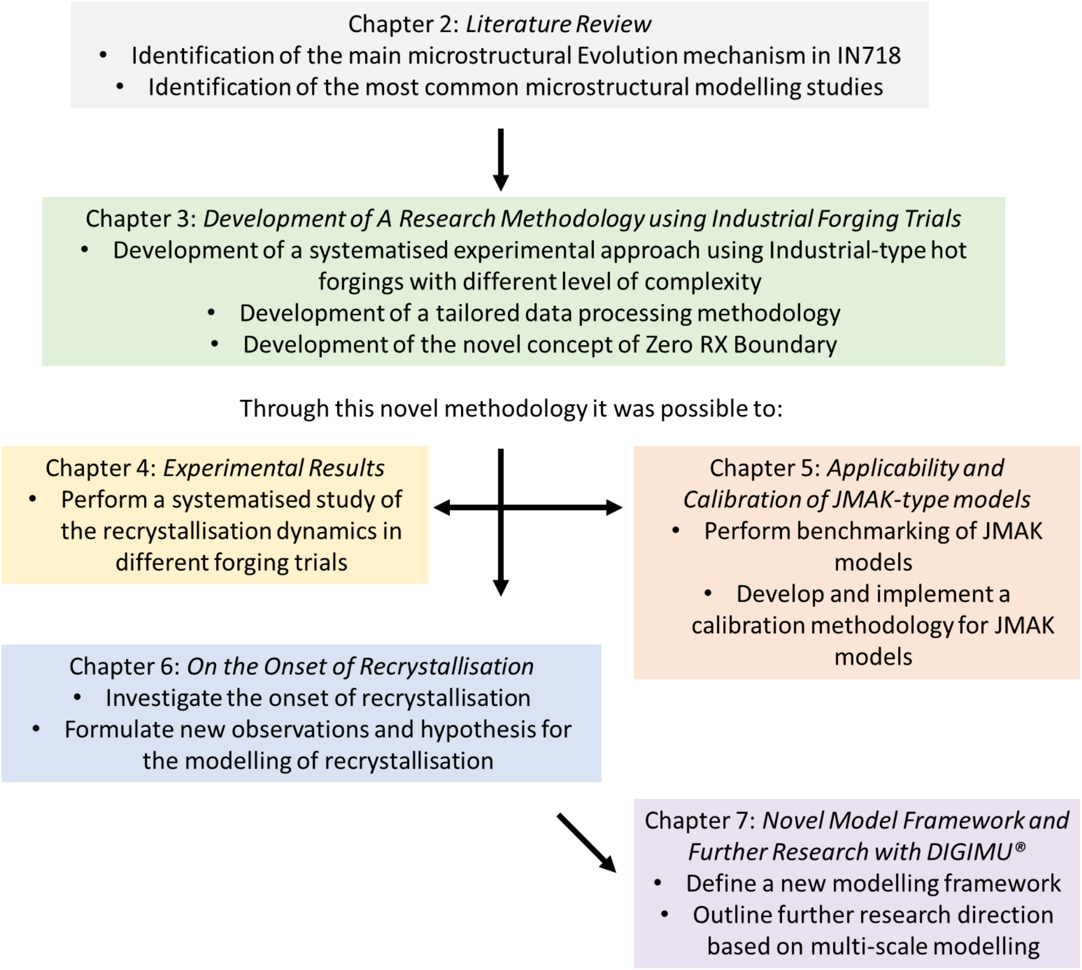

Figure 1.1. Structure of the thesis.

Chapter 2

Literature Review

2.1 Introduction

This chapter is intended to serve multiple purposes. Firstly, it will provide the reader with some background information on this multidisciplinary topic. However, it will not be as thorough as books on material science, plasticity or modelling and only some key principal concepts will be included. Secondly, it will serve to answer the following questions:

- What microstructural features are of key importance in the modelling of Nickel Superalloys and in particular Inconel 718?
- What are the main microstructural evolution phenomena taking place during the processing of these materials?
- What modelling approaches are already available in the literature? Are they applicable to industrial processes?

The results of this literature survey will lead to the identification of a research area of interest and thus the definition of a research methodology which will be the object of the next chapter. The topics to be investigated will be firstly history and metallurgy of IN718, then industrial processing of this alloy, microstructural evolution phenomena and lastly modelling aspects.

2.2 Inconel 718

2.2.1 Nickel Superalloys and the 718 family

In the mid-20th century, the growth of the aerospace sector and in particular the evolution of the gas turbine engine pushed the development of new materials characterised by high strength at elevated temperature. Nickel Superalloys are an example of these development efforts [1]. Despite being relatively dense (e.g. IN718 density is approximately 8200 Kg/m^3 [2] – compared to Ti6Al4V density of 4400 Kg/m^3 [3]) and not possessing the highest strength among the various alloys employed in the aerospace sector, the main advantage of this class of alloys is their ability to maintain their strength at high temperature as schematised in Fig. 2.1a. Thanks to this, Nickel Superalloys are used in many different sectors such as aerospace, marine, nuclear and petrochemical. It follows that they are mainly used for high-temperature applications, the most common being turbine disks [4]. An example of this is shown in Fig. 2.1b & 2.1c [5]:

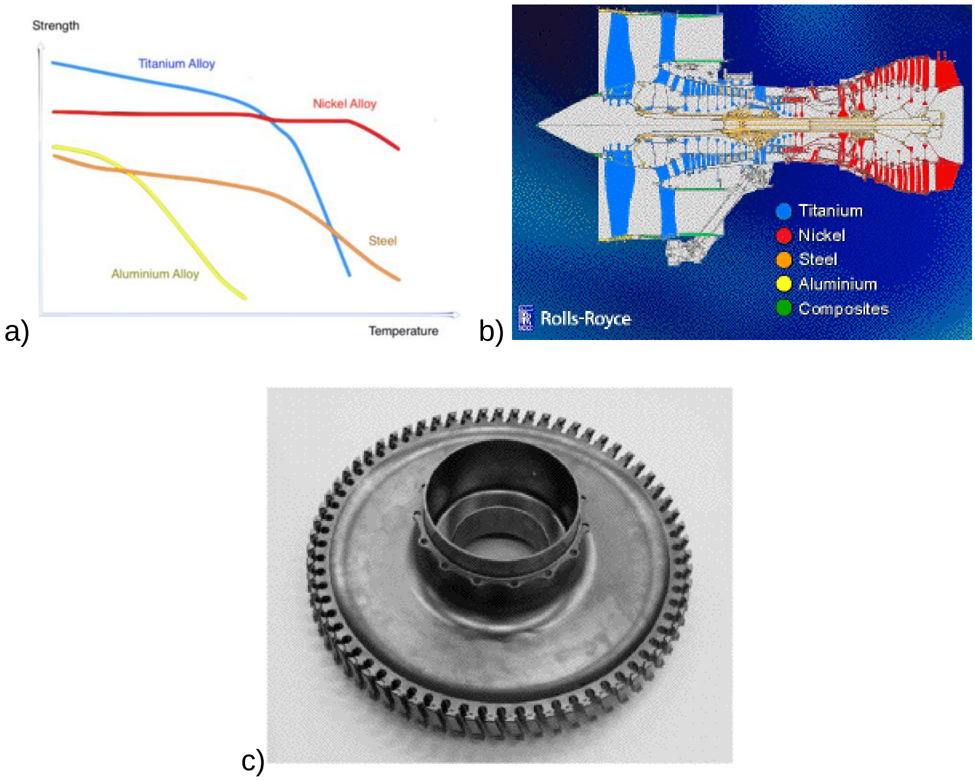

Figure 2. 1. a) Strength comparison of different materials with increasing temperature; b) the Rolls-Royce Trent Engine schematic showing cross section of the engine; c) aero-engine disk [5].

Inconel 718, often abbreviated as IN718, is one of the main exponents belonging to this category. It was developed in the late 1950s by INCO Huntington Alloys (now called Special Metals Co.), and featured a new hardening phase (y”) [1]. It quickly became the most used nickel alloy, replacing precipitation hardened steels in turbines owing to its mechanical properties, free licence to manufacture and manufacturing versatility [6].

The 718 family was later expanded with the Allvac° Alloy 718PLUS$^{\text{TM}}$ in order to raise the operational temperature of about 600°C characteristic of Inconel 718 while maintaining its good formability [7], however at the moment IN718 remains the most used alloy of the 718 family.

2.2.2 IN718 Microstructural Characteristics

Inconel 718, whose typical material composition is shown in Table 2.1, is characterised by the predominant gamma phase (y) and minor percentages of various intermetallic compounds. It can be therefore categorised as a quasi-single phase material. The gamma phase is composed by Nickel and Chromium and its crystal structure is an austenitic type face-centred cubic (FCC) matrix [8]. This phase forms the main grain structure of the material and is shown in Fig. 2.2. The secondary particles are classified as:

- y’ – Gamma Prime
- y” – Gamma Double Prime
- δ – Delta
- Other: Carbides/ Laves

The PTT diagram of this alloy can be seen in Fig. 2.3, while its characteristics are summarised in Table 2.2.

Table 2. 1. IN718 Typical Composition.

Element	Ni	Fe	Cr	Nb	Mo	Ti
Wt %	54.491	18.998	16.578	5.354	3.172	0.844
Element	Mn	Co	Cu	Al	P	Si
Wt %	0.307	0.155	0.090	0.005	0.003	0.003

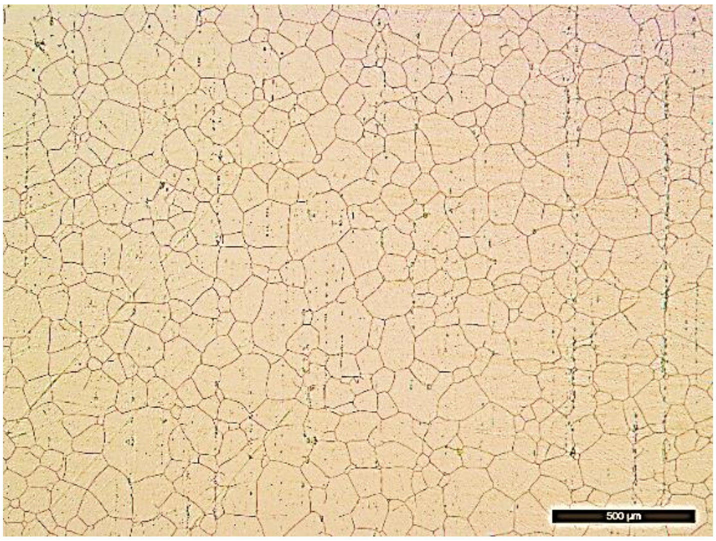

Figure 2. 2. Optical Micrograph of typical microstructure of hot rolled bars used for forging processes.

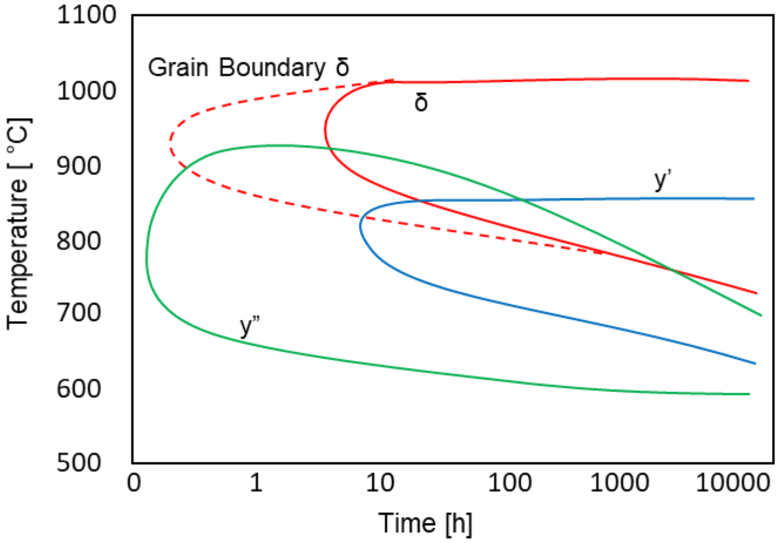

Figure 2. 3. PTT diagram of different phases for inconel718 [9].

Table 2. 2. Inconel 718 characteristics of relevant phases.

	γ	γ’’	δ
Composition [8]	Ni+Cr	3Ni+Nb	3Ni+Nb
Crystal Structure[8]	Face Centred Cubic	Centred Tetragonal	Orthorhombic
Formation [10]	/	Age Hardening	Sub-Solvus Heat Treatment (Fig. 2.5)
Size [8]	/	Nanometres	Micrometres
Position [8]	Matrix	Distributed within the grains	Starts at grain boundaries and grows into grain

2.2.2.1 Hardening Precipitates: γ` and γ``

The precipitates γ` and γ`` are responsible for the hardening in nickel superalloys [8]. In IN718, the main hardening effect is given by γ” [11]. This precipitate has a body centred tetragonal (BCT) crystal structure, it is distributed within the main matrix and its characteristic size is in the order of nanometres [8]. The positive effect of this precipitate is well documented in the literature [11], [12].

The γ`` solvus has been observed to be just above 900 °C. This precipitate has the same composition as another precipitate named Delta (3Ni+Nb) which when precipitating directly leads to the dissolution of γ’’ [13].Given the fact that performance of this alloy greatly depends on the presence of these hardening precipitates, commercially available IN718 is heat treated through the methods shown in Fig. 2.4.

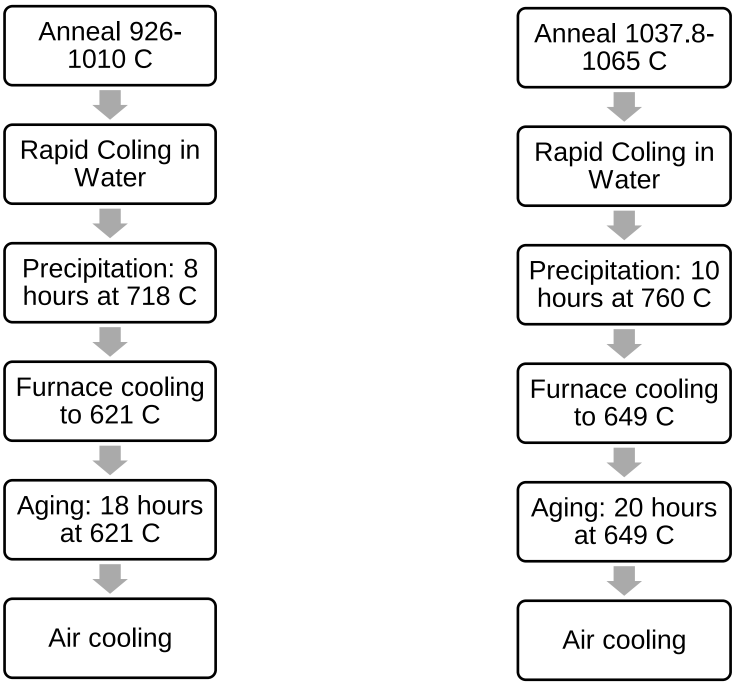

Figure 2. 4. Commercial heat treatments for age hardening [2].

2.2.2.2 Delta phase

Delta phase is an important phase in Inconel 718 due to its role in grain size control caused by a grain boundary pinning effect. Its composition is the same as γ``, however it is considerably different with its crystal structure being orthorhombic [8]. Under normal precipitation conditions, delta starts to precipitate at grain boundaries and then progress into the grains in plate form [8]. Its solvus temperature varies between 990 °C and 1020 °C depending on niobium content [10]. The equilibrium content of delta phase is shown in Fig. 2.5. Due to the proximity of the solvus to the forging range of IN718, often forging temperatures are referred to a super-solvus and sub-solvus depending on whether they are respectively above and below the solvus temperature. Precipitation of delta has been shown to be optimal at 900 °C and slowing with increasing temperature approaching the solvus. Even at 900 °C, this process is slow and a considerable amount of time is needed to precipitate 1% (approximately 1.5 hours) [14]. On the other hand, dissolution in the super-solvus range is much faster than precipitation [15]. In particular, it was shown that 10 minutes at 1060 °C were enough to dissolve 5-6% of this precipitate [14].

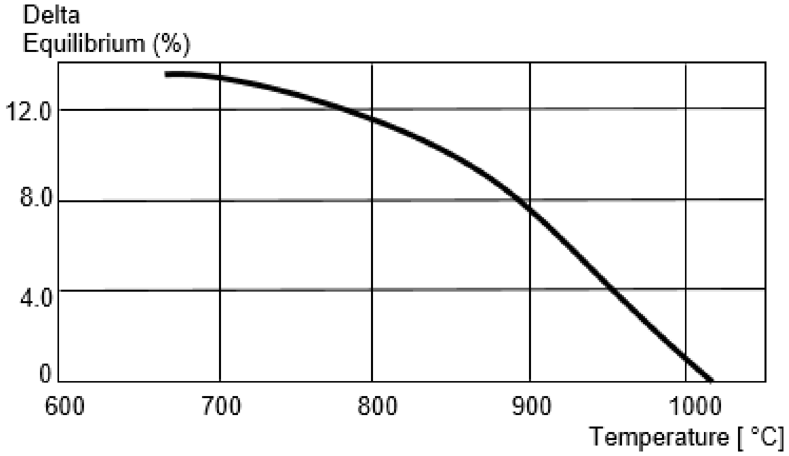

Figure 2. 5. Delta content equilibrium versus temperature [16].

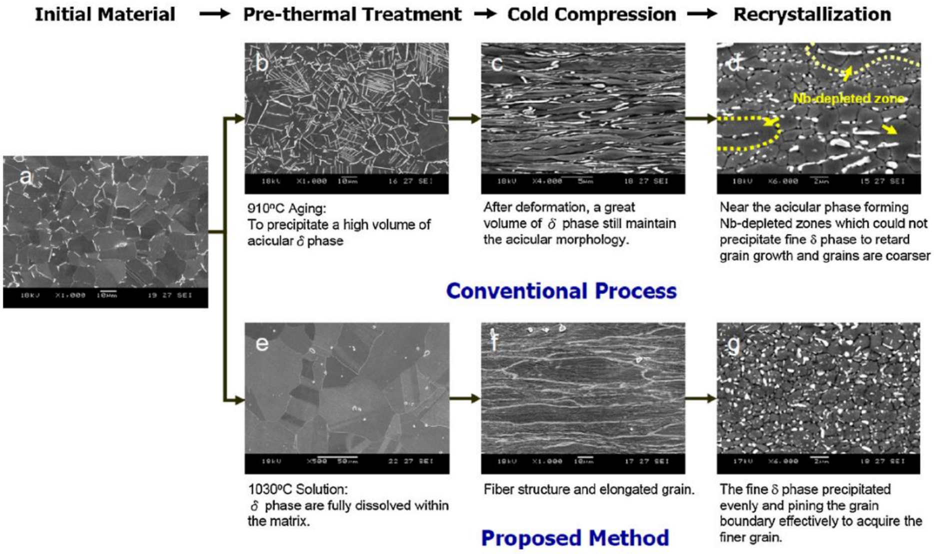

910ºC Aging:
To precipitate a high volume of acicular δ phase

After deformation, a great volume of δ phase still maintain the acicular morphology.

Near the acicular phase forming Nb-depleted zones which could not precipitate fine δ phase to retard grain growth and grains are coarser

1030ºC Solution:
δ phase are fully dissolved within the matrix.

Fiber structure and elongated grain.

The fine δ phase precipitated evenly and pining the grain boundary effectively to acquire the finer grain.

Figure 2. 6. Grain refinement process with and without delta [17].

As mentioned, delta has great influence on grain growth and thus grain size due to its pinning effect. Indeed, it was observed that an approximate 2.5x grain size growth resulted from delta dissolution [14]. However, its precipitation has been shown to have a negative influence on yield strength (-10% compared to standard 718) [16] and it has also been shown to affect the kinetics of recrystallisation [18]. An example of the importance of this precipitate during the processing of IN718 can be seen in Fig. 2.6. By controlling the presence of delta the authors of the study [17] obtained a considerably finer microstructure.

In the paragraph above it is discussed the effect of relatively large amounts of delta precipitates resulting from standard precipitation heat treatments, however it is important to mention that during complex forging there can be the possibility of precipitation and dissolution of a really small fraction of these precipitates in the form of a large number of very fine particles. While these particles may constitute only a considerably low volume fraction, they may lead to Zener pinning phenomenon [19], affecting the grain boundary and dislocation mobility and thus microstructural evolution phenomena such as recrystallisation and recovery.

2.2.2.3 Laves and Carbides

Laves is a brittle, intermetallic phase that may be present in IN718 due to segregation happening in the solidification process. Its crystal structure is hexagonally close packed and has a MgZn2 lattice type [20]. After casting, in order to dissolve this phase and avoid its detrimental effects, IN718 is usually homogenised at 1150 °C [21]. Laves phase, which forms during the solidification process of the alloys is particularly problematic in additive manufacturing processes for which homogenisation of the part after deposition may not be a viable option.

Carbides are another intermetallic phase present in IN718 which can form during solidification and age hardening treatments. Studies have shown that the most common carbide phase in IN718 is a niobium rich MC phase [22]. Homogenisation in this case does not provide the same effect as for Laves and some amount of these precipitates remain present in the microstructure as will be discussed in later chapters [23]. However, their presence is limited and for this reason it is almost always neglected during microstructure modelling.

2.2.3 Hot Working of Inconel 718

2.2.3.1 Characteristics of IN718 in Industrial Processing

As mentioned earlier, the main application of this class of alloys is in the aerospace sector for components like disks for gas turbines. An example of the manufacturing process used for the production of these components is shown in Fig. 2.7& 2.8 [24], [25]. Open and closed die hot forging play a primary role in the industrial manufacturing process of turbine disks and thus in the processing of IN718 [26]. Due to the complex geometry of the part, multiple forgings leading to high accumulated plastic strains, which may involve re-heating in between steps, are usually needed. Moreover, the specification of the forging equipment can change considerably. A classification of industrial forging processes can be performed based on the speed of forging by dividing between low strain rate and high strain rate forging processes. The former one is peculiar to forging on hydraulic presses where the strain rate usually does not exceed 1 s^{-1}. The second group of processes is characterised by high strain rates (>1 s^{-1}) which are obtained using hammers, screw presses and crankshaft presses [27]. In this type equipment, speed changes during the process and therefore strain rate is not constant. Another important feature of industrial forgings is that they are generally non-isothermal processes. Temperature changes are due to the lower temperature of the dies, which lead to cooling in the workpiece, and adiabitic heating in case of high strain rate forgings. Lastly, the size of industrial components can vary widely with workpiece reaching the order of meters [28]. As will be shown in Section 2.3, all of the steps in the industrial processing are going to affect the microstructural state of the part and thus its properties. The more complex the process, the harder it is therefore to predict the final microstructure and the properties of the part. Thus, robust process modelling is needed to ensure the achievement of optimal properties for the final components. Classic studies on the behaviour and microstructure of IN718 are based on laboratory experiments, however as discussed above, the industrial processing of these alloys is much more complex than these standard tests.

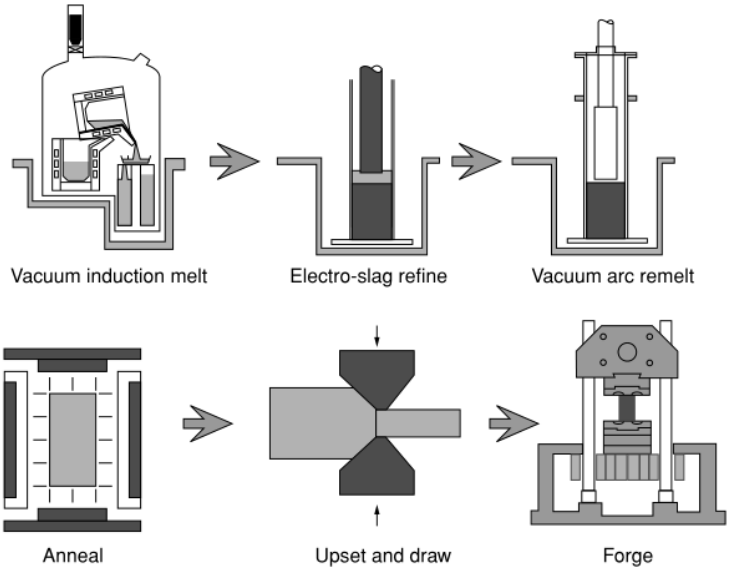

Figure 2. 7. Example of processing route for production of turbine disk [25].

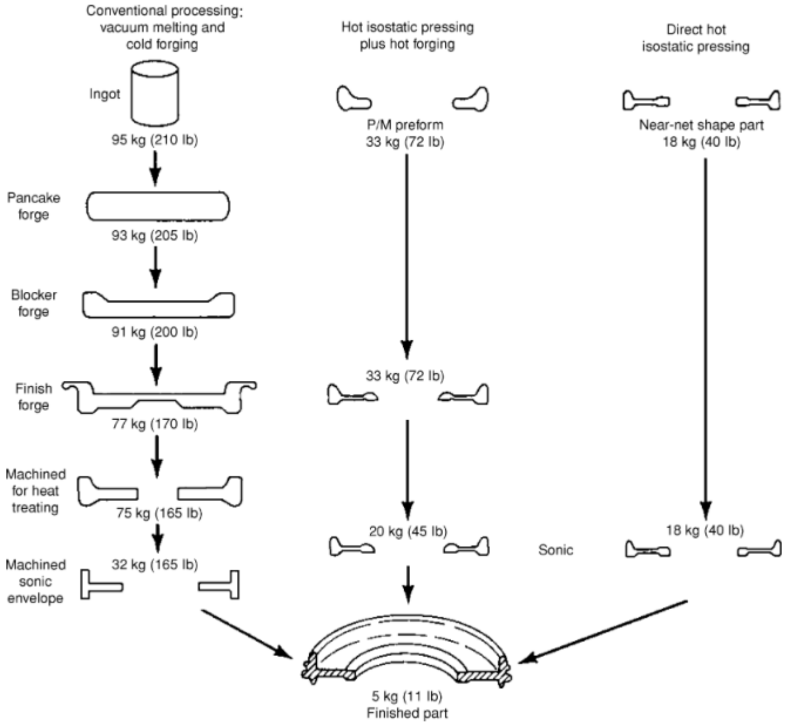

Figure 2. 8. Example of processing route for the production of turbine disk [24].

2.2.3.2 Forging Range and Mechanical Behaviour

As shown in Fig. 2.9, the recommended forging temperature range for IN718 is between 900 °C and 1150 °C [2]. As noted earlier, the forging temperature is often referred to as sub-solvus or super-solvus depending on whether it is below or above the solvus temperature of δ precipitate. This is of importance because in the sub-solvus domain the grain size may be controlled by boundary pinning by precipitates. Thus if δ precipitate is already present in the initial microstructure , then forging in the sub-δ-solvus domain leads to a finer grain size compared to forging in the super-δ-solvus domain [29].

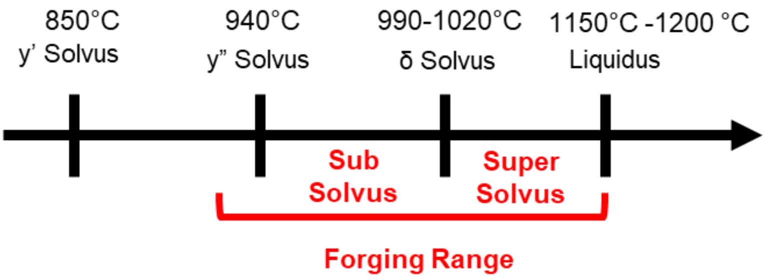

Figure 2. 9. Forging range and solvus temperatures of IN718 [29].

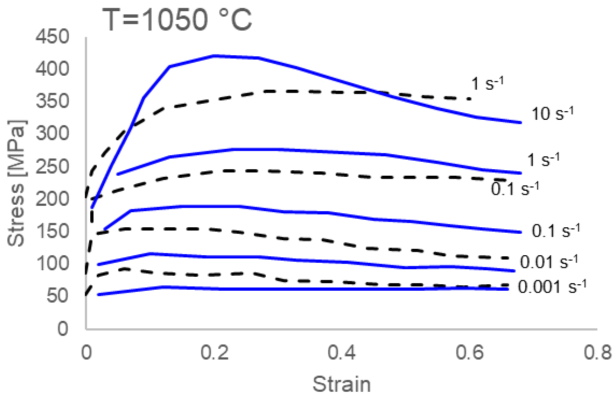

Figure 2. 10. Typical IN718 stress-strain curves [30], [31].

The rheology of IN718 is well documented in the literature with numerous studies based on uniaxial laboratory tests [30]–[36]. The test conditions are usually in the temperature range 900- 1200 °C, strain rate range 0.001 to 1-10 s$^{\wedge-1}$ and strains up to 0.6-0.7. The typical material behaviour can be observed in Fig. 2.10. This illustrates the strain rate sensitivity, hardening and, depending on the process conditions, softening. In order to ease the processing of this alloy, uniaxial tests have been used to create processing maps to provide a guide for the safe and unsafe forging domains. Here, “unsafe” reflects the possibility for the development of flow instabilities such as shear bands and cracking [37], [38]. The main limitation of this approach is that the developed process maps depend on the initial microstructure from which they were obtained. Moreover, they are based on uniaxial laboratory test conditions which do not necessarily resemble industrial forgings.

2.2.3.3 Challenges

Despite being a very popular material and having been used for more than half a century, the processing of IN718 is still characterised by considerable challenges. The complexity of the manufacturing process of turbine disks given by multiple operations, complex geometries, different forging conditions (non-constant and high strain rates, non-isothermal), large deformations (strains >> 0.7) and large billets leads to defects such as laps or incomplete filling of the dies as well as problems in the final mechanical properties of the material due to inadequate control of grain size [26]. As can be seen in Fig. 2.11 below, the grain size has a considerable influence on the properties of Nickel Superalloys [39]. While many studies have been carried out to study the behaviour of IN718, the vast majority of them have been performed using uniaxial laboratory tests with the following characteristics:

- Small and homogeneous deformations: up to 0.6-0.7 strain
- Constant strain rates: usually up to 1-10 s^-1
- Constant temperature

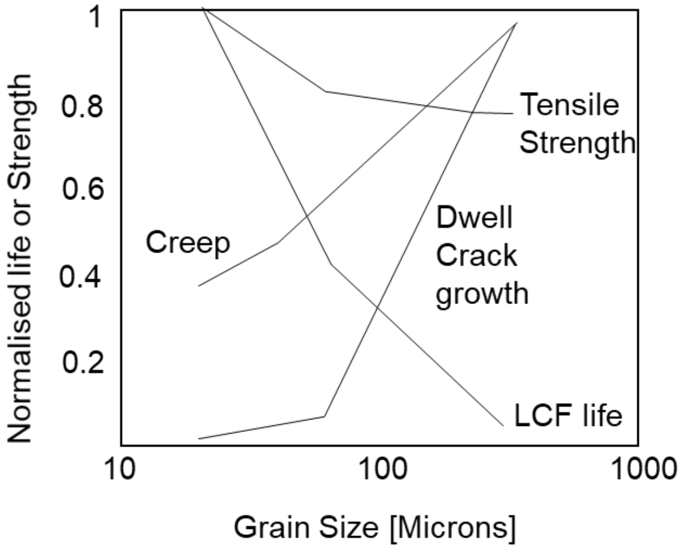

Figure 2. 11. Effect of grain size on mechanical properties of nickel superalloys [39].

The behaviour of this alloys is directly correlated to its microstructure, which changes during the industrial forging process. Therefore, an understanding of microstructural evolution in these conditions is necessary to understand and predict the mechanical behaviour of this alloy.

2.3 Microstructural Evolution

In this section there will be summarised some basic principles of material science which will be used throughout this thesis. The concepts presented are sufficient to support the on-going discussion and not intended to provide an exhaustive review of the subject.

Dislocations are defects present in the atomic structure of the material and have a major effect on the property and behaviour of materials. At room temperature the main deformation mechanism taking place in metals is slip of atomic planes due to movement of dislocations. On the other hand, at higher temperature other deformation mechanisms such as twinning and cross-slip become increasingly important. During deformation, new dislocations are generated leading to an increase in the dislocation density in a material. This increase in dislocation density inhibits the movement of slip planes and leads to an increase of the force required for deformation. This process takes the name of *Strain Hardening.* During deformation the strain energy transferred to the material is split into generation of heat (often approximated to 95%) and dislocation generation/movement. This stored energy associated with dislocations, at high temperature and in certain conditions, leads to a series of microstructural evolution processes (e.g. recovery, recrystallisation and grain growth) which function is to minimize the energy of the system. These fundamentals of material plasticity can be found in detail in the literature [40]–[42].

2.3.1 Microstructural changes during Hot Forging Process

During the forging process on IN718 the observable phenomena taking place are shown in Fig. 2.12 and can be summarised as:

- Grain deformation: It is characterised by changes in the aspect ratio of the grains related to macro changes in shape of the workpiece [43].
- Grain fragmentation: It is the rotation of low angle boundary sub-grains to form new grains [44].
- Boundary Serration: Grain boundaries shift locally due to boundary tensions and local dislocation density gradients [43].
- Recovery: The process through which micro and macro properties of the material may partially return to their pre-deformation state. This happens through annihilation and rearrangement of dislocations. Recovery affects sub-grains, but do not usually affect grain boundaries. If recovery takes

place during deformation, it is named dynamic, otherwise it is named static [43].

- Recrystallisation: The general definition of recrystallisation is: "*The heterogeneous formation of new, strain-free grains growing, by a migrating high-angle grain boundary, into the deformed matrix"* [45]. The classification of the recrystallisation phenomena is however more variegated and will be discussed in more detail in section 2.3.2.
- Grain growth: During this process larger grains grow at the expense of smaller grains which eventually disappear. Through this process the grain boundaries assume a lower energy configuration [43].
- Twinning: This involves the rotation, but not distortion of part of the crystal in a symmetrical direction. Mechanical twins are caused by deformation when slip is inhibited (most likely found in HCP materials) while annealing twins form during heating at high temperature (mostly in FCC materials) [46].

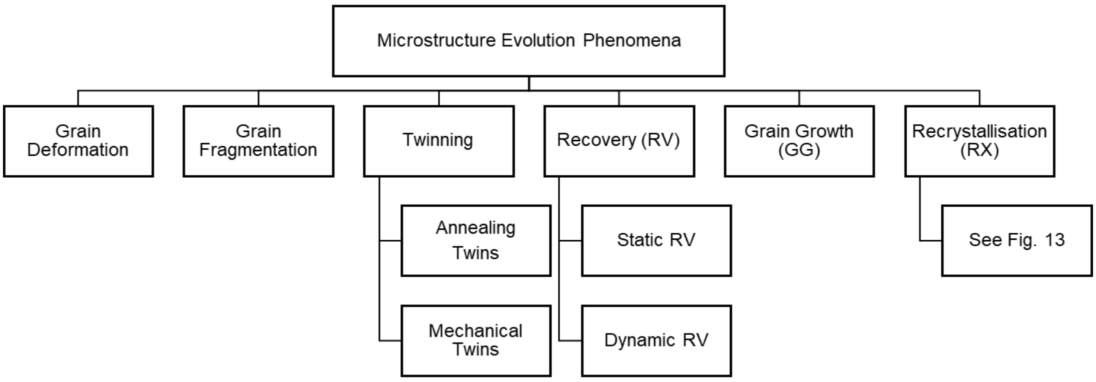

Figure 2. 12. Schematic list of microstructure evolution phenomena characteristic of IN718.

It is important to mention that all of these phenomena may take place individually or concurrently and they may affect each other's development. Depending on the material and process conditions, some of these processes may be more prominent than others. The stacking fault energy of the material, which is the energy associated with faults in the stacking sequence of atomic planes in a close-packed crystal structure, is usually used as an indication of whether recrystallisation or recovery is the main softening mechanism [46]. Materials are generally classified as having a high or low stacking fault energy. In the former materials class, glide, climb and cross slip of dislocations is relatively easy and given the fact that these are the mechanisms employed by recovery, then recovery is the main restoration process.

On the other hand, in low stacking fault energy materials, the mobility of dislocations is decreased, thus promoting recrystallisation [47].

In this work, the material examined; IN718, is characterised by low/medium stacking fault energy (40 mJ/m^2 [37]) and thus the main restoration process taking place during plastic deformation is recrystallisation.

Due to its importance, this phenomena will be the main objective of this thesis and in the next section, its characteristics will be discussed in more detail.

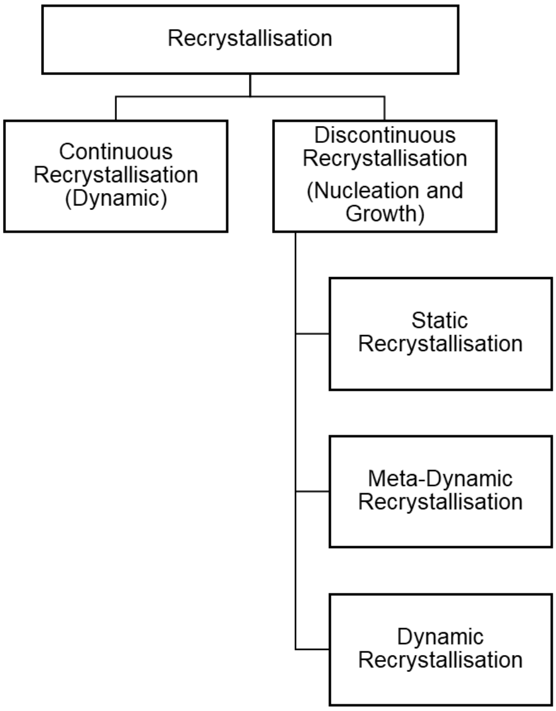

Figure 2. 13. Classification of the recrystallisation phenomena.

2.3.2 Recrystallisation

Recrystallisation, often abbreviated as RX, is a complex phenomenon, studied for more than a century. It is not a single process but a cluster of processes that have in common the development of new deformation-free grains in the existing microstructure. There exist different ways to classify these processes. In Fig. 2.13 a schematic representation is offered. The first important distinction to make is between continuous dynamic (CDRX) and discontinuous recrystallisation (RX). CDRX takes place at large strains during the deformation process, in which sub-grains formed through recovery rotate to form high angle boundaries, and it is usually found in high stacking fault energy materials such as aluminium [43]. On the other hand discontinuous recrystallisation (characteristic of low to medium stacking fault energy materials) is characterised by two sub-processes, nucleation and growth of the nuclei [43]. Nuclei are formed through dislocation pile-ups at grain boundaries [46]. The evolution of microstructure due to discontinuous recrystallisation is shown in Fig. 2.14. In the first stages nuclei appear at the grain boundaries, forming the so-called *necklace structure,* and then growth proceeds until the original grains disappear completely.

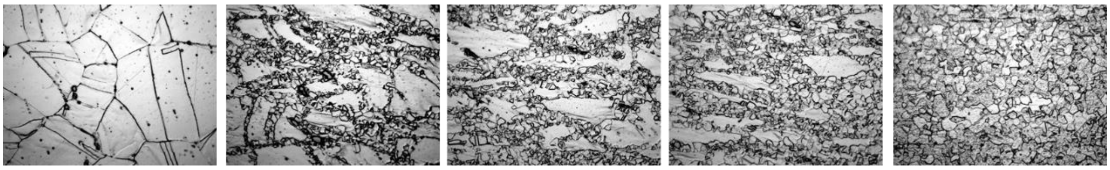

Figure 2. 14. The stages of discontinuous recrystallisation taken from experimental results.

Another important distinction can be made by relating the instance in which recrystallisation takes place to the time in which the material was deformed. If recrystallisation starts during deformation then it is called dynamic (DRX), while if it happens after deformation it is defined as post-dynamic. The latter can be further split into Meta-Dynamic recrystallisation (MDRX) which is the growth of the dynamically recrystallized nuclei, and static recrystallisation (SRX) which involves nucleation and growth after a certain incubation time [43]. Different authors have slightly different definitions for these phenomena, with overlapping boundaries between dynamic, meta-dynamic and static RX. It is debated, for example, whether growth of DRX nuclei is possible during deformation, or it can only be considered as meta-dynamic. This uncertainty originates from the fact that the characteristic time of these processes can be in the order of 10^-1 seconds [48] and therefore it is really hard to make a distinction between different mechanisms. Post-dynamic recrystallisation processes, are characterised by an incubation time which can vary depending on the deformation conditions [49]. All of these recrystallisation processes are influenced by time and the deformation conditions: principally strain, strain rate and temperature [43]. It is universally accepted that an increase in strain and in temperature lead to a higher level of recrystallisation [43]. However, the effect of strain rate is disputed. Some authors [50] suggest that recrystallisation decreases with increasing strain rates, while others suggest a decrease and then a further increase past a certain strain rate threshold [51].

When describing recrystallisation there are usually two main parameters that are taken into consideration, which are recrystallized volume fraction and size of recrystallized grains. This work is devoted to the study of microstructural evolution during the industrial forging process and therefore the dynamically recrystallised volume fraction and size of dynamically recrystallised grains are of the main interest. The former is dependent on initial microstructural state (grain distribution, precipitate, dislocation density) and thermo-mechanical conditions while the latter according to Humphries is dependent solely on stress [43] and many authors agree on the fact that when recrystallisation is complete the size of the recrystallized grains does not depend on original grain size [52]. Other studies on the other hand suggest that the size of recrystallized grains depends on the Zener-Hollomon parameter [53].

2.4 Microstructure Modelling

2.4.1 The Modelling of Recrystallisation

As the understanding of microstructure evolution increased in the last century, together with advanced computational means, the creation of predictive microstructure models has been the subject of many studies. Recrystallization is a complex phenomenon, so, to narrow the discussion, this study is mainly focused on the initial phase of recrystallisation. Burke et al. [54] suggested that the model of Kolmogorov, Johnson, Mehl and Avrami (1937-1942) (see original model in papers [55]–[59]) could be used not only for phase transformations but could be applied for recrystallization as well. Following this, J.E. Baily [60], suggested a physics-based criterion for the stability of a new nucleus, shown in Eq. (2.1):

$$\rho_{cr} = \frac{4\sigma_{surf}}{\tau d^*} \tag{2.1}$$

Where p_{cr} is the critical dislocation density needed for nucleation; σ_{surf} is the grain boundary energy per unit area, τ is the average energy per unit length of a dislocation and d* is the diameter of the recrystallization nucleus.

In 1972, Sandstrom and Lagneborg [61] suggested their model for recrystallization, part of which was a criterion of nucleation. They implemented an equation relating dislocation density with the macroscopic characteristics of the deformation process – notably true strain (all experiments were uniaxial):

$$\frac{d\rho}{dt} = \frac{\dot{\varepsilon}}{bl} - 2M\tau\,\rho^2 \tag{2.2}$$

Where *b* is Burgers vector, *l* is dislocation mean fee path, $M = M(T) = \frac{D_s b}{kT}$ is the mobility of recovery. This equation was followed with an important statement: the homogenous dislocation density between sub-grain dislocation walls on which Eq. (2.2) is based, cannot be used for the prediction of nucleation. Limiting analysis shows that the lower band of ρ_{cr} , defined by Eq. (2.1) is about an order higher than values of ρ obtained from stress-strain curves. For this reason, another variable, ρ_d, the total length of dislocations located in sub-grain walls per unit volume, was introduced. Eq. (2.2) was then modified to:

$$\frac{d\rho_d}{dt} = \frac{\dot{\varepsilon}}{bl_d} \tag{2.3}$$

This led to the proposition that there exists a critical strain for the beginning of DRX:

$$\varepsilon_{cr} = bl_d\rho_{cr} \tag{2.4}$$

In the same paper, the authors observed that strain softening during hot working of metals may be related to dynamic recrystallization. Later, other studies (Ponge [62], Sommitsch [63]) suggested that it might be possible to calibrate the microstructural equations using macroscopic stress-strain curves, assuming that that the critical stress is slightly less than the peak stress on the particular curve, which finally led to the empirical equation [63]:

$$\varepsilon_{cr} = k\varepsilon_p = k_1\dot{\varepsilon}^m exp\left(-\frac{Q}{RT}\right) + C_1 \tag{2.5}$$

Dependence on the temperature was traditionally taken in the form of the Arrhenius relationship where Q represents the activation energy for the phenomena (in this case dynamic recrystallisation). A few authors [64] reported also the existence of a lower threshold temperature below which dynamic recrystallization was not observed.

The majority of further developments in phenomenological recrystallization modelling were mainly based on various modifications of Eq. (2.1), (2.2) or (2.3) and (2.5). Among the most interesting, the work of J. Lin & Y. Liu [65] has to be mentioned. The authors made dislocation density dimensionless and normalised to the interval [0,1] by introducing a variable $\bar{\rho}$ as shown in the Eq. (2.6) below:

$$\bar{\rho} = \left(1 - \frac{\rho_i}{\rho}\right) \tag{2.6}$$

Where ρ_i is the initial dislocation density. Thus, in the beginning of the deformation process when $\rho = \rho_i$ the normalised density is 0 and then, when dislocation density rises, its value increases but does not exceed 1. This is very convenient for coding and machine computations. For the dislocation dynamics the authors used the equation:

$$\dot{\rho} = \left(\frac{d}{d_0}\right)^{\gamma_d} (1 - \bar{\rho})\dot{\varepsilon} - c_1\bar{\rho}^{c_2} - \left[\frac{c_3\bar{\rho}}{1-S}\right]\dot{S} \qquad (2.7)$$

Where S is the recrystallized volume fraction. It is easy to see that before the beginning of recrystallization when $\bar{\rho} < \bar{\rho}_{cr}$ both *S* as well as $\dot{S}$ are zero, so the last term of the equation vanishes and it becomes similar to Eq. (2.2). The critical dislocation density $\bar{\rho}_{cr}$ is assumed to be a fixed universal constant (independent of temperature and strain rate) equal to 0.184. All material parameters involved in this model are found using a generic algorithm based on optimisation technique for the best fitting of uniaxial stress-strain curves.

Alternatively, the model chosen by Zouari et al. [66] for full field modelling of DRX contained a modified version of Eq. (2.2) and (2.1):

$$\frac{\partial\rho}{\partial\varepsilon_{eff}^{P}} = K_1 - K_2\rho \qquad (2.8)$$

$$\rho_{cr} = \left[\frac{-\gamma_b\dot{\varepsilon}\frac{k_2}{M_b\tau^2}}{\ln 1 - \frac{K_2}{K_1}\rho_{cr}}\right] \qquad (2.9)$$

Where $M_b = M_0 \exp\left(\frac{-Q_m}{RT}\right)$ is the mobility of grain boundaries.

However, despite the quite complicated structure of these two equations, after integration of Eq. (2.8) and the resolution of Eq. (2.9) about ρ_{cr} the solution of this system is very similar to Eq. (2.5):

$$\varepsilon_{cr}^{p} \sim k\left(\dot{\varepsilon}\, exp\left(\frac{Q}{RT}\right)\right)^{n} \qquad (2.10)$$

Without going into a detailed analysis of all the various available modifications of DRX models, which is not the purpose of this thesis, the foregoing can be briefly summarised into a few basic assumptions which lay at the basis of these models:

1. There exists a certain dislocation density; ρ_{cr}, necessary for the beginning of recrystallisation.
2. This critical value can be universal or depend on temperature, strain rate and grain size.
3. As dislocation density is a microscopic parameter and cannot be observed/measured during macroscopic experiments, accumulated

plastic strain or effective strain (the same for uniaxial monotonic loading) can be used and associated with dislocation density.

4. The peak on the stress-strain curve can be used for finding ε_{cr} and calibration of DRX models.

This work will investigate the range of applicability of these assumptions to industrial-type forgings of Inconel 718 and, correspondingly, the suitability of this family of microstructural models for predictive modelling. To test this, JMAK-type models will be used as a reference. While there more recent mean field models available in the literature, there are multiple reasons why this research focuses on JMAK. Firstly as shown above, these models include the same assumptions of much more complicated models, and, secondly these models are the reality of commercial metal forming modelling which is of prime importance in the context of industrial applications. Indeed, these are the models that are currently used in many industrial companies as based on information from the AFRC's members and partners.

2.4.2 Microstructure modelling Capabilities in FE Software: JMAK Models

In recent years, the suppliers of commercial FE software recognised the industrial need for predictive microstructure tools and started offering embedded models for this purpose. The models present in such software tend to be variants of all the JMAK type models. The JMAK model originated in the 1930's from the work of Kolmogorov, Johnson and Mehl who described the crystallisation of melts, and Avrami who used it to describe the kinetics of phase transformation [55]–[59]). The original model was based on the concept that phase change takes place through the processes of nucleation and growth (similarly to discontinuous recrystallisation as discussed in 2.3.2). It was formalised with the now-famous simple mathematical relationship demonstrated through the theory of probability, shown in Eq. (2.11):

$$V(t) = 1 - e^{-V_e(t)} \tag{2.11}$$

where V(t) is the fraction of the transformed phase at time t and $V_E(t)$ is the extended volume of the transformed phase (the volume the transformed phase would acquire by omitting impingement of the growing nuclei).

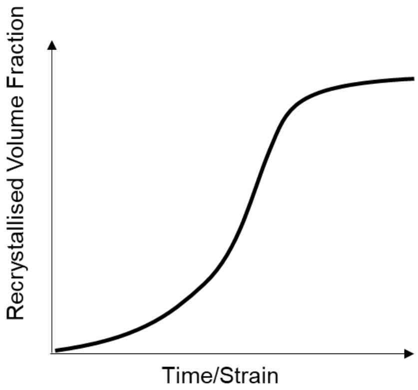

Figure 2. 15. Classic JMAK curve.

Eq. (2.11) describes an S-shaped curve which adapts well to evolution of recrystallisation in metals. Indeed, in simple conditions (e.g. constant temperature, strain rate) recrystallisation starts slowly, reaches a steady rate and then starts to slow down before coming to an end as shown in Fig. 2.15.

2.4.2.1 QFORM and DEFORM Models

JMAK was adapted to model recrystallisation through equations such as (2.5). The most popular JMAK adaptation present in many finite element software packages including QFORM and DEFORM [67], [68] is Huang's model [69] developed in 2001, which includes:

- Dynamically recrystallized volume fraction
- Meta-dynamically recrystallized volume fraction
- Statically recrystallized volume fraction
- Dynamic recrystallised grain size
- Meta-Dynamic recrystallised grain size
- Static recrystallised grain size

Dynamic recrystallization starts at critical strain (ε_c):

$$\varepsilon_c = a_2 \, \varepsilon_p \tag{2.12}$$

The critical strain (ε_c) is a function of the peak strain (ε_p) as shown in Eq. (2.12), which is the strain value corresponding to the maximum flow stress and is calculated as in Eq. (2.13). It is a function of initial grain size (d_0), apparent activation energy for the dynamic recrystallisation process (Q_1), strain rate ($\dot{\varepsilon}$) and temperature (T).

$$\varepsilon_p = a_1 d_0^{n1} \dot{\epsilon}^{m1} \exp\left(\frac{Q_1}{RT}\right) + c_1 \tag{2.13}$$

Eq. (2.14) calculates the dynamically recrystallized volume fraction (X_{drex}) and it was derived from the original Avrami equation which describes the S-shaped curve. It is a function of strain (ε), peak strain (ε_p) and $\varepsilon_{0.5}$ which corresponds to the strain required to achieve 50% DRX and it is calculated with Eq. (2.15). This is respectively a function of strain, initial grain size (d_0), activation energy for dynamic recrystallisation (Q_5), strain rate ($\dot{\varepsilon}$) and temperature (T).

$$X_{drex} = 1 - \exp\left[-\beta_d \left(\frac{\varepsilon - a_{10}\varepsilon_p}{\varepsilon_{0.5}}\right)^{k_d}\right] \tag{2.14}$$

$$\varepsilon_{0.5} = a_5 d_0^{h5} \varepsilon^{n5} \dot{\epsilon}^{m5} \exp\left(\frac{Q_5}{RT}\right) + c_5 \tag{2.15}$$

The dimension of the dynamically recrystallized grains (d_{drex}) is calculated through Eq. (2.16) in which it can be seen that if the DRX grain size is bigger than the original grain size (d_0) than the former parameter is set to be equal to the latter. The variable d_{drex} is a function of ε, d_0, activation energy for recrystallisation (Q_8), $\dot{\varepsilon}$, T, and various material coefficients.

$$d_{drex} = a_8 d_0^{h8} \varepsilon^{n8} \dot{\epsilon}^{m8} \exp\left(\frac{Q_8}{RT}\right) + c_8 \quad (if\ d_{drex} \geq d_0\ then\ d_{drex} = d_0) \tag{2.16}$$

Eq. (2.17) is used to calculate the statically recrystallized volume fraction (X_{srex}). It is a function of time t and the value $t_{0.5}$ which corresponds to the time required to achieve 50% static recrystallisation and it is calculated with Eq. (2.18). This in turn is a function of strain ε, d_0, activation energy for static recrystallisation (Q_3), $\dot{\varepsilon}$, T, and various material coefficients.

$$X_{srex} = 1 - \exp\left[-\beta_s \left(\frac{t}{t_{0.5}}\right)^{k_s}\right] \tag{2.17}$$

$$t_{0.5} = a_3 d^{h3} \varepsilon^{n3} \dot{\epsilon}^{m3} \exp\left(\frac{Q_3}{RT}\right) \tag{2.18}$$

The dimension of the statically recrystallized grains (d_{srex}) is found through Eq. (2.19). If the calculated value is bigger than the original grain size (d_0) then the size is not changed. The variable d_{srex} is a function of ε, d_0, activation energy for static recrytallisation (Q_6), $\dot{\varepsilon}$, T, and various material coefficients.

$$d_{srex} = a_6 d_0^{h6} \varepsilon^{n6} \dot{\epsilon}^{m6} \exp\left(\frac{Q_6}{RT}\right) + c_6 \quad (if\ d_{srex} \geq d_0\ then\ d_{srex} = d_0) \tag{2.19}$$

Eq. (2.20) is used to calculate the meta-dynamically recrystallized volume fraction (X_{mdrex}). It is a function of time (t) and the value $t_{0.5}$ which corresponds to the time required to achieve 50% MDRX and it is calculated with Eq. (2.21). This is a function of ε, d_0, activation energy for static recrystallisation (Q_4), $\dot{\varepsilon}$, T, and various material coefficients.

$$X_{mrex} = 1 - \exp\left[-\beta_m \left(\frac{t}{t_{0.5}}\right)^{k_m}\right] \tag{2.20}$$

$$t_{0.5} = a_4 d^{h4} \varepsilon^{n4} \dot{\epsilon}^{m4} \exp\left(\frac{Q_4}{RT}\right) \tag{2.21}$$

The dimension of the meta-dynamically recrystallized grains (d_{mdrex}) is found through Eq. (2.22). As in the previous cases, in the model a constraint is imposed such that the MDRX grain size cannot assume bigger values than d_0. The variable d_{mdrex} is a function of initial grain size (d_0), activation energy for meta-dynamic recrystallisation (Q_7), strain rate ($\dot{\varepsilon}$), temperature (T) and material coefficients.

$$d_{mdrex} = a_7 d_0^{h7} \dot{\epsilon}^{m7} \exp\left(\frac{Q_7}{RT}\right) + c_7 \quad (if\ d_{mdrex} \geq d_0\ then\ d_{mdrex} = d_0) \tag{2.22}$$

The grain growth process is modelled through Eq. (2.23). Final grain size depends on initial grain size (d_0), time (t), activation energy for grain growth Q_9 and temperature.

$$d_g = \left[d_0^m + a_9 t \exp\left(\frac{Q_9}{-RT}\right)\right]^{1/m} \tag{2.23}$$

Table 2. 3. QFORM and DEFORM JMAK model - original studies.

Equation	Testing Used
Dynamic Recrystallisation (DRX) / Critical Strain [70]	Compression tests: temperature range of 950 to 1150°C over a range of constant strain rates of 0.005, 0.05, 0.5,5, and 10 s^-1.
Meta-Dynamic Recrystallisation (MDRX) [69], [70]	Compression tests: temperature range of 950 to 1100 °C over a range of constant strain rates of 0.1, 0.05 and 0,005 s^-1 [71]. Compression Tests: temperature range of 950 to 1150 °C over a range of constant strain rates of 0.01, 0.1and 1 s^-1 [72].
Grain size (MDRX) same as Grain Size (DRX) [73], [74]	Compression Tests: temperature range of 900 to 1100 °C over a range of constant strain rates between 0.001 and 1 s^-1 [73]. Compression Tests: Temperature range of 960 to 1040 °C over a range of constant strain rates between 0.001 and 1 s^-1 [74].
Static Recrystallisation (SRX) and Grain Size SRX [75]	Compression Tests: Temperature range of 900 to 1120 °C over a range of constant strain rates between 0.001 and 1 s^-1.
Grain growth [74]	Isothermal heat treatments 0, 10, 30, and 60 min at 980 °C and 1020 ° C.

Eq. (2.12)-(2.23) are characterised by the presence of many material fitting parameters that have no physical meaning, for which both QFORM and DEFORM provides a default option (parameters are shown in the Appendix 2.1). These were taken from Huang's work [69] which in turn collected them from experimental data presented in the literature. Table 2.3 summarises where the various parts of the model originate from and the testing used to obtain them.

2.4.2.2 On the Applicability of JMAK Models

The widespread application of JMAK models is due to a range of factors. The model is intuitive, can be easily understood and it is not computationally demanding. These are important features which allows easy industrial implementation and its inclusion in commercial FE software. However, this type of model was created, calibrated and validated through uniaxial laboratory tests as shown in Table 2.3 and few applications on industrial-type forgings can be found in the literature. Examples where this has been used include the work of Reshetov et al., and Huber et al., who applied the JMAK model to extrusion and disk forgings respectively [77], [78]. They obtained good results in the central section of the billet which is characterised by steady flow and high deformation, when the material fully recrystallized, but did not provide results for other areas which could be more challenging for the applicability of the model, such as dead zones and partially recrystallised microstructures. Another case is given by Chen et al. who, recognising the limitations of standard JMAK for industrial forgings, proposed a variation of the model to account for a non-constant strain rate, [79]. This being said, the range of strain rates used was still limited to slow processes (up to 0.1 s^-1) and relatively small levels of deformation (true strain of 0.92). Alabort et al. [80] performed truncated double cones tests to higher deformation levels, however in this study iso-thermal tests with low strain rates were used. In summary, it can be seen that there exists a lack of systematic investigations on recrystallisation coving a range of industrial-type forging processes. Therefore, it raises the important question of whether these models and their underlying assumptions, which are common to many more complex models, are applicable to industrial hot forgings.

2.5 Conclusions

IN718 is widely used in the aerospace sector and industrial production of these components is characterised by complex thermo-mechanical processing which affects the microstructure and thus the properties of this alloy. Recrystallisation is the first most important microstructure evolution phenomenon to be considered when analysing microstructural evolution of IN718 during forging. There exist many approaches for the modelling of recrystallisation, with JMAK models being the most widely used and already available in FE software. However, the assumptions underlying JMAK, which are common to more complex models, are based on uniaxial laboratory tests and it is questionable whether these are still valid in an industrial setting. Indeed, while some attempts have been made to mimic industrial forgings, no systematised approach has been carried out so far. The necessity for an investigation based on industrial hot forging for the characterisation of recrystallisation and the assessment of commonly used phenomenological models together with their underlining assumptions can therefore be clearly made.

Chapter 3

Development of A Research Methodology using Industrial Hot Forging Trials

3.1 Introduction: A Novel Methodology

The literature review exposed a lack of investigations and systematised data on industrial forging trials of IN718. This was chosen as the research focus of this work and was made possible thanks to the capabilities of the Advanced Forming Research Centre, part of the University of Strathclyde. As opposed to laboratory testing, industrial forgings are characterised by non-uniform deformation which poses several challenges related to data analysis. Therefore, in addition to the design of industrial-type trials, it is necessary to develop an appropriate methodology of processing technology. Indeed, during uniaxial iso-thermal tests with constant strain rate the thermo-mechanical history of a specific test can be confidently assumed to be known by simply setting the temperature and strain rate parameters, and recording the deformation. However, this is not the case in more complex industrial forgings characterised by non-homogeneous deformation. In order to use industrial-type forgings to investigate microstructural evolution it is necessary to retrace the thermo-mechanical histories of points of interest and link them to their corresponding microstructures. The first step in this methodology is to design and perform experiments that would allow a systematic investigation of these processes (covering a range of different process parameters). Then a coherent methodology for the collection and processing of microstructural data from the forged billets must be defined. In addition to this, a method is needed for the extraction and construction of the thermo-mechanical histories in the workpiece. However, industrial equipment is characterised by many variations and uncertainties and capturing these represents the main challenge associated with the use of industrial forgings as opposed to uniaxial laboratory experiments. To overcome some of these challenges a method was developed, as described in section 3.3, which involves the creation of a digital twin.

3.1.1 New Opportunities given by the Proposed Methodology

The use of industrial forging suggested above is a clear deviation from traditional studies of microstructural evolution of IN718 and other alloys. One of the main problems when studying recrystallisation through traditional uniaxial tests is capturing the instance in which recrystallisation starts. This instant is often associated with peak strain and comes from the fact that softening is caused by recrystallisation [43]. However, to the best of the author’s knowledge no studies can with absolute confidence define the instance in which dynamic recrystallisation took place during these tests. One of the main advantages of such an approach is the fact that due to non-homogeneous deformation it is possible to observe areas in the workpiece in which recrystallisation just started but did not develop. This is termed within the present work, the *Zero Boundary*; see Fig. 3.1. By then looking at the thermo-mechanical history of the points lying along the zero boundary it is possible to associate them to the deformation conditions that lead to the onset of recrystallisation. The thermo-mechanical trajectories associated with points along this boundary may be varied. This novel concept can offer an opportunity to look at the recrystallisation phenomena from a new perspective. Another advantage of this approach is the fact that through the use of industrial forging it will be possible to benchmark, calibrate and validate existing microstructural models and thus directly evaluate their suitability for industrial implementation as will be shown in Chapter 5. It is important to stress that this is a powerful analysis tool which in addition to recrystallisation, can be applied to investigate any other microstructural features and/or phenomena such as abnormal grain growth, twinning, phase transformation and many others, making this methodology extremely versatile.

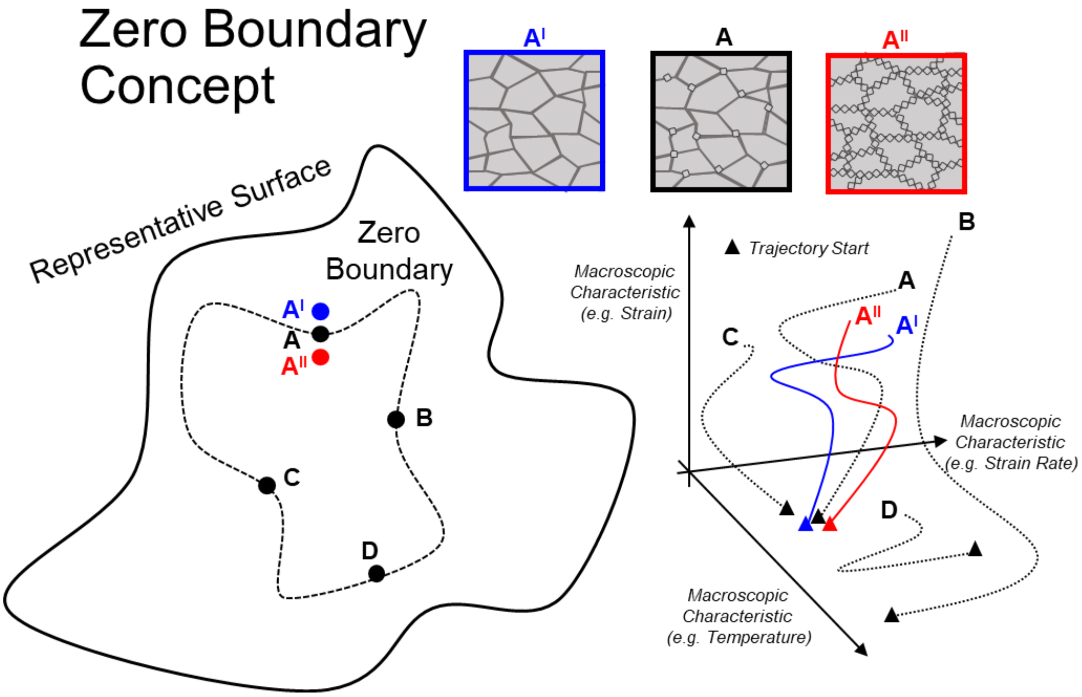

Figure 3. 1. Zero Boundary Concept: study different points in the forged specimen which are characterised by the same microstructural feature (e.g. onset of RX) and observe how different thermo-mechanical histories may lead to the same result.

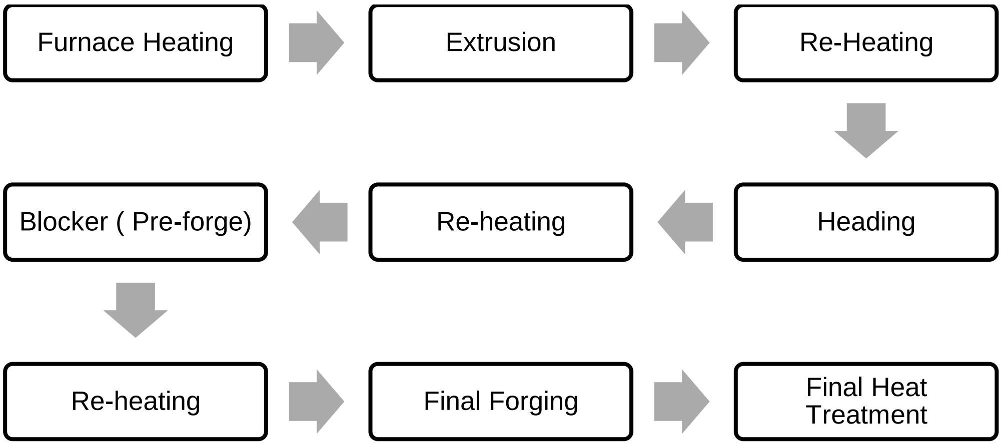

Figure 3. 2. Example of processing history for aerospace components, showing various heat treatments and forging operations.

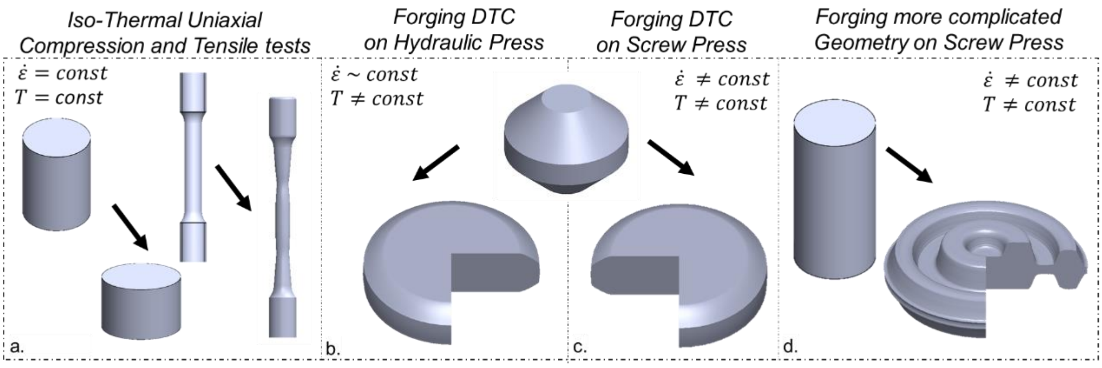

Figure 3. 3. Design of Experiment characterised by evolving complexity of loading history infographic.

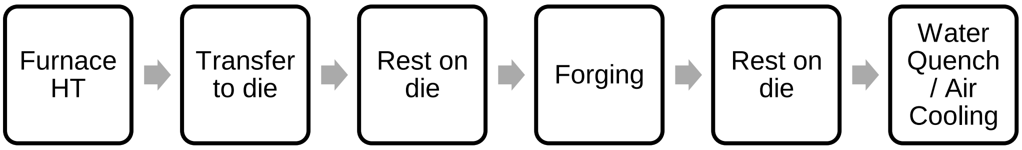

Figure 3. 4. Processing steps during hot forging on Inconel 718.

3.2 Design of Experiments

Industrial processing of nickel superalloys is a complex process as detailed in section 2.2.3. Multiple steps which include furnace heating, air transfer, resting on the die, multiple blows, re-heating, and different quenching may be employed as shown in Fig. 3.2.

Moreover, very different types of equipment may be used: slow forgings with hydraulic presses or fast processes with screw presses, hammers or extrusions. The thermo-mechanical histories resulting from these processes can be quite complex due to the fact that they are non-isothermal and have a non-constant strain rate. These conditions are very different from uniaxial laboratory tests in which temperature and deformation are constant throughout the process. To capture this diversity, the experimental approach shown in Fig. 3.3 was designed so as to systematically test different levels of complexity typical of industrial forgings. In the left-hand side of Fig. 3.3 are shown standard uniaxial laboratory tests characterized by constant temperature and strain rate. Compression tests are already present in many literature studies, as discussed in section 2.4, and were not replicated. On the other hand, some tensile tests, described in section 3.2.4, were performed. Fig. 3.3 b and c show the forging of double truncated cones (DTC). Deformation of this geometry is still relatively simple and resembles the uniaxial compression. However, while the hydraulic press maintains almost constant low strain rate, the billet is subjected to cooling during the process because of the lower temperature of the dies and air transfer making the process non-isothermal. Also shown are the forgings carried out on a screw press; here the strain rate was not constant. The disk geometry in Fig. 3.3 d maintained the non-constancy of strain rate and temperature with the additional feature of deformation complexity. The truncated double cone and disk geometry are shown in Appendix 3.1.1 and 3.1.2.

As mentioned above, the processing of these alloys has multiple steps in which at each stage different microstructure evolution phenomena as detailed in section 2.3.1 may take place. For this reason, to capture the total microstructural evolution of the process it is necessary to take into consideration all of the steps shown in Fig. 3.4.

Screw Press	*Hydraulic Press*
	
— 2100 Tonnes	— 500 Tonnes
— Maximum energy – 160KJ	— Cold and hot forming capability
— Die temperatures: up to 250°C	— Die Temperatures: up to 400°C
— Maximum stroke: 520 mm	— Max strokes: 400mm
— Maximum speed: 700 mm/s	— Max speed: 5 mm/sec

Figure 3. 5. Forging equipment used in this investigation.

3.2.1. Forging Equipment

As mentioned in the previous section, to capture the influence of different types of deformation, both screw and hydraulic presses were used to forge the workpieces. The former was used to generate complex thermo-mechanical histories with high strain rates, while the latter is characterised by slow constant deformation, resembling laboratory tests. Technical data on the equipment may be found in Fig. 3.5.

An important difference between these two machines is related to the input variables that will influence the forging process. The screw press is a so-called energy bound machine which means that is driven by energy. The energy is stored in a rotating fly wheel, which is then transferred to the ram and eventually to the billet during the forging. The only setting that can be inserted into the machine is the energy of the blow (expressed in KJ). This amount of energy will be achieved at the impact point between ram and workpiece, then the energy available will exhaust itself during the deformation. The final ram displacement is either due to exhaustion of energy or a stopping point given by spacer (kiss) plates. In the latter case, the remaining energy is transferred to the plates. The value of the energy is directly correlated to the speed of the press by the relation shown in Eq. 3.1:

$$V_i = \sqrt{\frac{E_i \cdot V_{max}^2}{2 \cdot E_{max}}} \tag{3.1}$$

Where E_i is the energy setting of the press, V_{max} and E_{max} are respectively the maximum velocity and energy of the press. Speed is maximum at impact and nil when energy is exhausted. An example of the energy usage and related speed during the process may be seen in Fig. 3.6.

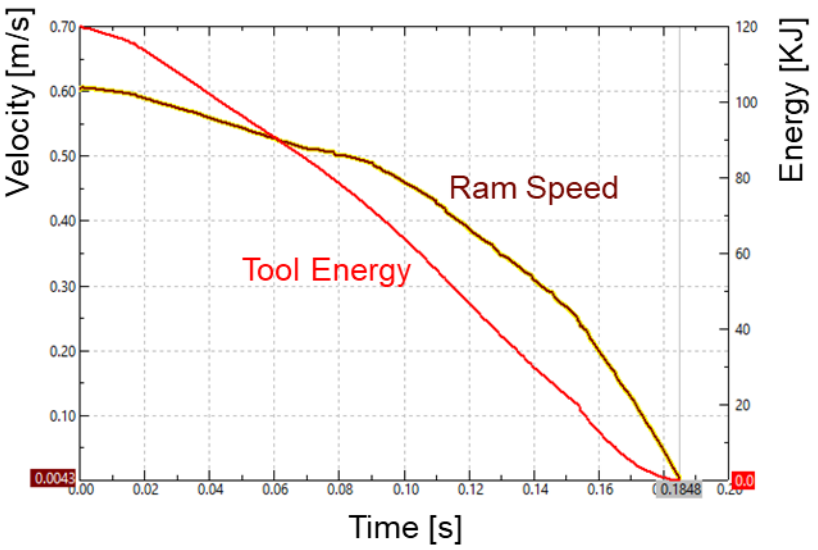

Figure 3. 6. Typical energy and speed profiles during screw press forgings.

Speed is an important parameter because it translates to strain rates. The non-constancy of speed in the screw press leads to a big variance in strain rate during deformation (10^-3 – 10^2). This contrasts with standard laboratory tests and the hydraulic press in which speed is relatively low and held approximately constant. Indeed, the input settings of the latter are characterised by ram speed and ram displacement. For the hydraulic press the final shape of the material will depend on the selected ram displacement unless the load required for the deformation exceeds the capacity of the press.

Another important factor to consider is die temperatures. This has a significant influence on the forging process and microstructural changes. IN718 is forged in the range 900-1200 °C [2], however the die temperature can only reach 400 °C for the hydraulic press and 250 °C for the screw press, which is typical for many industrial forges. Thus, the heat transfer between workpiece and dies happens before, during and after deformation. The cooling of the workpiece reduces its ductility and affects flow of the material. Moreover, several microstructure evolution phenomena are temperature driven and therefore greatly influenced by this cooling. In the hydraulic press this effect may be more marked due to longer contact time between die and workpiece during deformation (e.g. 10 s for hydraulic forging and 0.2 s for screw press forging).

Another boundary condition to be studied is friction. This can be partly reduced using lubricants. For both machines a layer of mixed graphite and water is sprayed on the dies and glass coating applied on the workpiece. Overall the workpiece-die interaction is an important parameter to consider and must be represented as closely as possible during the simulation to get reliable results. Indeed, it may greatly affect the final shape of the workpiece, the flow of the material and the microstructure. Unfortunately, this interaction is hard to control and there may be significant variation in friction and temperature conditions even in back-to-back forgings. This uncertainty is a characteristic of industrial forgings in which parameters like temperature or friction are taken within a range and not as discrete values.

3.2.2 Initial Material Characterisation and Heat Treatments

The first step in the processing chain is the receipt of the material batch. It is necessary to investigate its microstructure and perform preliminary heat treatments if required. The as-received material had an initial grain size of approximately 20 μm, with few traces of δ precipitate as shown in Fig. 3.7.a. The main research focus of this work was to be on recrystallisation in the forging process. This phenomena is characterised by the growth of newly formed grains. Thus, one of the required tasks for this study was to recognize recrystallised grains. For this reason, to ease the recognition of these newly formed grains it was chosen to perform grain growth of the initial material to an average grain size of approximately 100 μm. This was done through furnace heat treatment for approximately 30 min at 1080 °C, followed by air cooling. This temperature was chosen because it is above the solvus temperature of all the precipitates in the material as detailed in section 2.2.2. For this reason, during the heat treatment all secondary phases were dissolved. This is needed to simplify the problem at hand. The reason for this choice is that recrystallisation is a complex mechanism influenced by many parameters (Temperature, Strain Rate, Deformation Energy, Grain Size, etc.). In order to study the effect of these parameters on recrystallization it is useful to initially remove the effect of precipitates. It cannot be excluded however the possibility that a small amount of δ particles may precipitate and dissolve during complex thermo-mechanical history. The pre-form microstructure which will act as a comparison throughout this study is shown in Fig. 3.7.b Final grain size was calculated through the measurement of approximately 400 grains as shown in Fig. 3.8. Metallographic preparation and microscopy techniques will be discussed separately in section 3.4.

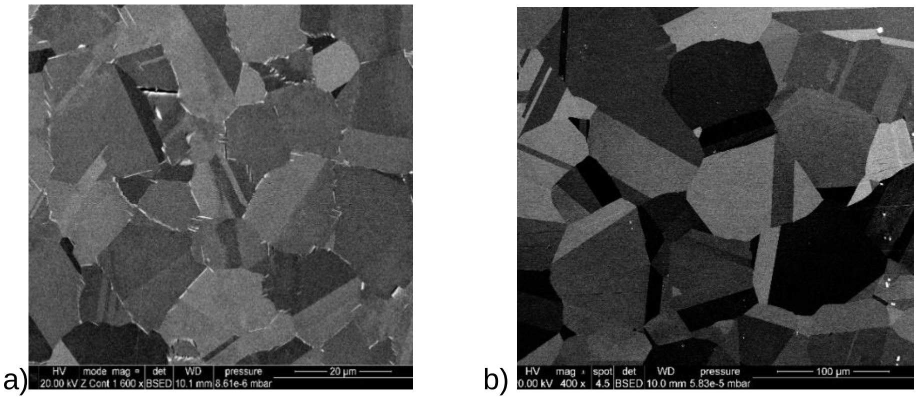

Figure 3. 7. (a) As-received Microstructure (b) microstructure after grain growth (SEM).

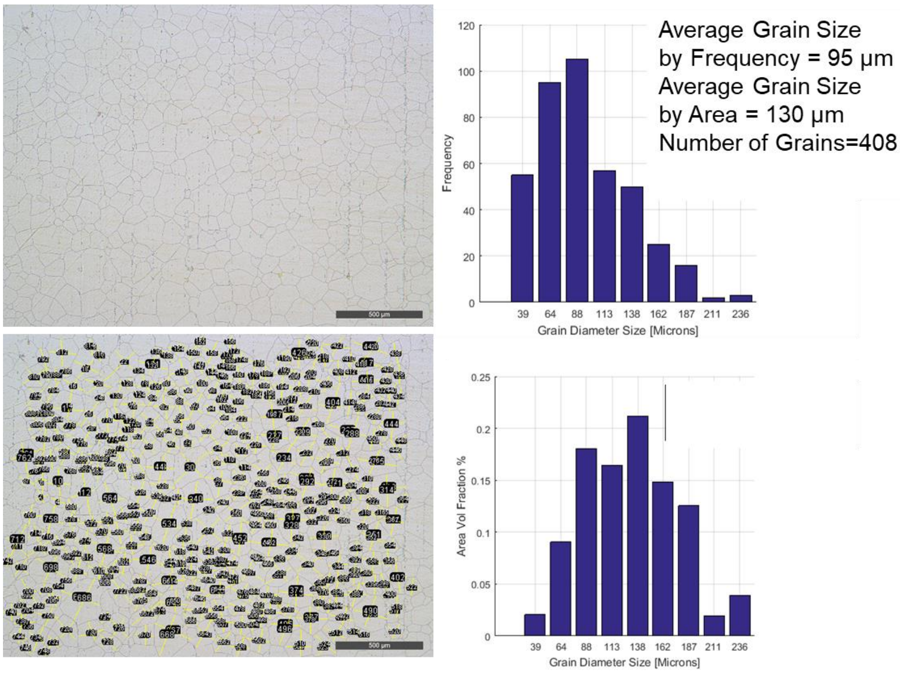

Figure 3. 8. Measurement of grain size after heat treatment on optical micrograph.

3.2.3 Selection of the Forging Parameters

A summary of the forging experiments may be found in Table 3.1. As seen in section 2.2.2, several microstructure evolution phenomena are temperature related and thus must be carefully considered. The factors determining the forging temperatures chosen, shown in Table 3.2, were:

- Forging range of IN718 (900-1200 °C [2]).
- Capability of the press: the presses are limited in terms of maximum load, thus it is important to choose temperatures that will allow the achievement of the desired deformation.
- Recrystallisation Temperature threshold: below a certain temperature recrystallisation cannot take place. According to the literature this temperature lays in the range 950-975 °C [64].
- Delta Solvus Temperature: delta precipitates are linked to stabilized grain size (through grain impingement) as detailed in section 2.2.2.

Temperatures of the dies were chosen to be as high as possible respective to the capabilities of the equipment (approximately 400 °C for hydraulic and 250 °C for the screw press). This was done to avoid excessive cooling of the workpiece. Similarly, lubrication was achieved through a combination of graphite and water on the die in addition to glass coating on the workpiece. The samples were held in a furnace to reach the desired temperature before forging. The energy setting for the screw press was chosen with two main drivers: to guarantee the desired deformation and to safeguard the press. This estimation was performed through finite element modelling. A range of energy settings were used, in particular, 75% was chosen so as to induce incomplete die filling at 970 °C (workpiece #9-#10 from table 2) and complete die filling at 1080 °C (workpiece #11 from table 2). The energy settings of the screw press have a direct influence on the impact speed between the ram and the workpiece. The resulting speeds for the chosen energy settings were approximately 350 mm/s for 25% energy, 500 mm/s for 50% energy and 600 mm/s for 75% energy leading to high strain rates (>10^1). The ram displacement was always influenced by the amount of the energy supplied except for workpiece #5-8 from Table 3.1 for which a separator plate was used between the dies so as to achieve specific deformations.

Lastly die displacement and speed for the hydraulic press were set respectively to 24 mm (≈50% reduction in height) and 2 mm/s. This speed was chosen to achieve relatively small strain rates (<10^0).

Table 3. 1. Experimental Design.

N	Geometry	Press	T (C)	Press Controls	Cooling
1	Double Truncated Cone (DTC)	Hydraulic Press	915	2 mm/s Speed	Water
2	Double Truncated Cone (DTC)	Hydraulic Press	970	2 mm/s Speed	Water
3	Double Truncated Cone (DTC)	Hydraulic Press	1080	2 mm/s Speed	Water
4	Double Truncated Cone (DTC)	Hydraulic Press	1150	2 mm/s Speed	Water
5	Double Truncated Cone (DTC)	Screw Press (with 24 mm Spacer)	860	25% Energy	Water
6	Double Truncated Cone (DTC)	Screw Press (with 24 mm Spacer)	970	25% Energy	Water
7	Double Truncated Cone (DTC)	Screw Press (with 24 mm Spacer)	1080	25% Energy	Water
8	Disk	Screw Press (with 21 mm Spacer)	970	75% Energy	Water
9	Disk	Screw Press	970	75% Energy	Air
10	Disk	Screw Press	970	75% Energy	Water
11	Disk	Screw Press	1080	75% Energy	Water

Table 3. 2. Temperature Selection for the Forgings.

T (C)	Precipitates Solvus	Recrystallisation Threshold
860	Sub-Solvus	Below
915	Sub-Solvus	Below
970	Sub-Solvus	Threshold
1080	Super-Solvus	Above
1150	Super-Solvus	Above

3.2.4 Tensile Tests

A small number of tensile tests were performed to be compared to compression tests used by most studies as shown in the literature review chapter and to the more complex forgings described above. High temperature tensile tests were performed through a Zwick/Roell Amsler Z250 Material Testing Machine and an extensometer was used to record exact deformation. The geometry of the tensile specimens can be found in Appendix 3.1.3. Tests were carried out with a strain rate of 0.005 mm/s and at temperatures of 950 °C and 1050 °C. These temperatures were chosen to replicate 970 °C and 1080 °C in the more complex forgings, taking into account some cooling in the latter due to air transfer and die resting times. Moreover, 950 °C and 1050 °C are standard temperatures which allow a direct comparison with literature data. Two different grain sizes were used for tests at 1050 °C (60 µm and 120 µm) while three were used for experiments at 950 °C (20µm with δ precipitate, 60 µm and 120 µm).

3.3 FE modelling

Simulations of the forging process for each workpiece were carried out with DEFORM and QFORM packages. Two types of simulations were employed: firstly preliminary simulation prior to the forgings to estimate parameters such as loads and forging energies necessary for the design of experiments and secondly *Digital Twin* simulations used to extract thermo-mechanical trajectories for data analysis and test microstructural models. In both cases, modelling settings of the forging process involved: workpiece and material data, drive means, friction settings, heat transfer and boundary conditions. No significant differences were found between the results of the two modelling packages as shown in Appendix 3.4.1. QFORM was chosen as the main software used for the modelling due to personal preference of the author. The process was modelled as a 2D problem given the axisymmetric geometries (disks and truncated double-cones). The process was modelled as the following sequence of operations:

1. Heating the billet in the furnace.
2. Transfer of billet from the furnace to the dies.
3. Chilling effect due to the billet resting on the die prior to forging.
4. Forging operation.
5. Chilling effect due to of billet resting on die after the forging;
6. Final quenching.

3.3.1 Pre-Forging Simulations

Pre-forging simulations were carried out to define and check several parameters for the experiments such as:

- Time in furnace needed for the sample to reach desired temperature.
- Check that maximum load required for the desired deformation does not exceed press limits.
- Find necessary screw press energy settings for desired deformation.
- Define hydraulic press velocity to achieve desired strain rate range.

The material was modelled as a rigid-plastic, isotropic, Huber-Mises material with flow stress depending on temperature, strain and strain rate. Material data used was taken from the 'Hot Working Guide' published by Prasad [37]. The complete material data sets can be found in Appendix 3.4.2. In Fig. 3.9 are shown the flow stress curves for a range of temperatures and strain rates relevant to the forgings (strain rate = 10–100 mm/s, T = 950–1050°C). Motion was assigned to the upper die to replicate the screw and hydraulic presses with settings shown in Fig. 3.10.

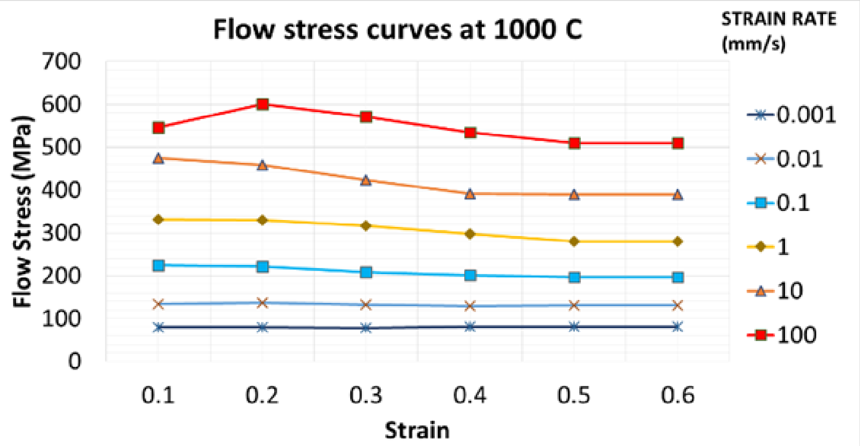

Figure 3. 9. Example of Inconel 718 flow stress data at 1000 °C for different strain rates.

Mesh element size was set to be maximum 0.5 mm per element as shown in Fig. 3.11. No significant difference in results were achieved with a smaller mesh and moreover measuring precision during metallographic analysis was limited to 0.5 mm.

Another important condition modelled was the friction at the contact between workpiece and dies. The standard configuration for hot forging of nickel superalloys available in the software; the Levanov Law, was used, with the following parameters:

Friction factor = 0.4; Levanov Coefficient = 1.25 W/(m^2 K). The heat transfer between dies and workpiece was set to simple for the screw press and coupled for the hydraulic press. This was due to the difference in forging time. Indeed, given the shortness of the screw press forging (approximately 0.2 s), heat transfer from workpiece to the die was neglected. On the other hand, hydraulic forgings lasting around the 10 second mark cannot neglect this heat exchange. Lastly air at room temperature was set as the environment around the workpiece.

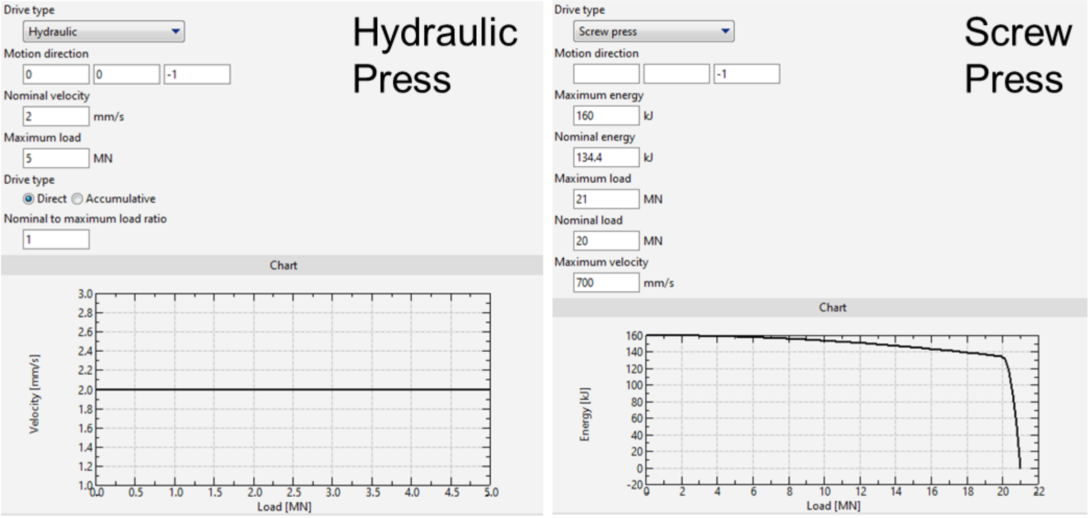

Hydraulic Press

Drive type: Hydraulic
Motion direction: 0 | 0 | -1
Nominal velocity: 2 mm/s
Maximum load: 5 MN
Drive type: ● Direct ○ Accumulative
Nominal to maximum load ratio: 1

Screw Press

Drive type: Screw press
Motion direction: | | -1
Maximum energy: 160 kJ
Nominal energy: 134.4 kJ
Maximum load: 21 MN
Nominal load: 20 MN
Maximum velocity: 700 mm/s

Figure 3. 10. Die movement settings for QFORM FE software.

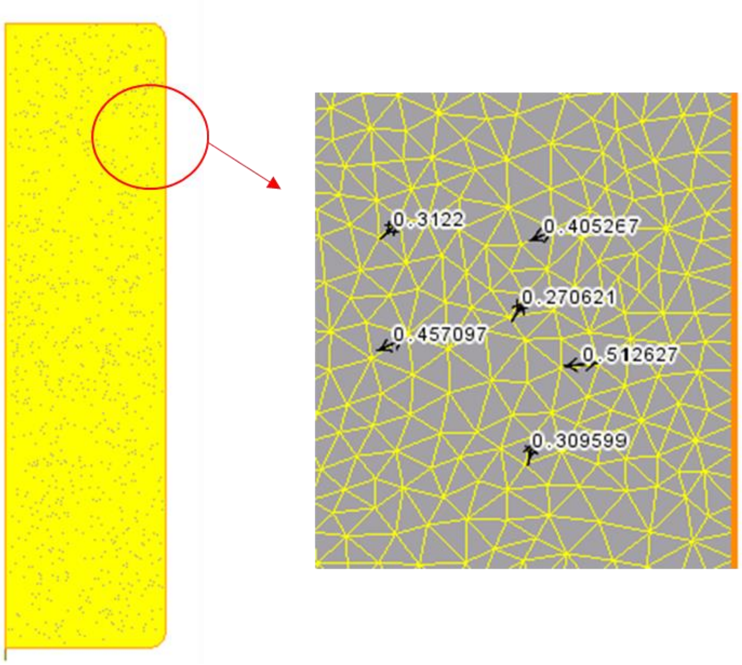

Figure 3. 11. Simulation mesh example for disk (Measurements in mm).

3.3.2 Development of the Digital Twin

Preliminary simulations are important to set parameters and have a general impression of the process at hand. However, while these simulations can give an approximation, they are very imprecise and cannot be used for the study of thermo-mechanical histories or for testing microstructural models. A complex process such as industrial-type forging is characterised by many uncertainties and deviations that a simple standard simulation cannot capture. For this reason it is necessary to develop a method that will allow to replicate as closely as possible the experiment in a digital version. It was therefore sought to develop a *digital twin.* In this research one of the main aims of FE modelling is to collect thermo-mechanical histories in various areas of the workpiece. These include the strain, strain rate, temperature and stress data throughout the process. To accurately predict all of these fields it is necessary to perform a series of recordings during the experimental trials to capture data that can be inserted into the simulation.

First of all it is important to record with a video camera the whole process so as to being able to capture with precision all the operation times. Thanks to this it is possible to set with accuracy all the times in the simulation. In Fig. 3.12 are shown screenshots of the forging process with recorded times. The processing times for all workpieces are recorded and detailed in Appendix 3.3.1.

Strain rate accuracy is related to the velocity of the ram of the hydraulic (constant speed) and screw press (variable speed). Velocities are recorded by the presses and can be exported as tabular data (raw data from presses are shown in Appendix 3.3.2 and Appendix 3.3.3). This data can in turn be inserted as an input into a simulation so as to replicate as closely as possible deformation speed.

Temperature is one of the most challenging parameters to control. Indeed, during these non-isothermal processes, cooling is given by heat exchange with the dies which are at a lower temperature compared to the workpiece. On the other hand, an increase in temperature may be generated by deformation through adiabatic heating, especially during high strain rate forgings. Temperature of the dies was measured through thermo-couples. Also, in order to monitor temperature changes as closely as possible three thermo-couples were inserted through drilled holes of 1 mm diameter in some billets as shown in Fig. 3.13.

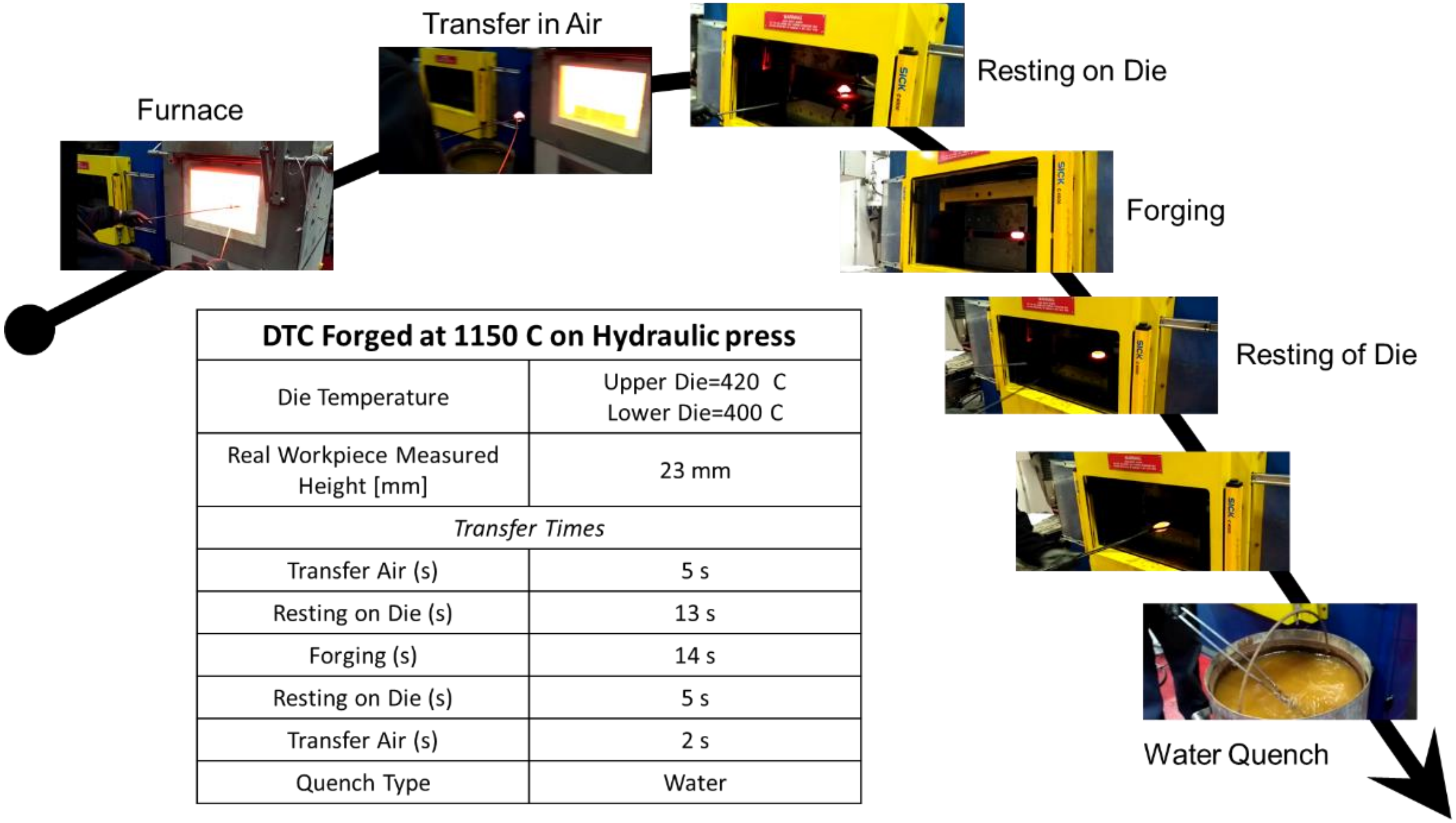

DTC Forged at 1150 C on Hydraulic press	
Die Temperature	Upper Die=420 C Lower Die=400 C
Real Workpiece Measured Height [mm]	23 mm
Transfer Times	
Transfer Air (s)	5 s
Resting on Die (s)	13 s
Forging (s)	14 s
Resting on Die (s)	5 s
Transfer Air (s)	2 s
Quench Type	Water

Figure 3. 12. Screenshots of forging process video and table with recordings of die temperature, final workpiece height, and operation times.

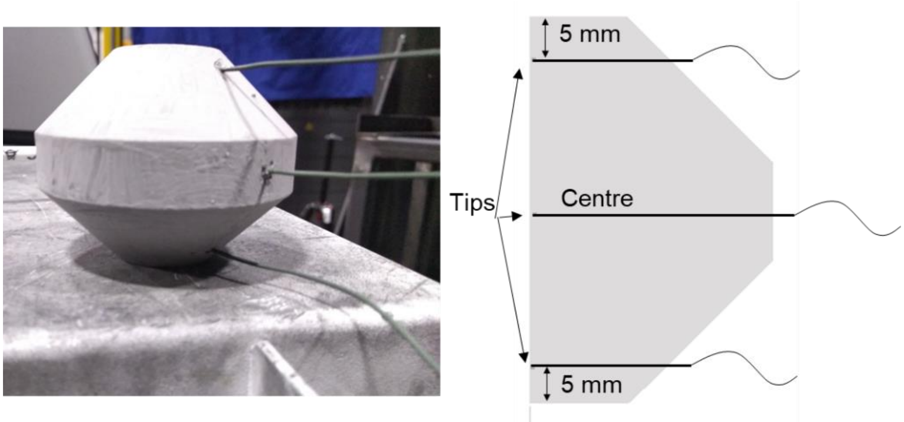

Figure 3. 13. Thermo-couples position in the workpiece.

Then by adjusting the thermal parameters in the simulation it was possible to match the temperature field of the experiment. In Fig. 3.14 a-c is displayed an example of the calibration of the screw press forgings. Unfortunately, the thermo-couples did not survive all of the experiments, especially the high strain rate ones. However, in general it was possible to record temperature up to the forging step (transfer from furnace, resting on die and forging). In the high strain rate forging, only the thermo-couple placed in the centre of the billets survived, recording data on adiabatic heating (sampling rate was set 1 ms to assure the recording of temperature during the fast process). In Fig. 3.14 d-e is shown calibration of hydraulic press forgings, and in this case the thermocouples survived the forging. It was possible to calibrate all temperatures within 10 °C. As is shown in Fig. 3.13 thermo-couples were placed in the central plane of the billet, thus while temperature can be assumed to be calibrated in the central section it remained a question of whether temperatures closer to the surface, and therefore far from the thermo-couple could be matched. In order to check surface temperature, some measurements were carried out using an Infrared (IR) camera. This showed a reasonably good agreement in temperature with predicted values. Through thermo-couple validation with screw and hydraulic presses it was possible to generate the material data thermal profiles shown in Appendix 3.4.4.

Strain validation can be performed through geometrical comparison. This process is easily done when deformation is symmetrical (e.g. complete filling of dies). In this case it is enough to compare measurement of ram displacement in the workpiece and the simulation. Nevertheless, it is interesting to investigate the case of non-symmetrical incomplete filling, as in workpiece#10 from Table 3.1. In this case to achieve the geometrical validation it is necessary to adjust the boundary conditions in the simulation to replicate the observed behaviour of the material as shown in Fig. 3.15.

Moreover, material flow can be compared between simulation and experiments by optical microscopy as shown in Fig. 3.16. It can be seen that the flow lines of the simulation closely resemble the flow lines in the workpiece.

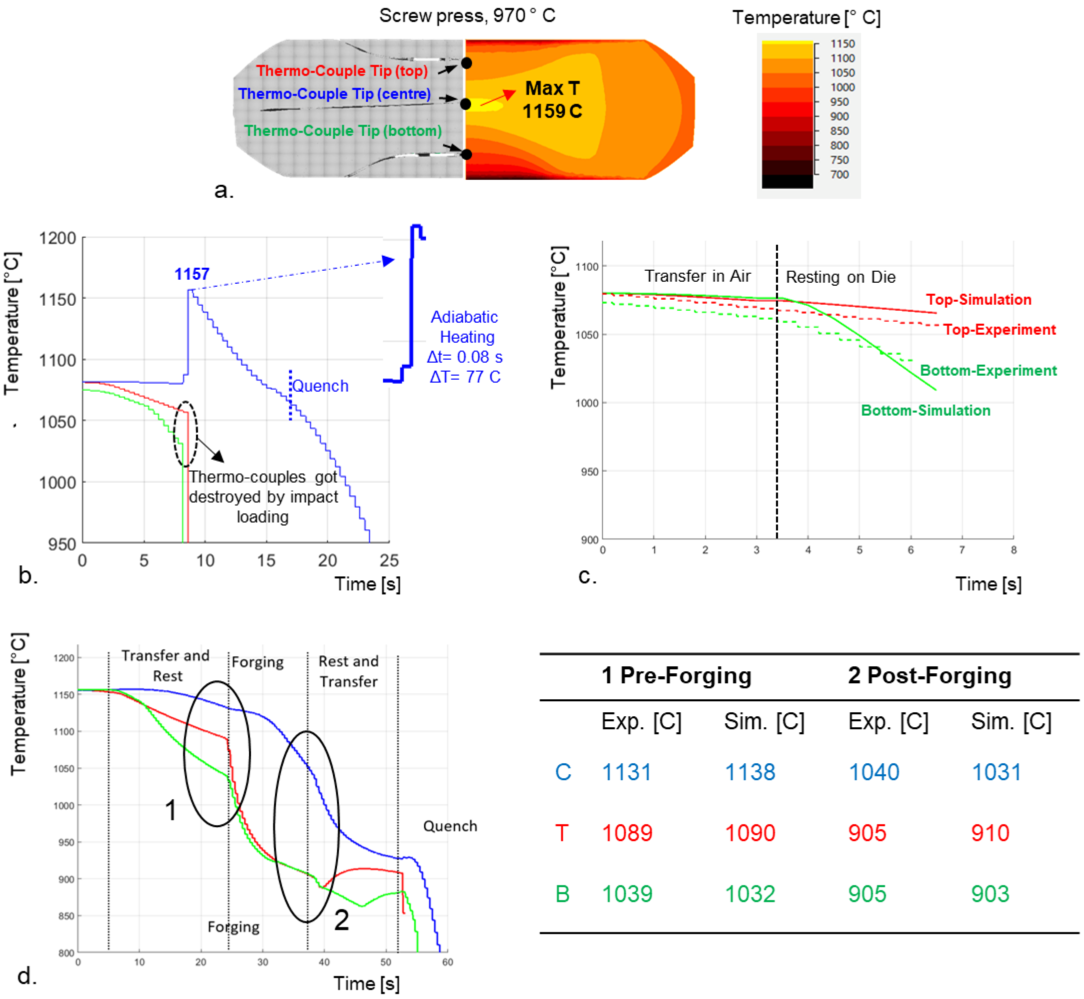

	1 Pre-Forging		2 Post-Forging	
	Exp. [C]	Sim. [C]	Exp. [C]	Sim. [C]
C	1131	1138	1040	1031
T	1089	1090	905	910
B	1039	1032	905	903

Figure 3. 14. Temperature field validation with thermo-couples: a) Thermo-couple position and temperature field from simulation, b) Thermo-couple recordings of screw press forgings, c) Comparison between thermo-couples and simulations, d) Thermo-couple recording of hydraulic press forging.

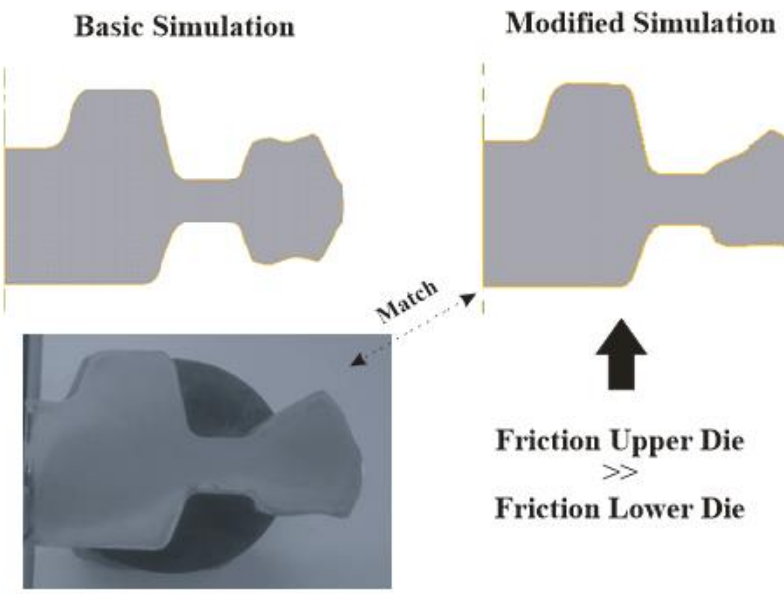

Figure 3. 15. Boundary condition adjustments. In the top part are shown screenshots of simulation, while in the bottom part it is shown a picture of the real workpiece.

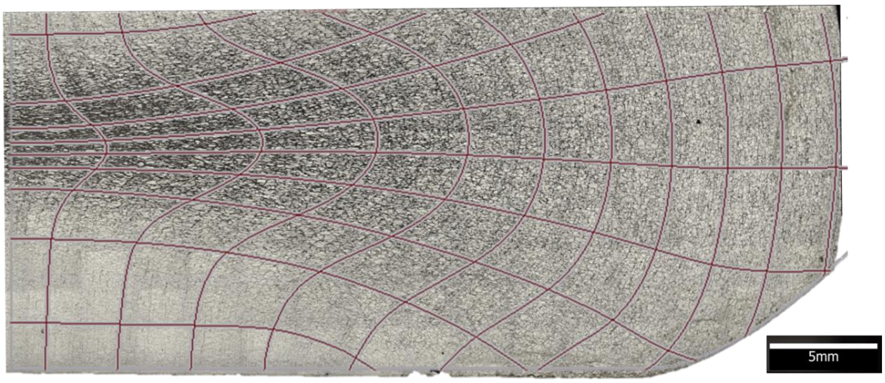

Figure 3. 16. Comparison of flow lines from optical microscope and simulation (purple overlapping lines).

Lastly, the recorded load of the press (raw load from presses are shown in Appendix 3.3.2 and 3.3.3) can be related to the stress state in the material, which depends mainly on the material data present in the database. This is one of the main constraints of FE modelling as the material data used is limited to 0.7 strain, and obtained from uniaxial loading conditions. After this point, the software extrapolates data, but in reality it is the microstructural evolution of the material that dictates its mechanical behaviour. Thus, without a coupled microstructural model it is not possible to accurately simulate loading conditions. However, a methodology was employed to try and replicate as closely as possible the load curve recorded by the press. This is illustrated for the example of the Double Truncated Cone forged at 1150 °C on the hydraulic press. Firstly, the standard data used in FE modelling of IN718 hot forging is available in the temperature range 900 °C to 1200 °C. However, during non-isothermal processes we have cooling due to air transfer and the low temperature of the dies. For this reason, several parts of the workpiece may have a temperature lower than 900 °C during deformation, especially in sub-solvus forgings. In order to bridge this gap, data for lower temperatures was adapted from other studies [81]. Moreover, standard data present in QFORM and Deform was taken from Prasad et al. [37]. However, this was obtained for a microstructure of 6 microns average grain size. As was noted previously, the initial microstructure in this study was approximately 100 microns, for this reason flow stress data was taken from Sui et al. [36] where experiments were carried out with a 90 microns average grain size.

The data taken from the press was then compared to the simulation prediction as shown in Fig. 3.17 a., where it can be seen that there is an underestimation of the load. This could be due to a variety of reasons. The first check that was done was the effect of the simulation type (2D vs 3D). In Fig. 3.18 b-d it is clear that no significant different is visible between 2D, full 3D and 3D with ¼ symmetry.

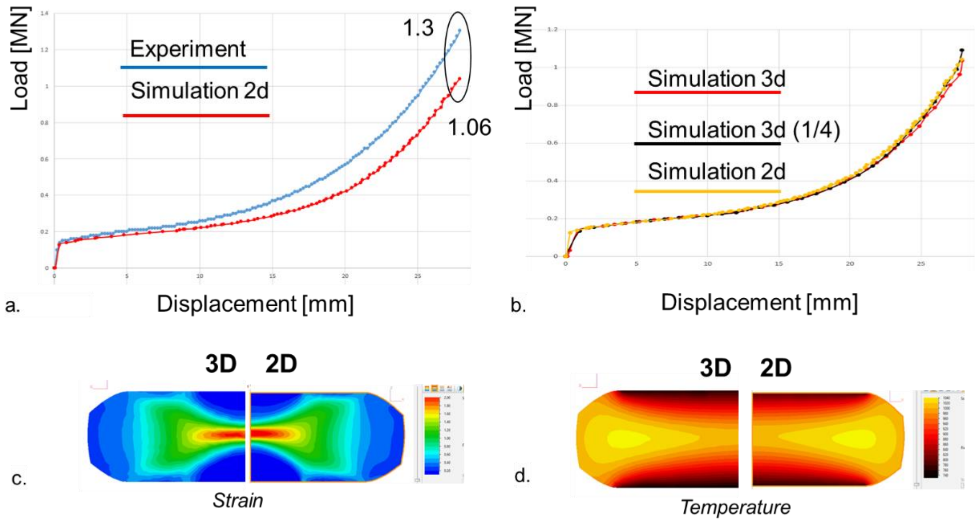

Figure 3. 17. a) Load Comparison between simulation and experiment for DTC forged at 1150 °C; b) Load comparison between different simulation set-ups; c-d) simulation comparison of 2D and 3D strain and temperature fields.

Other possible reasons for the difference in load are inaccuracies in the thermal field, friction, geometry and inaccurate material data. While the thermal field can be assumed to be calibrated through the use of thermo-couples, friction cannot be measured during the forging. For this reason a sensitivity study was carried out on the effect of the friction factor by varying it from 0.4 to 1, however even this sharp increase did not significantly change the load (increase of 0.05 MN). The volume of the billet was double checked and found to be correct. Thus, it can be hypothesised that the available material data was not reflective of material used in the experiments.

Load in the simulation is calculated by multiplying normal stress σ_{zz} by the contact area A as shown in Eq. (3.2)

$$P = \sigma_{zz} \cdot A \tag{3.2}$$

Assuming that the equivalent stress σ_{eq} is proportional to the normal stress σ_{zz}, and given that the ratio between the recorded load from the press and the simulated load is known, it is possible to derive the equivalent stress σ_{eq} to be inserted into the flow stress data to achieve the target load. To do this it is necessary to perform a 3D simulation of the process, identify the relevant strain rate and temperature ranges, take the known ratio of normal stress σ_{zz} and derive the required σ_{eq}.. This process is illustrated in Fig. 3.18 and Fig. 3.19. Given the fact that initial load is correct and discrepancy increases with displacement, two different instants were used: mid-deformation and at the end of deformation. It was found that in the range of strain rates between 0.05-0.1/s and temperatures 750-900 °C, the equivalent stress should be increased between 20% and 30%. By doing this it was possible to achieve the results shown in Fig. 3.20.

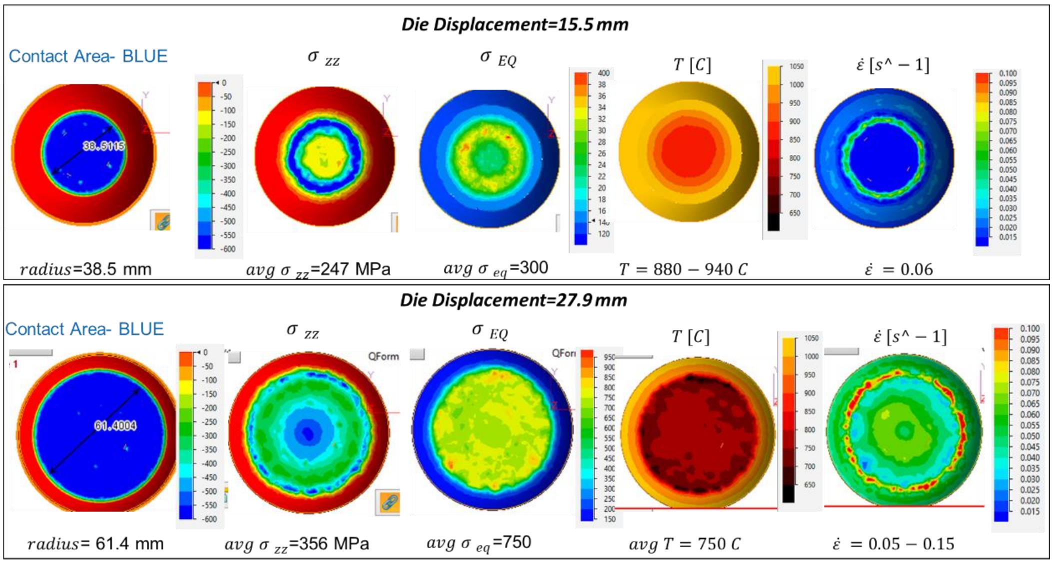

Figure 3. 18. Relevant strain rate, temperature, normal and equivalent stresses and contact area for two deformation instances.

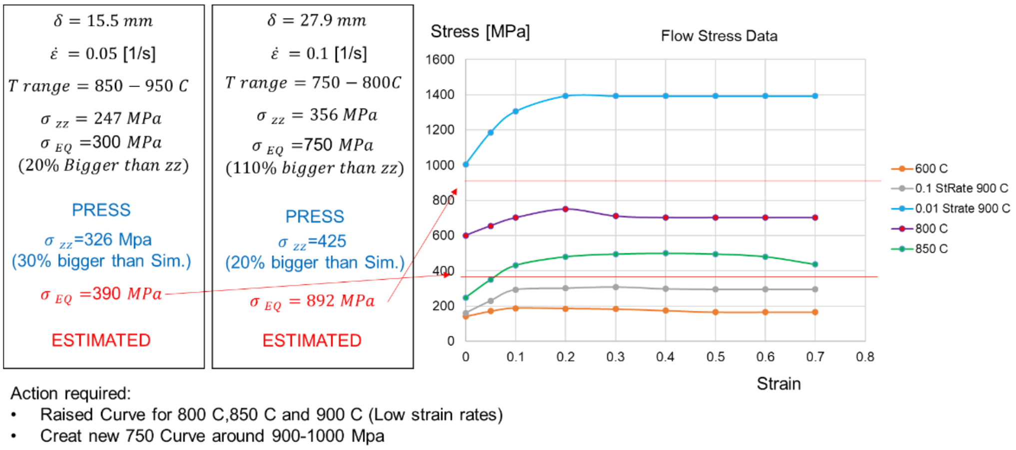

Figure 3. 19. Derivation of flow stress increment required for identified temperature and strain rate ranges.

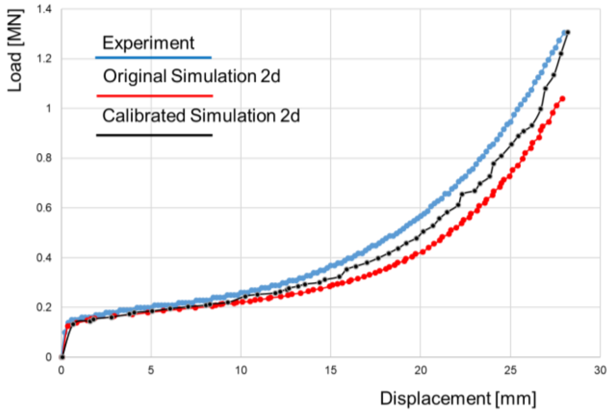

Figure 3. 20. Load comparison after calibration.

3.3.3 User Sub-routines

Most modern FE software packages offer capabilities for the implementation of customised user subroutines. These are codes that may be used to perform additional calculations on top of simulations involving parameters such as stress, temperature, strain rate, strain and so on. This functionality is of great importance because it greatly expands the capability of finite element software. Each software suite has its own language and capabilities. In this study, user-subroutines were written in the LUA language [68]. The two main types of user-subroutines are:

- Post-processor: these sub-routines will not impact the simulation while it is running.
- Coupled: these sub-routines will impact directly on the simulation while it is running (e.g. changing flow stress in material).

In the present work post-processor sub-routines were implemented. They were mainly used for two purposes: to get additional information from the simulation for calculation (e.g. strain energy) and to test the microstructural models.

Time, s	X, mm	Z, mm	Temperature, °C	Mean Stress, MPa	Plastic strain	Effective Stress, MP	Strain-rate, 1/s
0	1.028592	2.284482	864.9407127	-253.7914409	0	229.8341101	0.002802892
0.5	1.028977	2.283749	794.9613062	-248.842327	0.001401446	189.7827888	0.001161485
1	1.029134	2.283531	754.4965319	-244.8734241	0.001982189	166.4188493	0.000553197
1.12463	1.02915	2.283516	746.6263738	-243.7905974	0.002051134	149.0836901	0.000270461
1.477739	1.029167	2.283502	732.0568714	-220.7358371	0.002146636	135.6401474	0.000151788
1.967558	1.029175	2.283497	718.6500111	-199.6167175	0.002220985	121.5898341	7.34076E-05
2.000087	1.029175	2.283497	717.8096849	-200.1860332	0.002223372	112.6131401	4.16395E-05
2.407878	1.029177	2.283496	709.516923	-185.2372403	0.002240353	108.6951818	3.2691E-05
2.890457	1.029178	2.283495	701.6893087	-174.8621593	0.002256129	101.460064	1.97089E-05
3.280337	1.029178	2.283495	696.1949231	-163.0643182	0.002263813	99.52852976	1.67073E-05
3.746049	1.029178	2.283495	690.4883451	-154.8862021	0.002271594	96.0910916	1.16172E-05

Figure 3. 21. Example of tabular data extracted from QFORM simulation containing thermo-mechanical history.

3.3.4 Point Tracking and MATLAB Post-Processing

Another fundamental feature necessary for the methodology designed in this work is *Point-tracking*. This is a useful tool present in most finite element software packages. It allows the tracking of the thermo-mechanical histories of specific points in the simulated workpiece. This can be done by selecting points and tracking them forward or backwards. These data sets can be then imported into data analysis software (e.g. Excel, MATLAB) to be processed. All the fields calculated in the main simulation and in the sub-routines can be exported as shown in Fig. 3.21. Thermo-mechanical trajectories from the FE software were imported into MATLAB in the form of tables. These were then processed and analysed – the detail of this will be covered in later chapters.

3.3.5 Sensitivity Analysis: Finding the Error in the Extraction of Thermo-Mechanical Trajectories

A sensitivity analysis was carried out to establish the effect of uncertainties in the extraction of thermo-mechanical data from the modelling. This was needed to prevent the generation of hypotheses/conclusions from wrong data. In Fig. 3.22 the trajectories of points distanced 0.5 millimetre apart were compared. The direction of the displacement between the two points was chosen so as to represent the biggest gradient in properties. The 0.5 mm accuracy was taken as the value of the mesh size and the accuracy of the metallographic analysis, as detailed in a latter section of this chapter (see 3.4). The point locations were selected in different boundary zones as shown in Fig. 3.23. All of the points show a small deviation between the pair of trajectories, however some small differences can still be observed. When plotting thermo-mechanical histories these deviations results in an error of ±4°C, ±0.4 [1/mm] for high strain rate forgings, and ±0.003 strain. While these deviations errors in the plotting of the thermo-mechanical trajectories can play a marginal role in the quantitative measurements, they should not affect qualitative conclusions derived from this investigation.

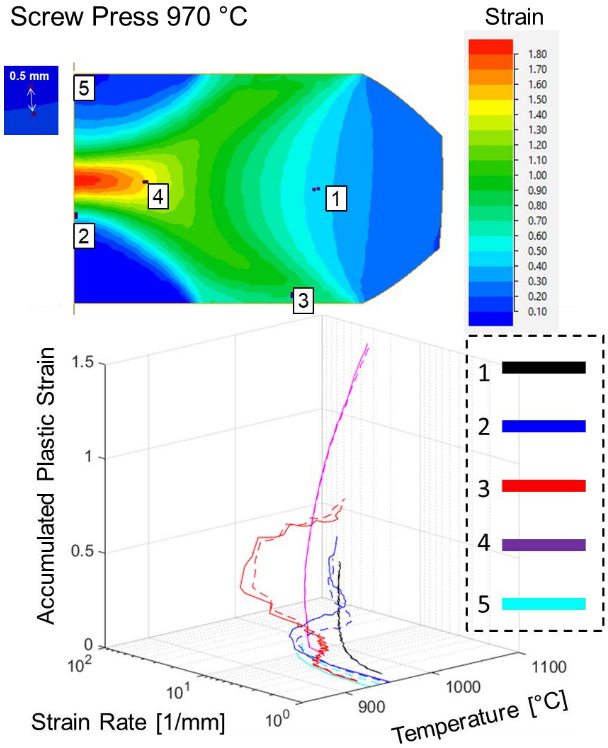

Figure 3. 22. Sensitivity analysis: Strain field from FE element simulation and point location (top); plotted thermo-mechanical trajectories of highlighted points (bottom).

3.4 Metallographic Analysis

A combination of optical and electronic microscopy was used to investigate the microstructure of samples. A schematic of the advantages and disadvantages of the two methods mentioned can be found in Table 3.3. The main investigated microstructural features were: deformation effects, grain sizes, grain morphologies, dislocation densities and levels of recrystallisation.

Optical microscopy was used for most of the analysis because it proved much faster in term of set-up and image capturing times. Moreover, it allowed the collection of bigger maps which gave a general overview of the various zones in the samples (e.g. Recrystallised, Deformed Grains, Dead-Zones). One of the main shortfalls of optical analysis is the low magnification achievable. This problem however was partially evaded due to the relatively large size of the grains (approximately 100 μm for original grains and 1-10μm for recrystallised grains), rendering the available magnifications sufficient. Nevertheless, SEM and EBSD analysis were performed for specific locations in which detailed information was needed (e.g. recrystallised volume fraction).

The results of the metallographic analysis had to be compared to the data from the finite element modelling. It was therefore necessary to know the exact location of the recorded microstructures. For this purpose, a template (shown in Appendix 3.2.1) was created in which the coordinates of the points of interest were documented together with reference points in the workpiece which would enable cross referencing to the respective positions in the simulations. However, this coordinate transposition had a limited precision level. Indeed, the magnification influences the accuracy for which these locations may be tracked (high magnifications correspond to less accuracy). Moreover, some microstructural characteristics (e.g. nucleation boundaries, recrystallisation zone boundaries etc.) are hard to distinguish with absolute certainty. It was for these reasons that the accuracy level obtained for the microstructural analysis corresponded to 0.5 millimetres.

Table 3. 3. Advantages and Disadvantages of Optical and Electronic Microscopy

	Advantages	**Disadvantages**
Optical	• Fast • Big Maps	• Low magnification • Basic Information
Electronic (SEM/EBSD)	• High magnification • Detailed information	• Slow • Small Maps

3.4.1 Material Preparation

Once the forgings were complete the workpieces had to be sandblasted and cut using wire EDM as shown in Fig. 3.23. Two central facing slices of the workpieces were taken: one slice was kept whole while the other was cut into sections to fit the size needed for electron microscopy. The metallographic preparation was the same for samples intended for both optical and SEM. The only difference in preparation between the two lay in the etching. Indeed, only the samples destined to optical analysis were etched to reveal the microstructure. An example of the final samples ready to be analysed at the microscope is given for workpiece#10 from Table 3.1 in Fig. 3.24.

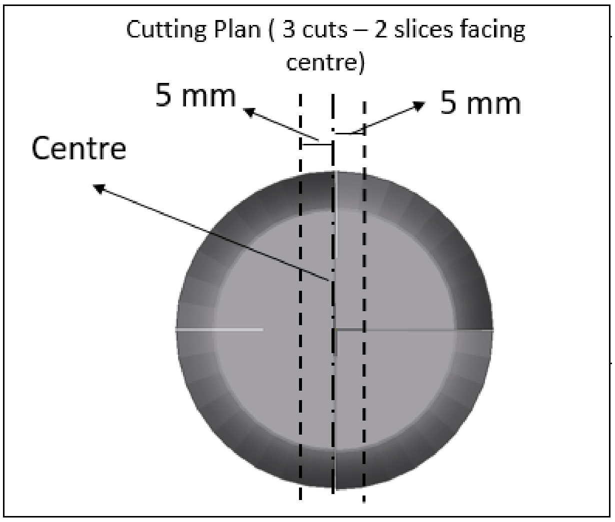

Figure 3. 23. Cutting explications – Example from DTC.

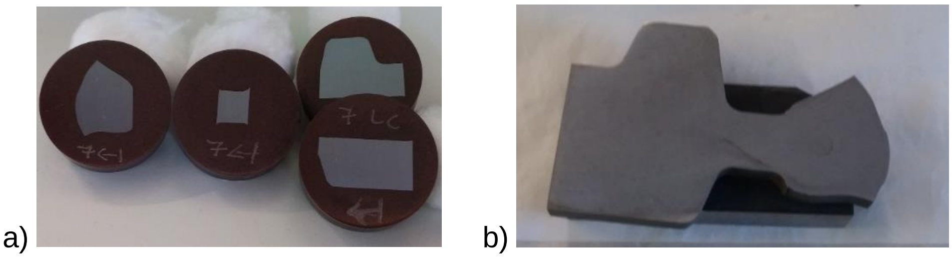

Figure 3. 24. Workpiece#10 final preparation for a) Electron Microscopy b) Optical Microscopy.

3.4.2 Optical Microscopy

Optical microscopy was carried out with two main purposes: get a fast overview of the main microstructural areas (e.g. dead and deformed or recrystallised zones) and capture specific metallographic features and/or characteristics (e.g. grain size). This analysis was carried out with the Leica DM12000M Optical Microscope (Magnification range 5x – 100x).

With regard to etching, the visual results of the etching process are influenced by many parameters (e.g. processing history, etchant contact time, etchant composition). In each sample there are present many different zones with unique characteristics, making it impossible to achieve uniform etching along the sample. For example, in different zones grain boundaries or twinning may be more visible and colour shades may be different as shown in Fig. 3.25.

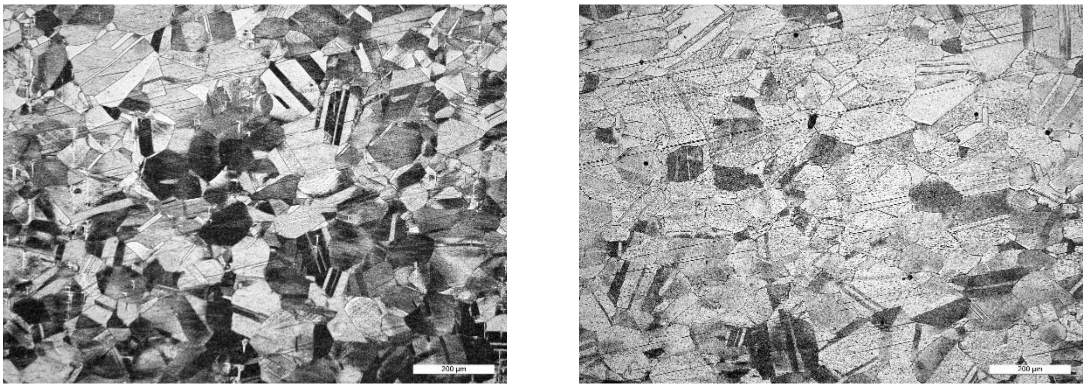

Figure 3. 25. Optical micrograph showing different etching effects.

3.4.3 Electron Microscopy

Scanning electron Microscope (SEM) and Electron Backscatter Diffraction (EBSD) analysis were employed in this study using an FEI/Oxford Instruments Quanta 250 FEG SEM. The image quality and magnification capability of the SEM are superior overall to the optical analysis. However, it is necessary to achieve a better material finish through the metallographic preparation to get quality images. One important distinction between the SEM and optical analysis is the ability of the SEM to capture deformation within the grains. Deformed material will appear distorted while unreformed material will be sharper. An example of this can be seen in Fig. 3.26.

The settings used for the SEM and EBSD were:

- Aperture: 3-4
- Voltage: 15KW – 20 KW
- Spot Size: 4.5
- Mag: 100x-10000x
- EBSD Tilting: 70°
- EBSD Spot Size: 0.2-1 µm

EBSD maps were used when necessary as will be discussed further on in this thesis. For example, to estimate the recrystallised volume fraction, and to get specific information not obtainable with other methods (e.g. grain and sub-grain orientations). The biggest limitation of EBSD is related to the resource availability. An EBSD map with the available equipment takes between 7-15 hours, thus making it impractical as the main metallographic tool.

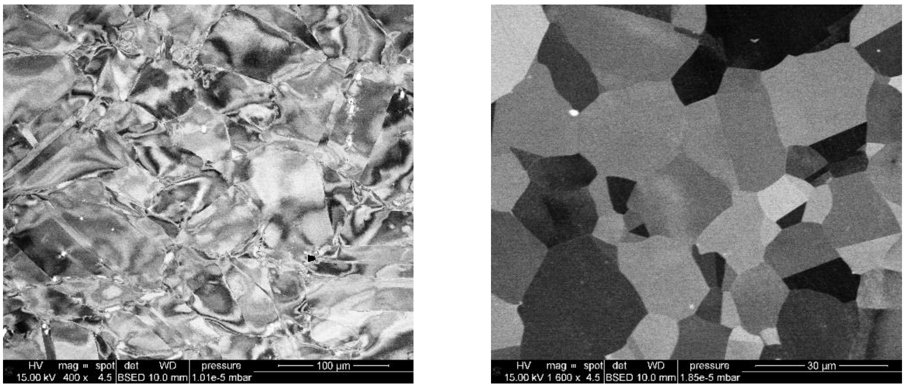

Figure 3. 26. SEM Images: a) Deformed Grains, b) Un-deformed Grains.

3.4.4 Image Analysis For Optical and EBSD Images

The analysis of the images involves the extraction of relevant data such as grain size, aspect ratio of grains and recrystallised zones. There are numerous methods to calculate average grain size in a material as specified in ASTM Standards [11]. If the grain structure is homogeneous then the Planimetric (Jeffries) procedure can be used, in which a circle of is drawn on the image. The average grain size can be estimated by calculating the number of grains per square millimetre at 1X *(N_A)* through Eq. (3.3):

$$N_A = f\left(N_{\text{Inside}} + \frac{N_{\text{Intercepted}}}{2}\right) \tag{3.3}$$

in which, N_{inside} correspond to the number of grains inside the circle, $N_{intercepted}$ to the number of grains crossed by the circle and *f* is factor dependent on magnification which can be taken from the ASTM standard. An example of this is shown in Fig. 3.27 in which the data for the initial grain size is shown. In this case the calculated parameters were:

$N_{Inside} = 39$, $N_{Intercepted} = 23$, $f=1.3$, $N_A = 65.65$

By comparing the number of grains per square millimetre, it is possible to identify the closest grain class which is represented by N_A= 62, Grain Size number

=3.0 and thus an average grain size of 127 μm. However, since the calculated concentration N_A is higher than the value presented above it is fair to assume a slightly lower average grain size.

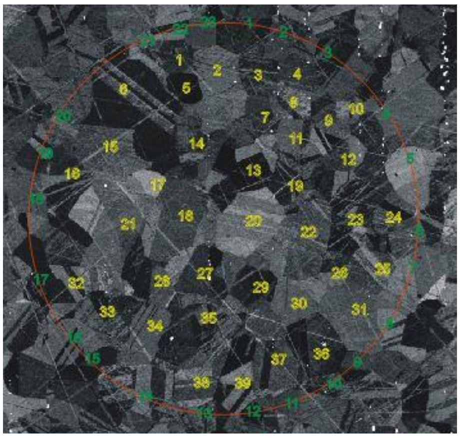

Figure 3. 27. Illustration of Jeffries Method for calculating average grain size (SEM micrograph).

This method can be used to calculate grain size in homogeneous microstructures. However, it is often not known if the grain distribution at hand is homogeneous or not. For this reason, another method was employed for the measurement of grain size. Taking an optical image, the measurement of at least 50 grains was recorded through the software, ImageJ. Each grain would be measured along its biggest dimension and the orthogonal to this. Then the results would be processed through MATLAB using an original code (shown in Appendix 3.5.1), to plot grain distribution and obtain average grain size. This latter parameter can be obtained in different ways. One of the common ways of calculating average grain size is by considering the number of grains which correspond to specific grain size and thus calculate the average by frequency, however the results of this calculation may not be representative of an area. If we consider a microstructure with many small grains and a few big grains, the effect of the big grains would not impact the average. A more representative parameter is average grain size by area, in which the area volume fraction occupied by grains is counted towards the average. The MATLAB code used in this investigation can plot both distribution of grains by frequency and by area as well as calculating the average grain sizes as shown in Fig. 3.8.

Recrystallisation volume fractions and related zones were analysed mainly through optical images. This was done through qualitative comparison and in certain instances a method proposed by Chen et al. [82] which calculates the recrystallised volume fraction based on the equation:

$$X = 1 - \frac{N_{in}}{N_0} \tag{3.4}$$

Where N_{in} is the number of pixels for initial grains which are not replaced by DRX grains, and N_0 is the total number of pixels of the optical micrograph.

3.4.5 EBSD Post-Processing

Where appropriate, EBSD maps were taken and then processed through the MATLAB free extension MTEX [83]. In contrast to the Channel 5 suite, with MTEX it is possible to directly manipulate data obtained from maps as MATLAB variables. Scripts can be generated to automate tasks and repeat analyses on multiple scans. This however results in much more complexity compared to other software, as MTEX is used through the MATLAB command line and thus much less user friendly. For this reason an original MATLAB application, shown in Fig. 3.28-31, was developed using the MATLAB App Designer package to process EBSD data and generate a variety of maps, among which are:

- Grain Boundary
- Grain Orientation Spread
- Twin Boundary
- Kernel Average Misorientation (KAM)
- Grain Average Misorientation (GAM)
- Grain Orientation (Euler)
- Inverse Pole Figures

Moreover, several calculation capabilities were added such as calculation of recrystallised volume fraction and average grain size distributions (both by frequency and by area). The recrystallised volume fraction was estimated through different techniques as illustrated in Fig. 3.32. In addition to grain orientation spread, given the big difference between original grains (≈100 µm) and recrystallised grains (≈1-10 µm), grain size was used as a parameter to calculate RX volume fraction. The error through which the recrystallisation boundary was identified was approximately 5%.

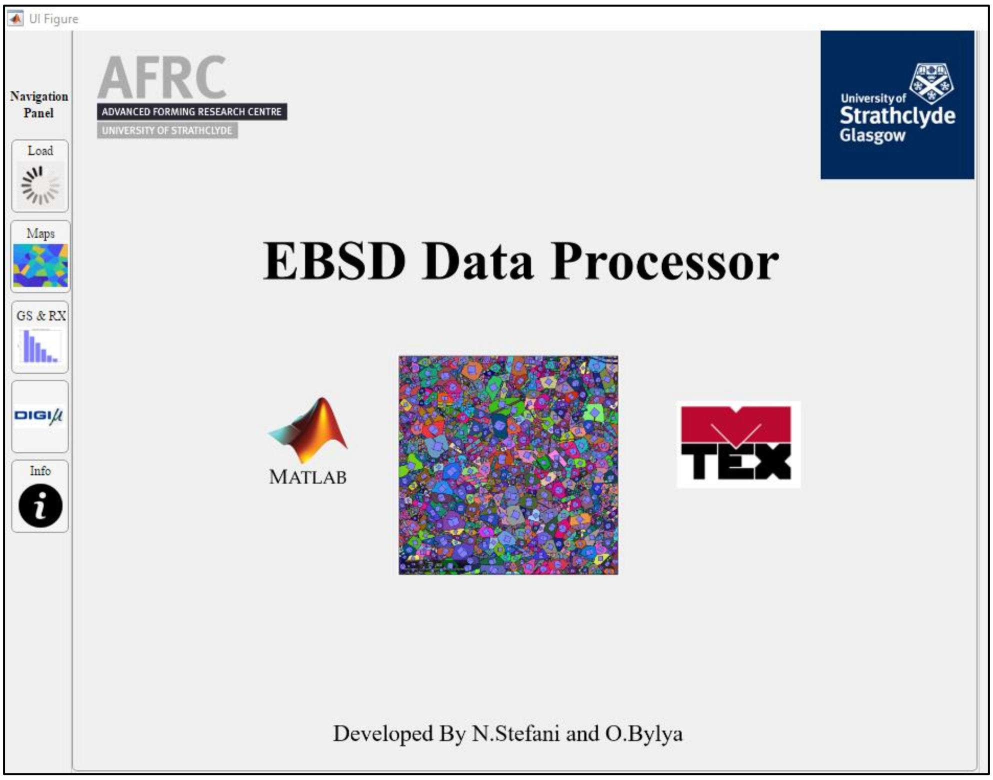

Figure 3. 28. MATLAB GUI using MTEX for processing of EBSD data-Main page.

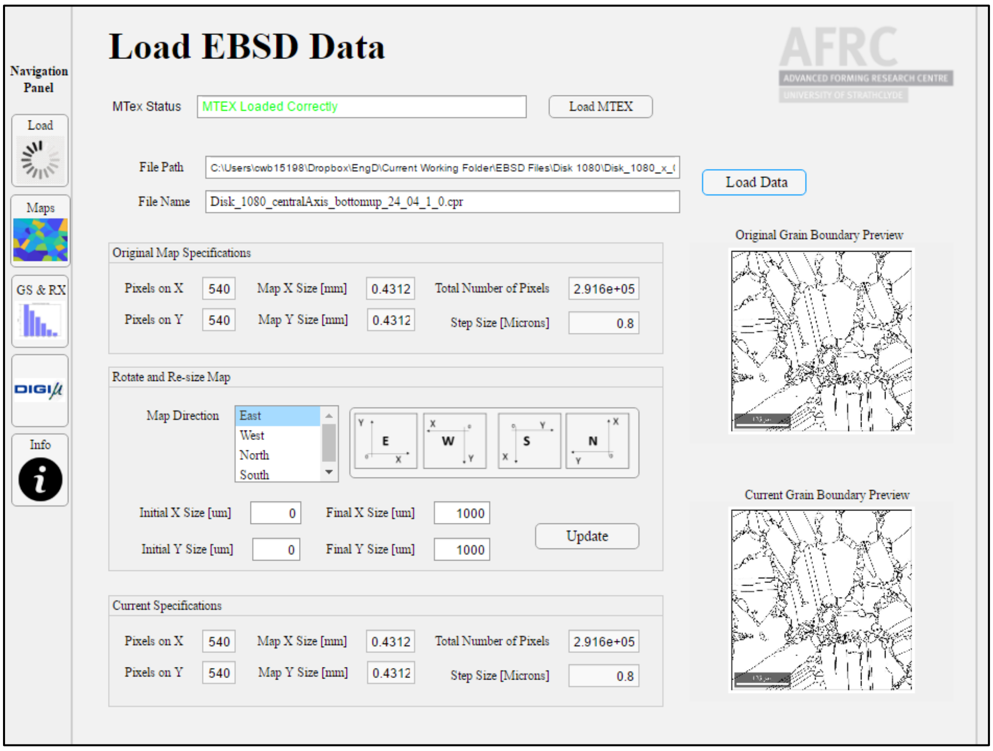

MTex Status: MTEX Loaded Correctly

File Path: C:\Users\cwb15198\Dropbox\EngD\Current Working Folder\EBSD Files\Disk 1080\Disk_1080_x_(

File Name: Disk_1080_centralAxis_bottomup_24_04_1_0.cpr

Original Map Specifications

Pixels on X: 540
Map X Size [mm]: 0.4312
Total Number of Pixels: 2.916e+05
Pixels on Y: 540
Map Y Size [mm]: 0.4312
Step Size [Microns]: 0.8

Rotate and Re-size Map

Map Direction: East (West, North, South)
Initial X Size [um]: 0
Final X Size [um]: 1000
Initial Y Size [um]: 0
Final Y Size [um]: 1000

Current Specifications

Pixels on X: 540
Map X Size [mm]: 0.4312
Total Number of Pixels: 2.916e+05
Pixels on Y: 540
Map Y Size [mm]: 0.4312
Step Size [Microns]: 0.8

Figure 3. 29. MATLAB GUI using MTEX for processing of EBSD data-Loading page.

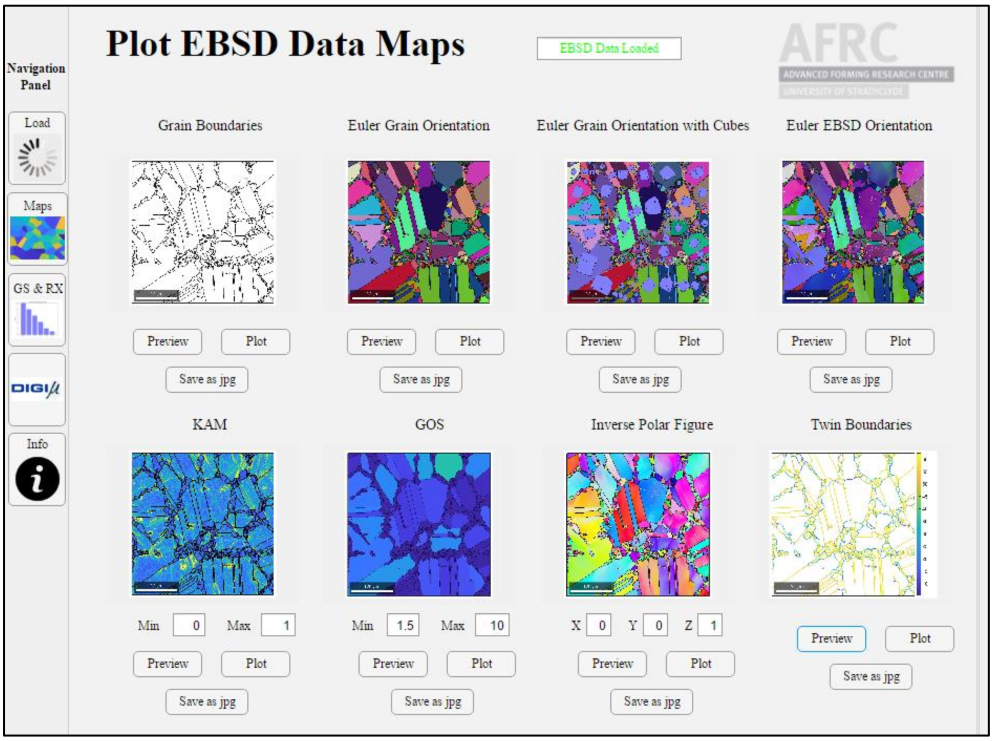

KAM: Min 0, Max 1

GOS: Min 1.5, Max 10

Inverse Polar Figure: X 0, Y 0, Z 1

Figure 3. 30. MATLAB GUI using MTEX for processing of EBSD data-Maps page.

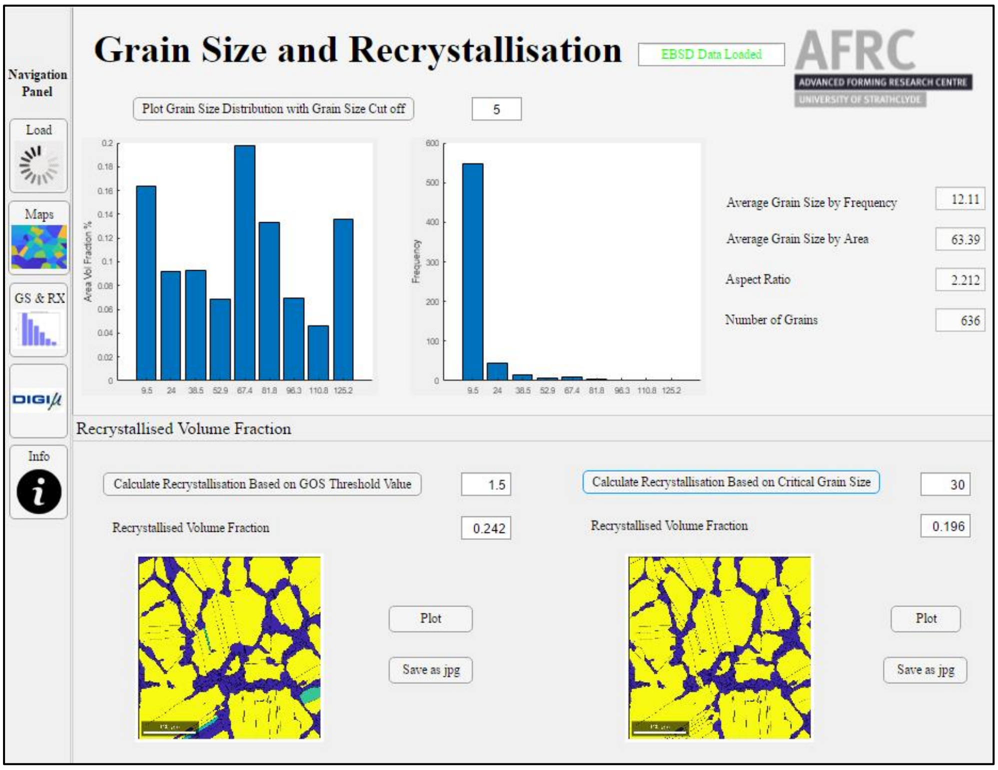

Plot Grain Size Distribution with Grain Size Cut off: 5

Average Grain Size by Frequency: 12.11

Average Grain Size by Area: 63.39

Aspect Ratio: 2.212

Number of Grains: 636

Calculate Recrystallisation Based on GOS Threshold Value: 1.5

Recrystallised Volume Fraction: 0.242

Calculate Recrystallisation Based on Critical Grain Size: 30

Recrystallised Volume Fraction: 0.196

Figure 3. 31. MATLAB GUI using MTEX for processing of EBSD data-Grain Size and RX page.

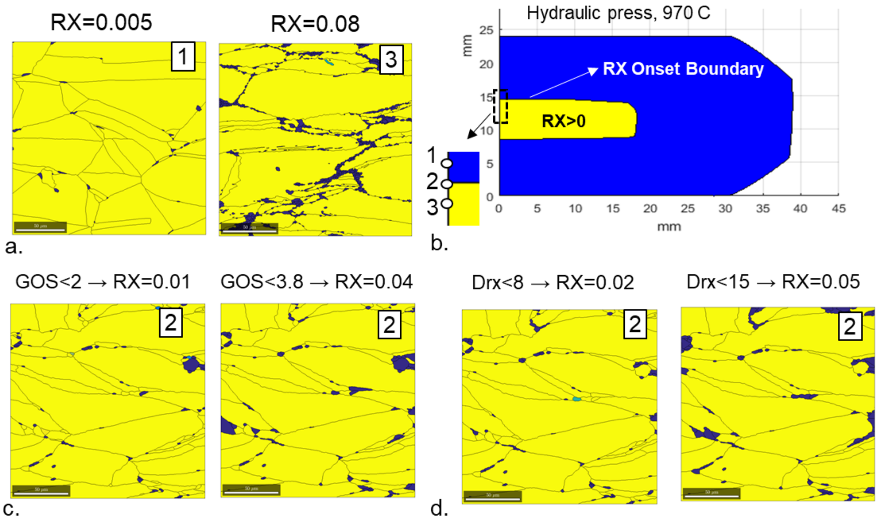

Figure 3. 32. Calculating recrystallised volume fraction through developed EBSD processor using both a GOS and a grain size threshold as shown above each micrograph (experimental iso-contour showing zero boundary is displayed in the top right).

3.5 Summary

An original methodology using industrial forging trials coupled with a tailored data processing procedure was designed and successfully implemented to bring together the parameters of microstructural transformation and mechanical behaviour. Thanks to this as shown in the next chapters, it was possible to investigate the recrystallisation phenomena from a different perspective compared to the available literature. In particular, through the zero boundary concept it was possible to analyse the onset of recrystallisation, and how different trajectories led to the same conditions. Moreover, this methodology provided an opportunity to benchmark calibrate existing microstructural models in an industrial setting.

Chapter 4

Experimental Results

4.1 Introduction

This chapter provides a summary of the experimental results. These are mainly based on hot forging experiments mimicking industrial practices and are characterised by a wide spectrum of thermo-mechanical conditions, offering a new perspective for the observation of microstructural evolution in IN718. Firstly, the results from uniaxial laboratory tests are detailed, then hydraulic and screw press forgings for the DTC geometry and lastly results from a number of disk forgings.

4.2 Uniaxial Laboratory Tests

Fig. 4.1, presents the flow stress curves resulting from the uniaxial laboratory tests. An interesting aspect from these curves, is that softening is present but not pronounced, especially at lower temperatures and in many of the curves there is no clear peak. In addition, these tests were carried out with different grain sizes. By comparing SP3, SP6 and SP4 and SP2, SP7 and SP1 it appeared the results were within the experimental error (approximately 10-20 MPa).

Microstructures in the homogeneous sections are shown in Fig. 4.2. In each specimen recrystallised grains are observed, however very limited information is available by looking at the homogeneous part of the deformation; only one final microstructural condition per sample. Moreover, it is not possible to define when recrystallisation started in the test using usual methodologies mentioned in Chapter 2, due to unclear peaks as seen in Fig. 4.1.

More information can however be obtained by analysing parts of specimens where deformation is not homogeneous (e.g. in the neck). This was done for SP3 and is the results are shown in Fig. 4.3. In this case the evolution of discontinuous recrystallisation can be observed; it appeared that serration of grain boundaries occurred before nucleation. At 950 °C, no growth of nuclei seemed to take place and recrystallised grains are characterised by a similar small grain size at different level of recrystallisation.

In this case, looking at non-homogeneous deformation the first example of a zero boundary can be observed (concept detailed in section 3.1.1). This will provide the exact amount of deformation that is associated with the onset of recrystallisation which for this specimen is approximately 0.6 strain. However, a limitation of this approach for tensile tests is that only one trajectory is available per sample. More information could be obtained by analysing non-uniaxial and non-homogeneous forgings, which will be the object of the next sections.

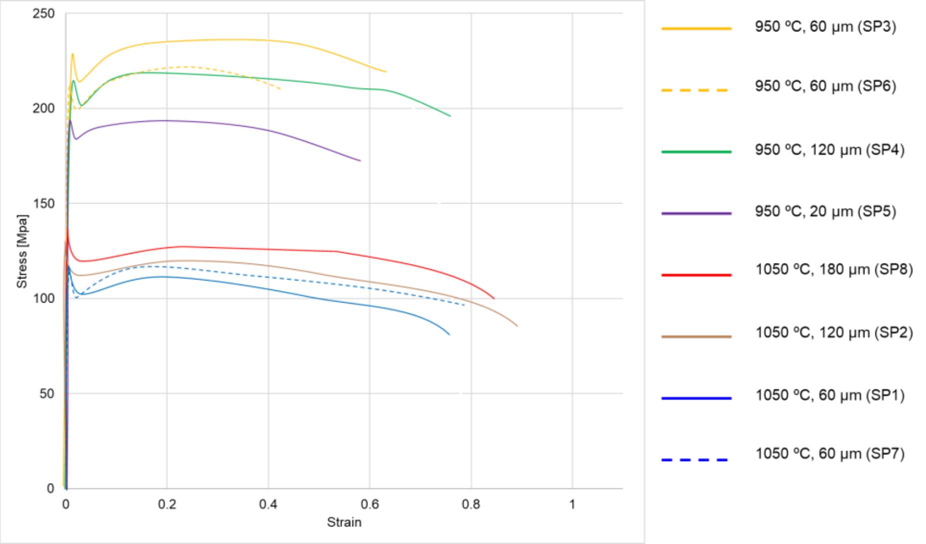

Figure 4. 1. Flow stress curves obtained from uniaxial tensile tests performed different temperatures and grain sizes.

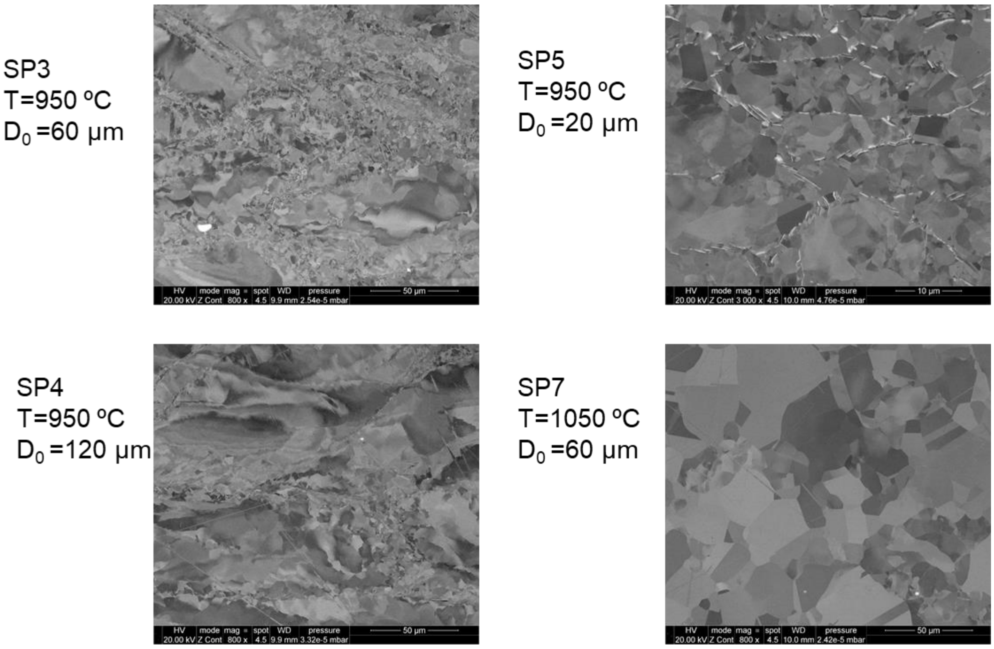

Figure 4. 2. SEM micrographs of tensile test specimens deformed at 0.005 s^{-1}.

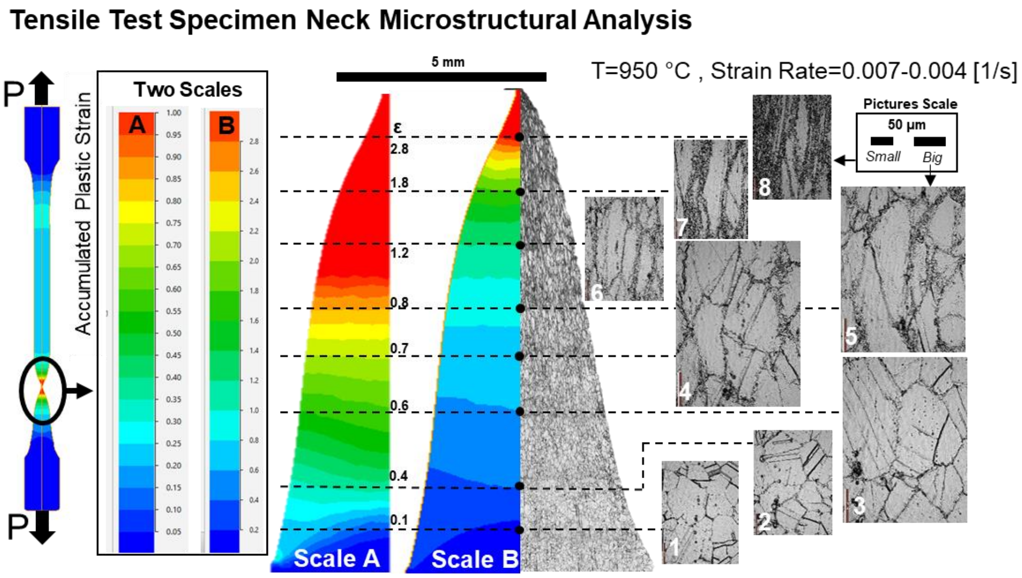

Figure 4. 3. Analysis of non-homogeneous deformation in the neck of tensile specimen. In the left side it is shown the strain field from FE simulation. In the right side are shown images taken through optical microscope of the neck area.

4.3 Hydraulic Press Forgings of DTC

Hydraulic press forgings of truncated double cones are the experiments that resemble more closely uniaxial laboratory tests due to the low and almost constant strain rates and simple geometry. However, it is important to remember that these forgings are non-isothermal and considerable cooling is present due to the lower temperature of the dies (at approximately 400 °C).

Fig. 4.4 shows the initial microstructure present in the pre-forging billets, through different maps obtained with EBSD analysis. It can be seen that there was a high amount of twin boundaries caused by preliminary heat treatment. Moreover, low levels of KAM and GOS values indicate that no deformation is stored in the material.

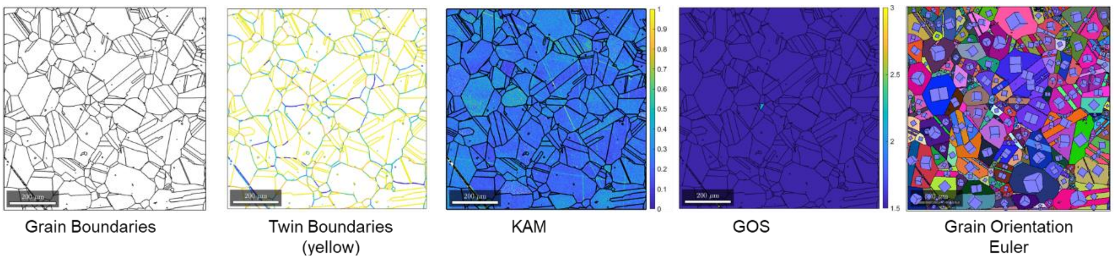

Figure 4. 4. Processed EBSD maps of preform microstructure (see Appendix 1.1 for enlarged version).

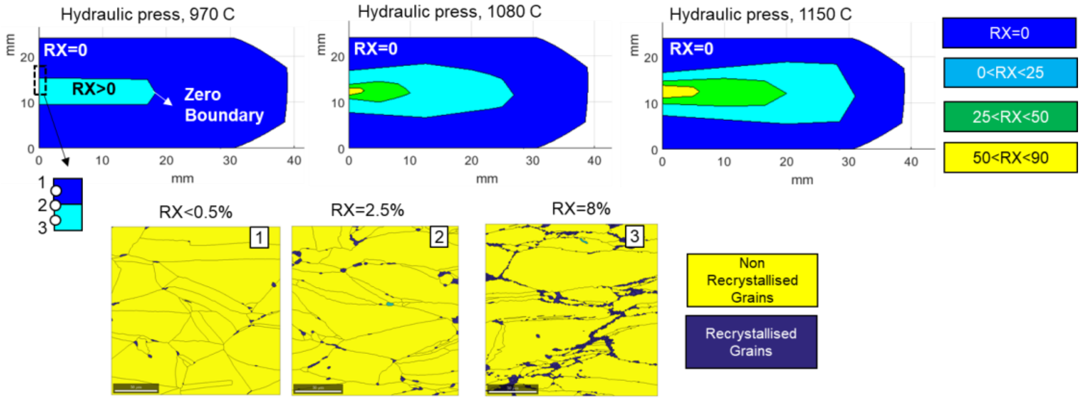

Figure 4. 5. In the top of the figure are shown experimental iso-contour maps for recrystallisation from hydraulic press forgings. In the bottom part of the figure EBSD micrographs highlighting recrystallised and non-recrystallised grains (see Appendix 1.2 for enlarged version).

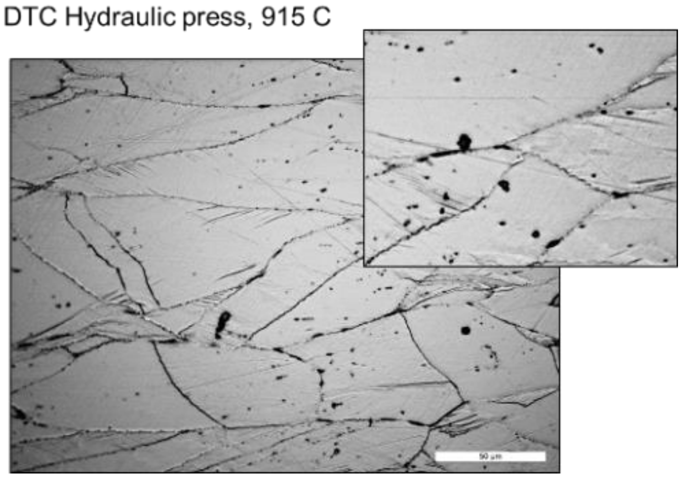

Figure 4. 6. Optical image of microstructure from DTC forged at 915 °C.

Fig. 4.5 shows the isolines for various levels of recrystallisation. Among these zones is shown the zero boundary. As a general observation, it can be seen that the shape of the boundaries is similar and as expected higher temperatures led to higher values of recrystallised volume fraction. Overall, the level of recrystallisation is relatively low. In particular, only 15% was achieved in the centre of the DTC forged at 970 °C and 55% in the centre of the specimen forged at 1080 °C. Even with an initial forging temperature of 1150 °C and a final accumulated plastic strain of approximately 2, only 60% recrystallised volume fraction was achieved. Lastly, it can be seen from Fig. 4.6 that no recrystallisation was observed in the DTC forged at 915 °C.

Fig. 4.7 shows the thermo-mechanical fields taken from the FE simulation in the final instance of deformation. It can be observed that the final temperature for both specimens is lower than the initial billet temperature due to cooling. Deformation (strain) is characterised by a cross shape, however this shape is not present in the RX iso-lines observed through microstructural analysis, which on the other hand seem to follow more closely the temperature distribution.

In the upper part of Fig. 4.8 are shown the microstructural pictures taken from the central section of the DTCs forged at 970 °C and 1080 °C. As mentioned, relatively low recrystallised volume fractions were observed. In the lower part of Fig. 4.8 sections for the central axis of the workpiece forged at 970°C are shown. With the accumulation of deformation the following microstructural changes appeared to take place: at first, grain fragmentation (or CDRX), then serration of grain boundaries and lastly nucleation. The recrystallised grains are relatively small and reach a grain size of 1-2 µm at 970 °C and 2-3 µm at 1080 °C. Similarly, local boundary serration seems to be characterised by more extensive bulging at higher temperatures. A relatively small recrystallised grain size for hydraulic press forgings seems to be in accordance with the work of Kienl et al. in which low strain rate deformation resulted in nucleation but no significant growth of the grains [84]. KAM maps show the accumulation of dislocation density closer to grain boundaries and relatively low dislocation content in the central part of the grains. In addition, it seems that recrystallised grains present a significant level of deformation.

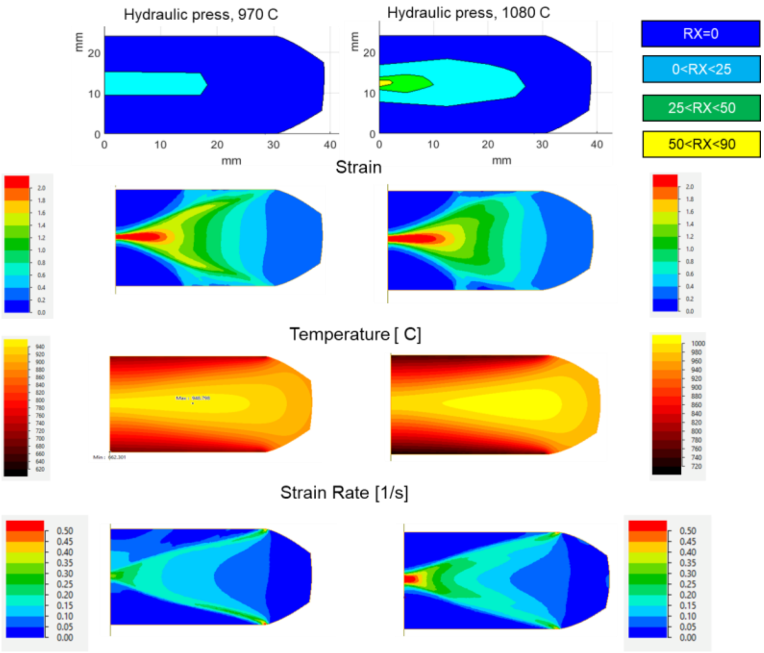

Figure 4. 7. Comparison between experimental iso-contour recrystallisation maps (top) and thermo-mechanical fields of hydraulic press forgings taken from FE simulation.

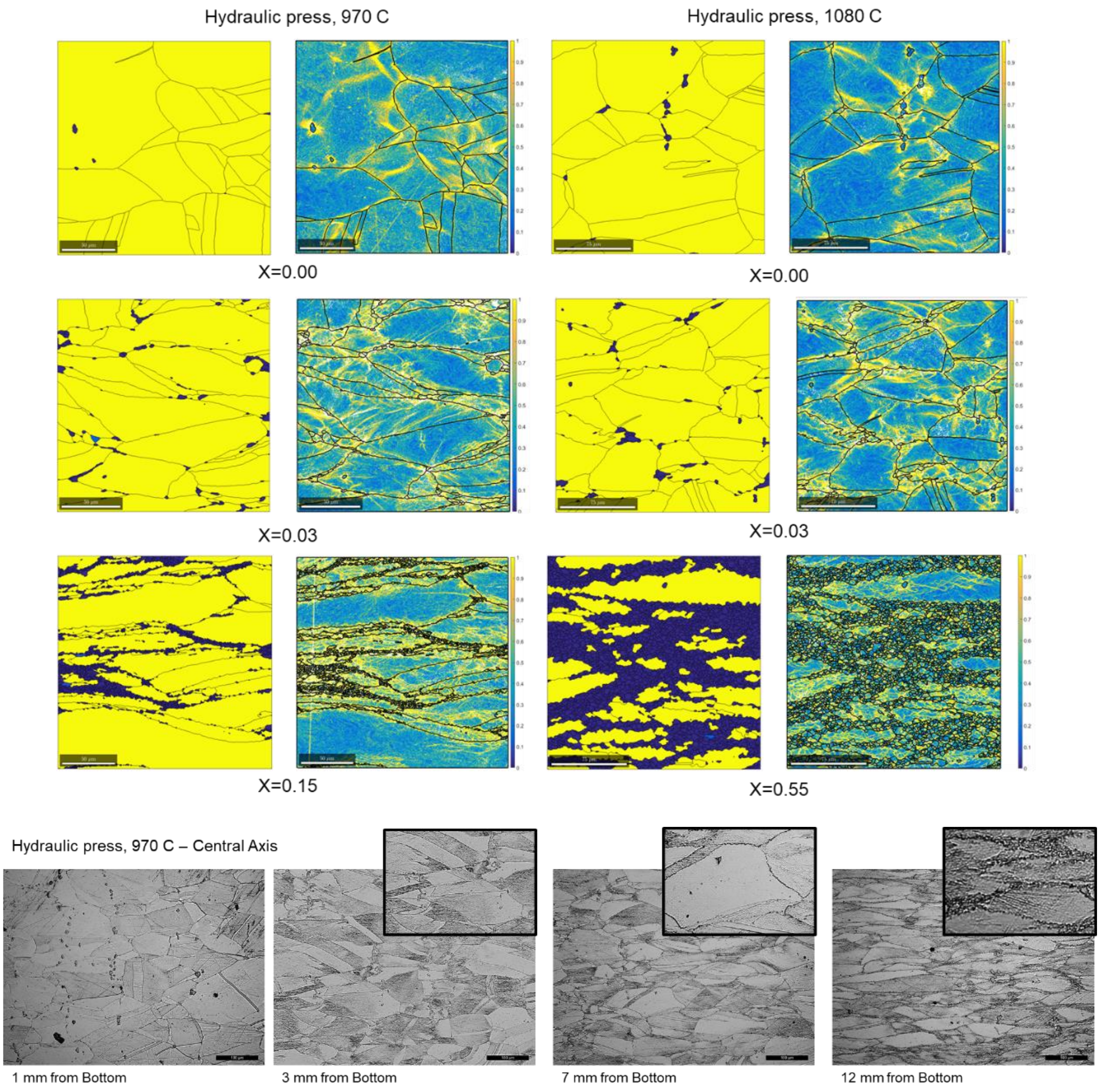

Figure 4. 8. Evolution of recrystallisation in hydraulic press forgings (see Appendix 1.3 for enlarged version). In the top part are shown EBSD micrographs of recrystallised and non-recrystallised grains (blue/yellow figure) and KAM maps. In the bottom part of the figure are shown optical micrographs taken along the central axis of the specimen.

Fig. 4.9 shows the zero recrystallisation boundary for the DTC forged at 970 °C on the hydraulic press. It can be qualitatively observed that some areas seem more deformed than others: with squeezed and fractured grains. Looking at the thermo-mechanical trajectories it can be seen that cooling took place in most points, with trajectories leaning towards the left (lower temperatures) as deformation accumulates in the strain rate range of 0-0.15/s. It can be noted that recrystallisation is initiated at very different level of strain (from 0.1 to more than 1). Fig. 4.10 shows the zero recrystallisation boundary for the DTC forged at 1080 °C on the hydraulic press. Similar observations to the previous figure with respects to temperature, strain rate and strain can be formulated and hence will not be repeated. From a qualitative perspective less fragmentation (or CDRX) and bigger bulging in grain boundaries appeared to be present compared to the DTC forged at 970 °C. Higher levels of CDRX at low temperatures have already been observed in various nickel superalloys [85]–[87].

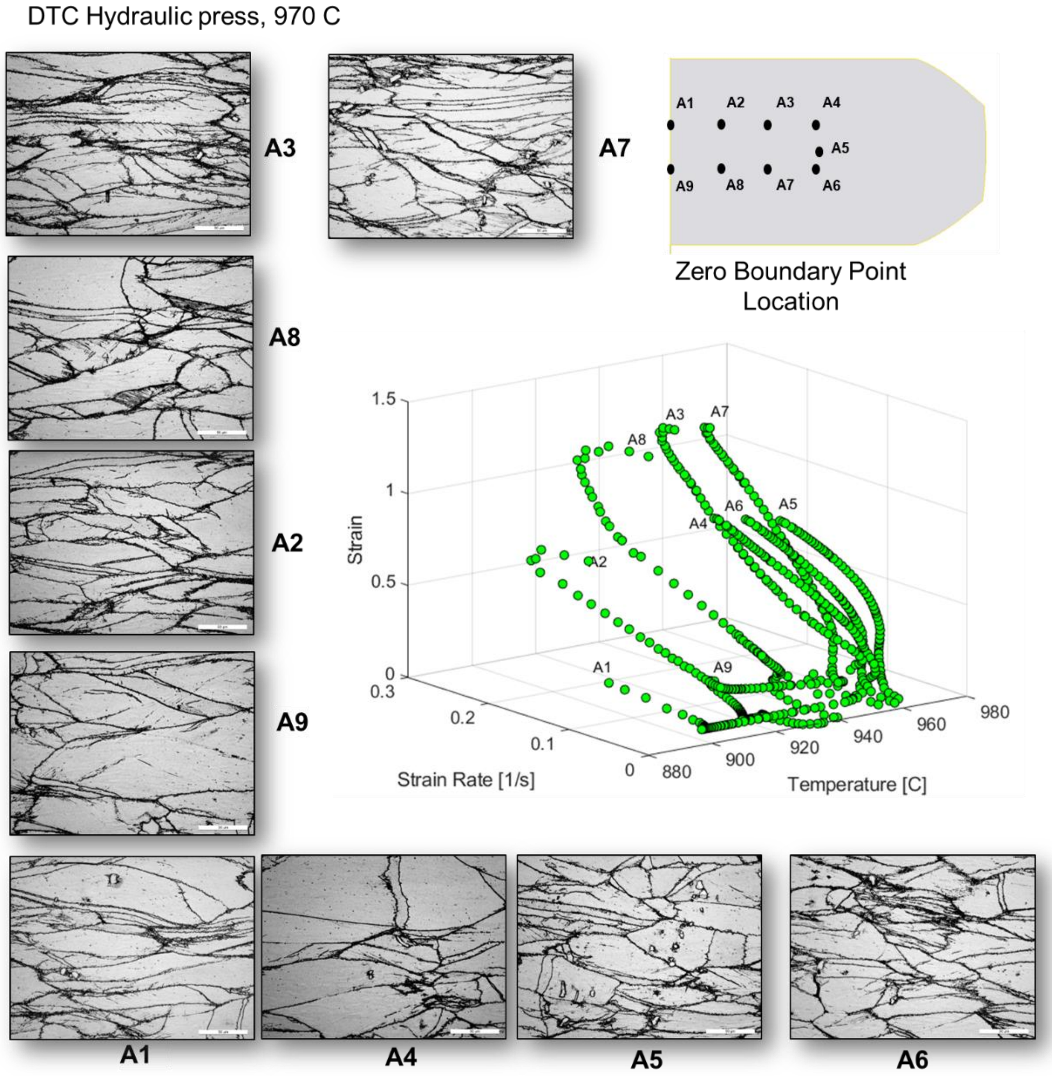

Figure 4. 9. Microstructures (taken from optical microscope) and trajectories of zero recrystallisation boundary (taken from FE simulation) for DTC forged at 970°C on hydraulic press (see Appendix 1.4 for enlarged version).

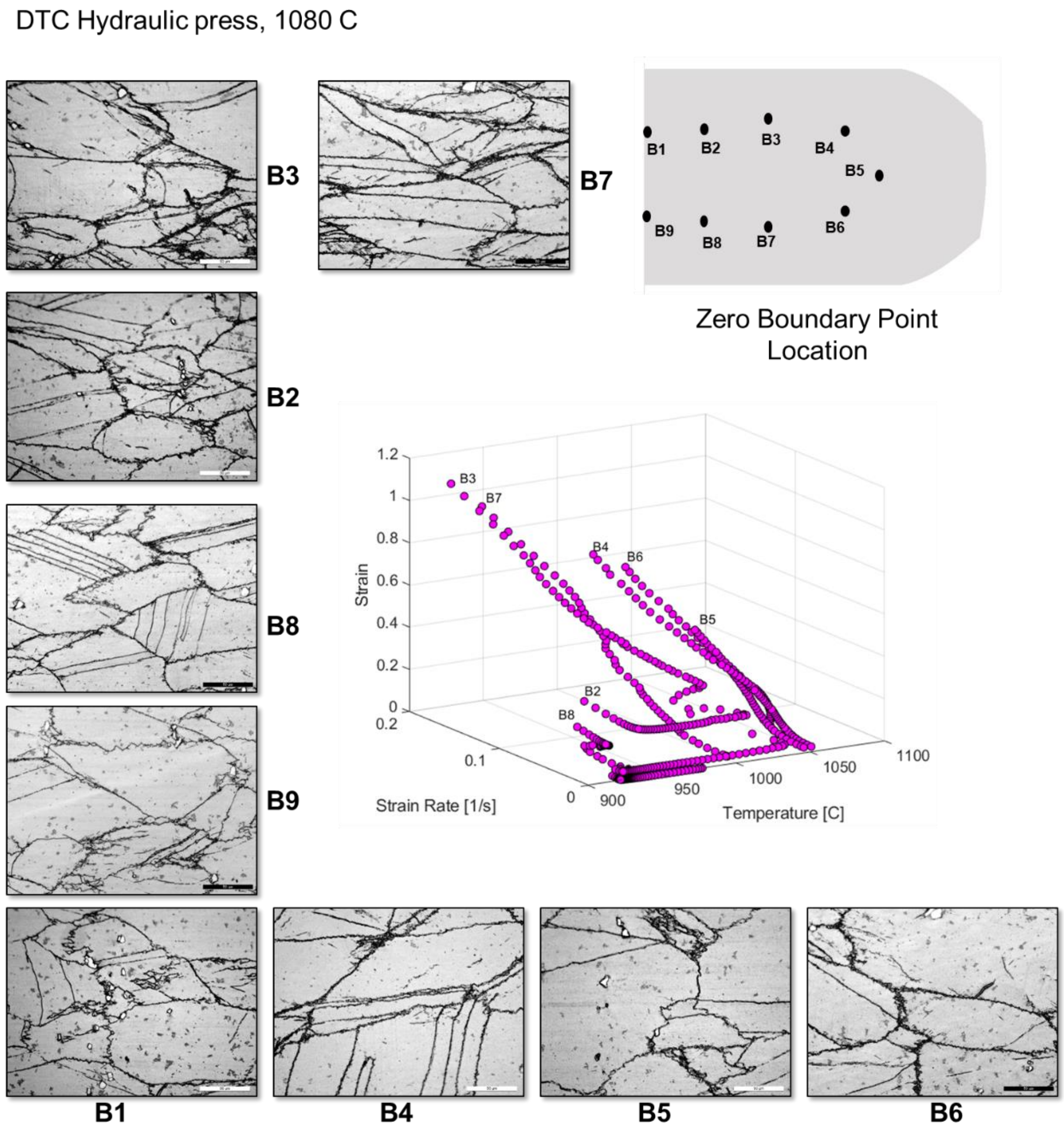

Figure 4. 10. Microstructures (taken from optical microscope) and trajectories of zero boundary (taken from FE simulation) for DTC forged at 1080 °C on the hydraulic press (see Appendix 1.5 for enlarged version).

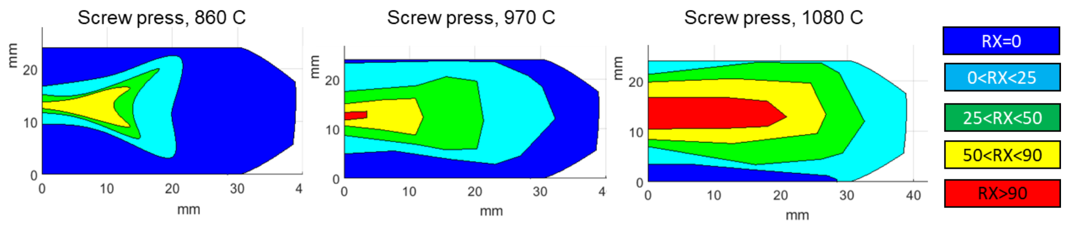

Figure 4. 11. Experimental iso-contour recrystallisation maps for screw press forgings of DTC.

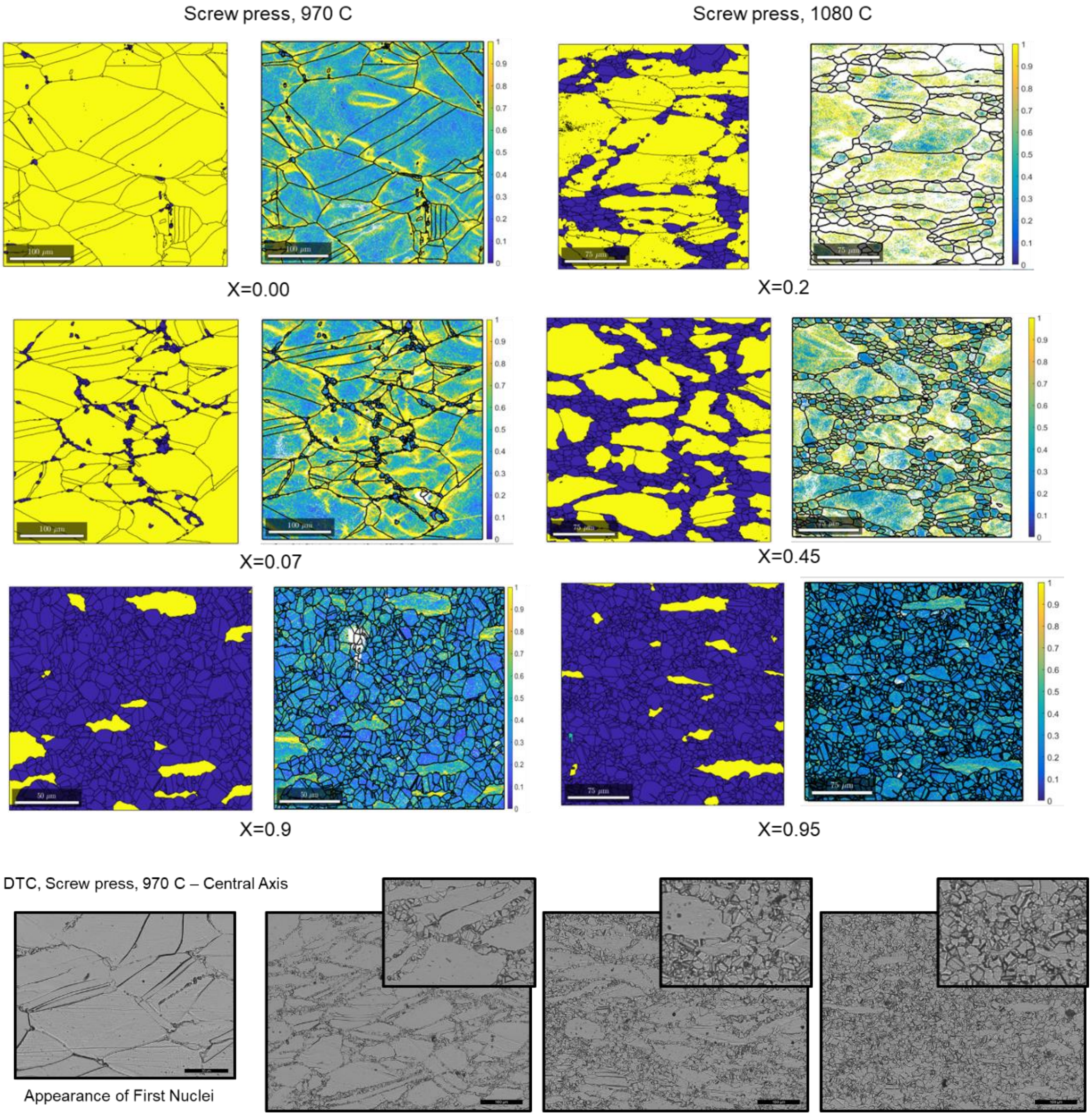

Figure 4. 12. Evolution of recrystallisation in screw press forgings (see Appendix 1.6 for enlarged version). In the top part of the picture are shown EBSD micrograph of recrystallised and non-recrystallised grains (blue/yellow figure) and KAM maps. In the bottom part of the figure are shown optical micrograph along the central axis of the specimen.

4.4 Screw Press Forgings of DTC

In Fig. 4.11 are shown the recrystallisation boundaries for the DTCs forged on the screw press. It is evident that the recrystallised areas are considerably more extensive than the ones observed in the forgings on the hydraulic press and higher absolute values of recrystallisation are achieved during the forging process. The shape of the RX boundaries appears to be different between forging at 860 °C and higher temperatures. The microstructures along the central axis following screw press forging are shown in Fig. 4.12. Contrary to what was observed in tensile tests and in hydraulic press forgings, no serration is visible at the grain boundaries. Moreover, KAM maps show a more dispersed deformation inside the grains (in particular at higher temperature). Recrystallised grains are largest at 1080 °C and in all forgings are considerably bigger than the ones observed in the hydraulic press experiments. Moreover, in opposition to the hydraulic tests, the recrystallised grains present almost no sign of accumulated deformation as displayed by KAM maps.

Fig. 4.13 and Fig. 4.14 show the zero recrystallisation boundaries for the DTCs forged at 970 °C and 1080 °C on the screw press. The vast majority of thermo-mechanical trajectories are characterised by an increase in temperature due to adiabatic heating and strain rates in the range of 10^{-3} - 10^{2} [1/s]. The increase in temperature in the centre of the workpiece was measured with thermocouples and proved to be approximately 100 °C across different forgings. Similarly to previous observations in hydraulic press forgings, very different levels of deformation can be observed in the thermo-mechanical trajectories, however the grains were considerably less distorted, squeezed and fractured compared to the hydraulic forgings.

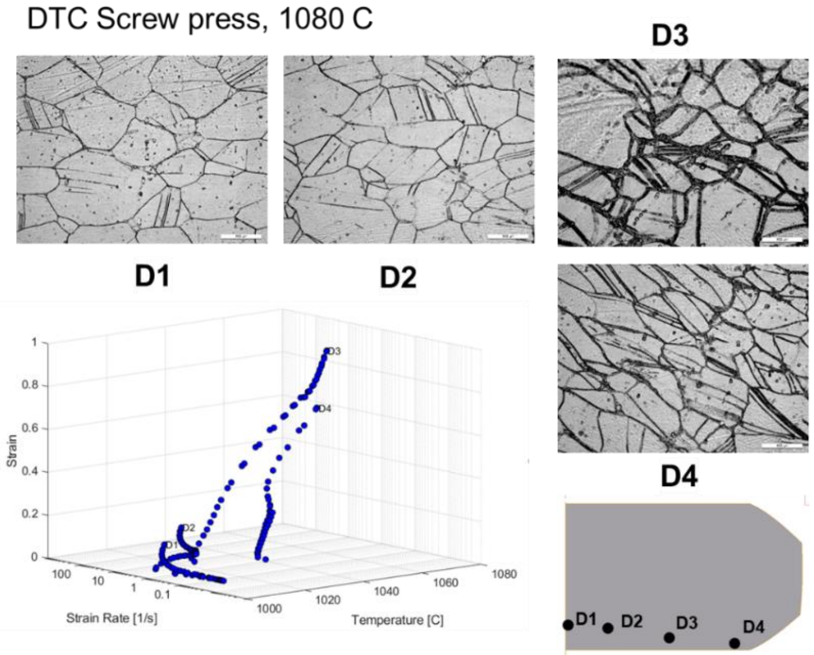

Figure 4. 13. Microstructures (taken from optical microscope) and trajectories of zero boundary (taken from FE simulation) for DTC forged at 1080 °C on screw press (see Appendix 1.7 for enlarged version).

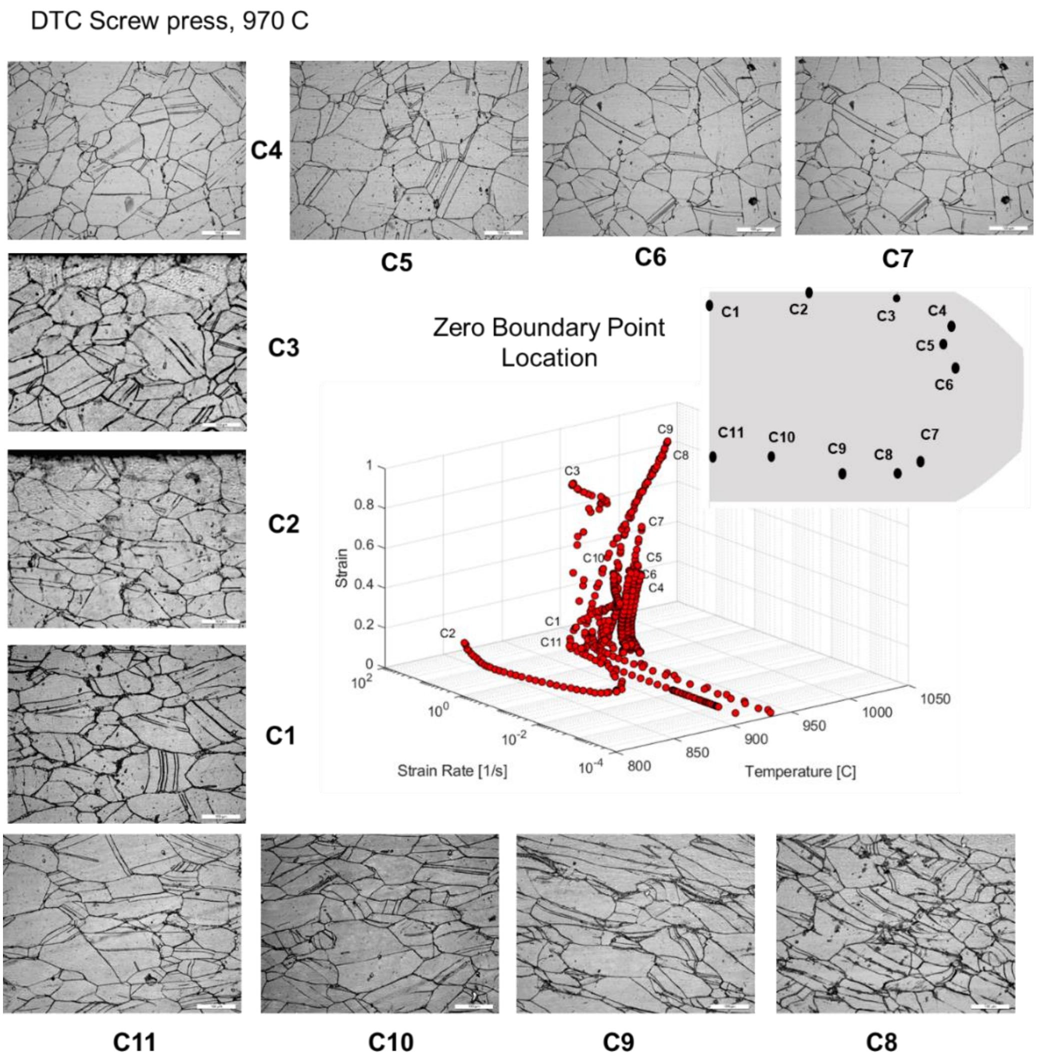

Figure 4. 14. Microstructure (taken from optical microscope) and trajectories of zero boundary (taken from FE simulation) for DTC forged at 970 °C on Screw Press (see Appendix 1.8 for enlarged version).

Fig. 4.15 illustrates the thermo-mechanical fields in the final instance of deformation for the DTCs forged on the screw press. It can be observed that the final temperature for both specimens was not homogeneous. As noted previously, due to adiabatic heating the temperature in the central section of the workpiece was considerably higher than the instance at the start of deformation. However, closer to the surface, cooling leads to a considerable drop in temperature. The familiar deformation cross observed in hydraulic press forgings is still present here and again this shape is not replicated in the recrystallisation boundaries, which appeared to reflect the temperature boundaries. This factor, in both hydraulic and screw press forgings, leads to a puzzling situation: there are areas in which the temperature and strain are high, however there is no recrystallisation and at the same time there exist some zones with very low levels of deformation presenting recrystallised grains.

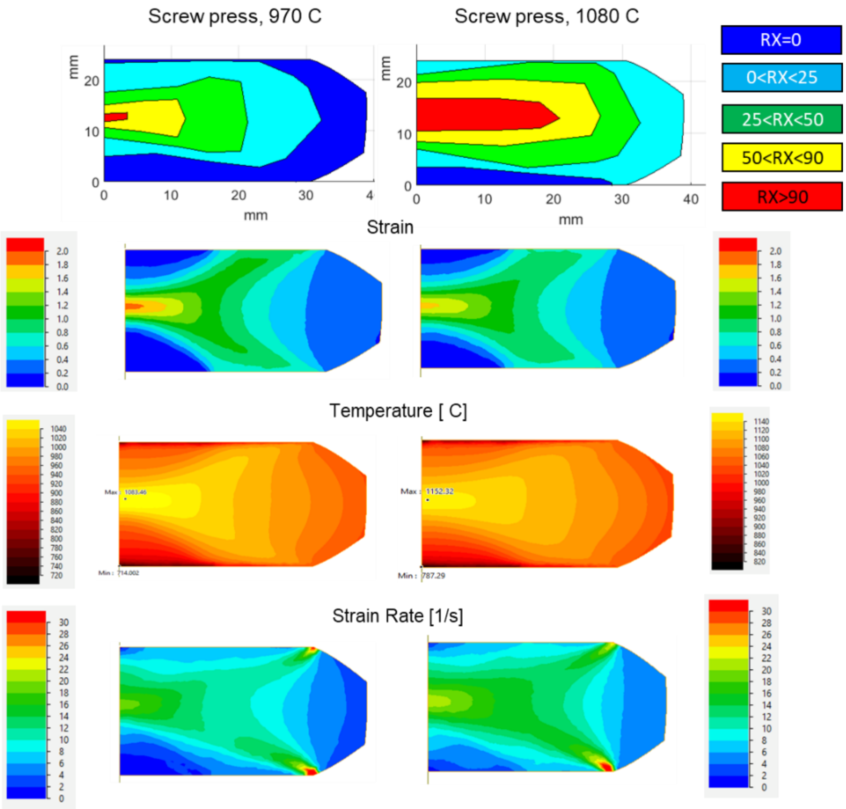
Screw press, 970 C

Screw press, 1080 C

Strain

Temperature [C]

Strain Rate [1/s]

Figure 4. 15. Comparison between experimental iso-contour recrystallisation maps (top) and thermo-mechanical fields of screw press forgings taken from FE simulation.

4.5 Screw Press Forgings of Disks

Fig. 4.16 displays the recrystallisation iso-lines for disk forgings from the screw press. Similarly to what was observed in the DTCs forged on the screw press, a high level of recrystallisation and large recrystallised areas are present. Due to the complex geometry a similarly recrystallised volume fraction is found in different areas of the analysed sections.

In Fig. 4.17 and Fig. 4.18 are collected respectively the strain, temperature and strain rate fields for disk forgings at 970 °C and 1080 °C. These forgings are characterised both by high levels of deformation with strain exceeding 3 and wide dead-zones in which deformation is almost nil. Due to the high strain rates, significant adiabatic heating is present the central section of the workpieces while considerable cooling is given by the contact with cooler dies. Strain rate fluctuates in the range between 0 and 50 s^{-1}. Some resemblance between the deformation map and recrystallisation iso-lines is observed but, similarly to what was observed in the DTCs, a few unexpected features were observed. These are detailed in Fig. 4.19, where it can be seen that a lower temperature and lower strain lead to a considerably higher level of recrystallisation. This is counter intuitive and raises the question of whether modelling can predict this discrepancy.

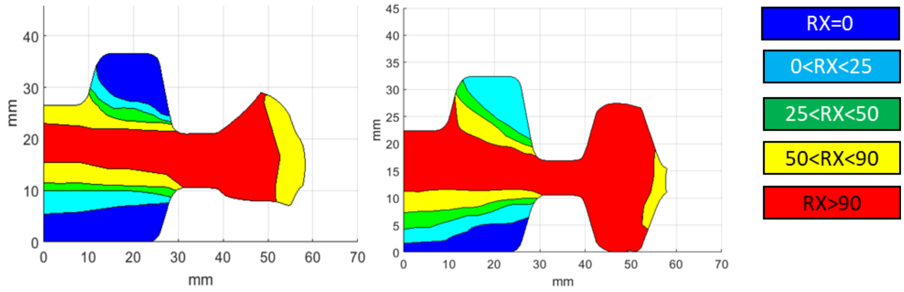

Figure 4. 16. Experimental iso-contour recrystallisation maps for disk forgings, 970 °C on the left-side and 1080 °C on the right-side.

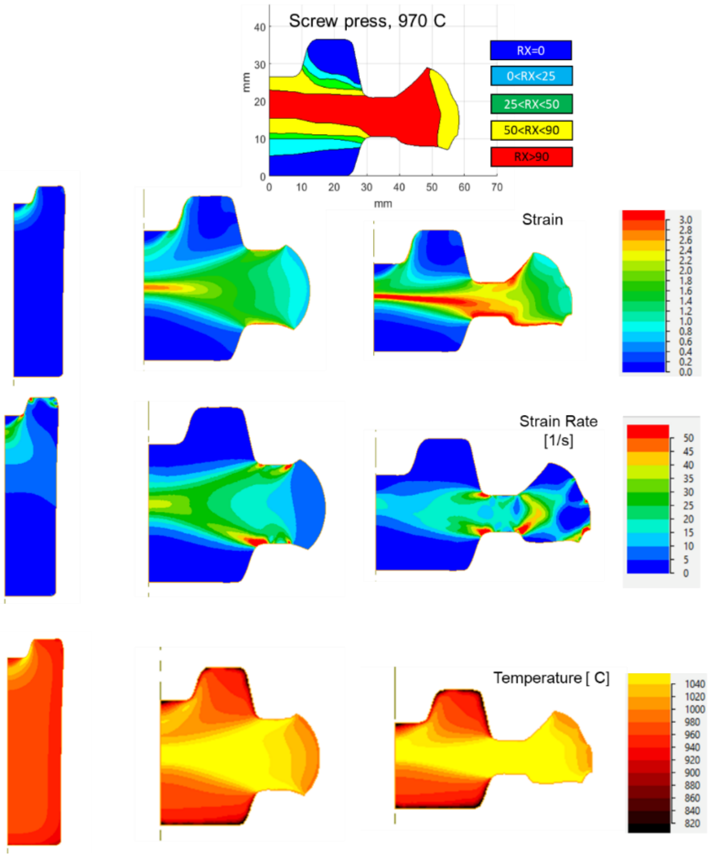

Figure 4. 17. Comparison between experimental iso-contour recrystallisation maps (top) and thermo-mechanical fields in disk forging taken from FE simulation.

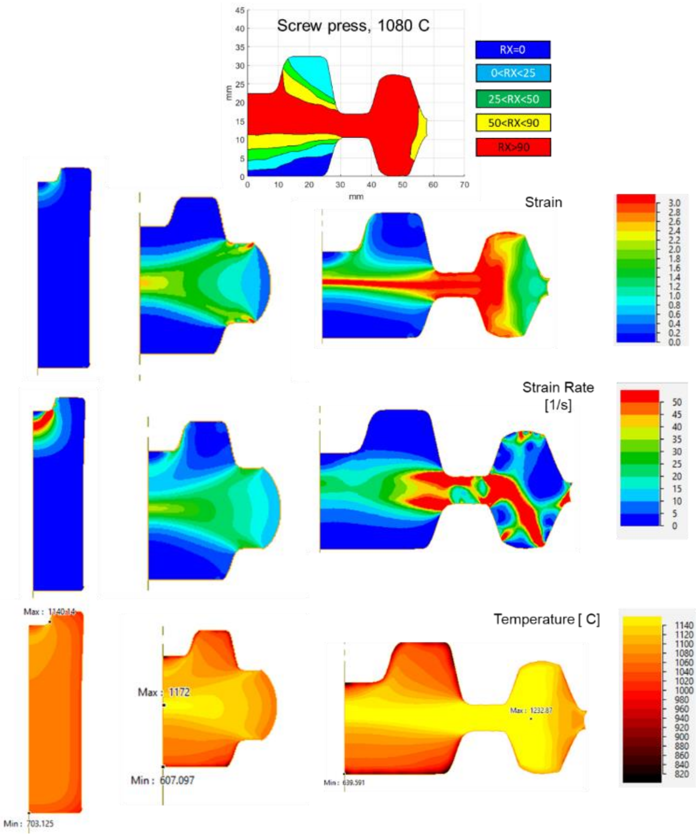

Figure 4. 18. Comparison between experimental iso-contour recrystallisation maps (top) and thermo-mechanical fields in disk forging taken from FE simulation.

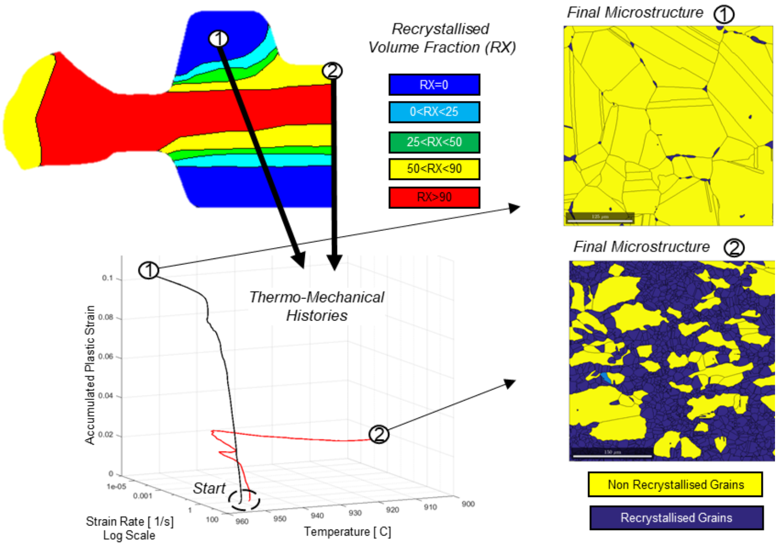

Figure 4. 19. Trajectory comparison between two points in disk forging. In the top left side is shown the experimental iso-contour recrystallisation map for disk forged at 970 ° C. In the bottom left thermo-mechanical histories taken from FE simulation. In the right side EBSD maps distinguishing between recrystallised and non-recrystallised grains

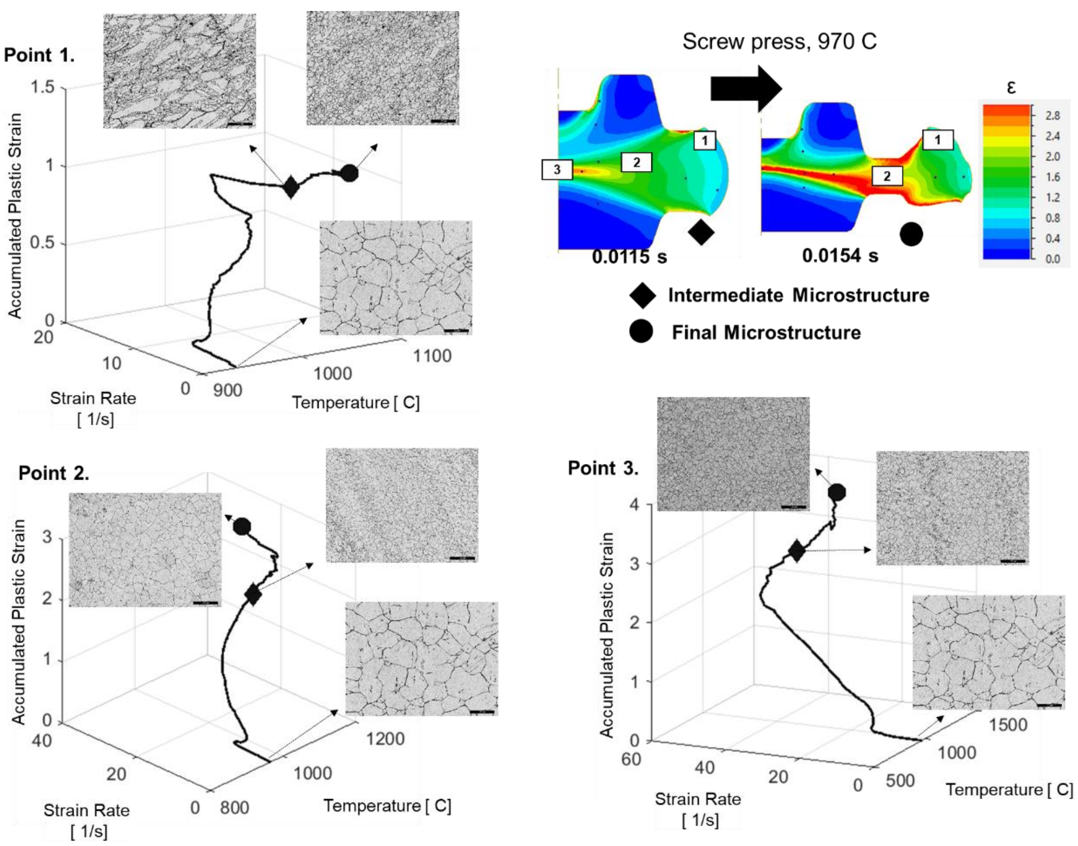

Figure 4. 20. Comparison between partially and fully forged disks at 970 °C. The sections of the disks in the top right show the strain field taken from FE simulation. The trajectories are plotted in the space plastic strain, strain rate and temperature and linked their corresponding microstructures (optical micrographs).

In Fig. 4.20, the half forged workpiece at 970 °C is compared to its fully forged counterpart. By comparing the progression of the thermo-mechanical trajectories to the corresponding microstructures a few different scenarios can be observed. In Point 1, almost no rise in strain leads to a considerable increase of recrystallisation. On the other hand at Point 2, an increase in strain leads to bigger grains, while at point 3 a similar increase in strain leads to no significant difference being observed between the two partially and fully forged sections. A full comparison of 12 points and their trajectories can be found in Appendix 4.1. It must be mentioned that this trajectory comparison, and in general this chapter, has the limitation of not taking into account the post-forgings cooling effects. While efforts were made to limit post-forging grain evolution by quenching in water as fast as practicably possible, at least 5 seconds elapsed before the forging and the quenching. To evaluate such effects, in Fig. 4.21 the microstructure of disks forged at 970 °C with two different cooling methods (air cooling and water quenching) is compared and no qualitative difference was observed between the two. Lastly, in this investigation it is assumed that no secondary particle such as δ precipitates are present. However, due to the complex thermo-mechanical processing it cannot be excluded that fine delta particles in sub-micron size may appear and disappear during the process affecting the observed microstructural changes.

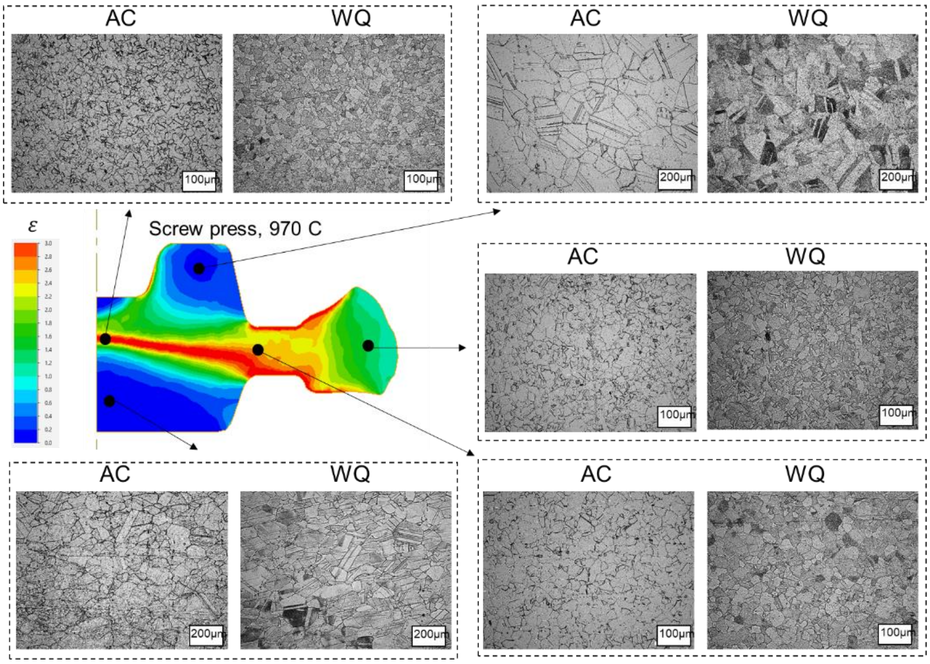

Figure 4. 21. Comparison of microstructures (optical micrographs) between water quenching and air cooling in disks forged at 970 °C on screw press (see Appendix 1.9 for enlarged version).

During this investigation many microstructural images were taken but not all of them were inserted in the main text. However, these may be useful to other researchers and for this reason some of them were included in the Appendix section 4.2.

4.6 Conclusions

In summary it was found that:

- Non-homogeneous industrial testing provides numerous insights on recrystallization.
- The onset of recrystallization and its development, analysed through the Zero Boundary methodology, are found to be different depending on the thermo-mechanical conditions during the forging process.
- Recrystallization, even within the same DTC, is achieved at very different strains. Moreover, the accumulation of strain does not seem to be necessarily correlated to an increase in recrystallised volume fraction.
- Contradictory trends were noted: there were areas within the forgings in which little/ no deformation led to a high level of recrystallization, while high levels of deformation led to very low levels of recrystallization.
- The dislocation density distribution, estimated through KAM maps, and the evolution of recrystallization varies depending on the temperature and speed of the process.

Following these observations it raises the significant question of whether standard microstructure modelling solutions offered in current FE software can predict these differences. This will be examined in Chapter 5.

Chapter 5

On the Applicability and Calibration of JMAK Models

5.1 Introduction

As observed in the literature survey, JMAK models are the most common tools used for the prediction of microstructural phenomena in Nickel superalloys, and in particular IN718. Several derivatives of the basic JMAK model are presently available and nowadays, modern commercial Finite-Element Analysis (FEA) packages (e.g. DEFORM, QFORM, Forge) offer these models as embedded solutions in the finite element code.

In the literature, there are many successful implementations of such JMAK-type models for modelling recrystallisation in hot forging. The majority of these normally address rather idealised processes (relatively slow forging, constant temperature, simple geometry). However, the complexity in industrial processes, raises the need to re-examine the available approaches to evaluate the range of their applicability, which is often not specified. In Chapter 4, the inconclusive experimental observations reinforced the non-triviality of the question of whether these models can predict accurately microstructural evolution during industrial forging. In this chapter the question of applicability is addressed through a benchmark of standard available models and in addition a novel calibration methodology for these models is proposed.

5.2 JMAK Models

A full description of the JMAK models can be found in Chapter 2. Using these models metal forming FE software offers capabilities for the prediction of Dynamic, Meta-Dynamic and Static Recrystallisation. The focus of this research is devoted in particular to recrystallization in the forging process. Although FE packages offer different material databases for microstructure models, the mathematical structure of these models was found to be almost identical.

There are two main modes in which such microstructural models are implemented: coupled models operating during the simulation itself and those using a post-processor. In the former, the microstructure model and the metal forming simulation run at the same time, allowing the microstructure model to influence the simulated deformation process. In the post-processor approach, the metal forming simulation is carried out first, and then the sequence of the thermo- mechanical states is used as an input for the microstructure evolution model. For this investigation the post-processor model found in DEFORM [67] and QFORM [68] based on the work of

Huang et al. will be used as a representative example of the commonly used approach. This was re-modelled in a *Lua* (Programming Language) subroutine for QFORM and is available in Appendix 5.1. The main structure of the model is presented in Eq. (5.1-5.5). The beginning of recrystallisation is achieved when the accumulated plastic strain (ε) becomes equal to the critical strain (ε_c). The factor, $\varepsilon_{0.5}$ corresponds to the strain needed to achieve 50% recrystallisation.

$$X_{rx} = 1 - exp\left(\ln(0.5)\left(\frac{\varepsilon - \varepsilon_{cr}}{\varepsilon_{0.5}}\right)^{n}\right) \tag{5.1}$$

$$\varepsilon_{cr} = k_1 d_0^{n_1} \dot{\varepsilon}^{m_1} exp\left(\frac{Q_1}{RT}\right) + f_1 \tag{5.2}$$

$$\varepsilon_{05} = k_2 d_0^{n_2} \dot{\varepsilon}^{m_2} exp\left(\frac{Q_2}{RT}\right) + f_2 \tag{5.3}$$

$$d_{drx} = k_4 d_0^{n_4} \dot{\varepsilon}^{m_4} exp\left(\frac{Q_4}{RT}\right) + f_4 \tag{5.4}$$

$$d_{avg} = X_{rx} d_{rx} + (1 - X_{rx}) d_{Nrx} \tag{5.5}$$

Here $\dot{\varepsilon}$ (strain rate) and T (temperature) are the process variables, R is the gas constant, k_1, k_2, k_4, f_1, f_2, f_4, and n, are fitting parameters, $Q_{1,2,4}$ are the activation energies for dynamic recrystallisation while $n_{1,2,4}$ and $m_{1,2,4}$ are material parameters which characterise the sensitivity to respectively initial grain size d_0 and strain rate.

These equations are often simplified by the fact that n_1, n_2, f_1, f_2, f_4 are set to zero. The full list of the parameters used can be found in Appendix 2.1.

In this chapter results from the forging of double truncated cones (DTC) will be used to investigate the applicability of JMAK models. A full description of the experimental methods can be found in Chapter 3.

5.3 JMAK Output Applicability

As mentioned, the aim of this chapter is to investigate the applicability of JMAK-type models in industrial manufacturing processes. Such processes are characterised by complicated thermo-mechanical history and flow trajectories, which may result in a variety of microstructural evolution phenomena (e.g. Discontinuous Recrystallisation, Continuous Recrystallization, grain growth etc.). However, JMAK-type models are mainly used specifically for the description of recrystallisation. Therefore, when evaluating the applicability of these models it cannot be implied that they are wrongly predicting microstructure, because their use may be inappropriate. To give an example, it could be the case that additional models and/or parameters may be needed in conjunction with the JMAK-type model used. Hence, there arises the first important question of when and where it is appropriate to use these models. Only then can their applicability be investigated in terms of numerical mismatch between the between the microstructure model outputs and experimental results.

Fig. 5.1 shows through SEM images the presence of a few different final structural states taken from a single disk geometry forging (e.g., duplex and triplex grain structures, quasi-original and heavily deformed grains). Based on microstructural observations three zones have been classified: non-recrystallised (A), partially recrystallised (B) and completely recrystallised (C). Each zone was further clustered into sub-groups as detailed below:

A. Non-Recrystallised:

   A1. Original Grains with Small Deformation- where grains have maintained the original shape and size with the addition of slight deformation features (i.e. little intragranular deformation has occurred).

   A2. Heavily Deformed Grains with Fragmentation- where heavy deformation features can be seen (significant intragranular deformation) and a portion of the grains seem fractured.

B. Partially Recrystallised:

   B1. Duplex Necklace- where two types of grains – larger, deformed grains with smaller, recrystallized, grains on the boundaries – are observed.

   B2. Triplex- where 3 different types of grains – larger, deformed; small, recrystallised (necklace); and an intermediate size with a clean surface (possibly recrystallised) – can be observed. Each grain type has a clear prevailing size with no smooth transition between the types (no intermediate grain sizes).

C. Completely Recrystallised:

   C1. Homogeneous - where all the grains have approximately the same grain size and a deformation free surface.

   C2. Duplex - containing two distinctive grain sizes (no intermediate grain sizes).

However, as outlined in the previous section, there are only three main outputs from the model, namely, X_{drx} - Recrystallised volume fraction, d_{drx} - Dimensions of recrystallised grains and d_{avg} - Average grain size. To analyse the applicability of the JMAK-type model, the significance of these three outputs in describing the different zones and sub-groups was studied:

- X_{drx} is an important parameter that has to be implemented to allow the main distinction between zones A, B and C.
- d_{drx} may be used as is to describe homogeneous recrystallisation (C1). For duplex necklace structures (B1), it can be used for calculating the size of the smaller recrystallised grains; however the remaining (un-recrystallised) grains need to be described by an additional parameter. For duplex and triplex structures (B2, C2), d_{drx} may not be sufficient because, as observed, there may be different sizes of recrystallised grains.
- d_{avg} can be used only for original and homogeneous grain sizes (A1 and C1). In contrast, for morphologies like C1, C2 and B2, this parameter may become misleading as it may specify a size that does not actually exist in the material.

Evidently, additional parameters are necessary to characterise the microstructural states identified. However, it must be remembered that JMAK-based models are used in industrial applications because of their simplicity. Therefore, it is important not to overcomplicate these models and to add only sufficient parameters to be able to adequately describe the microstructure in a more thorough way. As observed, the average grain size is insufficient for description in zones where different grain sizes are present. In these cases, the easiest solution can be the use of a grain-size distribution. However, implementation of this in the model may be difficult. Fortunately, there was an absence of intermediate sizes between each grain-type in the subgroups, resulting in distribution functions characterised by a few main peaks (one for each grain-type). Consequently, it may be possible to use the mean values of the peaks. To do this, it is necessary to find the volume fraction of each peak. While this may be easy for A1, B1 and C1 (only X_{drx} required), more parameters are required for duplex and triplex structures (B2, C2).

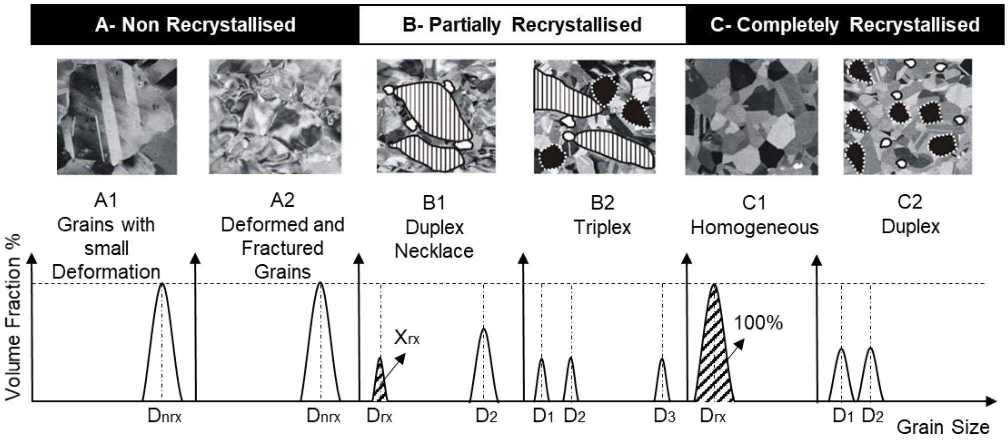

Figure 5. 1. SEM Images of characteristic microstructures shown on top and microstructure groups and related grain-size distributions displayed on bottom (see Appendix 1.10 for enlarged version).

Now that it was assessed where the model could in principle be used, it is possible to examine how well it performed. The two most relevant aspects to be addressed for industrial applications are the initial and final stages of recrystallisation (the 0% and 100% boundary).

The initial stage or 0% boundary corresponds to the “dead-zone” boundary, wherein are found the biggest gradients in material properties. On the other hand the final stage, or 100% boundary, generally represents industry’s desired microstructure outcome (i.e. complete homogeneous recrystallisation). This outcome is sought because it would prevent uneven grain sizes leading to a gradient in mechanical properties of the forged workpiece as discussed in section 2.2.3.1. In the cases in which 100% recrystallisation is not achieved the maximum predicted value will be taken as an indicator. Intermediate stages of recrystallisation and grain sizes are still important, but are only secondary to these. Hence this chapter will focus on recrystallized volume fraction.

5.4 Benchmark Result

A comparison was made between JMAK predictions and metallographic analysis for DTC forged at 970 °C and 1080 °C for both screw and hydraulic presses. The results are shown in Fig. 5.3. Two scales are used, the first one takes all the recrystallisation ranges, while the second one shows anything above 5% in red. This is because experimental data on recrystallisation can only be given with a 5%

accuracy as detailed in Chapter 3. It can be seen that the predictions for the hydraulic press correlate more closely to the results than the ones for the screw press. In particular the shape of the predicted recrystallized areas loosely resembles the experimental data. On the other hand the quantitative values are dissimilar. For example, the cone forged at 970 °C on the hydraulic press is predicted to have 81% recrystallized volume fraction in the centre, while in reality it is only 15%. Similarly, the cone forged at 1080 °C, shows 95% recrystallized volume fraction compared to 55% obtained experimentally. In the screw press forgings, the difference in shape of the recrystallisation zones is evident both in the zero recrystallisation boundary and the intermediate levels. While the recrystallized fraction in the central points of the cones is within 5-10% from the experimental value, the area of complete recrystallisation is considerably different.

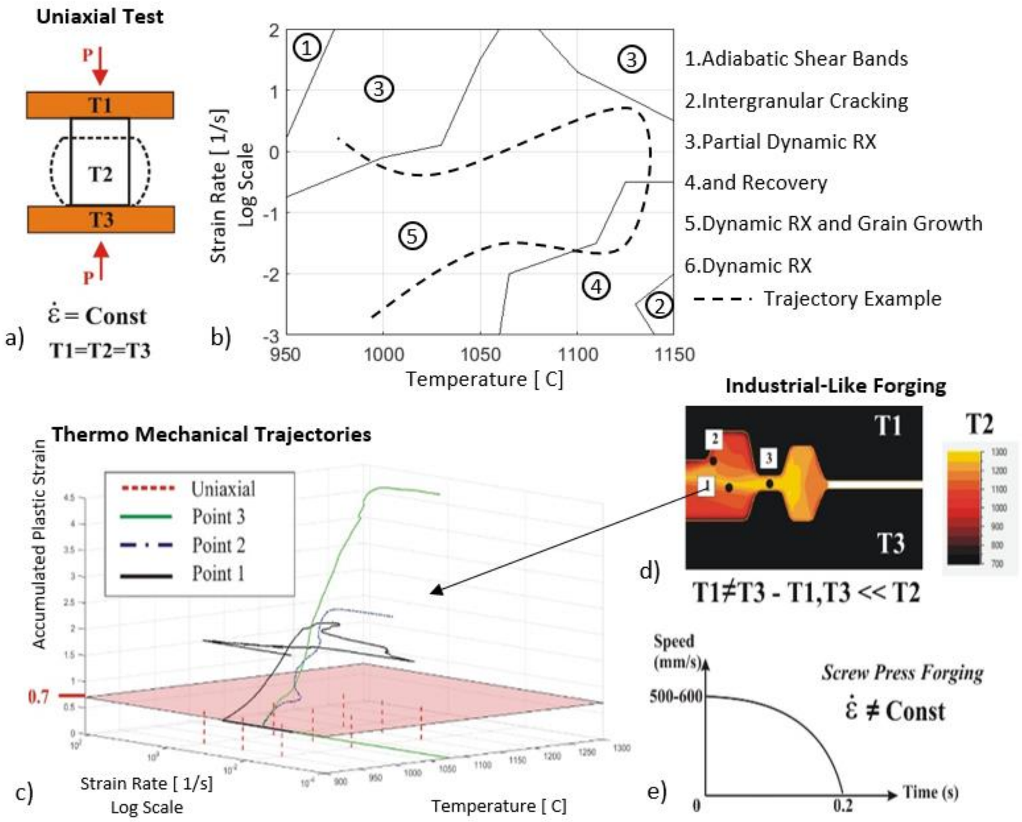

Figure 5. 2 a) Scheme of uniaxial test, b) Processing map adapted from Sui et Al. [38], c) Comparison between thermo-mechanical history of uniaxial lab tests and industrial forgings, d) Temperature field from FE simulation of disk forging, e) graph displaying ram speed versus time of the screw press machine.

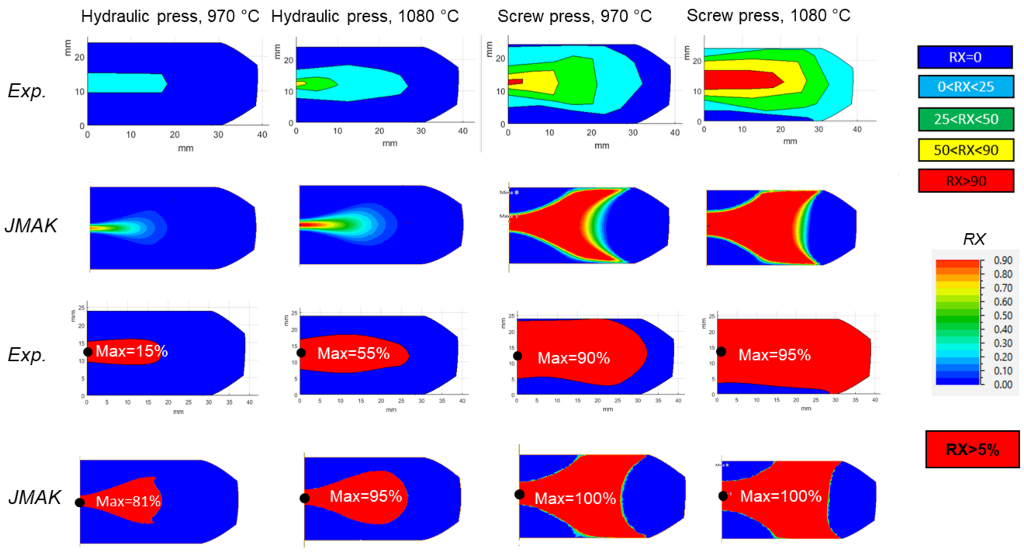

Figure 5. 3. Comparison of recrystallised volume fraction, between experimental results (recrystallisation iso-contours in the first and third row) and standard JMAK predictions using two scales: 0-5%, 0-100%.

Due to the big difference between predicted and actual microstructure, it is clear that this model cannot be applied as it is. However, without more information it is not possible to state whether the problems lie with the model's mathematical structure, or, the material parameters used which were obtained with uniaxial lab tests. The bigger the deviation from the calibration tests, the bigger the chance of mismatch in the prediction. As can be seen from Fig. 5.2 there is a big difference between the thermo-mechanical histories of uniaxial lab tests and these forgings. Thus it is not possible to say that JMAK models are not applicable to industrial hot forging as the reason for the mismatch may be due to a poor calibration methodology.

The calibration used for the coefficients of Eq. (5.1), (5.2) and (5.3) used the peak stress and strain values taken from the mechanical stress-strain curve [88]. However, it is clear that this method is somewhat approximate. The accuracy of the experimental location of the peak in the stress-strain curve is quite limited as shown in Chapter 4 and its relation to the beginning of DRX is questionable (due to the simultaneous presence of other microstructural mechanisms that can be also responsible for the softening such as CDRX and recovery). Besides this, as noted previously uniaxial tests with constant temperature and strain rate may not give the full picture of the phenomena involved in complex forging processes. The replication of industrial conditions in uniaxial tests presents several challenges. Calibration, especially for high strain rates, is really challenging due to the high loads incurred and therefore special machines are needed, making it a significant challenge for in-house industrial applications. An answer to this problem is proposed in the next section where a novel calibration methodology, which can be viable in an industrial setting, is proposed and tested.

5.5 Novel JMAK Calibration Methodology

A combination of forging trials, modelling and microstructural analysis can provide more opportunity for the improvement of the calibration methodology. As was noted earlier, industrial forging processes give rise to very different sequences of thermo-mechanical conditions across a workpiece. The microstructure formed at the end of the process is the accumulated result of the total history (changes in temperature, strain rates, triaxiality, etc.). Hence, it is not surprising that any instantaneous values of accumulated plastic strain, temperature or strain rate sometimes give a confusing picture and poor calibration results. To overcome this problem, the schematic approach shown in Fig. 5.5 is suggested. This involves the forging of double truncated cones (DTC) on the equipment for which the calibration is sought. Then the microstructure of the central plane of the DTCs should be analysed and recrystallisation isolines should be drawn for 0%, 25% and 50%.

If Eq. (5.2) is plotted in the space of temperature, strain rate and accumulated plastic strain, this equation will form a surface, splitting the space into two parts – where recrystallisation should, or should not take place. At the same time, for every point in the forged part, the history of the process (tracked through the FE simulation) can be depicted as a trajectory in the same space. Then, if the threshold part of the model is calibrated correctly, a picture would form where the trajectories of all the points with zero recrystallisation are located inside the surface described with Eq. (5.2); this is shown in Fig. 5.4.

The same approach can then be used to find the coefficients of Eq. (5.3). The remaining material parameter to be found is *n* in Eq. (5.1). To find this, the strain for the achievement of 25% recrystallisation is found through Eq. (5.6). Then by inserting Eq. (5.6) in (5.1), Eq. (5.7) is obtained.

$$\varepsilon_{0.25} = k_3 \dot{\varepsilon}^{m_3} exp\left(\frac{Q_3}{RT}\right) + f_3 \tag{5.6}$$

$$n = \frac{ln\left(\frac{0.75}{0.5}\right)}{ln\left(\frac{\varepsilon_{0.25}-\varepsilon_{cr}}{\varepsilon_{0.5}}\right)} \tag{5.7}$$

Here, $\dot{\varepsilon}$ (strain rate) and T (temperature) are the process variables, R is the gas constant, while k_3, f_3 and Q_3 are fitting parameters with no real physical meaning.

The value of n will change for every combination of temperature and strain rate. To simplify things an average value is taken over the range of temperatures and strains characteristic of the forging.

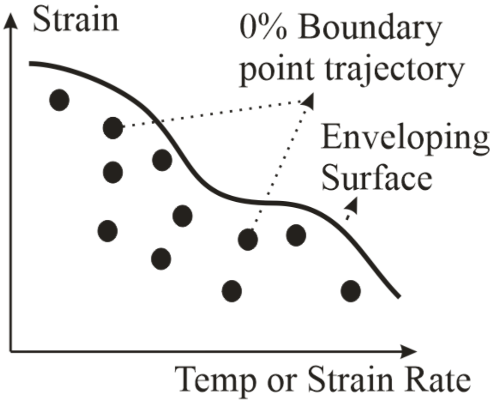

Figure 5. 4. Enveloping surface scheme in 2D.

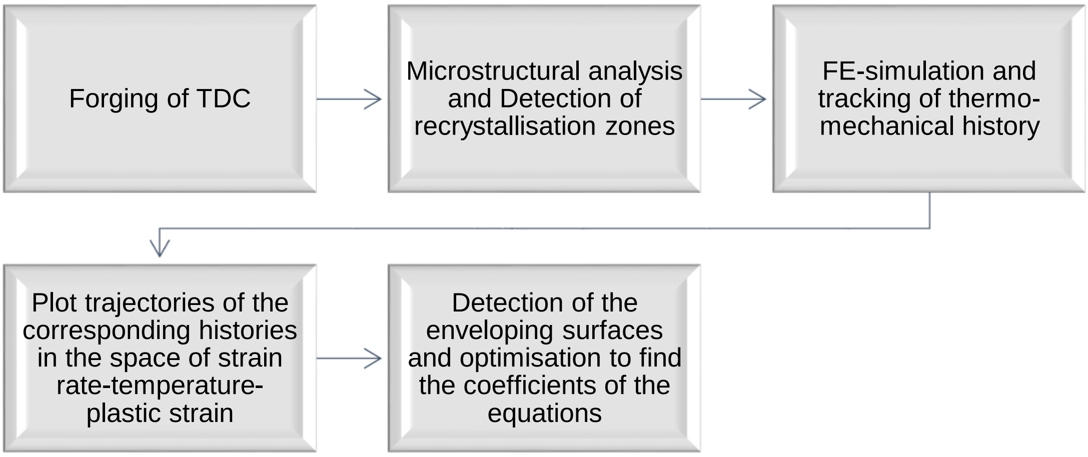

Figure 5. 5. Block scheme of calibration methodology.

5.5.1 Calibration of Hydraulic Press DTCs

The following paragraphs detail all the steps of the calibration through using as examples the forgings from the hydraulic press. The DTC forged at 1150 °C was used to calibrate the model, while to validate it the DTC's forged at 970 °C and 1080 °C were used. Given the fact that 0%, 25% and 50% recrystallisation zones are needed, it was necessary to use an adequate temperature for the calibration forgings.

During forging on the hydraulic press at 970 °C for example, it can be seen that the maximum amount of recrystallisation reached was 17%. In this case, no reference can be found for 25% and 50% recrystallised volume fraction. To work around this problem, the surface found for critical strain could be used for the 25% and 50% by simply raising it through the parameters f_2 and f_3 from Eq. (5.3) and (5.6).

The first step after the forging is to perform microstructure analysis of the samples and detect the recrystallisation iso-lines as shown in Fig. 5.6. This analysis was done through optical microscopy, which is suited for a rapid detection of the required boundaries.

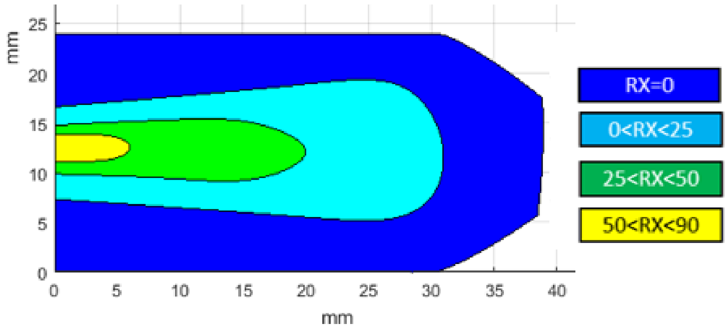

Figure 5. 6. Experimental recrystallisation iso-contour for DTC forged at 1150 °C on the hydraulic press.

For the points in the forged samples belonging to the boundary zones, the history of the temperature, strain rate and plastic strain are taken from the results of the FE-simulation as shown in Fig. 5.7.

Once the data has been taken from the simulation software, it must be processed so that the trajectories of the corresponding histories are plotted in the space of temperature- strain rate -plastic strain. These trajectories may be plotted as points or continuous lines (see MATLAB codes in Appendix 5.2.1-5.2.2).

As previously mentioned, the recrystallisation surfaces should split the 3d space, made of temperature, strain rate and strain into several parts: where recrystallisation starts and where it reaches 25% and 50%. For this reason, if the surface is calibrated correctly all the plotted trajectories from the tracked boundary points should fall below or on the respective surface as shown in Fig 5.4.

In order to find the calibrated coefficients for the equation and plot the zero-recrystallisation surface several MATLAB algorithms were written to: find top points for each trajectory in each strain rate-temperature interval, multiply trajectory points if data is sparse, find coefficients and adjust the curves. All of these can be found in

Appendix 5.2.3-5.2.7. In Fig. 5.7 below are presented the results of the calibration with the three surfaces representing ε_c, $\varepsilon_{0.5}$ and $\varepsilon_{0.25}$.

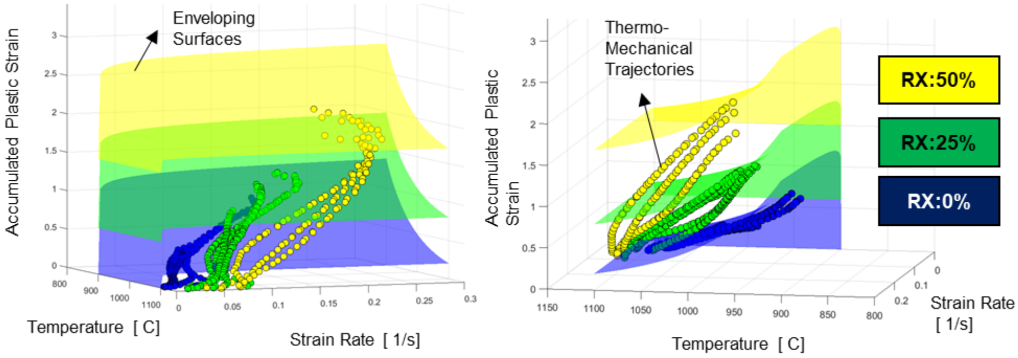

Figure 5. 7. Thermo-mechanical trajectories extracted from FE simulation and recrystallisation surfaces for 0%, 25% and 50% boundaries plotted through Eq. (5.2), (5.3) and (5.6).

As will be noted, the points lay either below the surface, or just above it. The final calibration coefficients can be seen in Table 5.1. The validity of the coefficients is only limited within the boundaries of the obtained data, thus: 0.01-0.5 [1/s], and 900-1150 °C.

Table 5. 1. Comparison between Standard and Calibrated JMAK Coefficients.

Coefficient	**Standard Model**	**Calibrated Model**
k_1	3.83-03	2.5e-06
m_1	0.1238	0.045
Q_1	49520	128510
f_1	0	0
k_2	5.043e-09	2.5e-06
m_2	-0.408	0.045
Q_2	196000	128510
f_2	0	1.5
f_3	/	0.6
k_3	/	2.5e-06
m_3	/	0.045
Q_3	/	128510
n	1	1

5.5.2 Results after calibration of Hydraulic Press DTCs

In Fig. 5.8 the results are presented after the calibration. Both the shape and value of recrystallisation is closer to the experimental observation. In particular, the highest recrystallized volume fraction for the DTC forged at 970 °C, is now predicted to be 35% compared to the 81% predicted by standard JMAK. This is considerably closer to the experimental value of 15%. For the case of 1080 °C, the results improved drastically, from a 45% difference to only 6%. The reason for which the 1080 °C cone benefitted more from the calibration, may be that the cone used for calibration was forged at 1150 °C. Therefore, it was a closer temperature. Indeed, a model works well when tested in conditions similar to ones for which it has been calibrated. It can be seen that the shape of the boundary is still slightly different from the experimental results. This may be due to other microstructural phenomena (e.g. CDRX, recovery etc.) or the specific limitations of JMAK models, which will be discussed later in this thesis.

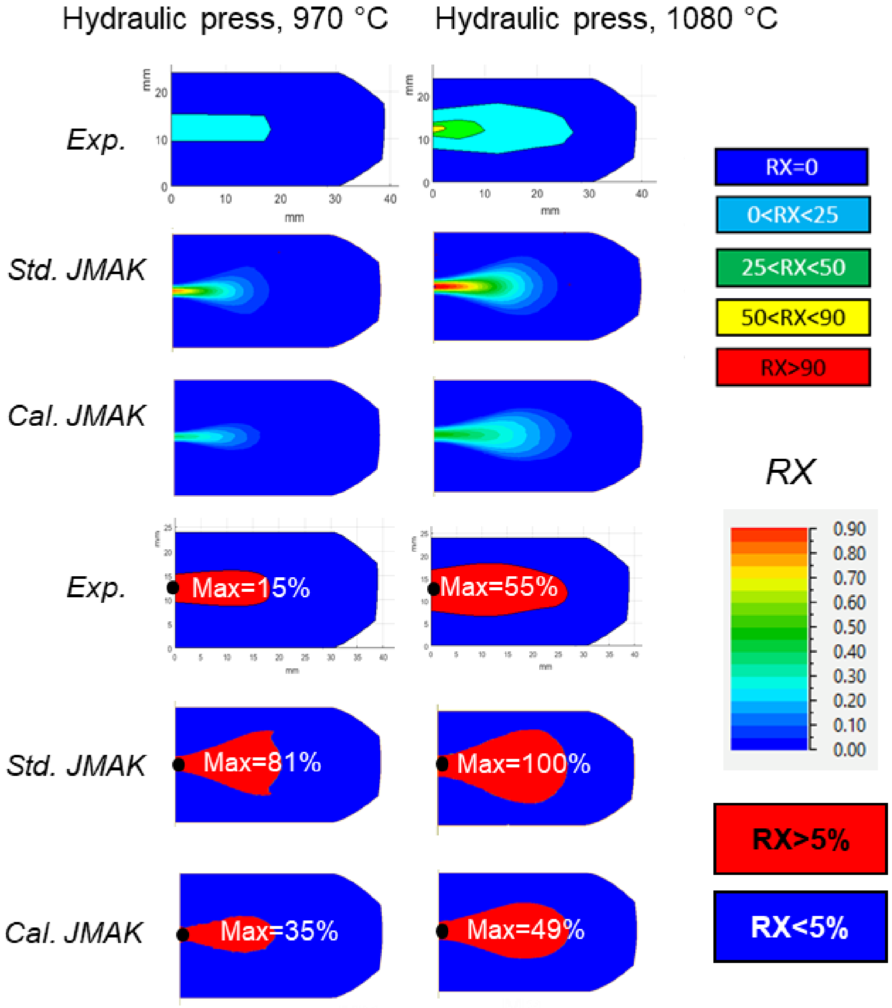

Figure 5. 8. Comparison between experimental data (recrystallisation iso-contours in rows one and four) and standard JMAK results and calibrated JMAK results for two scales (0-5%, 0-100%).

5.5.3 Calibration of Screw Press DTCs

To calibrate the model for high strain rates the DTC forged at 860 °C on the screw press was used. For validation, the cones forged at 970 °C and 1080 °C on the screw press were utilised. Despite the low temperature, the workpiece forged at 860 °C as shown in Fig. 5.9.a presented high levels or recrystallisation (up to 90% in the centre). This is due to the fact that even if the forging temperature is below what is considered the recrystallisation temperature threshold of 975 °C [64], owing to the high strain rates and large deformation, there is considerable adiabatic heating in the workpiece leading to a significant increase in temperature.

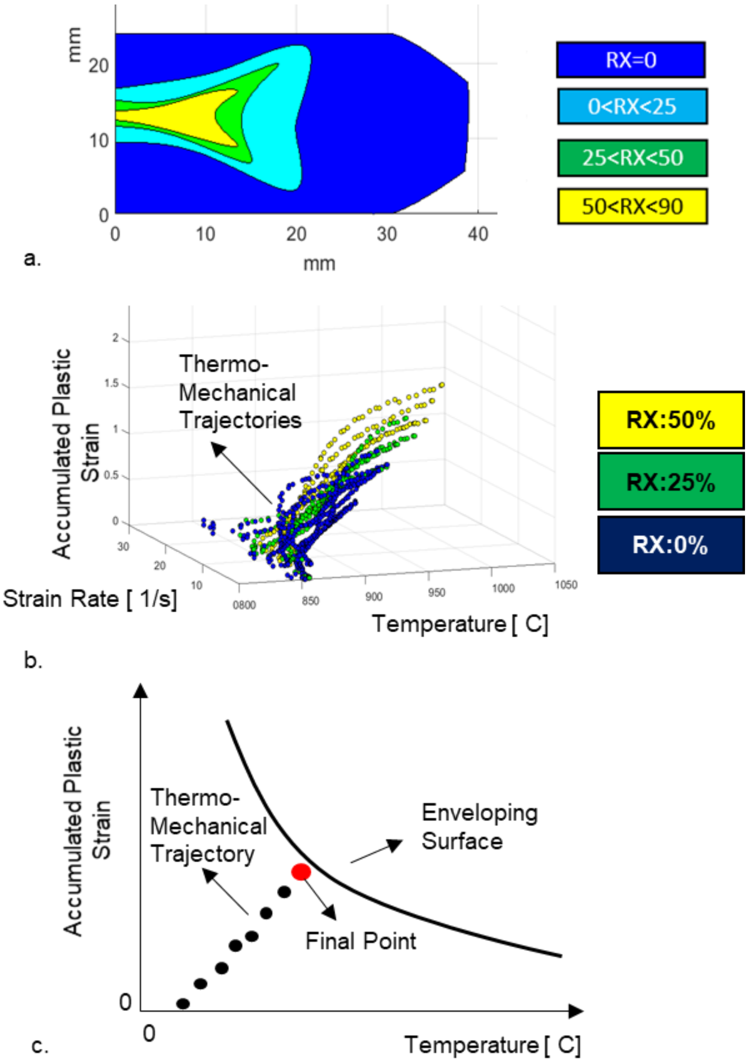

Figure 5. 9. a) Recrystallisation iso-contour for DTC forged at 860 °C on screw press, b) Thermo-mechanical trajectories of points tracked from DTC forged at 860 °C on screw press, c) Schematization of point selection from the thermo-mechanical trajectories.

This increase in temperature can be observed in the thermo-mechanical trajectories of the points in Fig. 5.9.b. This, however, poses some problems for calibration. The values of ε_c, $\varepsilon_{0.5}$ and $\varepsilon_{0.25}$ increase with temperature and due to the shape of the trajectories, only the final points of the thermo-mechanical histories can be taken for calibration as schematised in Fig. 5.9.c. When only the final points of the trajectories are taken, the data points are clustered in almost a straight line and there is overlapping of points belonging to different recrystallisation zones. Moreover, from Fig. 5.9b it can be seen that with increasing temperatures, recrystallisation strains are higher. This is the opposite of what would be expected as it is generally accepted that higher temperature leads to higher amount of recrystallisation [43]. This poses questions on the structure of the model and the fact that strain may not be an optimal parameter for the prediction of recrystallisation and further understanding of this phenomenon during forging is needed. However, for the moment, in order to solve the problem, the average of the points for each recrystallised volume fraction (0%, 25% and 50%) is taken into account. This leaves only a few data points from which curves can be obtained. Thus, many different fittings and consequent coefficients can be found to fit the data obtained. This shows that this calibration methodology is not robust and thus it is not recommended for high strain rate forgings. However, to test the applicability of the model for these types of forgings, a small study using different coefficient combinations was performed. In Table 5.2 are shown the coefficients chosen. The most important material parameters are m and Q, which give respectively strain rate and temperature sensitivity. The lower the value of m the less influence the strain rate will have and thus the flatter will be recrystallisation surfaces with regards to the strain rate axis. In contrast, the higher the Q value, the less impact a change of temperature will have on the curve. The remaining parameters, K and f, were used to fit the data obtained. In particular K, was used so as to make sure that the critical strain surface will fit the zero boundary data, and the f_2 and f_3 used to adjust the 25% and 50% surfaces. The results of these investigations are presented in Fig. 5.10-5.12. There can be seen to be an improvement from standard JMAK, with respect to the recrystallisation area fraction and gradient, in particular with regards to the 970 °C forging. Nevertheless, the shape of the recrystallized volume fraction areas is considerably different as compared to the experimental data. It can be concluded that, contrary to what was observed in the hydraulic press forgings, the results of the various calibration attempts did not significantly improve the results. This suggests that there are limitations with this approach for high strain rate forgings.

Table 5. 2. Comparison between different sets of JMAK Coefficients

	Hydraulic Cal.	**Cal. 1: Low Q, Low m**	**Cal. 2 Low Q, High m**	**Cal. 3 High Q, High m**	**Cal. 4 High Q, Low m**
k_1	2.5e-06	5e-03	6e-04	1.8e-10	1.85e-9
m_1	0.045	0.045	1	1	0.045
Q_1	128510	50000	50000	200000	200000
f_1	0	0	0	0	0
k_2	2.5e-06	5e-03	6e-04	1.8e-10	1.8e-10
m_2	0.045	0.045	1	1	0.045
Q_2	128510	50000	50000	200000	200000
f_2	1.5	0.6	0.35	0.75	0.85
f_3	0.6	0.4	0.2	0.5	0.55
k_3	2.5e-06	5e-03	6e-04	1.8e-10	1.8e-10
m_3	0.045	0.045	1	1	0.045
Q_3	128510	50000	50000	200000	200000
n	1	0.8	0.6	1	1.1

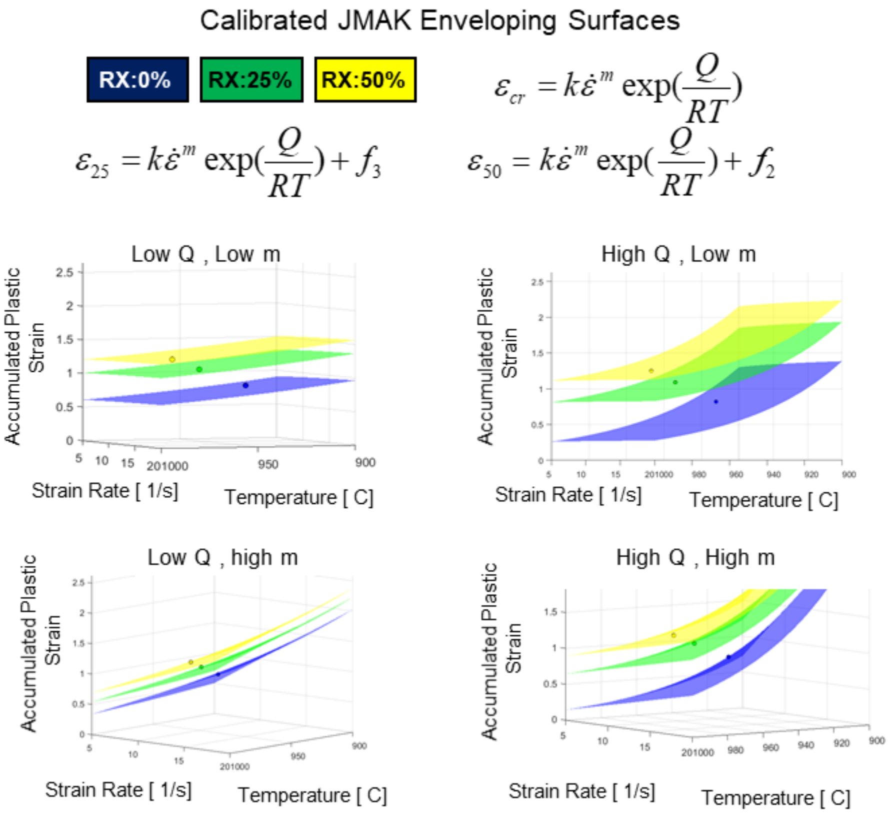

Figure 5. 10. Comparison between boundary surfaces generated by different calibrations of JMAK model.

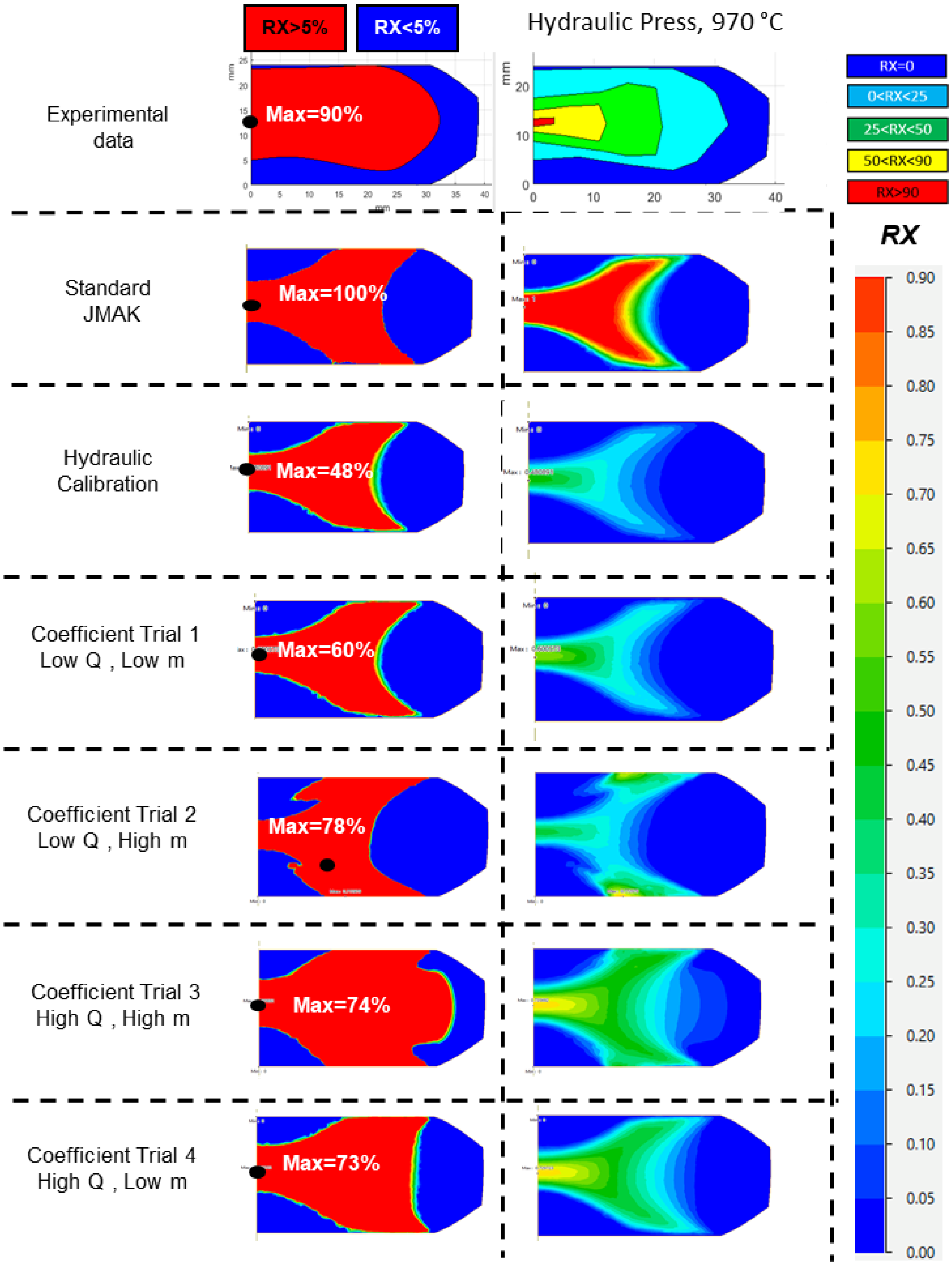

Figure 5. 11. Comparison between experimental data (recrystallisation iso-contours on top) and different calibrations of JMAK model with two different recrystallisation scales.

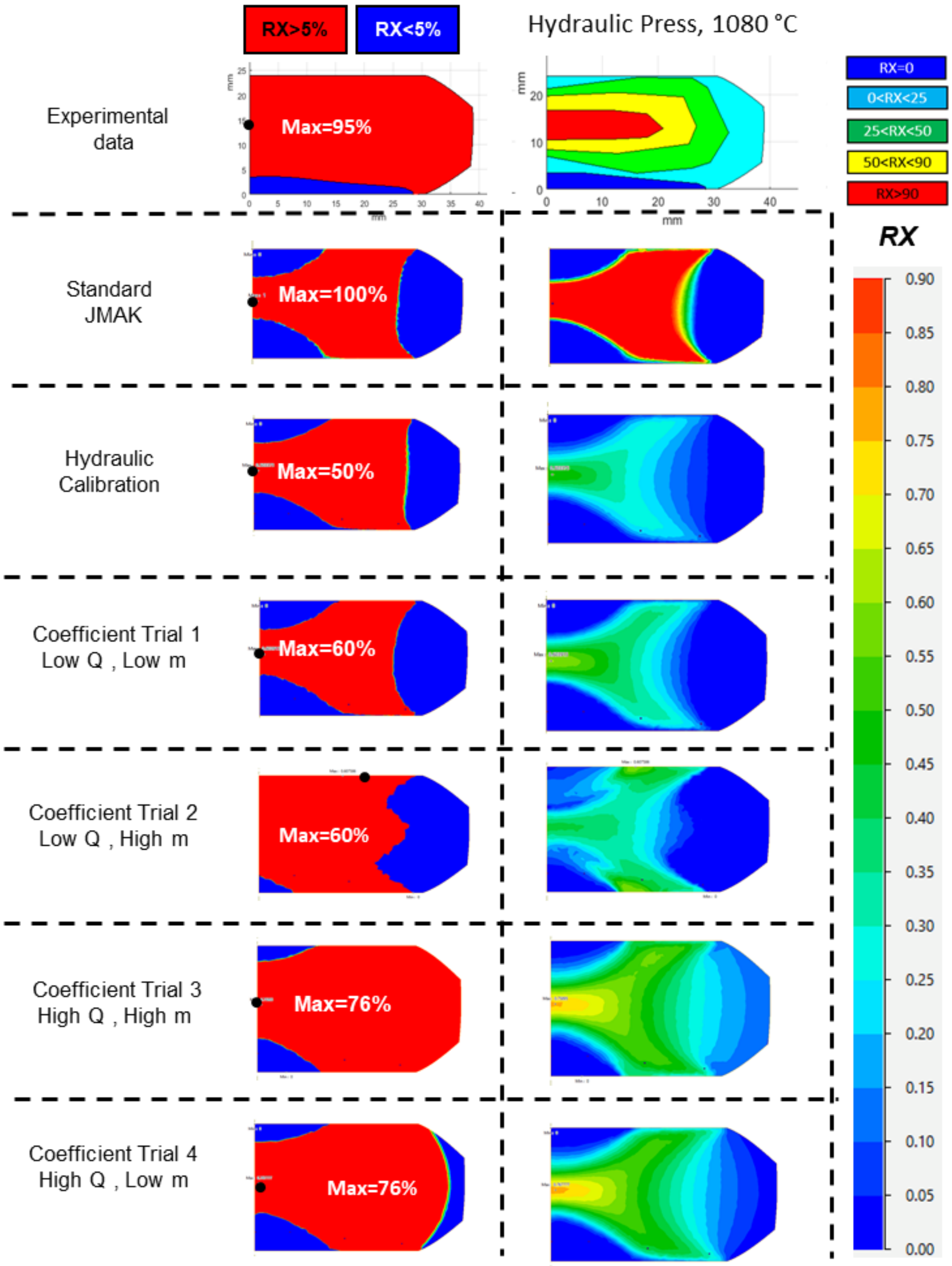

Figure 5. 12. Comparison between experimental data (recrystallisation iso-contours on top) and different calibrations of JMAK model.

5.6 Effect of Post-Dynamic Recrystallisation Modelling on Results

It could be argued that the reason for the discrepancies observed in the results above may be due to post-dynamic recrystallisation phenomena such as meta-dynamic and static recrystallisation. Meta-dynamic recrystallisation is defined as the growth of the dynamically recrystallized grain size [43], [89] and some studies suggest that a few seconds before quenching are enough for meta-dynamic recrystallisation to take place [49], [71]. By not involving nucleation, meta-dynamic recrystallisation should not affect the shape of the recrystallized area, but only the volume fraction recrystallized. From what is observed in the results the amount of recrystallisation is already over-estimated in the standard modelling results. Thus, a further increase of the recrystallised volume fraction through the use of static and meta-dynamic recrystallisation equations will only worsen the predictions.

Static recrystallisation on the other hand is characterised by nucleation and growth of new nuclei [43]. According to the literature, an incubation time is necessary for the start of static recrystallisation. This was observed to be at least 30 s, [49] which is considerably more than the approximately 3-6 seconds employed before quenching. Static recrystallisation was however modelled and within the post forging time period no static recrystallisation was predicted by the standard model.

In the calibrated model, the effects of meta-dynamic or static recrystallisation if present are combined with dynamic recrystallisation and cannot be divided. This is often representative of industrial conditions, in which for components of large dimensions it is not possible to stop meta-dynamic recrystallisation occurring.

5.7 Remarks on the Applicability of JMAK models

JMAK models are a great tool that are intuitive and can be easily used for the prediction of microstructural evolution features. They have a proven record of successful applications, most of which, however, are limited to laboratory-like trials. The demand for a higher level of accuracy, together with increased industrial complexity required a re-evaluation of this tool. The inaccuracies of the results observed in both hydraulic and screw forgings prove that these model cannot be applied blindly to industrial processes. Models are already provided with material parameters obtained through curve fitting from uniaxial laboratory tests [10], [71], [72], [74], [90], [91]. If the model is applied within the specific data range from the calibration experiment and data is interpolated, prediction can in theory be accurate. However, complications arise when extrapolation is required. The majority of these models do not come with clear applicability limits, thus preventing an informed use of their capabilities, and therefore posing questions with regard to their trustworthiness. A novel calibration methodology which has the benefit of fitting data from industrial trials, extending the range of applicability from standard models, led to improved results with hydraulic press forgings, but did not greatly benefit screw press forgings. Considering that in this latter case, recalibration did not work, the problems can be traced to the mathematical structure and assumptions implicit within the model. One possibility may be to the structure of Eq. (5.2). The use of strain rate in this way is a problem when dealing with equipment like screw presses, in which the strain rate is not constant. Indeed, if we look at the critical strain equation, when the stain rate approaches 0, recrystallisation would take place even with an infinitesimal amount of strain. Conversely, if the strain rate increases (e.g. >10 s^{-1}) it is almost impossible for recrystallisation to happen. This is a common assumption from uniaxial laboratory tests carried out in the strain rate range of 0.01-1 [1/s] [7], [8] in which dynamic recrystallisation is thought to decrease with increasing strain rate. However, this may not always be the case. This relation will be analysed further in Chapter 6.

In general it can be hypothesised that hydraulic press forgings proved more suitable than screw press forging because they resemble more closely simple uniaxial tests which were the foundations for the developments of these models. Even these forgings however, showed inaccuracies in the prediction. This may be attributed to another structural characteristic of this model as implemented into FE software; namely the fact that such models are instantaneous in nature. This means that it is not the history of the process that leads to a certain level of recrystallisation, but only the instantaneous parameters of temperature, strain rate and strain. At each iteration a value of recrystallisation is calculated, if that value is higher than the previous step it is taken as the new reference, if lower it is discarded. This approach may be valid when the history of the process is simple. Indeed, if temperature and strain rate are constant, then strain is the parameter that dictates the amount of recrystallisation achieved. However, as noted, complicated forgings are subjected to jumps in temperature and strain rate. Given the instantaneous nature of the model, if even for an instant strain rate approaches zero, recrystallisation may be predicted. A solution to this could be to change the form of the model from instantaneous to incremental, or shift to macroscopic parameters more representative of the history of the process (e.g. strain energy).

Concerning the outputs of the model related to grain size, it is clear from the observed microstructure that other features such as a non-recrystallized grain size, and/or an incorporation of multiple peaks in the grain size distribution would be needed to better represent the microstructure.

5.8 Conclusions

The applicability of JMAK type models in relation to forging processes representative of those conducted in manufacturing practice was evaluated and it can be concluded that these models cannot be applied blindly. The further the deformation conditions were from the simple monotonous laboratory test conditions that were used to develop the models the greater was the discrepancy between the predicted and measured results. A novel calibration methodology was proposed and successfully implemented for hydraulic press forgings. Yet, this was not possible for screw press forgings due to the incompatibility of the variable strain rate with the model structure. It is clear that something different should be used. To do this, it is necessary to have a deeper understanding of the recrystallisation phenomena in industrial conditions, which will be the subject of the next chapter.

Chapter 6

On the Onset of Recrystallisation

6.1 Introduction

In the previous chapter, the benchmark and calibration of the models available in commercial FE software gave unsatisfactory results, especially at higher strain rates. In order to better comprehend the reason for this mismatch and formulate possible improvements it is necessary to gain a deeper understanding of the recrystallisation phenomena and to evaluate the assumptions at the base of these models. As shown in Chapter 4, the use of experiments resembling industrial practice provides new opportunities to evaluate microstructural evolution in IN718. The first important area to focus on is the beginning of recrystallisation and in Chapter 2, it was found that the majority of models predicting this phenomena, shared a few basic assumptions:

- There exists a certain dislocation density ρ_{cr} necessary for the beginning of recrystallisation.
- This critical value can be universal or depend on temperature, strain rate and grain size.
- Dislocation density is a microscopic parameter and cannot be observed/measured during macroscopic experiments. Accumulated plastic strain can be used and associated with dislocation density.
- The peak on the stress-strain curve can be used for finding ε_{cr} and calibration of RX models.

6.2 Recrystallisation and Stress-Strain Curves

One of the shared modelling traits found in the literature is the use of the peak on the stress-strain curve as a tool for finding the critical strain associated with start of recrystallisation. However, as can be seen from Fig. 6.1, the curves (both, obtained by the author as well as by others) do not have clearly pronounced peaks, which could be robustly located, uninfluenced by natural experimental errors related to the tolerance of the specimen geometry, fluctuation of strain rate, etc. The small peak in the beginning of the curves in Fig. 6.1a refers rather to the interaction of the specimen with the testing machine than to the material properties. It is specific to tensile testing and it is not seen on similar curves obtained from compression tests in the works of other authors [30], [51], see for example Fig. 6.1b. Apparently, a feature of IN718 is that recrystallization does not lead to significant softening. The results shown in Fig.

6.1a demonstrate a relatively low, in comparison to other materials (see Fig. 6.1d), sensitivity of the flow stress to the grain size, which further decreases at higher temperatures. This renders problematic the identification of a peak and therefore the definition of a critical strain or dislocation density corresponding the onset of recrystallisation.

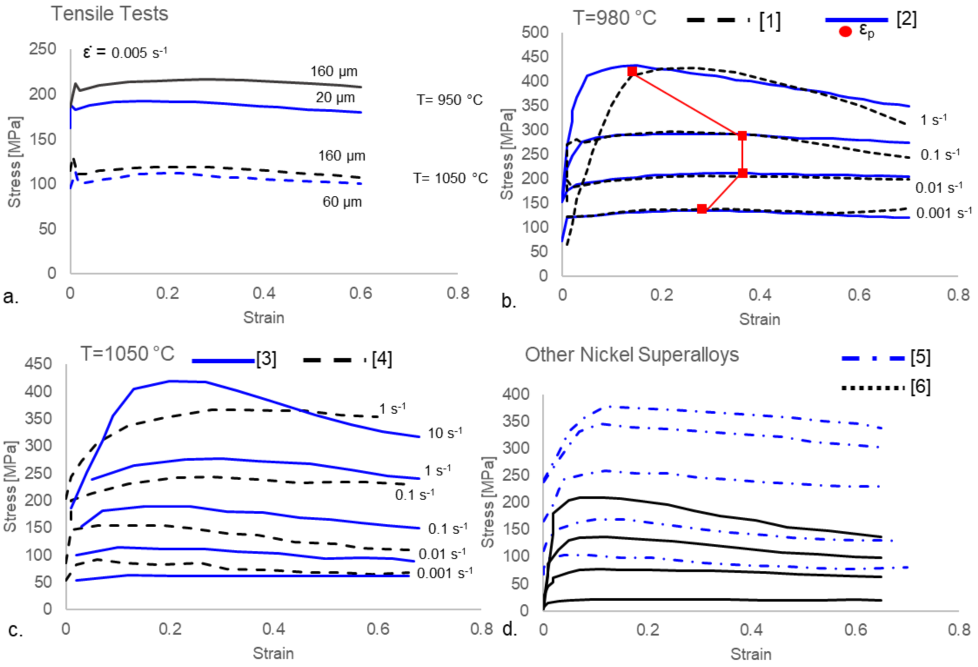

Figure 6. 1. Uniaxial Tests: a) Stress-strain curves for Inconel 718 obtained from tensile experiments, strain rate 0,005^{-1}, temperatures 950 °C and 1050°C, b) Experimental data from compression test at 980 °C and identification of peak stress [32], [51], c) Experimental data from compression test at 1050 °C [30], [31], d) Experimental data from uniaxial test of two different Nickel Superalloys (not IN718) [92], [93].

6.3 Recrystallisation and Strain

Almost all observations underlying the basis of the RX theory and models describing this process were obtained from miniaturised lab tests under isothermal conditions, strain rates close to constant and limited plastic strains. As detailed in Chapter 3, to understand the applicability of these hypothesis to processes with more complicated conditions, hot forging of double truncated cones (DTC), was performed using two industrial forging presses: hydraulic (relatively slow process) and screw (fast process). To characterise the onset of recrystallization, through the microstructural analysis of the forged samples, the “zero recrystallization boundary” was mapped for each specimen. As detailed in previous chapters, this boundary represents the line dividing zones with and without recrystallization. One of the problems of classic uniaxial tests with a uniform stress-strain state (before flow localization) is the inability to determine exactly the instant when recrystallization has started – ideally tests should be terminated at different levels of deformation, without any guarantee that it will be too early or too late. Non-isothermal industrial forging creates a non-homogeneous distribution of temperatures, strain rates and strains inside the part. As a result, points with different levels of recrystallization can be investigated. By locating the zero recrystallisation boundary (ZB) the conditions of nucleation can be identified. Some of the results from Chapter 4 are summarised in Fig. 6.2 which shows the zero boundaries in the DTC forgings. The thermo-mechanical history of the points on the boundaries was tracked through finite element modelling and some characteristic trajectories are plotted in the space of temperature, strain and strain rate. It is notable that the pattern of the ZB in all four forgings of Fig. 6.2a is very different from the pattern of strain distribution in Fig. 6.2b. In some points with low accumulated plastic strain RX has started, while in others with significantly higher strains, it has not. The most obvious reason for this should be the difference in thermo-mechanical history – how temperature and strain rate was changing in these points during forging. However, analysis of the thermo-mechanical trajectories does not resolve this discrepancy. Points A3 and A6 (green trajectories in Fig.6.2c) experience a similar temperature and strain rate (see table data in Fig.6.2e), however, at point A6 recrystallization started at 0.9 accumulated plastic strain, while for the onset of RX at A3 the strain had to reach 1.4. The green trajectories represent forging at 970°C and purple trajectories forging at 1080°C. This was with the same press, time of the process, and similar strain rates. It could be expected that purple trajectories will end at lower strains (RX will start faster at higher temperature) than green ones. Being true for the points like B2, it is not, however not true for points such as B6 and B7. Given these observations, it seems that strain as a macroscopic measure of the recrystallisation process may not be the best suited parameter.

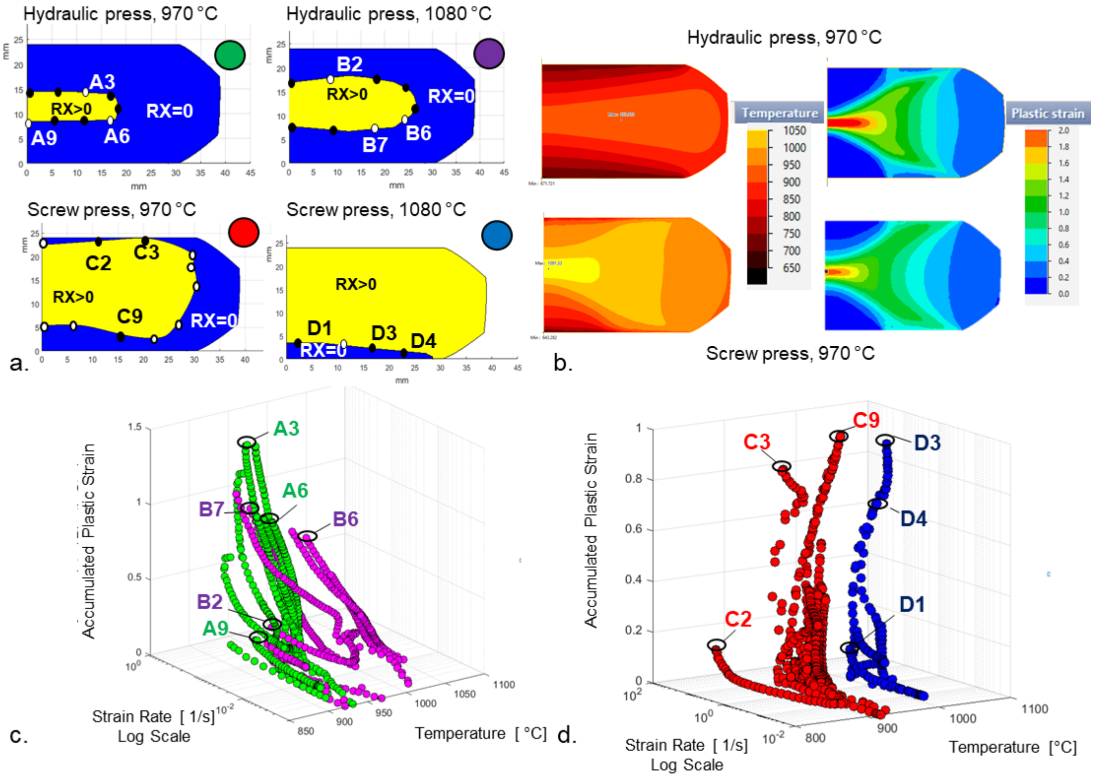

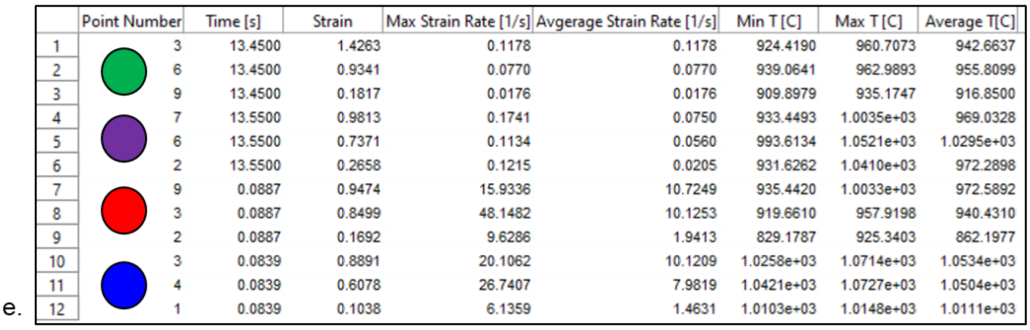

e.

	Point Number	Time [s]	Strain	Max Strain Rate [1/s]	Avgerage Strain Rate [1/s]	Min T [C]	Max T [C]	Average T[C]
1	🟢 3	13.4500	1.4263	0.1178	0.1178	924.4190	960.7073	942.6637
2	6	13.4500	0.9341	0.0770	0.0770	939.0641	962.9893	955.8099
3	9	13.4500	0.1817	0.0176	0.0176	909.8979	935.1747	916.8500
4	🟣 7	13.5500	0.9813	0.1741	0.0750	933.4493	1.0035e+03	969.0328
5	6	13.5500	0.7371	0.1134	0.0560	993.6134	1.0521e+03	1.0295e+03
6	2	13.5500	0.2658	0.1215	0.0205	931.6262	1.0410e+03	972.2898
7	🔴 9	0.0887	0.9474	15.9336	10.7249	935.4420	1.0033e+03	972.5892
8	3	0.0887	0.8499	48.1482	10.1253	919.6610	957.9198	940.4310
9	2	0.0887	0.1692	9.6286	1.9413	829.1787	925.3403	862.1977
10	🔵 3	0.0839	0.8891	20.1062	10.1209	1.0258e+03	1.0714e+03	1.0534e+03
11	4	0.0839	0.6078	26.7407	7.9819	1.0421e+03	1.0727e+03	1.0504e+03
12	1	0.0839	0.1038	6.1359	1.4631	1.0103e+03	1.0148e+03	1.0111e+03

Figure 6. 2. Trajectories of Zero RX boundaries: a) Experimental zero RX boundaries mapped on four DTC at two temperatures 970°C and 1080°C using hydraulic and screw presses, b) plastic strain and temperature taken from FE simulation, c&d) thermo-mechanical history in different points of zero boundaries, e) summary table for strain, temperature, average strain rate and process time for mapped points.

6.4 Recrystallisation and Strain Rate

As was seen in Chapter 5, JMAK models seemed to be unreliable with higher strain rate forgings. This could be a limitation of Eq. 5.2 used to calculate critical strain. A common assumption resulting from uniaxial laboratory tests carried out in the strain rate range of 0.01-1 [1/s] [7], [8] is that dynamic recrystallisation is thought to decrease with increasing strain rate. However, other studies have shown that when the strain rate passes a certain threshold (1-10 1/s) the recrystallisation volume fraction starts increasing again [5], [9]. The mathematical structure of Eq. (5.2) however does not allow for this to happen because the curve obtained is monotonous.

Unfortunately, among a large number of papers devoted to recrystallization in Inconel 718 and similar Ni-based superalloys only a few papers deal with relatively high strain rates. It is difficult to gauge which observations are more correct – the final recrystallized fraction can include a contribution from several processes such as dynamic or meta-dynamic (MRX) recrystallization which can have a different dependence on strain rate [51].

Fig. 6.3 presents the main trends in the effect of strain rate on the RX onset, obtained from the analysis of zero boundary points. It is notable that by limiting the analysis only to data from the hydraulic press (strain rates up to $0.1s^{-1}$) a nice monotonous trend can be observed (Fig.6.3a) which can be easily fitted into the relationship:

$$\varepsilon_{cr} = k(T)\dot{\varepsilon} + C_1 \tag{6.1}$$

However, if the data from the higher strain rate (screw press) forgings is added as well then the fit is compromised (Fig. 6.3b). Compared with the observations of other authors, mentioned earlier, these results are closer to the position of Nicolaÿ et al [51]. In these, the low range of strain rates (10^{-2} - 10^{-1} s^{-1}) an increase of strain rate shifts nucleation to higher values of strain, then in the middle range of strain rates (10^{-1} - $5{\cdot}10^{0}$ s^{-1}) the situation inverts, quite low values of plastic strain appear to be sufficient for the onset of RX. However, in the region of higher strain rates ($5{\cdot}10^{0}$- 10^{2} s^{-1}) the trend changes again. Besides the questions regarding the possible reasons for this phenomenon, these results raise again doubts about the suitability of accumulated or effective plastic strain as a measure of the process' progress when characterising recrystallization.

The general shape of the surface determined by Eq. (5.2) or (6.1) and suggested as a RX onset criteria is shown in Fig. 6.3c. It is apparent that the experimental data cannot be fitted into it with mere calibration of the constants. More clearly this mismatch is evident from Fig. 6.3 d. These observations lead to the conclusion that the traditional criteria of RX onset in the form of Eq. (5.2) can only be safely used for a window of low strain rates (10^{-4} to $10^{-1}s^{-1}$). In Chapter 5, microstructural predictions obtained in FE simulations using an optimised calibration of that equation gave reasonably good results for both forgings performed on the hydraulic press. However, the same model, calibrated for low strain rates gives an incorrect prediction when the model is generalised to include high strain rates (10^0 - 10^2 s^{-1}). The underlying point here is that models optimised in simple laboratory tests (often under isothermal conditions) can only be safely used in an industrial setting that approximates to the lab-based tests. Most models however do not come with an applicability range of the temperature, strain and strain rate.

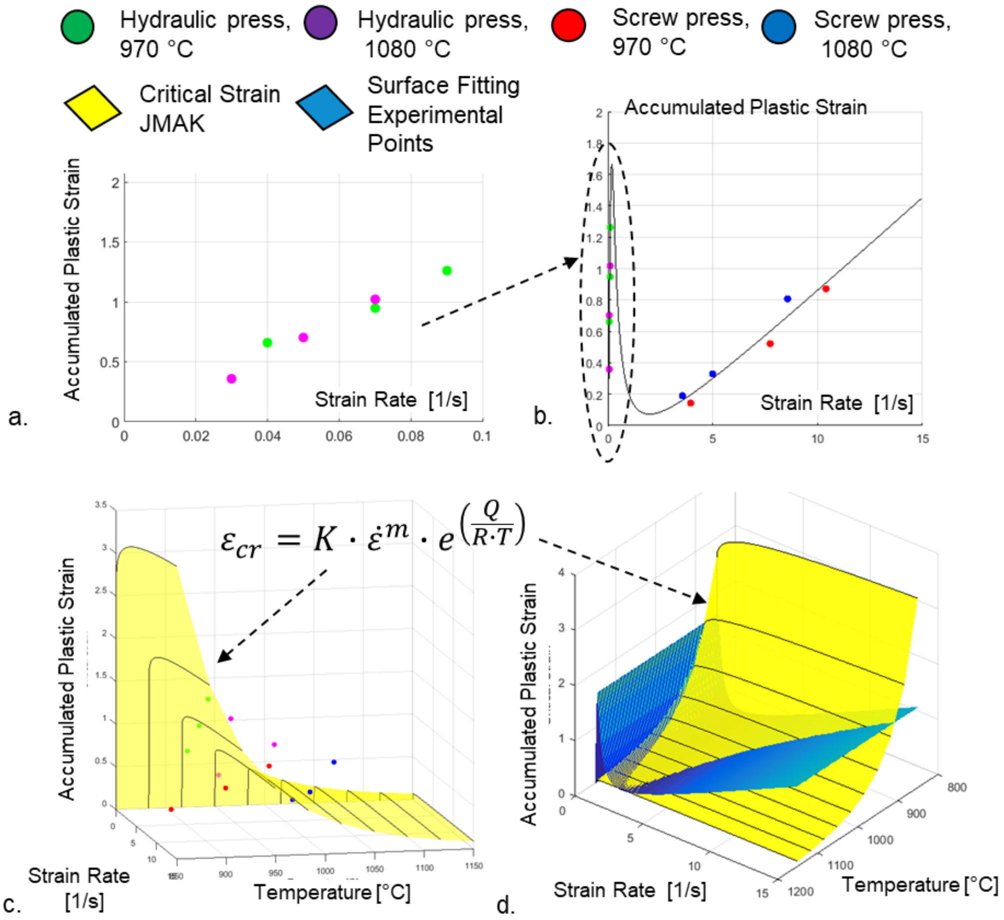

Figure 6. 3. Dependence of RX onset on the strain rate: a) curve fitting for the set of data obtained from only low strain rates – hydraulic press forging, b) the shape of the trend curve in the case of using both low and higher strain rate data, c) the shape of the 3D surface defined with the Eq. (5.2) in the space of temperature, strain rate and strain, d) the difference between trend surface matching experimental data and one defined by Eq. (5.2).

6.5 Recrystallisation and Temperature

Processing of experimental data to establish thermal dependence of the recrystallisation onset is not straightforward. Due to the non-isothermal nature of most forging processes, the temperature at the point of the zero RX boundary varies during the process within a range of about 100°C (due to cooling, or adiabatic heating). Fig. 6.4 shows temperature and accumulated plastic strain for various points of the zero RX boundary for four forging tests. The results show considerable scatter. The only conclusion which can be made with a high level of confidence is that this data cannot be fitted to the critical strain Eq. (5.2). For example, point C2 has the lowest temperature, but despite that RX has started at about just 15% plastic strain while point D3, which has one of the highest temperatures, remained uncrystallised until 80% deformation (both points belong to the "fast" screw press forging). These discrepancies raise many questions. Being pre-heated to 970°C, the preform in which C2 is located, lost about 40 degrees due to the contact with air, then it further cooled due to the contact with the forging die (which was 250°C) and finally the temperature there dropped below 900°C which is considerably lower than the RX threshold reported temperature of 975°C up to 70% deformation by Guimaraes [64] and the experimental DTC forged at 915°C in this work. This problem is further complicated by the question of which temperature should be taken into consideration? As shown in Fig. 6.4b & c, the green and purple points (representing hydraulic press forging) are shifted towards lower temperatures during the process due to heat losses with the cooler dies. Conversely, the majority of red and blue points (screw press) move towards higher temperatures due to adiabatic heating. In the former case, the use of the initial temperature within the RX equations (e.g. Eq. 5.2) appears to be inappropriate. In case of cooling, the initial temperature does not look a representative parameter for the description of this phenomenon. In fact, for example the purple points had this temperature when deformation was too low for nucleation (although it can be theoretically possible that recrystallisation did not happen at the very end of the process), so the final temperature seems more appropriate. However, in the case of "fast forging", the final temperature is higher due to adiabatic heating which lasts a fraction of a second (e.g. 100 °C in 8 ms). It is uncertain if this time is sufficient for the increment of the temperature to play its role, either fully, or partially. Often, commercial software uses the average process temperature instead of an instantaneous temperature in the equations of microstructural models. However, as is clear from Fig. 6.4, choosing any of these temperatures does not help with the rearrangements of points in order to produce a reasonable trend in temperature dependence. This situation points again to the question of whether critical strain is a good choice as a measure for the formulation of a RX onset criteria.

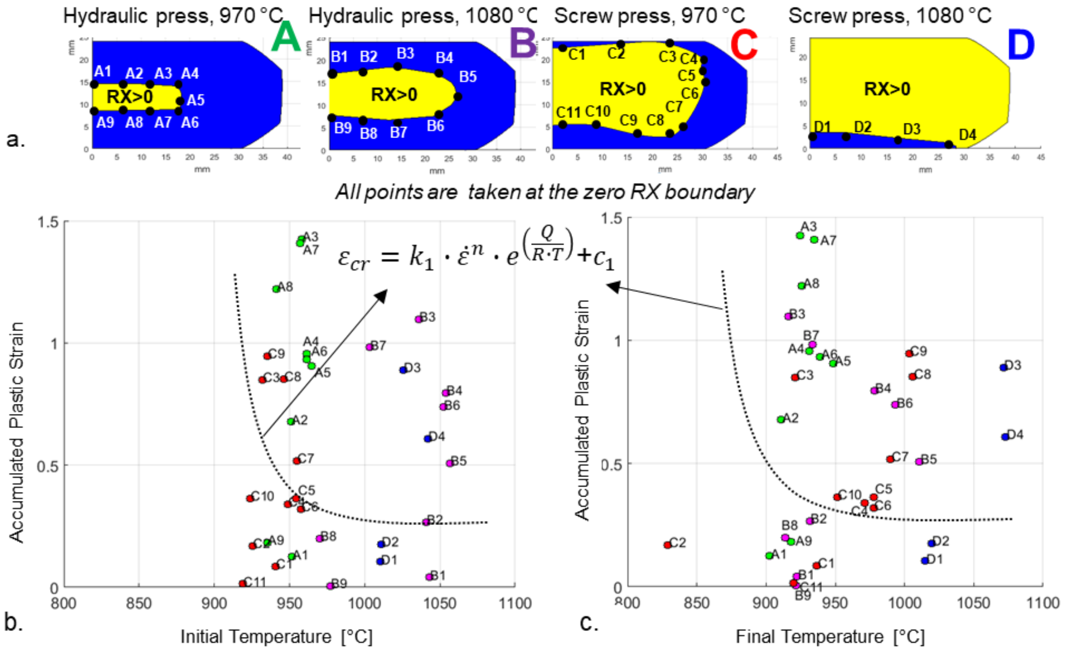

Figure 6. 4. Dependence of RX onset on temperature: a) Experimental zero recrystallisation boundaries mapped for four forging trials and location of the tracked points, b & c) conditions of RX onset – b) initial temperature, c) final temperature.

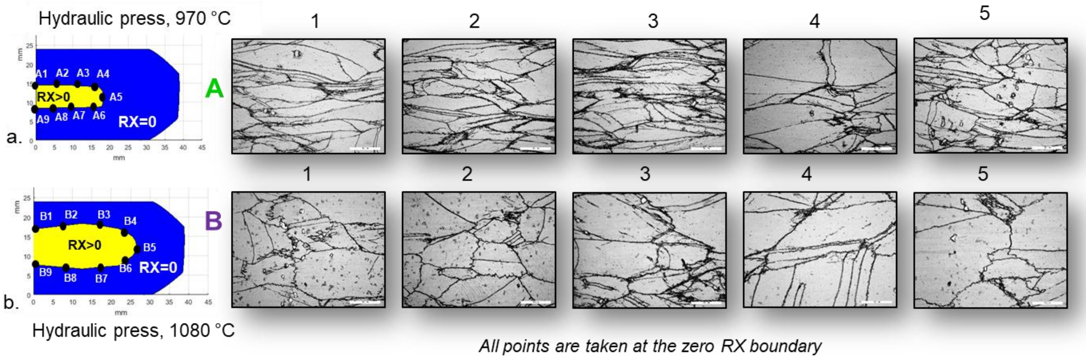

Figure 6. 5. Optical microstructure of zero boundary (shown as iso-contour on the left side): a) Hydraulic press forgings at 970 °C, b) Hydraulic press forgings at 1080 °C (see Appendix 1.11 for enlarged version).

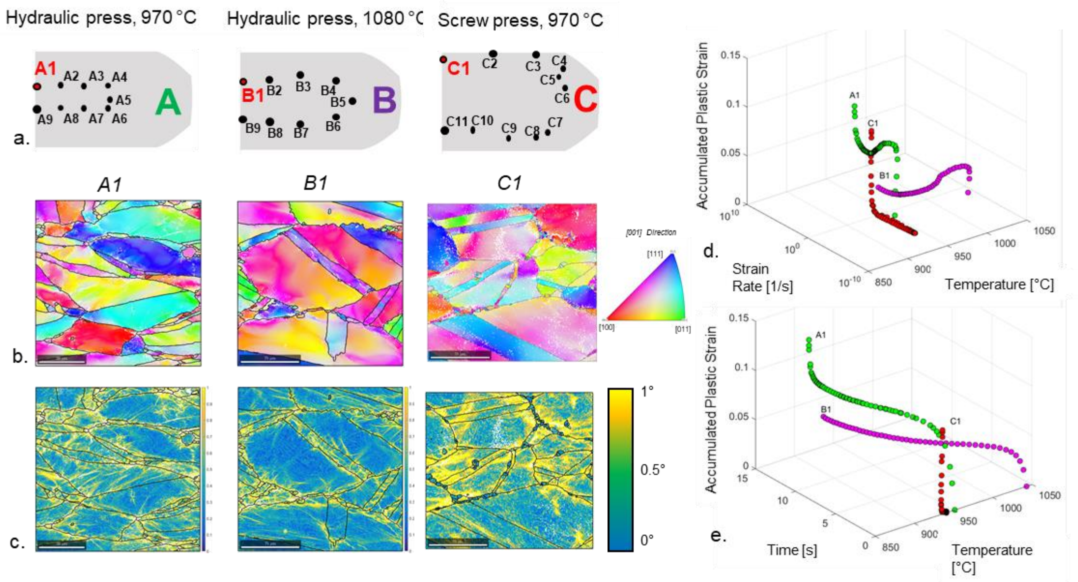

Figure 6. 6. EBSD maps of zero boundaries: a) investigated points, b) corresponding EBSD maps (Inverse Pole Figure), c) corresponding EBSD KAM maps, d) trajectories of thermo-mechanical states in strain rate – temperature-strain space, e) trajectories of thermo-mechanical states in time – temperature-strain space (see Appendix 1.12 for enlarged version).

6.6 Alternatives Measures to Strain

Returning back to the retrospective of RX modelling, described in Chapter 2, it can be seen that the main factors needed for nucleation are groups of dislocations accumulated near grain boundaries. Strain took then the place of dislocations because dislocation density is difficult to measure, but it is not evident that measures of strain reflect the required dislocation density correctly.

In Fig. 6.5, the analysis of the microstructure along the zero RX boundary, indirectly offers some clarification on this point. The onset of nucleation means that at a given instant all the points shown had the required dislocation density:

$$\rho \geq \rho_{cr}(T) \tag{6.2}$$

However, it is clear that the microstructural state in terms of the level of local strain within the grains varied considerably. This is true even when comparing positions at approximately the same temperature e.g. point A3 is different from A4, point B5 is different from B3 etc. At positions A4 and B5 the grains appear to have experienced different levels of deformation as against those at A3 and B3. Comparing these observations with the thermo-mechanical trajectories, see Fig. 6.4, it can be seen that trajectories A4 and B5 present lower values of accumulated plastic strain compared to A3 and B3. A potential explanation for this difference can be the assumption that in points A3 and B3 for some reason (possibly due to the temperature) while relatively big plastic strains were accumulated in deforming (squeezing) and fracturing of grains (or CDRX), piles of dislocations suitable for nucleation were not formed.

More information about possible reasons for the difference in the RX onset can be obtained from EBSD analysis. Orientation and KAM maps for three similar points are shown in Fig. 6.6 along with their respective thermo-mechanical trajectories. These three points illustrate different deformation scenarios. Point B1 has the shortest trajectory (Fig. 6.6d, 6.6e) and its KAM map at the end of the process shows the smallest dislocation density of the three points inside the grains (majority of dislocations are accumulated around grain boundaries). Due to the high temperature (despite the cooling from 1080°C to 960°C) and sufficient time, it can be hypothesised that the dislocations had enough mobility to move to the grain boundaries and nucleate into new grains. In this case strain could be associated as a measure of RX progress. However, the other two cases (A1 and C1) are significantly different. A1 has the longest trajectory and recrystallization began at a higher accumulated plastic strain than B1. The temperature of this point (A1) is quite low (initially heated to 970°C it cools down to almost the reported bottom threshold of RX temperature), thus the mobility of dislocations is reduced, and therefore an higher amount of dislocations stay in the grains and with the longer period available due to the relatively low strain rate hydraulic press forging heavy deformation and fracturing of grains is observed, see Fig.6.6c. Correspondingly, part of accumulated plastic strain belonging to this point would not contribute to RX and should not be counted in the prediction of RX. However, this unused dislocation density may become relevant in further processing, such as re-heating for precipitation treatments, leading to post-dynamic recrystallisation phenomena and possibly enhanced precipitation rates. Point C1 represents the opposite situation, being forged in the high strain rate screw press, this process is characterised by the shortest time (just a few milliseconds), as shown in Fig. 6.6e. Due to the dynamic nature of the loading, a high dislocation density would be generated across the grain volume, however in this case there is insufficient time to allow glide and the formation of dislocation pile ups at grain boundaries to facilitate nucleation of new grains. Despite the fact that all forged specimens were water quenched after forging, recrystallized grains observed at point

C1 are most probably post-dynamic recrystallized grains, which formed during transfer of the forging to the quenching tank. This is further indicated by the absence of dislocations in these newly formed grains (Fig.6.6c), similar observations and conclusions were made by Zouari et al [49].

All these observations lead to two important conclusions. The accumulated plastic strain cannot always be successfully used as a measure for the prediction of the RX onset for all types of forging process. Considering the need for phenomenological modelling of microstructural transformations in industrial forgings, two alternative approaches can be proposed: either to find another universal measure (if it exists) or to classify all processes into different groups and use an individual measure for each one. The same is valid for multi-scale modelling as in these models the accumulation of dislocation density is often taken as a function of accumulated plastic strain. For example after integration of Eq. (2.8), used in the model of Zouari et al [66], the following relationship is obtained:

$$\frac{\partial \rho}{\partial \varepsilon^{p}} = K_1 - K_2 \rho \;\rightarrow\; \rho = \frac{K_1}{K_2} - \exp(-K_2 \varepsilon^{P}) \tag{6.3}$$

which, as was shown above, may not be suitable for all processes.

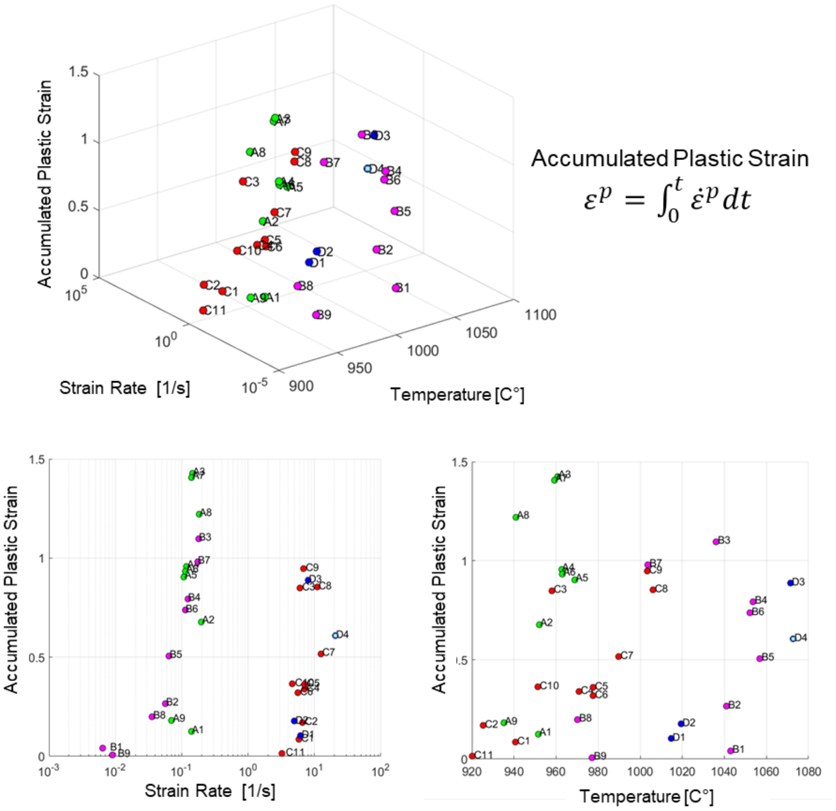

Figure 6. 7. Final positions in the history of accumulated plastic strain versus temperature and strain rate for zero boundary points.

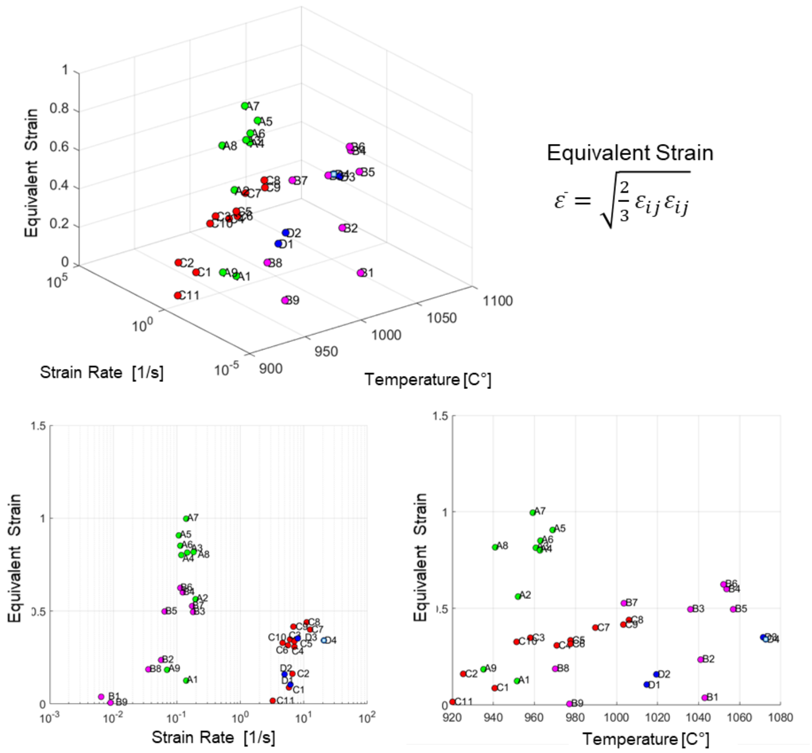

Figure 6. 8. Final positions in the history of equivalent strain versus temperature and strain rate for zero boundary points.

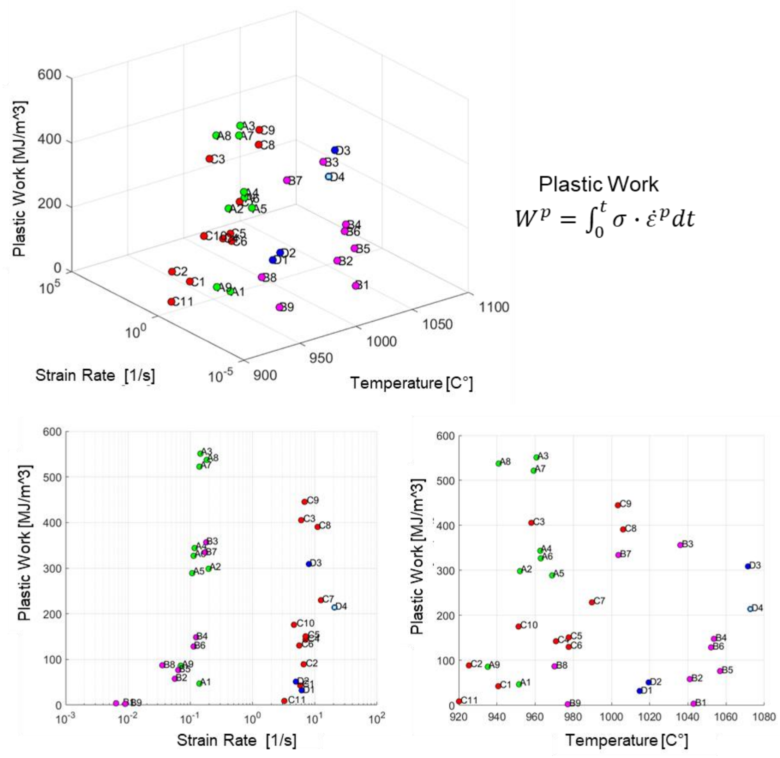

Figure 6. 9. Final positions in the history of equivalent plastic work versus temperature and strain rate for zero boundary points.

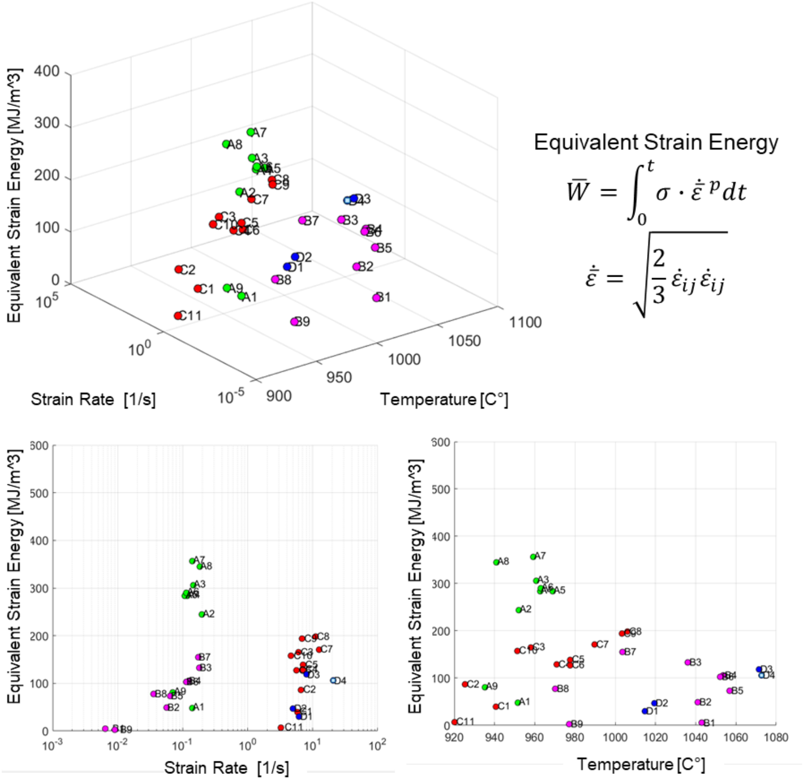

$$\bar{W} = \int_0^t \sigma \cdot \dot{\bar{\varepsilon}}^p dt$$

$$\dot{\bar{\varepsilon}} = \sqrt{\frac{2}{3}\dot{\varepsilon}_{ij}\dot{\varepsilon}_{ij}}$$

Figure 6. 10. Final positions in the history of equivalent strain energy versus temperature and strain rate for zero boundary points.

In principle, an investigation on the existence of alternative macroscopic measures can be performed without attempts to justify any relation to the required dislocation density. The choice is however limited; it can either be another feature such as equivalent strain, or an energy-type characteristic such as plastic work, or strain energy calculated with equivalent strain. Fig. 6.7-6.10 show how the configuration of the zero boundary points changes depending on the choice of the measure.

From the figures it can be seen that equivalent strain energy gives a slightly more consistent representation of the data, however, in general, no single macroscopic measure is suitable for the broad range of experimental data. This means that it is most likely impossible to generate some universal phenomenological model similar to JMAK suitable for the prediction of recrystallization for complex processes such as industrial hot forging, characterised by a complicated thermo-mechanical history spanning a broad range of strain rates and temperatures. The main problem associated with all macroscopic phenomenological measurable parameters lies in their integral nature, which most probably correlates with the total amount of generated dislocations. To more correctly predict the recrystallization phenomenon it seems to be necessary to design a method that splits: (a) dislocations used by other deformation mechanisms (e.g. grain distortion, fragmentation/CDRX), (b) dislocations piled on the grain boundaries and suitable for RX nuclei and, (c) dislocations spread across the grain volume (as shown in Fig. 6.6) which will play a role in post-dynamic recrystallization during further heat treatments. Unfortunately, the answer to this requires further investigation. Nevertheless, the first step is performed by making an attempt to split different points of the Zero Boundary into a few groups depending on their histories (see Fig. 6.11). The points can be classified into: points following a JMAK-type trend (green cloud), points following a similar trend but with very low energy (red cloud) and points located in-between these two. The bottom cloud mainly contains points from the zones close to the contact with the tools (forging dead-zones). Besides 4 points from the hydraulic press tests (A1, A9, B1 and B9), all of these points belong to the “fast forging” category. It can be assumed that recrystallization in these points occurred after completion of forging during transfer to the quenching tank.

Fig. 6.12 shows the post forging thermal history of all these points. It can be seen, that the temperature for the majority of the points (belonging to screw press forgings) remain elevated for about 6-8 seconds, which could lead to post dynamic recrystallization. However, the temperature at points A1, A9, B1 and B9 in the hydraulic press forging drops very fast to considerably low temperatures below the recrystallisation range. If we assume that the red category of points present post-dynamic recrystallisation, it raises the question of why other zones of the workpiece are not post-dynamically recrystallised. The reason might be the existence of a temperature threshold for post-dynamic recrystallisation. This is further supported by the observations made in in Fig. 6.13. In the screw press forging point C2 accumulates a higher energy (≈80 MJ/m^3) than C1 (≈40 MJ/m^3) however while in C1 RX already started, no RX nuclei are found in C2. KAM maps show a similar distribution of dislocations for the two points but the temperature of C2 during the post-forging operations decreases while C1 temperature rises (Fig. 6.13d). It can be supposed that the post-dynamic recrystallisation is hindered in C2 due to the temperature drop after the forging further suggesting the existence of a temperature threshold.

As mentioned in Chapter 3 the plotting of the thermo-mechanical trajectories is characterised by errors deriving from macroscale simulations and experimental measurements, however these are small and while they can slightly influence the quantitative measurements displayed in this chapter, they do not affect qualitative conclusions derived from this investigation.

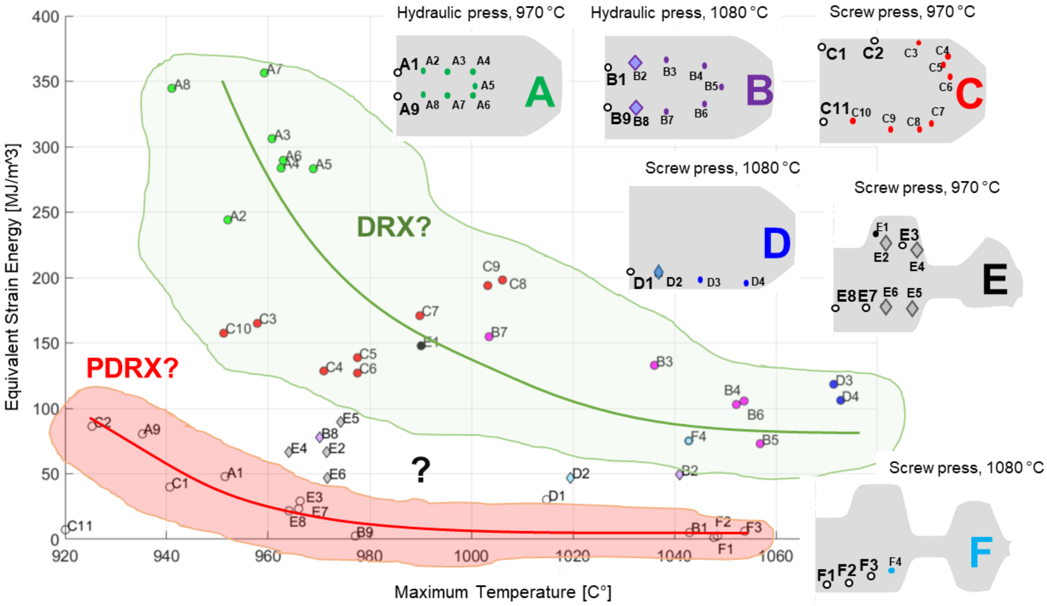

Figure 6. 11. Plotting final instant of the thermo-mechanical trajectory of the zero boundary points and classification into dynamic and post-dynamic recrystallisation. On the right side is shown the location of the points in the section of the forged specimens.

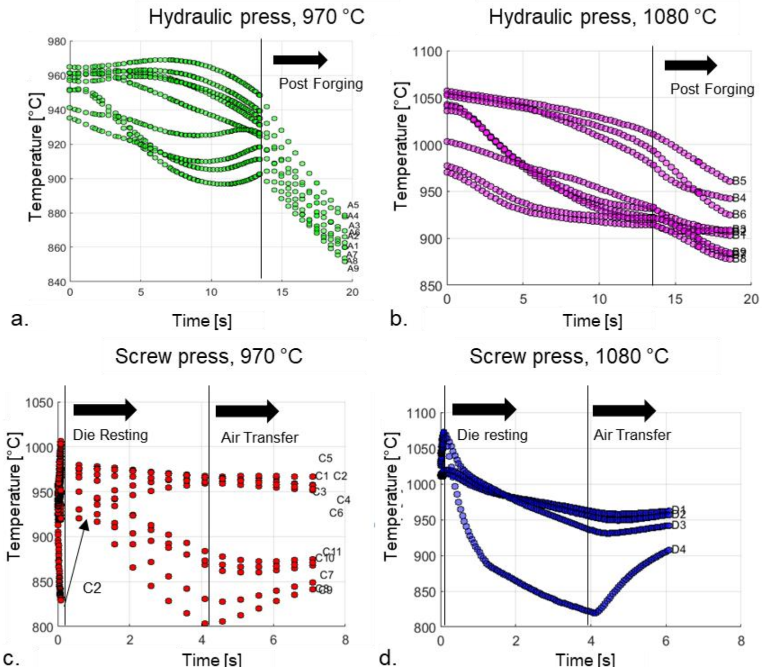

Figure 6. 12. Post forging thermal history of the Zero Boundary points: DTC forged at a) 970°C, hydraulic press, b) 1080°C, hydraulic press, c) 970°C, screw press, d) 1080°C, screw press.

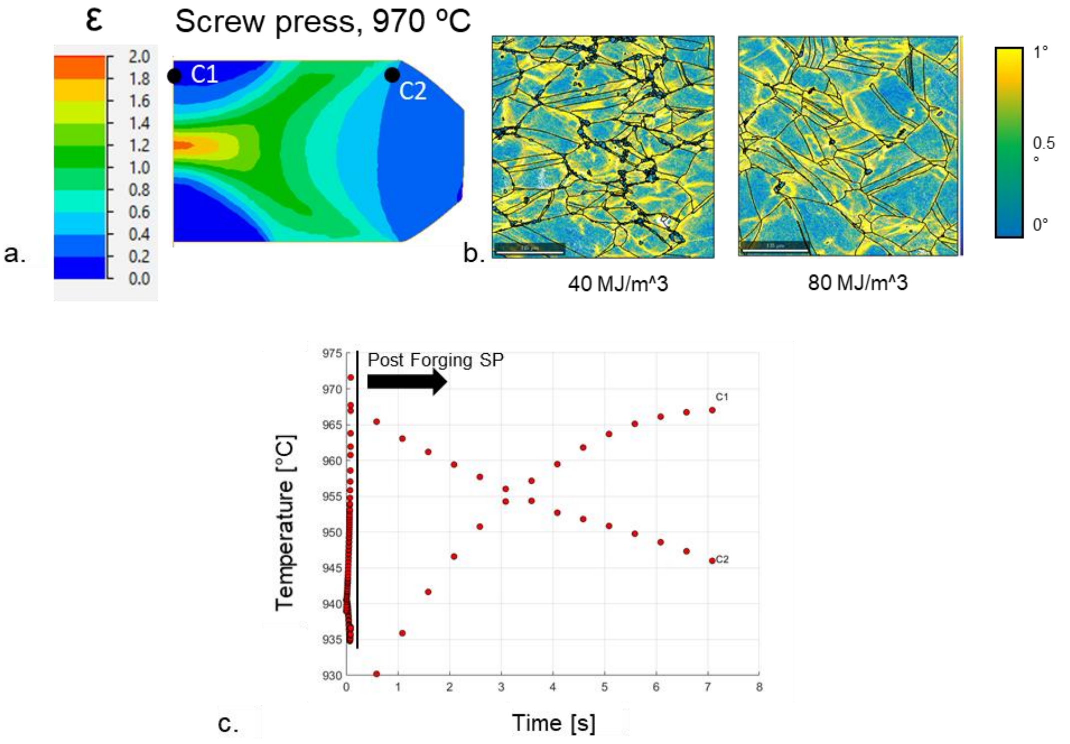

Figure 6. 13. Comparison between RX and non-RX points in screw press forgings: a) Strain field from FE simulation, b) KAM maps (EBSD), c) Post forging Thermal history of the points taken from FE simulation.

6.7 Conclusions

The analysis of microstructural transformations in Inconel 718 during non-isothermal hot forgings on industrial hydraulic and screw presses leads to following conclusions:

- Recrystallisation in Inconel 718 does not seem to result in pronounced softening, so for this material it is problematic to determine the onset of recrystallization using the peak on the stress-strain curves.
- Traditional criteria for the RX onset in the form of Eq. (5.2) can be safely used for a window of the low strain rates of 10^{-4} to $10^{-1}s^{-1}$, but appear to be unsuited for a broader range of strain rates, including the higher ones (10^{0} - $10^{2}\,s^{-1}$).
- Total accumulated plastic strain as well as the total dislocation density (of the dislocations generated as a result of strain) is not the best measure for the characterisation of the onset and development of dynamic and meta-dynamic recrystallization. The main reason for this is the fact that in contrast to simple deformation conditions, recrystallization may not be the only deformation mode (and may not be the dominating mode) during the complex loading seen in industrial hot forging.
- There does not seem to be an alternative macroscopic measure that can capture the recrystallisation onset in industrial hot forging. To correctly predict the recrystallization phenomenon a method is suggested that splits dislocations used by other deformation mechanisms, dislocations piled on the grain boundaries (used for nucleation) and dislocations dispersed across the grains (associated with post-dynamic recrystallisation phenomena).

In the next chapter recommendations for the implementation of the above conclusions in a model framework will be discussed.

Chapter 7

Novel Model Framework and Further Research with DIGIMU®

7.1 Introduction

The first part of this chapter will address the modelling implications of the conclusions drawn from Chapter 6 regarding the recrystallisation phenomena in industrial hot forging of IN718. In particular, it was observed that the total accumulated plastic strain or total dislocation density does not seem to be the best measure for the characterisation of the onset and development of dynamic and meta-dynamic recrystallization. Similarly, no other macroscopic measure seems to capture the recrystallisation onset in industrial hot forging, due to the fact that discontinuous dynamic recrystallisation may not be the dominating microstructural evolution mechanism. In the second part of this chapter, the use of multi-scale modelling through DIGIMU® as a tool for further research will be discussed.

7.2 Modelling Recommendations

As shown in Chapter 2 many models, including the work of Zouari et al. [94] are based on the total accumulation of dislocations. At each iteration *i*, characterised by a time step *dt*, a deformation increment is given and as a result dislocations are generated following the relationship shown in Eq. (7.1), which integrated results in Eq. (7.2):

$$\frac{\partial \rho}{\partial \varepsilon_{eff}^{P}} = K_1 - K_2 \rho \tag{7.1}$$

$$\rho = \frac{K_1}{K_2} - Ae^{-K_2 \varepsilon} \tag{7.2}$$

At each iteration i, the increment in dislocation density depends on the balance between the dislocations that are generated and contribute to hardening and the ones that are annihilated by recovery. These two contrasting processes are represented by K_1 and K_2 which are respectively the hardening and recovery parameters. The dislocation density increases with plastic deformation until the point at which a critical dislocation density is reached and recrystallisation starts. Models based on Eq. (7.1) are generally generated and calibrated through the analysis of flow stress curves which are characterised by a pronounced peak in the curve and thus by initial hardening and then softening (associated with recrystallisation). As strain is related to dislocation density following Eq. 7.2, the latter is linked to stress by the relation:

$$\sigma = \sigma_0 + \alpha_T M_T \mu b \sqrt{\rho} \tag{7.3}$$

Where σ_0 is the flow stress of the unhardened material, α_T and M_T are material parameters, μ is the shear modulus and b is the length of burger's vector. However, as noted in previous chapters, experimental observations and literature studies show that IN718 stress-strain curves do not always seem to be characterised by a strong peak making it problematic to calibrate the above mentioned relations. In early fundamental work on recrystallisation performed by Sandstrom et al. [61] it was suggested that the dislocation density should be divided into two groups: homogeneous dislocations between sub-grain walls and dislocations located in sub-grains walls (dislocation piles). In this work it is shown that homogeneous dislocations contribute to flow stress, following a similar relation to Eq. (6.3). On the other hand dislocation pile-ups are the main driver for recrystallisation. Moreover, it is shown that these two types of dislocations can have a different order of magnitude.

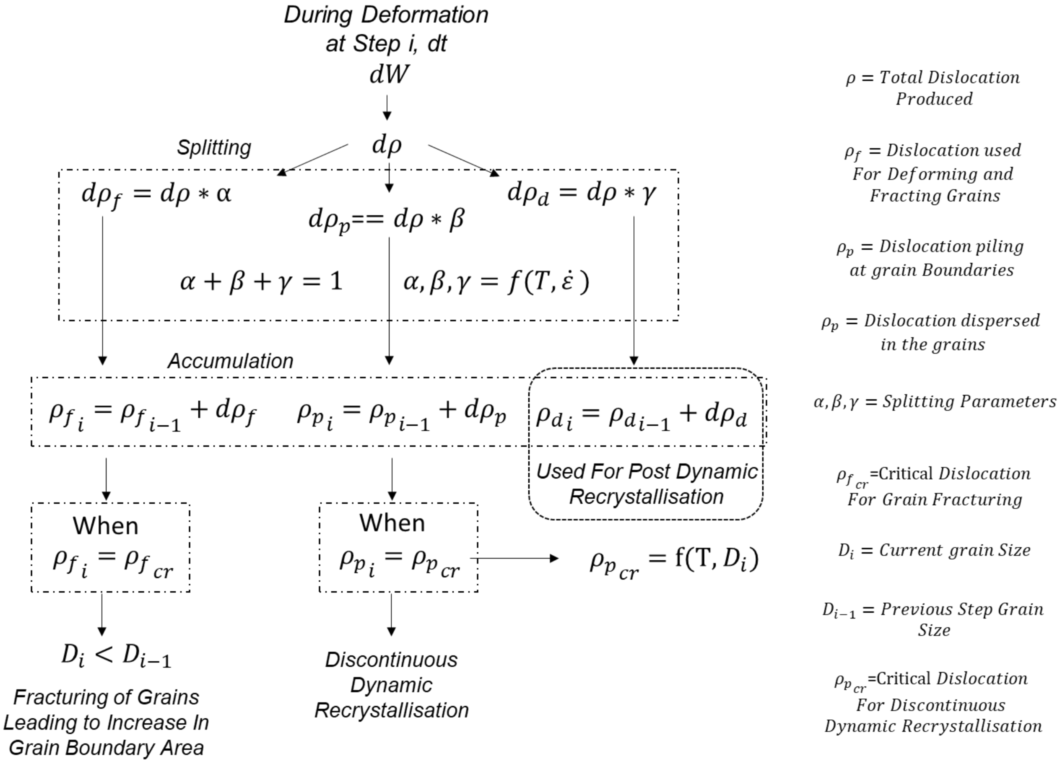

Figure 7. 1. Proposed model scheme.

Similarly to the observations of Sandstrom et al., the experimental observations in Chapter 6 suggest that the total generated dislocations at each time step should be split into:

- ρ_f - Dislocations used by mechanisms other than recrystallisation (e.g. grain deformation, fracturing etc.).

- ρ_p - Dislocations piled up on the grain boundaries used for Discontinuous Dynamic Recrystallisation
- ρ_d - Dislocations dispersed across the grains which are later used in post-dynamic recrystallisation phenomena.

The model framework based on this theory is summarised in Fig. 7.1. In this case, after the increment in dislocation density is generated, it is split into the three values: $\rho_f, \rho_d \text{ and } \rho_p$. The fraction of the total dislocations going to each separate group is defined by the parameters α, β, and γ, which follow the relation:

$$\alpha+\beta+\gamma=1\ ,\ \alpha,\beta,\gamma \in [0,1] \tag{7.4}$$

These material parameters are dependent on strain rate and temperature. Once the increment in dislocations is distributed, an accumulation step is computed in which the total amount of dislocations is calculated for each dislocation group. When ρ_f reaches a critical value, it is assumed that the grains start fracturing, resulting in a decrease in grain size and thus an increase in grain boundary area (GBA). Looking at the dislocations that are piled against the boundaries, when these reach a critical density value $\rho_{p_{cr}}$ discontinuous dynamic recrystallisation will take place.

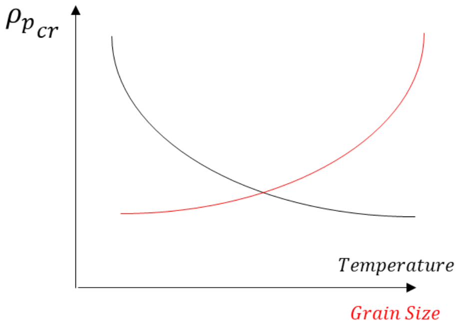

Figure 7. 2. Critical dislocation density as a function of Temperature and Grain size for DDRX.

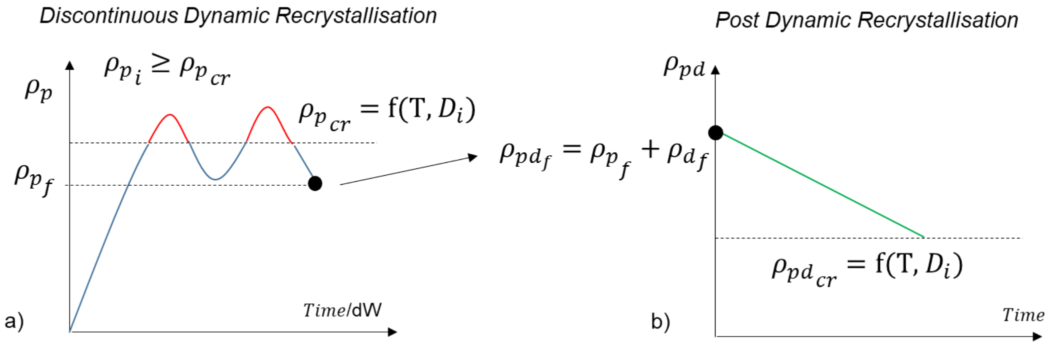

Figure 7. 3. Effect of DDRX and PDRX on the dislocation density value.

The $\rho_{p_{cr}}$ critical value will be decreasing with increasing temperature and will depend on grain size as shown in Fig. 7.2. Indeed, smaller grain sizes correspond to a bigger amount of grain boundary area in which nucleation can take place. The progress of the value ρ_d, can be seen in Fig. 7.3a. Dislocation pileups on grain boundaries accumulate with time during deformation and when DDRX is initiated ($\rho_p > \rho_{p_{cr}}$), ρ_p decreases as the dislocations are used to form nuclei. When deformation halts, the dislocations dispersed in the grains plus the dislocations that are still piled-up at the grain boundaries which have not been used yet can be combined to form the available dislocation density for post-dynamic recrystallisation ρ_{pd}. Contrary to what was seen for dynamic recrystallisation, new dislocations are not formed due to absence of deformation. For this reason, while dislocation density is above the critical value, post-dynamic RX will take place resulting in a monotonous decrease of the ρ_d value shown in Fig. 7.3 b.

Even if the framework has been outlined, the model is far from completion. Indeed, more research is needed to evaluate the assumptions made and to calibrate parameters such as: *α, β*, and *γ* used to categorise the dislocations, critical dislocation densities and dislocation consumption rates for each microstructure evolution phenomena.

Of particular complexity it is the question of how to split the dislocations into the various sub-groups. As observed in Chapter 6, forging conditions can be broadly categorised as: low temperature and low strain rate, high temperature and low strain rate, and similarly for high strain rates. It could be speculated that, each of these categories is in turn characterised by a dominating mechanism in addition to one or more secondary microstructural evolution mechanisms. For example in the first case: due to the low temperature and slow accumulation of dislocations, grain fragmentation (or CDRX) seems to be the principal phenomena as in the mechanism which is consuming more dislocations while DDRX is only secondary.

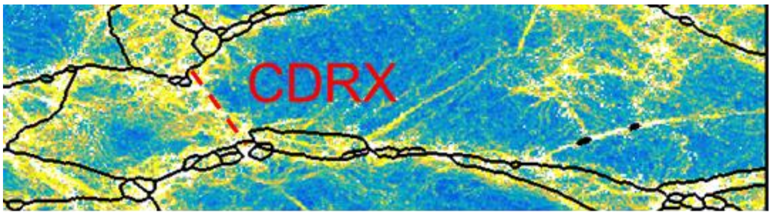

Figure 7. 4. KAM map (EBSD) showing an example of dislocation wall which will eventually lead to grain fragmentation/CDRX.

In this context, grain fragmentation (or CDRX) is assumed to be the transformation of sub-grains into new grains. The newly formed grain boundaries seem to either originate from existing twin boundaries or from dislocation walls as shown in Fig. 7. 4. Contrary to what is observed in DDRX the dislocation density within the detached grain does not dissolve. This is in accordance with the CDRX observations made by Chen et al [87].

For the second category, it is the inverse of the previous one with DDRX seemingly being predominant and fragmentation secondary. Lastly, in high strain rate forging PDRX appears to be the primary process while fragmentation and DDRX seem only secondary to it. While some evidence is available for the above classification, it is still hypothetical and further research is needed. The idea of defining different areas and boundaries in the strain rate-temperature space, in which selected phenomena are more probable than others is not new. Indeed, processing maps [37] are a common tool used in hot forging and are often related to energy dissipation and flow instabilities, however Sui et al. [36] created microstructural processing maps for hot working of IN718. These were the results of uniaxial laboratory tests and thus, did not take into account all of the microstructural evolution phenomena observed in industrial forging. In fact, dynamic recrystallisation was taken into account, while PDRX and grain fragmentation (or CDRX) were not mentioned. A qualitative figure of the processing map space based on experimental observation is shown in Fig. 7.5. Unfortunately, for this the use of macroscopic models and data, does not seem to be enough and a different approach is needed.

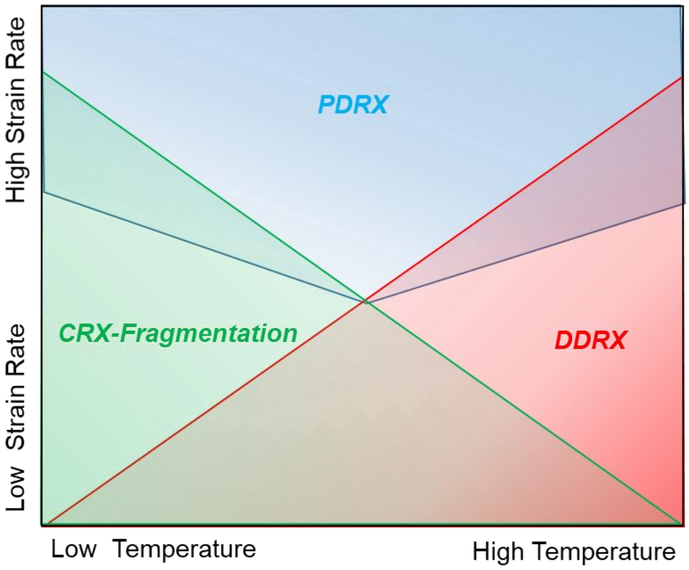

Figure 7. 5. Qualitative processing map.

Another suggestion on how to split the different phenomena noted earlier is shown in Fig. 7.6. A factor affecting the splitting of dislocations could be based on how the process times relates to the characteristic time needed for the dislocations to move to the boundary and pile up in order to generate new nuclei. If the process is too fast, it can be supposed that there is not enough time for dislocations to move to the boundaries, pile-up and for nuclei to appear. It remains an open question however, how dislocations used by grain distortion and fragmentation/CDRX are affected by this characteristic time.

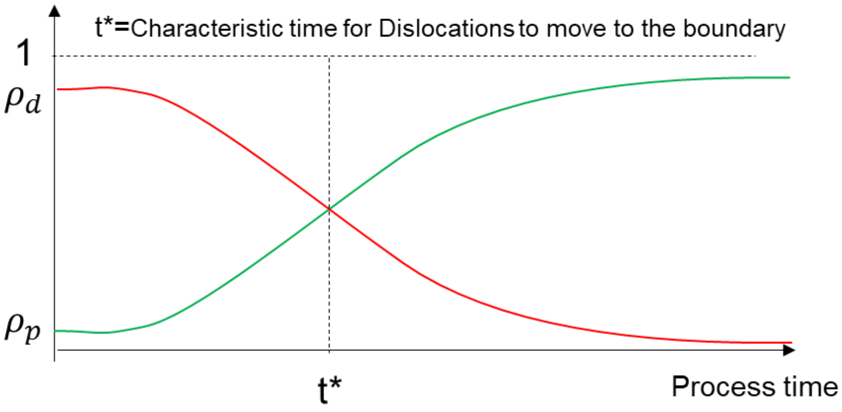

Figure 7. 6. Splitting of dislocations contributing to different phenomena.

7.3 Conceptual Modelling and DIGIMU®

While a general model framework has been outlined, it is required to develop a method through which it is possible to test the hypothesis at the base of the model generated through experimental observation. Up to this point this study has been purely phenomenological in nature. Thanks to the methodology developed in this work a set of observations was generated and to move forward it is now needed to link these observations to more detailed micro-scale phenomena. An opportunity for this may be given by multi scale modelling through the use of software like DIGIMU® which offer the chance of simulating phenomena that are undetectable to larger order models [95]. In DIGIMU® a polycrystal can be generated and then subjected to purely thermal or thermo-mechanical simulation. This software may help to understand the observations made through the developed methodology and in return those observations may highlight development suggestions for this software.

7.3.1. DIGIMU® Toolkit Development

In DIGIMU® polycrystals can be generated either via the input of EBSD data, or through an embedded polycrystal creator. In addition to this, different dislocation density fields can be added to the microstructure. Suitable EBSD input formats for the software are: .txt (1 pixel per line, and for each pixel the index of the grain), ang or .ctf EBSD files. However, the current equipment and software capabilities at the AFRC do not support these formats. In Chapter 3, the development of an original MATLAB application was mentioned for the processing of EBSD maps based on an MTex toolkit named *EBSD Data Processor* (see Fig. 7.7). To solve the EBSD format problem a functionality which can be used to generate a suitable input data format for DIGIMU® was developed and added to the GUI. Once the EBSD data has been imported into the Data Processor, it is possible to generate both input data variables for the grain structure and the dislocation density (see Fig. 7.8-7.9). Dislocation density can be estimated from KAM values [96]. In the developed app, KAM values can either be normalised over an interval given as an input by the user, or calculated automatically though the methodology proposed by Agnoli et al. [97]. If the plotted grain and dislocation maps are satisfactory, the input text files for DIGIMU® can be obtained by pressing the appropriate button and imported into DIGIMU® resulting in a polycrystal of the type shown in Fig. 7.10.

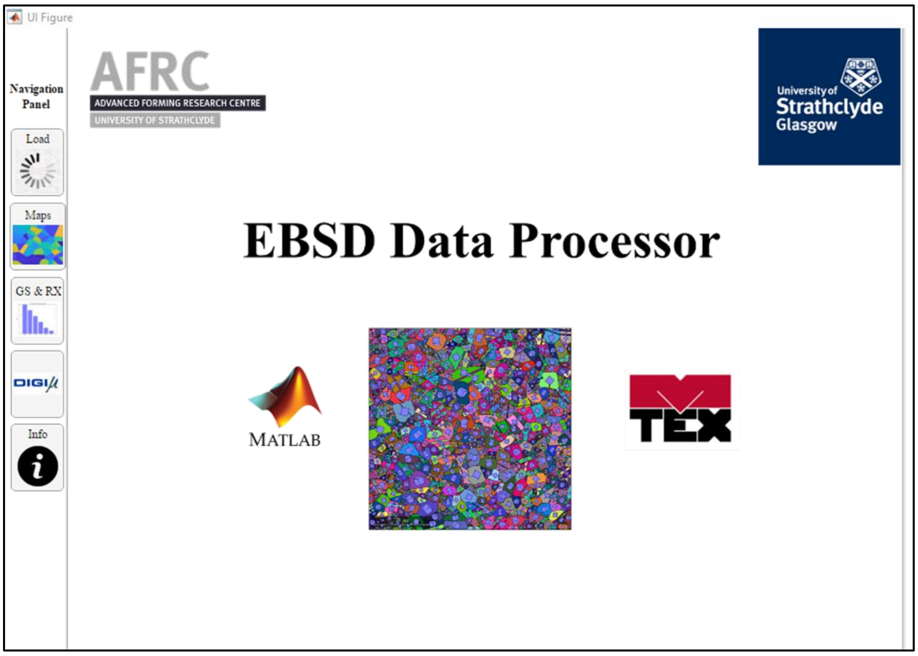

Figure 7. 7. GUI main page.

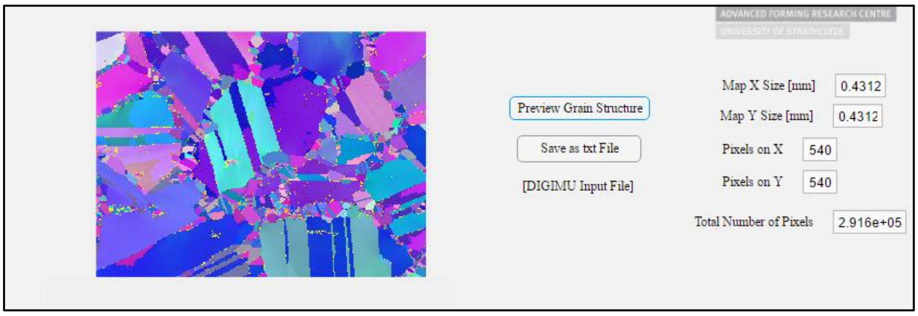

Map X Size [mm] 0.4312
Map Y Size [mm] 0.4312
Pixels on X 540
Pixels on Y 540
Total Number of Pixels 2.916e+05

Figure 7. 8. Preview of the grain structure.

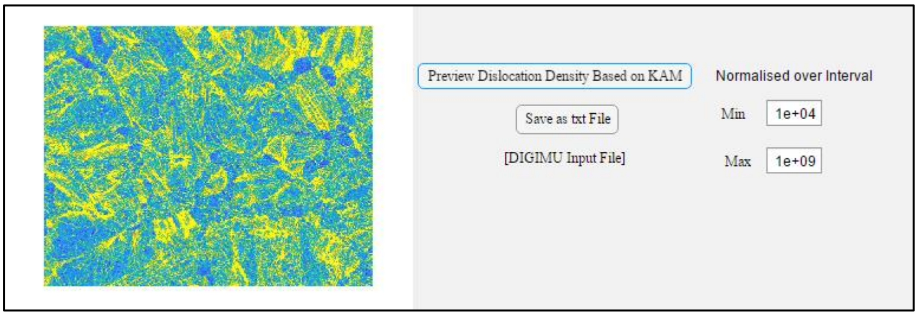

Normalised over Interval
Min 1e+04
Max 1e+09

Figure 7. 9. Preview of the dislocation density map.

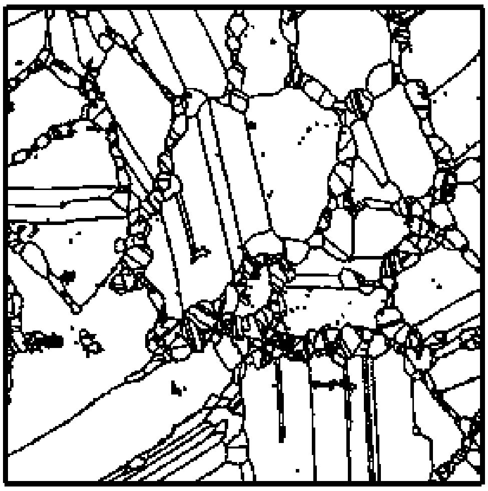

Figure 7. 10. Generated DIGIMU polycrystal.

The use of EBSD maps in the simulation gives the opportunity to test the behaviour of a model with real data, however it may be computationally unfriendly. Due to large amount of noise in an EBSD map (5-15% of points not indexed), the first computational steps can be quite demanding (in the order of hours). Moreover, EBSD maps require many resources in terms of time and equipment and thus they may not be suitable for the development and/or calibration of a model. Indeed, conceptual modelling requires many simulations to check hypothesis and make adjustments. For this reason it is of primary importance that the simulations should be reasonably fast. To solve this problem an additional toolkit was developed to create dummy polycrystals (see Fig. 7.11). There already exists a tool in DIGIMU® for the creation of polycrystals, however this has some limitations: it is not easily possible to create duplex structures, representative of non recrystallised and recrystallised grains. Similarly, it is not possible to assign selective dislocation densities based on grain types, or to selected grains. With the developed Microstructure Generator GUI it is possible to create three types of microstructure as shown in Fig. 7.12:

- Homogeneous
- Necklace Recrystallisation
- Recrystallised grains with a few large non-recrystallised grains

Many different variables can be changed, such as the size of maps in pixels, the number of big and small grains, dislocation density of big and small grains, etc. An additional feature of this microstructure generator is the chance to select individual grains and to change the dislocation density of the grains as shown in Fig. 7.13-7.15. Further developments can include the assignment of more properties to the grains such as orientation and setting different dislocation density distributions within grains. Videos showing how to use GUIs can be found at: https://youtu.be/ablEtTJGRVs and https://youtu.be/Fk7tqzIKZWo, while .exe versions can be requested by emailing nicola.stefani@strath.ac.uk.

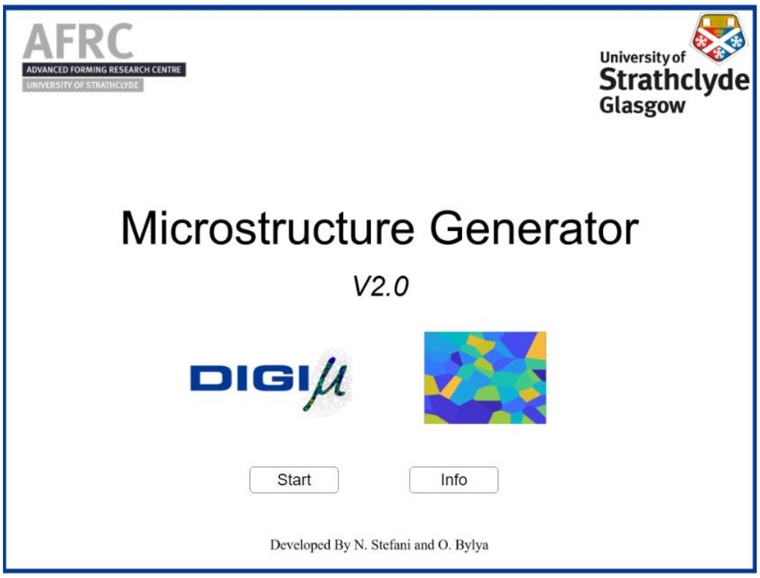

Figure 7. 11. Microstructure Generator main page.

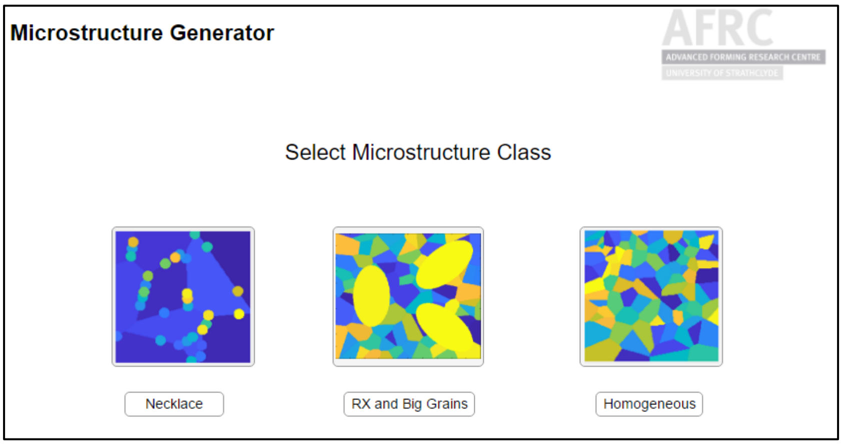

Figure 7. 12. Microstructure classes.

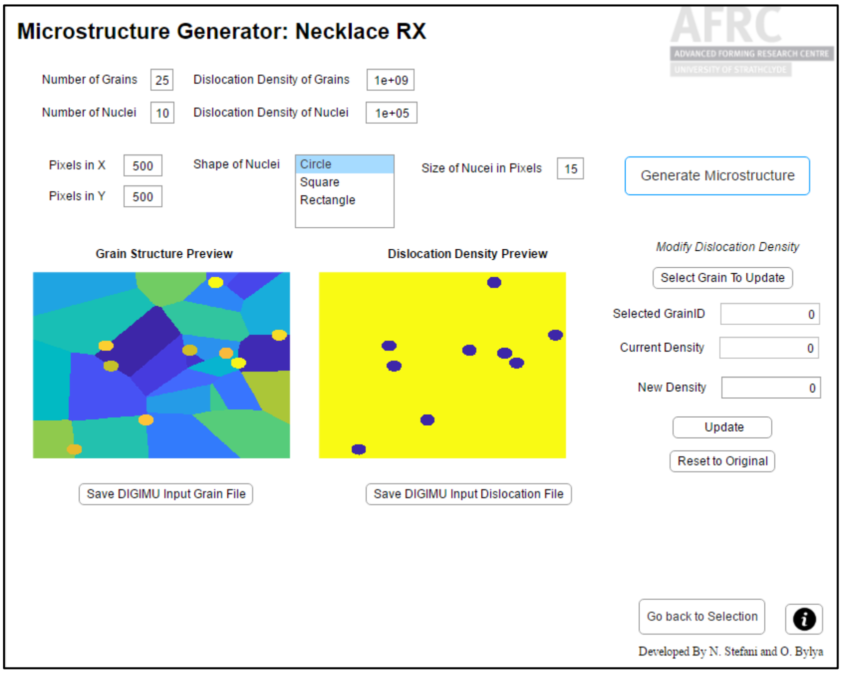

Number of Grains: 25
Dislocation Density of Grains: 1e+09
Number of Nuclei: 10
Dislocation Density of Nuclei: 1e+05
Pixels in X: 500
Pixels in Y: 500
Shape of Nuclei: Circle
Size of Nucei in Pixels: 15
Selected GrainID: 0
Current Density: 0
New Density: 0

Developed By N. Stefani and O. Bylya

Figure 7. 13. Necklace microstructure generation.

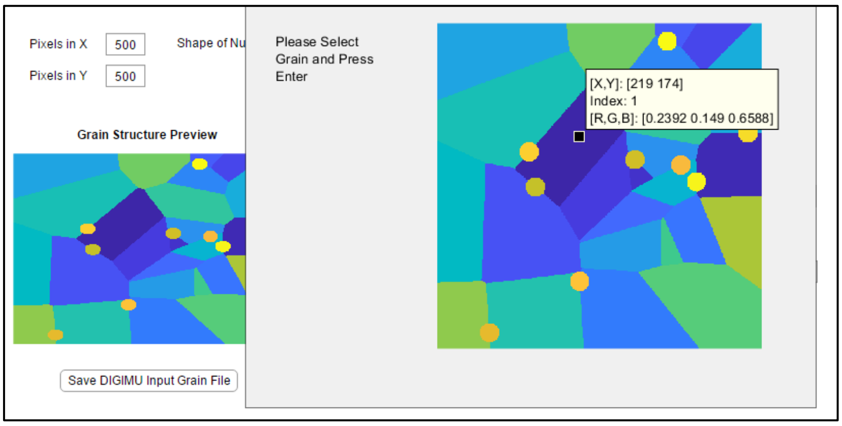

Pixels in X: 500
Pixels in Y: 500

Please Select
Grain and Press
Enter

[X,Y]: [219 174]
Index: 1
[R,G,B]: [0.2392 0.149 0.6588]

Figure 7. 14. Selecting a grain to change dislocation density.

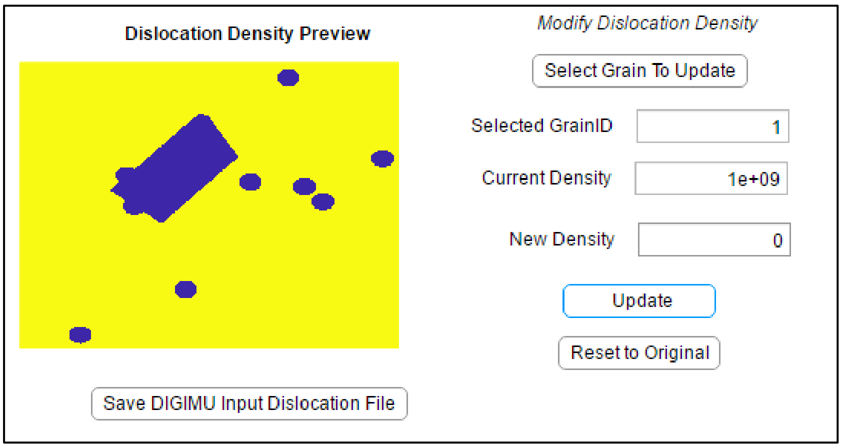

Selected GrainID 1

Current Density 1e+09

New Density 0

Figure 7. 15. Modifying dislocation density of selected grain.

7.3.2. Working with DIGIMU®

A drawback of the experiments performed is the inability to observe microstructural development in-situ. However, this is balanced by the advantage of seeing the different dynamics of the process and the ability to check neighbouring states. Indeed, for example, it is possible to see the development of a microstructure by moving half a millimetre up or down across the section of the workpiece. Fig. 7.16. shows a point on the zero boundary of the DTC forged at 970 °C on the hydraulic press (P1) and a microstructure taken 1 millimetre apart (P2). The thermo-mechanical trajectories for the two points are very similar with P2 undergoing more deformation and therefore receiving slightly more energy. In DIGIMU® the grain boundary kinetics can be approximated by the simplified relations:

$$V = M(\delta[\![E]\!]\text{-}\gamma k) \tag{7.4}$$

$$[\![E]\!]=E_i\text{-}E_j \tag{7.5}$$

$$E = \mu b^2\alpha\,\rho \tag{7.6}$$

Where V is the velocity of the boundary, M is the mobility of the boundary, $[\![\boldsymbol{E}]\!]$ is the difference in Energy between grains, δ is a material parameter, γ is grain boundary energy and k is a curvature factor (1/R for 2d case, 2/R for 3d case), µ is the shear modulus, α is a constant material parameter and *b* is the burger's vector. If the difference in energy derived by dislocation density of two neighbouring grains is the same, then the bigger grain will consume the smaller one. On the other hand, if two grains have the same size but different energy states, the lower energy grain will consume the neighbouring grain.

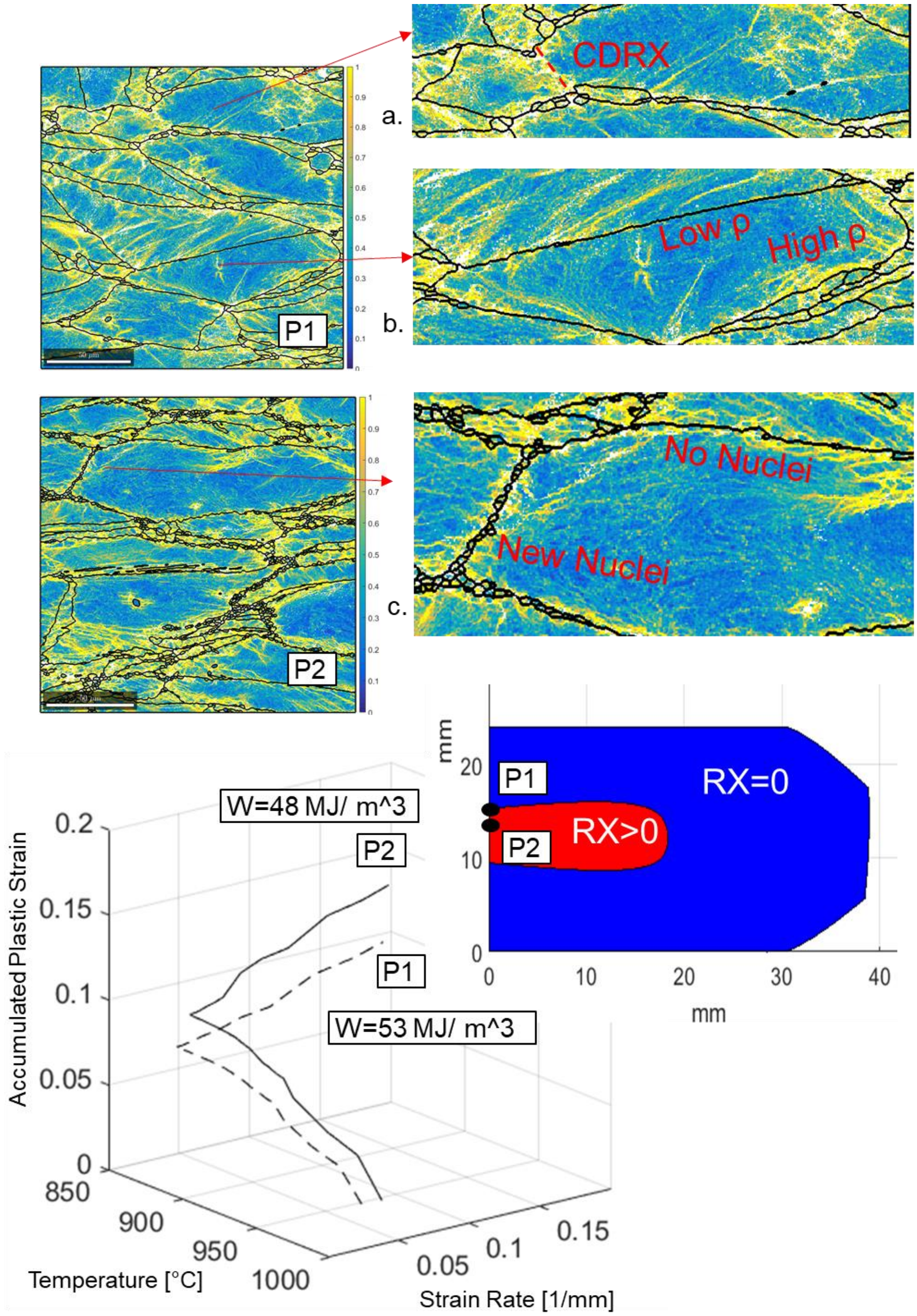

Figure 7. 16. On top of the picture is shown KAM maps (EBSD) of zero boundary point (P1) and neighbour (P2) forged at 970 °C on hydraulic press, In bottom side it is shown the experimental recrystallisation iso-contour and the thermo-mechanical trajectories of P1 and P2 tracked through FE modelling (see Appendix 1.13 for enlarged version).

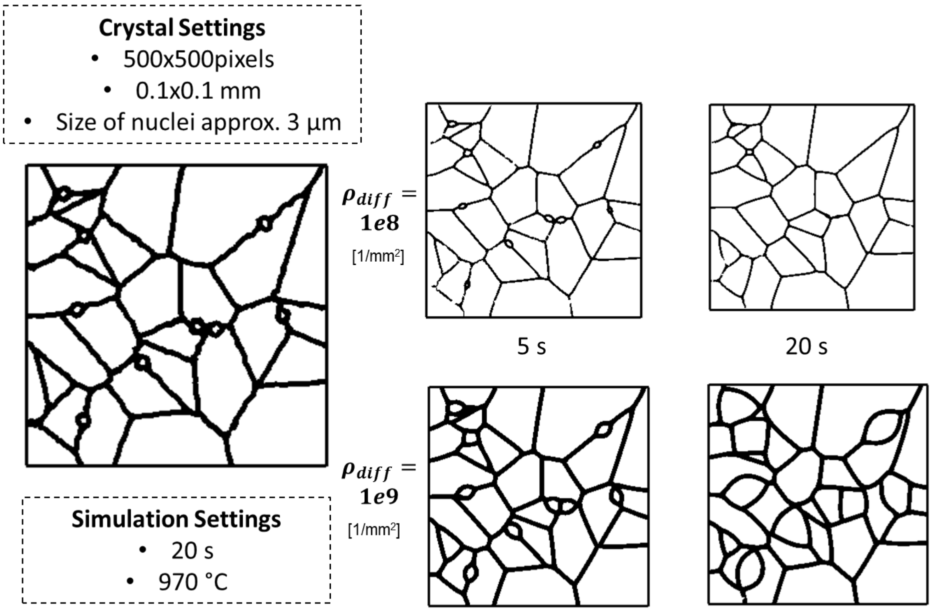

Figure 7. 17. Effects of dislocation density difference on grain mobility modelled through DIGIMU®.

This is shown in Fig. 7.17, where the microstructure generator was used to create a necklace microstructure characterised by nuclei of approximately 3 µm. Then two input files based on different dislocation density gradients between RX and non-RX grains were generated and imported into DIGIMU®. Heat treatment simulations of the two polycrystals (same grain structure and different dislocation densities) were set up for 20s at 970 °C. It can be seen that for the same microstructure the difference in dislocation density dictates whether nuclei are stable or not, according to the model. As noted earlier to calculate the dislocation density from EBSD data it is possible to use the methodology used by Agnoli et al. [97] in which dislocation density is calculated through the equation:

$$\rho = \frac{k \cdot GAM}{D_{SS} \cdot b} \tag{7.7}$$

Where GAM is the grain average misorientation, D_{SS} is the EBSD step size and k is constant parameter. The GAM map and dislocation density maps of P1 are shown in Fig. 7.18. It can be observed that by averaging the grains the GAM, and thus dislocation density values, the original grains present a lower energy state than the recrystallised grains. Thus, according to Eq. (7.4), they should be consumed by the bigger grains. However, what is observed in P2 is quite different. A further increase in energy does not result in the disappearance of these RX grains. It can be observed that energy is spent both through CRX and the formation of new nuclei around the old ones. For example in 7.16a an area is highlighted in which CRX seems to be ready to take place. Moreover, it is interesting to observe in Fig 7.16c, that nucleation is not uniform along all grain boundaries. This can be explained by observing the KAM maps. In Fig. 7.16b it can be seen that dislocation density inside the large deformed grains is not uniform and in particular:

- Dislocation Density is higher in the proximity of the boundary
- Dislocation Density is not distributed evenly along every boundary

While the average dislocation density of big grains is lower than the small ones, the local dislocation gradient between the two around the boundary area can be quite different. To accurately describe the observed microstructure it can be suggested that the inclusion of two additional field variables might be considered: a coefficient of non-uniformity for dislocation density which specifies how ρ varies within a grain, and possibly a grain orientation variable which may designate along which boundaries dislocations are piled-up.

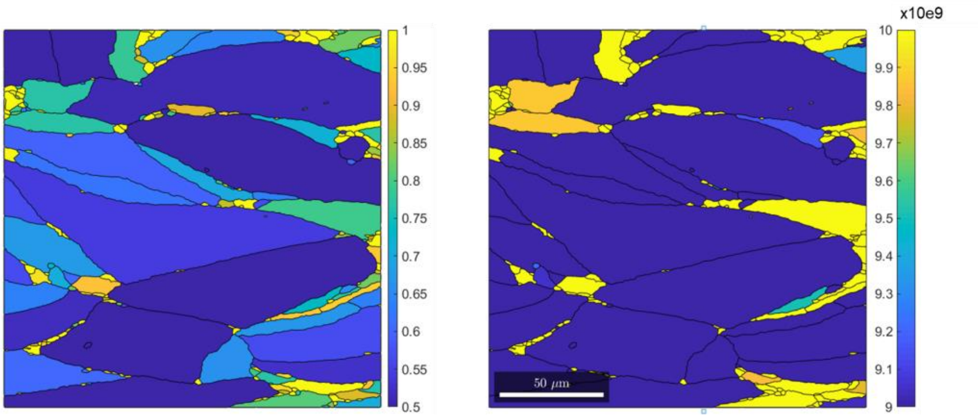

Figure 7. 18. GAM [degrees] and dislocation density [1/mm^2] EBSD maps of microstructure taken from the onset of recrystallisation in DTC forged at 970 °C on Hydraulic Press.

7.1 Conclusions

A modelling structure which takes into account the findings of Chapter 6, with regards to the generation of different dislocation distributions contributing to competitive microstructural evolution phenomena has been proposed. However, challenges associated with the calibration of the proposed model and validation of the hypothesis require further research and cannot be achieved only through macroscopic studies. The use of DIGIMU® has been suggested for further research and some tools for the exploitation of this new software have been developed.

Chapter 8

Conclusions

8.1 Research Outputs

In this section the findings will be presented against the research questions and objectives outlined in Chapter 1.

The overall research question defined in the introductory chapter was: *How can industrial-type forgings be used to investigate microstructural evolution of IN718?* In uniaxial laboratory tests single experimental parameters such as temperature, strain rate and final strain can be used to describe the conditions that lead to a specific microstructure. However, this is not the case in more complex industrial forgings characterised by non-homogeneous deformation. In order to use industrial-type forgings to investigate microstructural evolution it is necessary to retrace the thermo-mechanical histories of points of interest and link them to their corresponding microstructures. This was accomplished through the development of a novel methodology which included:

- Design and execution of systematic industrial-scale forging trials with different levels of complexity (Section 3.2).
- Collection and processing of Microstructural Data (Section 3.4).
- Construction of the Digital Twin (Section 3.3.2).
- Construction of Thermo-Mechanical Trajectories (Section 3.3.4).
- Creation of Zero Boundary Concept (Section 3.1.1).

Through this methodology and thus the exploitation of industrial forgings for the investigation of recrystallisation during hot forging of IN718 it was possible to achieve the objectives stated in the introductory chapter.

Assess the current microstructural prediction capabilities for Industrial Forging of IN718.

Due to their broad range of strains, strain rates and temperatures, it is not clear *a priori* whether models developed and calibrated through uniaxial laboratory tests may be successfully used for industrial-type forgings.

Thanks to the developed methodology it was possible to benchmark microstructure models using industrial-scale equipment (Section 5.4).

It was observed that standard models can produce unsatisfactory results, but due to their lack of specific applicability limits it was not clear whether this was due to poor calibration (Section 5.4).

To solve this problem a calibration methodology was designed and applied, resulting in an improvement of the modelling results (Section 5.5).

It was found that traditional JMAK models can be safely used for a window of low strain rates (<1 s^{-1}), but may result in wrong predictions at high strain rates (Section 5.4-5.7). To explore the reasons behind these applicability limits the different kinetics of recrystallisation were analysed.

Investigate the difference in the kinetics of recrystallisation between classic experiments and industrial forgings of IN718, and how these can be used to formulate microstructural models.

Industrial forgings are characterised by a broad spectrum of thermo-mechanical histories and no systematic study of these processes is available. Through the developed methodology a selection of non-homogeneous testing mimicking industrial forging conditions provided a new platform onto which evaluate recrystallization compared to classic experiments. It was found that:

- Accumulated Plastic Strain does not seem to be a good measure for the prediction of recrystallisation. In particular, there appears not to be a direct correlation between critical strain and onset of recrystallisation (Section 6.3).
- Similarly, other macroscopic measures do not seem to be suitable for the prediction of recrystallisation (Section 6.6).
- The above points seem to be due to the overlapping of a few different microstructural evolution mechanisms: CRX, DDRX and PDRX *(*Section 6.3-6.6*).*
- For more accurate prediction of the recrystallization phenomenon it was suggested that the relative roles of dislocations distributed in different regions of the grains be considered further, namely: dislocations used by other deformation mechanisms, dislocations piled-up on the grain boundaries (used for nucleation) and dislocations dispersed across the grains (used in post-dynamic recrystallisation phenomena) *(*Section 6.6*).*

Suggest improvements on current microstructural prediction capabilities of microstructural evolution in Inconel 718.

A novel modelling structure which takes into account the generation of dislocations contributing to competitive microstructural evolution phenomena was proposed (Section 7.2). However, challenges associated with the conceptualisation and calibration of the proposed model require further research and cannot be achieved only through macroscopic studies.

It was therefore suggested that use is made of the commercial modelling software DIGIMU® as a tool for the validation of hypotheses and for the interpretation of experimental results (Section 7.3).

Moreover, it was shown how in return the observations made through the methodology developed in this work may point to a development direction for DIGIMU® (Section 7.3.2).

In addition to the above objectives, through this research software tools were developed with the AppDesigner MATLAB package. The first developed application was the EBSD Data Processor based on the MTex Toolbox. Indeed, while this MATLAB toolbox is one of the best processors for EBSD data, it requires either pre-existing MATLAB coding knowledge or the development of those skills. An application which can be used without any, or limited knowledge, of the MATLAB interface was developed to process EBSD data with particular focus to nickel superalloys. The features of the developed GUI are the following:

- Import EBSD data
- Re-size and Rotate Map
- Plot Grain Boundaries
- Plot Twin Boundaries
- Plot Grain Orientation (per grain/per pixel – Euler/IPF)
- Plot KAM/GOS/GAM maps
- Calculate and plot Grain Size Distribution
- Calculate Average Grain Size Based on Frequency and Area
- Calculate and Plot RX Volume Fraction Based on GOS
- Calculate and Plot RX Volume Fraction Based on Grain Size
- Calculate Dislocation Density
- Generate input files for DIGIMU® for both grain structure and dislocation density

In addition to this, another application was developed to generate a variety of dummy microstructures (different grain structures and dislocation densities) for DIGIMU® to perform computationally less demanding simulations on various combinations of grain structures and dislocation densities. The reduction in computational time is an important factor for design, calibration and testing of models. Lastly, a set of MATLAB codes for the analysis of the thermo-mechanical trajectories was developed as part of this project (Appendix 3.5).

8.2 Research Dissemination

Parts of the present work were presented and published in the proceedings of a series of conferences:

- KomPlasTech 2017 in Zakopane, Poland
    - Stefani, N., Bylya, O., Reshetov, A., & Blackwell, P. (2017). On the applicability of JMAK-type models in predicting IN718 microstructural evolution. Computer Methods in Materials Science, 17(1), 59-68.
- ICTP 2017 in Cambridge, UK
    - Bylya, O., Reshetov, A., Stefani, N., Rosochowska, M., & Blackwell, P. (2017). Applicability of JMAK-type model for predicting microstructural evolution in nickel-based superalloys. Procedia Engineering.
- Superalloys 2016 in Seven Springs, Pennsylvania, United States.
    - Reshetov, A., Bylya, O., Stefani, N., Rosochowska, M., & Blackwell, P. (2016). An approach to microstructure modelling in nickel-based superalloys. 531-538.

References

[1] C. T. Sims, “A History of Superalloy Metallurgy for Superalloy Metallurgists,” *Superalloys 1984 (Fifth Int. Symp.*, pp. 399–419, 1984, doi: 10.7449/1984/Superalloys_1984_399_419.

[2] Special Metal Corporation, “Special Metals: Inconel 718,” *SMC-045*, 2007. [Online]. Available: http://www.specialmetals.com/documents/Inconel alloy 718.pdf.

[3] Arcam EBM System, “Ti6Al4V Titanium Alloy.” [Online]. Available: www.arcam.comArcamEBMsystemTi6Al4VTitaniumAlloy. [Accessed: 14-Oct-2019].

[4] C. Sims, N. Stoloff, and W. Hagel, “Superalloys IL John Wiley and Sons,” *superalloys*, 1972.

[5] H. K. D. H. Bhadeshia, “Superalloys,” *Cambridge University- Materials and Metallurgy Dept:, http: //www. msm.cam.ac.uk/phase-trans/2003/Superalloys /superalloys.html*, 2019. [Online]. Available: https://www.phase-trans.msm.cam.ac.uk/2003/nickel.html. [Accessed: 14-Oct-2019].

[6] R. E. Schafrik, D. D. Ward, and J. R. Groh, “Application of Alloy 718 in GE Aircraft Engines : Past , Present and Next Five Years,” *Superalloys 718, 625, 706 Var. Deriv.*, pp. 1–11, 2001.

[7] D. S. Bergstrom and T. D. Bayha, “Properties and Microstructure of ALLVAC ® 718PLUS^{TM} Alloy Rolled Sheet Rolled Sheet,” in *Superalloys 718, 625, 706 and Various Derivatives*, 2005, pp. 243–252.

[8] A. Thomas, M. El-Wahabi, J. M. Cabrera, and J. M. Prado, “High temperature deformation of Inconel 718,” *J. Mater. Process. Technol.*, vol. 177, no. 1–3, pp. 469–472, 2006, doi: 10.1016/j.jmatprotec.2006.04.072.

[9] C. Slama and G. Cizeron, “Étude du comportement structural de l’alliage NC 19 Fe Nb (Inconel 718),” *J. Phys. III*, vol. 7, no. 3, pp. 665–688, 1997, doi: 10.1051/jp3:1997148.

[10] P. E. Mosser, G. Leconte, J. Leray, A. Lasalmonie, and Y. Honnorat, “Metallurgical Aspects of Forge Modelling in Alloy 718,” *Superalloys 718 Metall. Appl.*, pp. 179–188, 1989, doi:

10.7449/1989/Superalloys_1989_179_188.

[11] R. Cozar and A. Pineau, “Morphology of y’ and y" precipitates and thermal stability of inconel 718 type alloys,” *Metall. Trans.*, vol. 4, no. 1, pp. 47–59, Jan. 1973, doi: 10.1007/BF02649604.

[12] M. C. Chaturvedi and Y. Han, “Effect of particle size on the creep rate of superalloy Inconel 718,” *Mater. Sci. Eng.*, vol. 89, no. C, pp. 7–10, 1987, doi: 10.1016/0025-5416(87)90264-3.

[13] P. J. P. Kañetas, L. A. R. Osorio, M. P. G. Mata, M. D. La Garza, and V. P. López, “Influence of the Delta Phase in the Microstructure of the Inconel 718 subjected to ‘Delta-processing’ Heat Treatment and Hot Deformed,” *Procedia Mater. Sci.*, vol. 8, pp. 1160–1165, 2015, doi: 10.1016/j.mspro.2015.04.180.

[14] S. Azadian, L. Y. Wei, and R. Warren, “Delta phase precipitation in inconel 718,” *Mater. Charact.*, vol. 53, no. 1, pp. 7–16, 2004, doi: 10.1016/j.matchar.2004.07.004.

[15] D. Cai, W. Zhang, P. Nie, W. Liu, and M. Yao, “Dissolution kinetics of Delta phase and its influence on the notch sensitivity of Inconel 718,” *Mater. Charact.*, vol. 58, no. 3, pp. 220–225, 2007, doi: 10.1016/j.matchar.2006.04.020.

[16] Y. Desvallees, M. Bouzidi, F. Bois, and N. Beaude, “Delta Phase in INCONEL 718: Mechanical Properties and Forging Process Requirements,” *Superalloys 718, 625, 706 Var. Deriv.*, pp. 281–291, 1994, doi: 10.7449/1994/Superalloys_1994_281_291.

[17] H. T. Lee and W. H. Hou, “Development of fine-grained structure and the mechanical properties of nickel-based Superalloy 718,” *Mater. Sci. Eng. A*, vol. 555, pp. 13–20, Oct. 2012, doi: 10.1016/j.msea.2012.06.027.

[18] H. Lalvani, “Hot Deformation of IN718 with Various Initial Microstructures Experiments and State-variable Modelling,” A Thesis submmited to The Open University (UK) for the degree of Doctor of Philosophy ýP`, 2010.

[19] A. Agnoli *et al.*, “Understanding and modeling of gain boundary pinning in Inconel718,” in *Superalloys 12th International Symposium*, 2012, pp. 73, 82.

[20] J. J. Schirra, R. H. Caless, and R. W. Hatala, “The effect of laves phases on the mechanical properties of wrought and cast+HIP Inconel 718,” *Superalloys 718,625 Var. Deriv.*, pp. 375–388, 1991, doi: 10.7449/1991/Superalloys_1991_375_388.

[21] M. J. Sohrabi, H. Mirzadeh, and M. Rafiei, “Solidification behavior and Laves

phase dissolution during homogenization heat treatment of Inconel 718 superalloy," *Vacuum*, vol. 154, pp. 235–243, Aug. 2018, doi: 10.1016/j.vacuum.2018.05.019.

[22] M. Sundararaman, P. Mukhopadhyay, and S. Banerjee, "Carbide Precipitation In Nickel Base Superalloys 718 and 625 and their effect on mechanical properties," in *Superalloys 718, 625, 706 and Derivatives*, 1997, pp. 367–278.

[23] A. Mitchell, "PRIMARY CARBIDES IN ALLOY 718," in *7th internation Symposium on Superalloy 718 and Derivatives*, 2010, pp. 161–167.

[24] B. L. Ferguson, "Aerospace applications," in *ASM Handbook Volume 7: Powder Metallurgy 6th Edn*, 1997, pp. 646–656.

[25] M. G. Benz, "Preparation of Clean Superalloys," in *Impurities in Engineering Materials*, Routledge, 2017, pp. 31–48.

[26] R. C. Reed, "Chapter 4: Superalloys for turbine disc applications," in *The Superalloys: Fundamentals and Applications*, 2006, pp. 217–282.

[27] T. Altan and G. Ngaile, *Cold and Hot Forging*. 2005.

[28] P. P. Petit -J, A. & Fesland, L. Duval, and F. Ancizes, "Manufacturing of Large IN718 and IN718 Forging Parts," in *Superalloys 718, 625, 706 and Derivatives*, 1997, pp. 153–161.

[29] J. De Jaeger *et al.*, "Inconel 718 Single and Multipass Modelling of Hot Forging," in *superalloys*, 2012, pp. 663–672.

[30] M. Azarbarmas, M. Aghaie-Khafri, J. M. Cabrera, and J. Calvo, "Microstructural evolution and constitutive equations of Inconel 718 alloy under quasi-static and quasi-dynamic conditions," *Mater. Des.*, vol. 94, pp. 28–38, Mar. 2016, doi: 10.1016/j.matdes.2015.12.157.

[31] Y. Wang, W. Z. Shao, L. Zhen, L. Yang, and X. M. Zhang, "Flow behavior and microstructures of superalloy 718 during high temperature deformation," *Mater. Sci. Eng. A*, vol. 497, no. 1–2, pp. 479–486, Dec. 2008, doi: 10.1016/j.msea.2008.07.046.

[32] J. M. Zhang, Z. Y. Gao, J. Y. Zhuang, Z. Y. Zhong, and P. Janschek, "Strain-rate hardening behavior of superalloy IN718," *J. Mater. Process. Technol.*, vol. 70, no. 1–3, pp. 252–257, 1997, doi: 10.1016/S0924-0136(97)00073-3.

[33] N. Srinivasan, "Microstructural Control in Hot Working of IN-718 Superalloy Using Processing Map," *Metall. Mater. Trans. A*, vol. 25, no. October, pp. 2275–2284, 1994.

[34] J. Liu and Z. Cui, "Flow characteristics and intrinsic workability of IN718

superalloy," *Mater. Sci. Eng. A*, vol. 642, no. August, pp. 279–287, 2015, doi: 10.1016/j.msea.2015.06.093.

[35] P. Chaudhury and D. Zhao, *Atlas of Formability: Inconel 718*. 1992.

[36] F. L. Sui, L. X. Xu, L. Q. Chen, and X. H. Liu, "Processing map for hot working of Inconel 718 alloy," *J. Mater. Process. Technol.*, vol. 211, no. 3, pp. 433–440, 2011, doi: 10.1016/j.jmatprotec.2010.10.015.

[37] Y. V. R. K. Prasad, K. P. Rao, and S. Sasidhara, *Hot Working Guide: A Compendium of Processing Maps*, Second Edi. 1997.

[38] F. L. Sui, L. X. Xu, L. Q. Chen, and X. H. Liu, "Processing map for hot working of Inconel 718 alloy," *J. Mater. Process. Technol.*, vol. 211, no. 3, pp. 433–440, 2011, doi: 10.1016/j.jmatprotec.2010.10.015.

[39] R. C. Reed, *The Superalloys fundamentals and applications*, vol. 9780521859042. Cambridge University Press, 2006.

[40] J. J. Gilman, *Micromechanics of Flow in Solids*. 1969.

[41] G. E. Dieter, *Mechanical metallurgy*. McGraw-Hill, 1976.

[42] R. W. K. (Robert W. K. Honeycombe, *The plastic deformation of metals*. E. Arnold, 1984.

[43] F. J. Humphreys and M. Hatherly, *Recrystallization and related annealing phenomena*. Elsevier, 2004.

[44] J. P. Thomas, F. Montheillet, and C. Dumont, "Microstructural evolutions of superalloy 718 during dynamic and metadynamic recrystallizatlons," *Mater. Sci. Forum*, vol. 426–432, no. 1, pp. 791–796, 2003, doi: 10.4028/www.scientific.net/MSF.426-432.791.

[45] E. J. Mittemeijer, *Fundamentals of Materials Science*. Springer, 2010.

[46] N. Hansen and C. Y. Barlow, "Plastic Deformation of Metals and Alloys," in *Physical Metallurgy: Fifth Edition*, 2014, pp. 1682–1758.

[47] K. Huang and R. E. Logé, "A review of dynamic recrystallization phenomena in metallic materials," *Materials and Design*, vol. 111. Elsevier Ltd, pp. 548–574, 05-Dec-2016, doi: 10.1016/j.matdes.2016.09.012.

[48] N. Stefani, O. Bylya, A. Reshetov, and P. Blackwell, "On the Applicability of JMAK-Type models in Prediction IN718 Microstructural Evolution," *Comput. Methods Mater. Sci. Inform. w Technol. Mater.*, vol. 17, no. 1, 2017.

[49] M. Zouari, R. E. Logé, and N. Bozzolo, "In situ characterization of inconel 718 post-dynamic recrystallization within a scanning electron microscope," *Metals (Basel).*, vol. 7, no. 476, 2017, doi: 10.3390/met7110476.

[50] Y. C. Lin, C. Xiao-min, and D. Wen, “EBSD study of a hot deformed nickel-based superalloy,” *J. Alloys Compd.*, vol. 640, no. December, pp. 101–113, 2015, doi: 10.1016/j.jallcom.2015.04.008.

[51] A. Nicolaÿ, G. Fiorucci, J. M. Franchet, J. Cormier, and N. Bozzolo, “Influence of strain rate on subsolvus dynamic and post-dynamic recrystallization kinetics of Inconel 718,” *Acta Mater.*, vol. 174, pp. 406–417, 2019, doi: 10.1016/j.actamat.2019.05.061.

[52] D. Zhao and P. K. Chaudhury, “Effect of Starting Grain Size on As-Deformed Microstructure in High Temperature Deformation of Alloy 718,” *Superalloys 718, 625, 706 Var. Deriv.*, pp. 303–313, 1994, doi: 10.7449/1994/Superalloys_1994_303_313.

[53] S. C. Medeiros, Y. V. R. K. Prasad, W. G. Frazier, and R. Srinivasan, “Modeling Grain Size During Hot Deformation of in 718,” *Scr. Mater.*, vol. 42, pp. 17–23, 2000.

[54] J. E. Burke and D. Turnbull, “Recrystallization and grain growth,” *Prog. Met. Phys.*, vol. 3, no. C, 1952, doi: 10.1016/0502-8205(52)90009-9.

[55] W. Johnson and R. Mehl, “Reaction kinetics in processes of nucleation and growth,” *Trans. Am. Inst. Min. Metall. Eng.*, no. 135, pp. 416–458, 1939.

[56] A. N. Kolmogorov, “On the Statistical Theory of the Crystallization of Metals,” *Bull. Acad. Sci. USSR*, vol. 1, no. Mathematics Series, pp. 355–359, 1937.

[57] M. Avrami, “Kinetics of phase change. I general theory,” *J. Chem. Phys.*, vol. 7, no. 12, p. 1103, 1939, doi: 10.1063/1.1750380.

[58] M. Avrami, “Kinetics of Phase Change. II - Transformation-Time Relations for Random Distribution of Nuclei,” *J. Chem. Phys.*, vol. 8, no. 1940, pp. 212–224, 1940, doi: 10.1063/1.1750631.

[59] M. Avrami, “Granulation, Phase Change, and Microstructure Kinetics of Phase Change. III,” *J. Chem. Phys.*, vol. 9, no. 2, p. 177, 1941, doi: 10.1063/1.1750872.

[60] J. E. Bailey and P. B. . Hirsch, “The recrystallization process in some polycrystalline metals,” *Proc. R. Soc. London. Ser. A. Math. Phys. Sci.*, vol. 267, no. 1328, pp. 11–30, Apr. 1962, doi: 10.1098/rspa.1962.0080.

[61] R. Sandström and R. Lagneborg, “A model for hot working occurring by recrystallization,” *Acta Metall.*, vol. 23, no. 3, pp. 387–398, 1975, doi: 10.1016/0001-6160(75)90132-7.

[62] D. Ponge and G. Gottstein, “Necklace formation during dynamic

recrystallization: Mechanisms and impact on flow behavior,” *Acta Mater.*, vol. 46, no. 1, pp. 69–90, 1998, doi: 10.1016/S1359-6454(97)00233-4.

[63] C. Sommitsch and W. Mitter, “On modelling of dynamic recrystallisation of fcc materials with low stacking fault energy,” *Acta Mater.*, vol. 54, pp. 357–375, 2005, doi: 10.1016/j.actamat.2005.09.008.

[64] A. A. Guimaraes and J. J. Jonas, “Recrystallization and Aging Effects Associated with the High Temperature Deformation of Waspaloy and Inconel 718,” *Metall. Trans. A*, vol. 12, no. September, pp. 1655–1666, 1981.

[65] J. Lin and Y. Liu, “A set of unified constitutive equations for modelling microstructure evolution in hot deformation,” *J. Mater. Process. Technol.*, vol. 143–144, no. 1, pp. 281–285, 2003, doi: 10.1016/S0924-0136(03)00472-2.

[66] M. Zouari, N. Bozzolo, and R. E. Loge, “Mean Field Modelling of dynamic and post Dynamic RX,” *Mater. Sci. Eng. A*, vol. 655, pp. 408–424, 2016.

[67] “DEFORMTM V11.0.1 System Documentation (Reed Road Columbus, Ohio: Scientific Forming Technologies Corporation).” pp. 175–180, 2014.

[68] Micas Simulation LTD, “QFORM v8 FE package documentation: Description of Microstructure evolution model,” 2016. [Online]. Available: http://www.qform3d.co.uk/db_files/17/123.pdf. [Accessed: 01-Sep-2016].

[69] D. Huang, W. T. Wu, D. Lambert, and S. L. Semiatin, “Computer simulation of microstructure evolution during hot forging of Waspaloy and nickel alloy 718,” *Proc. Microstruct. Model. Predict. Dur. thermomechanical Process. TMS, Indianapolis, Indiana*, pp. 137–146, 2001.

[70] a. J. Brand, K. Karhausen, and R. Kopp, “Microstructural simulation of nickel base alloy Incone* 718 in production of turbine discs,” *Mater. Sci. Technol.*, vol. 12, no. 11, pp. 963–969, 1996, doi: 10.1179/026708396790122134.

[71] L. X. Zhou and T. N. Baker, “Effects on dynamic and metadynamic recrystallization on microstructures of wrought IN-718 due to hot deformation,” *Mater. Sci. Eng. A*, vol. 196, no. 1–2, pp. 89–95, 1995, doi: 10.1016/0921-5093(94)09717-8.

[72] M. J. Weis, M. C. Mataya, S. W. Thompson, and D. K. Matlock, “The Hot Deformation Behavior of an As-Cast Alloy 718 Ingot,” *Superalloys 718 Metall. Appl.*, pp. 135–154, 1989, doi: 10.7449/1989/Superalloys_1989_135_154.

[73] S. C. Medeiros, Y. V. R. K. Prasad, W. G. Frazier, and R. Srinivasan, “Microstructural modeling of metadynamic recrystallization in hot working of IN 718 superalloy,” *Mater. Sci. Eng. A*, vol. 293, no. 1, pp. 198–207, 2000, doi:

10.1016/S0921-5093(00)01053-4.

[74] J. M. Zhang, Z. Y. Gao, J. Y. Zhuang, and Z. Y. Zhong, “Mathematical modeling of the hot-deformation behavior of superalloy IN718,” *Metall. Mater. …*, vol. 30, no. 10, pp. 2701–1712, 1999, doi: 10.1007/s11661-999-0310-7.

[75] D. Zhao, S. Guillard, and a T. Male, “High Temperature Deformation Behavior of Cast Alloy 718,” *Superalloys 718,625,706 Var. Deriv. Miner. Met. Mater. Soc.*, vol. 15, pp. 193–204, 1997.

[76] J. M. Zhang, Z. Y. Gao, J. Y. Zhuang, and Z. Y. Zhong, “Grain growth model of IN718 during holding period after hot deformation,” *J. Mater. Process. Technol.*, no. 101, pp. 25–30, 2000, doi: 10.1016/S0924-0136(99)00437-9.

[77] A. Reshetov, O. Bylya, N. Stefani, M. Rosochowska, and P. Blackwell, “An Approach To Microstructure Modelling In Nickel Based Superalloys,” in *Superalloys 2016: Proceedings of the 13th International Symposium on Superalloys Edited*, 2016, pp. 531–538.

[78] D. Huber *et al.*, “Microstructure modeling of the dynamic recrystallization kinetics during turbine disc forging of the nickel based superalloy Allvac 718Plus^{TM},” *Superalloys 2008*, no. August 2016, pp. 855–861, 2008, doi: 10.7449/2008/Superalloys_2008_855_861.

[79] M. Chen and Y. C. Lin, “An improved kinetics model to describe dynamic recrystallization behavior under inconstant deformation conditions,” *J. Mater. Res.*, vol. 19, no. Nov, 2016, doi: 10.1557/jmr.2016.325.

[80] E. Alabort, R. C. Reed, and D. Barba, “Combined modelling and miniaturised characterisation of high-temperature forging in a nickel-based superalloy,” *Mater. Des.*, vol. 160, pp. 683–697, 2018, doi: 10.1016/j.matdes.2018.09.048.

[81] A. M. Ressa, “Plastic Deformation and Ductile Fracture Behavior of Inconel 718 Presented,” *Thesis for Master of Science in the Graduate School of The Ohio State University*. 2015, doi: 10.1145/3132847.3132886.

[82] M. Chen, “An improved kinetics model to describe dynamic recrystallization behavior under inconstant deformation conditions,” no. November, 2016, doi: 10.1557/jmr.2016.325.

[83] R. Hielscher, “Mtex Documentation,” 2019. [Online]. Available: https://mtex-toolbox.github.io/documentation.html. [Accessed: 07-Nov-2019].

[84] C. Kienl, A. Casanova, O. M. D. M. Messè, C. Argyrakis, and C. M. F. Rae, “Characterization of the Initial Stages of Dynamic Recrystallisation in ATI718Plus,” in *Proceedings of the 9th International Symposium on Superalloy*

718 & Derivates, 2018, pp. 405–420.

[85] M. Azarbarmas, M. Aghaie-Khafri, J. M. Cabrera, and J. Calvo, “Dynamic recrystallization mechanisms and twining evolution during hot deformation of Inconel 718,” *Mater. Sci. Eng. A*, vol. 678, no. March, pp. 137–152, 2016, doi: 10.1016/j.msea.2016.09.100.

[86] Y. Wang, W. Z. Shao, L. Zhen, and X. M. Zhang, “Microstructure evolution during dynamic recrystallization of hot deformed superalloy 718,” *Mater. Sci. Eng. A*, vol. 486, no. 1–2, pp. 321–332, 2008, doi: 10.1016/j.msea.2007.09.008.

[87] K. Chen *et al.*, “Transition of deformation behavior and its related microstructure evolution in Nimonic 80A under hot-to-warm working,” *Mater. Charact.*, vol. 106, pp. 175–184, 2015, doi: 10.1016/j.matchar.2015.05.034.

[88] H. Mirzadeh, A. Najafizadeh, and M. Moazeny, “Flow curve analysis of 17-4 PH stainless steel under hot compression test,” *Metall. Mater. Trans. A Phys. Metall. Mater. Sci.*, vol. 40, no. 12, pp. 2950–2958, 2009, doi: 10.1007/s11661-009-0029-5.

[89] R. P. Guest and S. Tin, “Modelling Microstructural Transformations of Nickel Base Superalloy IN 718 During Hot Deformation,” *Superalloys 718, 625, 706 Deriv.*, pp. 385–397, 2005.

[90] A. J. Brand, K. Karhausen, and R. Kopp, “Microstructural simulation of nickel base alloy Incone* 718 in production of turbine discs,” *Mater. Sci. Technol.*, vol. 12, no. 11, pp. 963–969, Nov. 1996, doi: 10.1179/mst.1996.12.11.963.

[91] S. C. Medeiros, Y. V. R. K. Prasad, W. G. Frazier, and R. Srinivasan, “Modeling grain size during hot deformation of IN 718,” *J. Mater. Process. Technol.*, vol. 88, pp. 244–250, 1999, doi: 10.1016/S1359-6462(99)00316-4.

[92] H. Zhang, K. Zhang, H. Zhou, Z. Lu, C. Zhao, and X. Yang, “Effect of strain rate on microstructure evolution of a nickel-based superalloy during hot deformation,” *Mater. Des.*, vol. 80, pp. 51–62, 2015, doi: 10.1016/j.matdes.2015.05.004.

[93] S. S. S. Kumar, T. Raghu, P. P. Bhattacharjee, and G. A. Rao, “Strain rate dependent microstructural evolution during hot deformation of a hot isostatically processed nickel base superalloy,” *J. Alloys Compd.*, vol. 681, pp. 28–42, 2016, doi: 10.1016/j.jallcom.2016.04.185.

[94] M. Zouari, N. Bozzolo, and R. E. Loge, “Mean field modelling of dynamic and post-dynamic recrystallization during hot deformation of Inconel 718 in the

absence of δ phase particles,” *Mater. Sci. Eng. A*, vol. 655, pp. 408–424, 2016, doi: 10.1016/j.msea.2015.12.102.

[95] Trasnvalor, “DIGIMU® - Microstruture evolution simulation software - Transvalor,” 2020. [Online]. Available: https://www.transvalor.com/en/cmspages/digimu.86.html. [Accessed: 30-Jan-2020].

[96] A. Seret, C. Moussa, M. Bernacki, J. Signorelli, and N. Bozzolo, “Estimation of geometrically necessary dislocation density from filtered EBSD data by a local linear adaptation of smoothing splines,” *J. Appl. Crystallogr.*, vol. 52, no. 3, pp. 548–563, Jun. 2019, doi: 10.1107/S1600576719004035.

[97] A. Agnoli, M. Bernacki, R. Logé, J. M. Franchet, J. Laigo, and N. Bozzolo, “Selective Growth of Low Stored Energy Grains During δ Sub-solvus Annealing in the Inconel 718 Nickel-Based Superalloy,” *Metall. Mater. Trans. A Phys. Metall. Mater. Sci.*, vol. 46, no. 9, pp. 4405–4421, 2015, doi: 10.1007/s11661-015-3035-9.

Appendix

Appendix 1

1.1 Figure 4.4

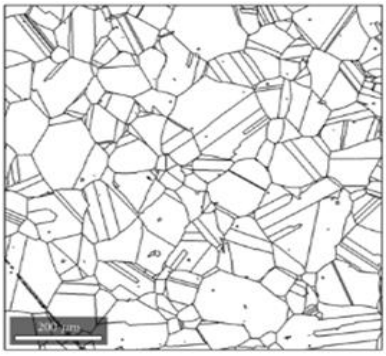

Grain Boundaries

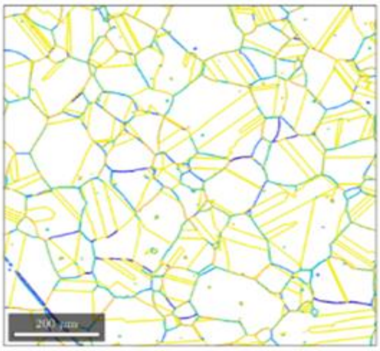

Twin Boundaries (yellow)

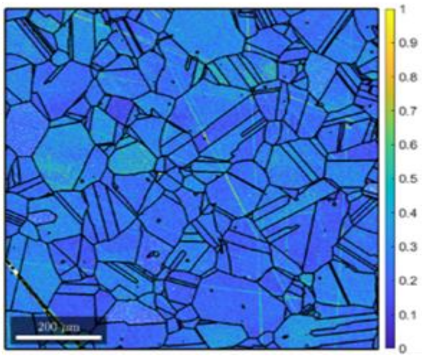

KAM

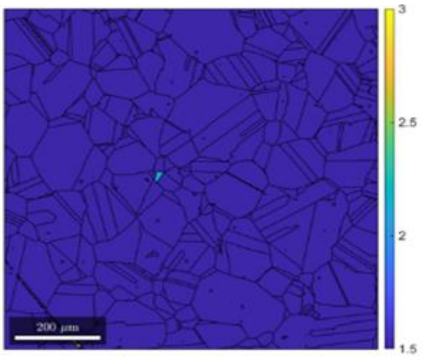

GOS

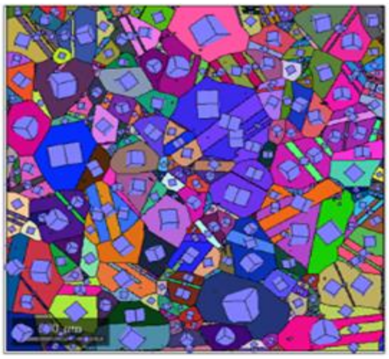

Grain Orientation Euler

1.2 Figure 4.5

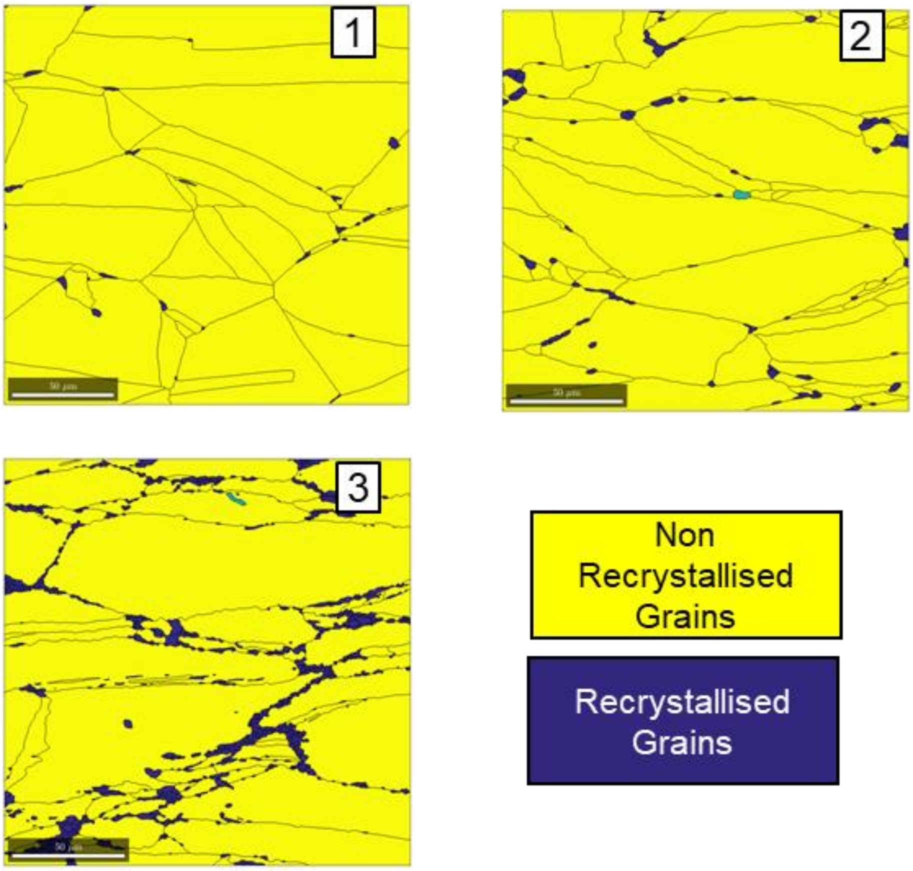
1
2
3
50 µm
50 µm
50 µm
Non Recrystallised Grains
Recrystallised Grains

1.3 Figure 4.8

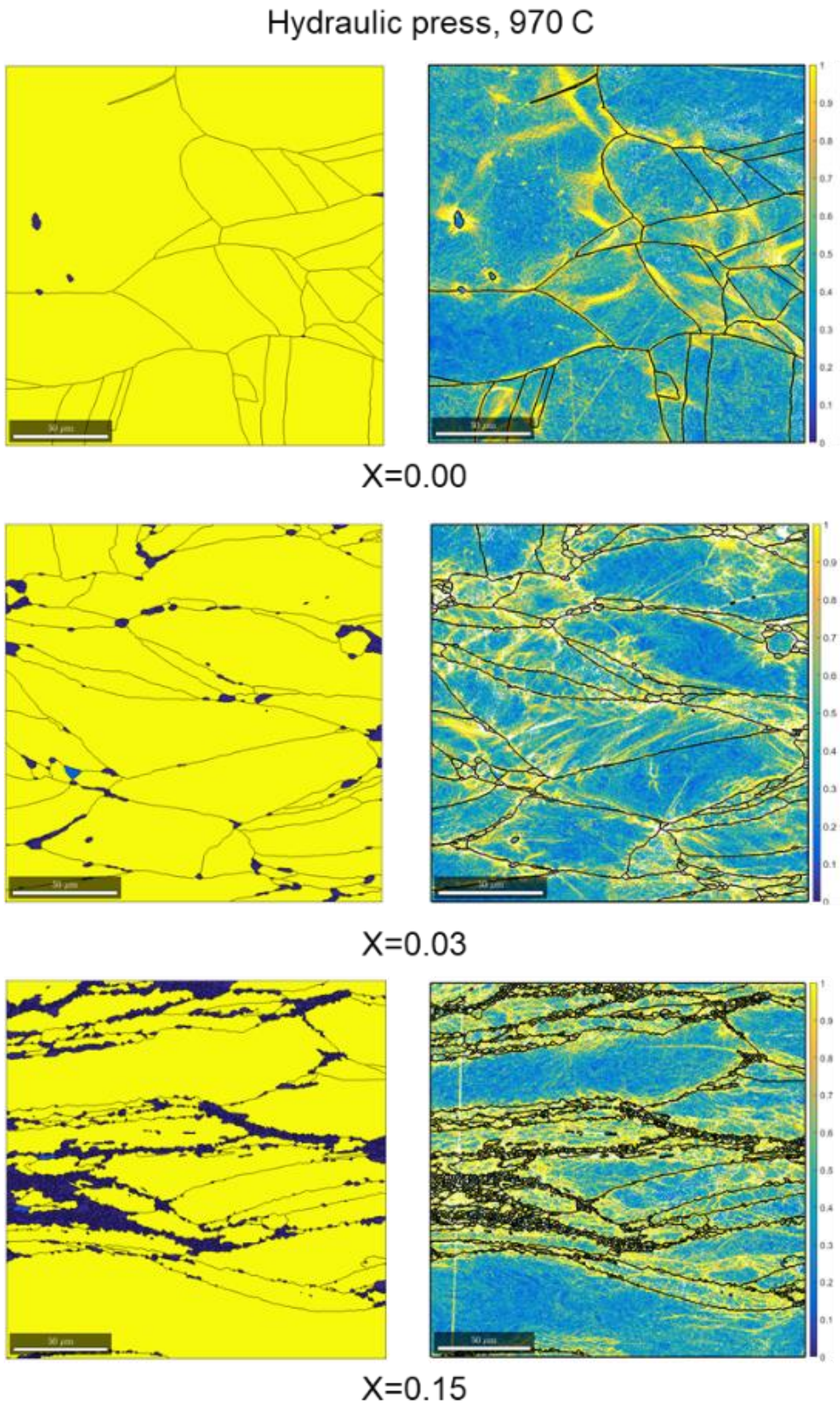
Hydraulic press, 970 C
50 μm
1
0.9
0.8
0.7
0.6
0.5
0.4
0.3
0.2
0.1
0
X=0.00
X=0.03
X=0.15

Hydraulic press, 1080 C

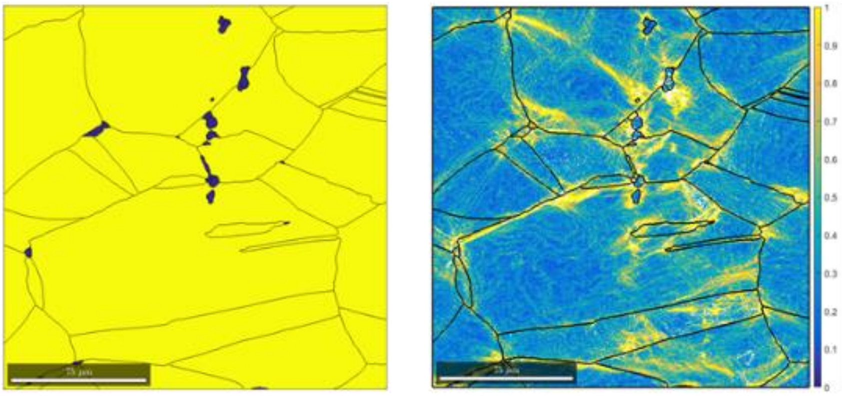

X=0.00

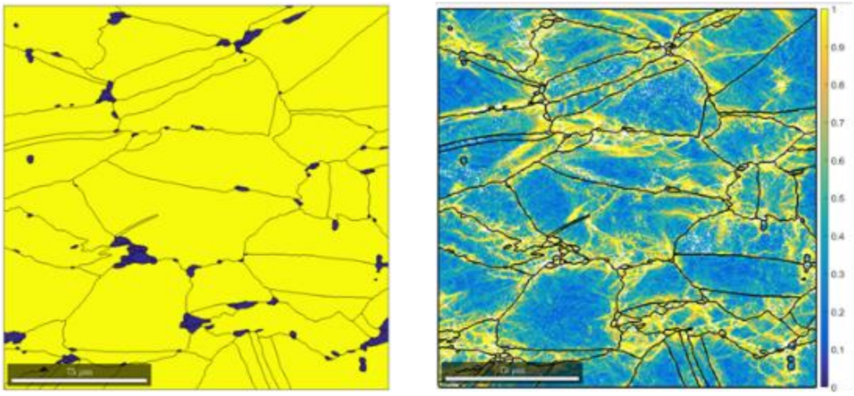

X=0.03

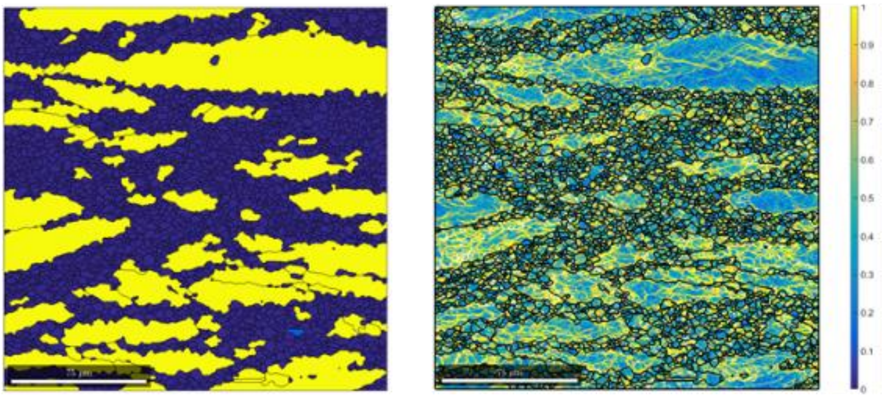

X=0.55

DTC, Hydraulic press, 970 C – Central Axis

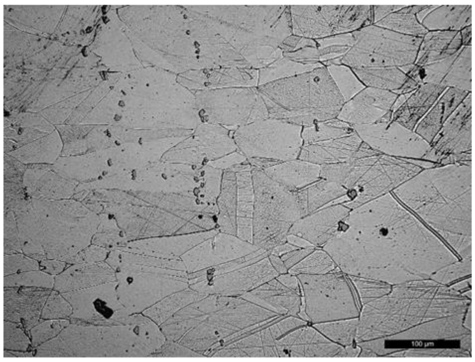

1 mm from Bottom

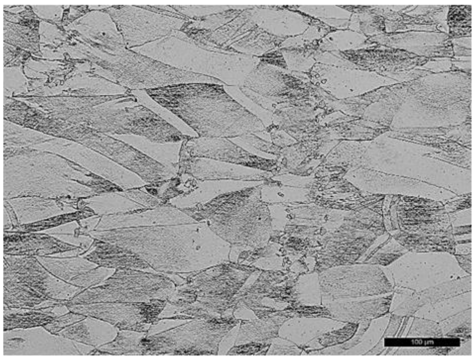

3 mm from Bottom

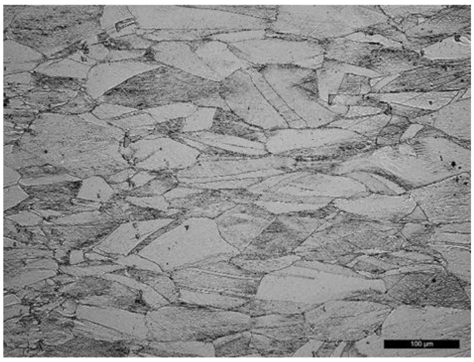

7 mm from Bottom

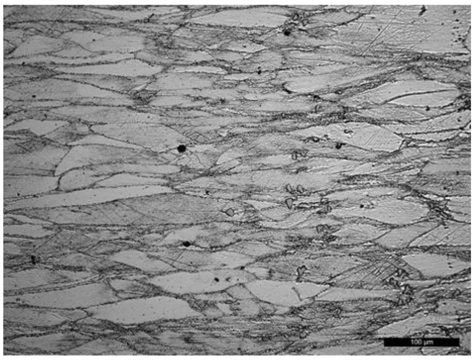

12 mm from Bottom

1.4 Figure 4.9

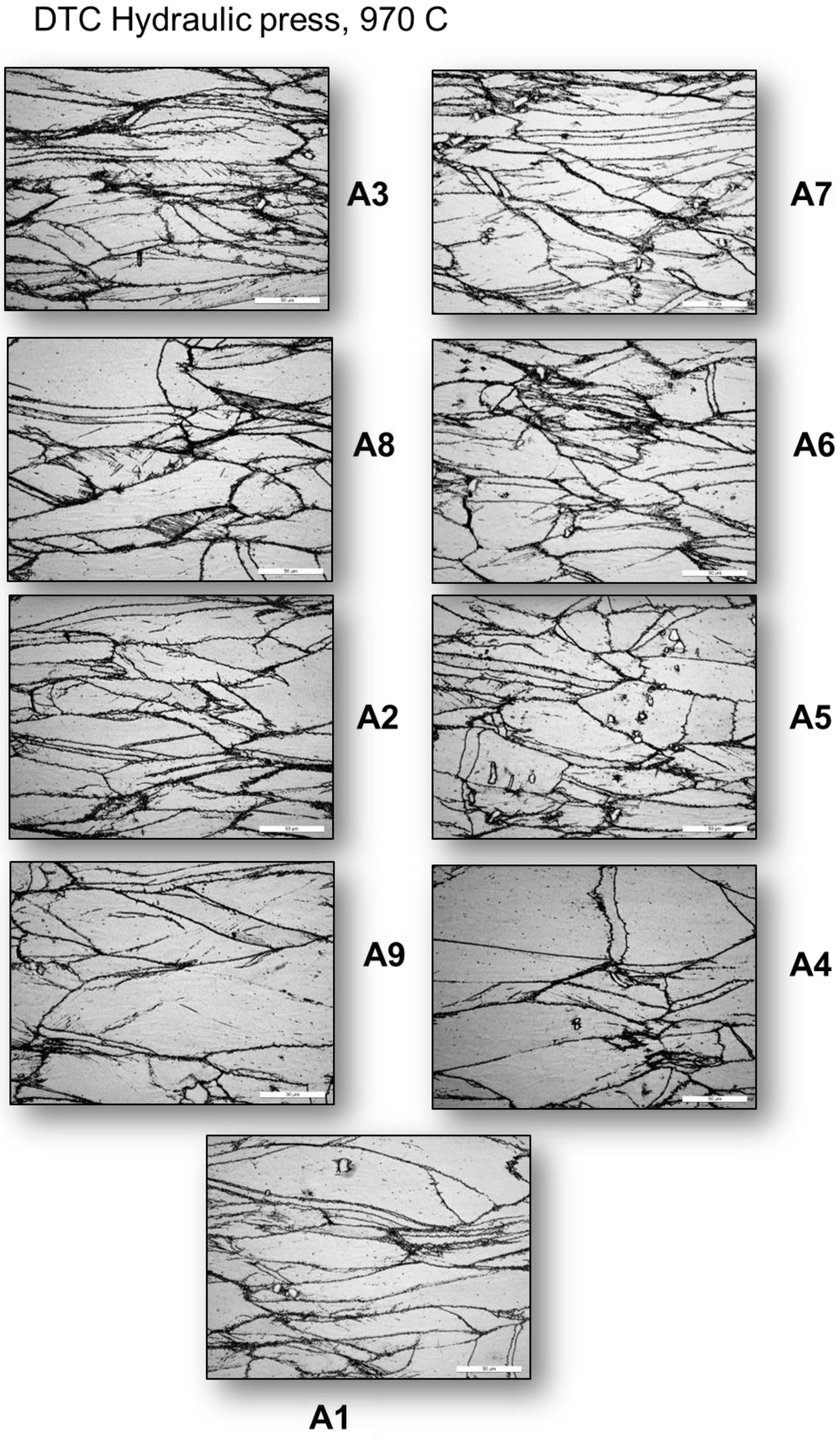

1.5 Figure 4.10

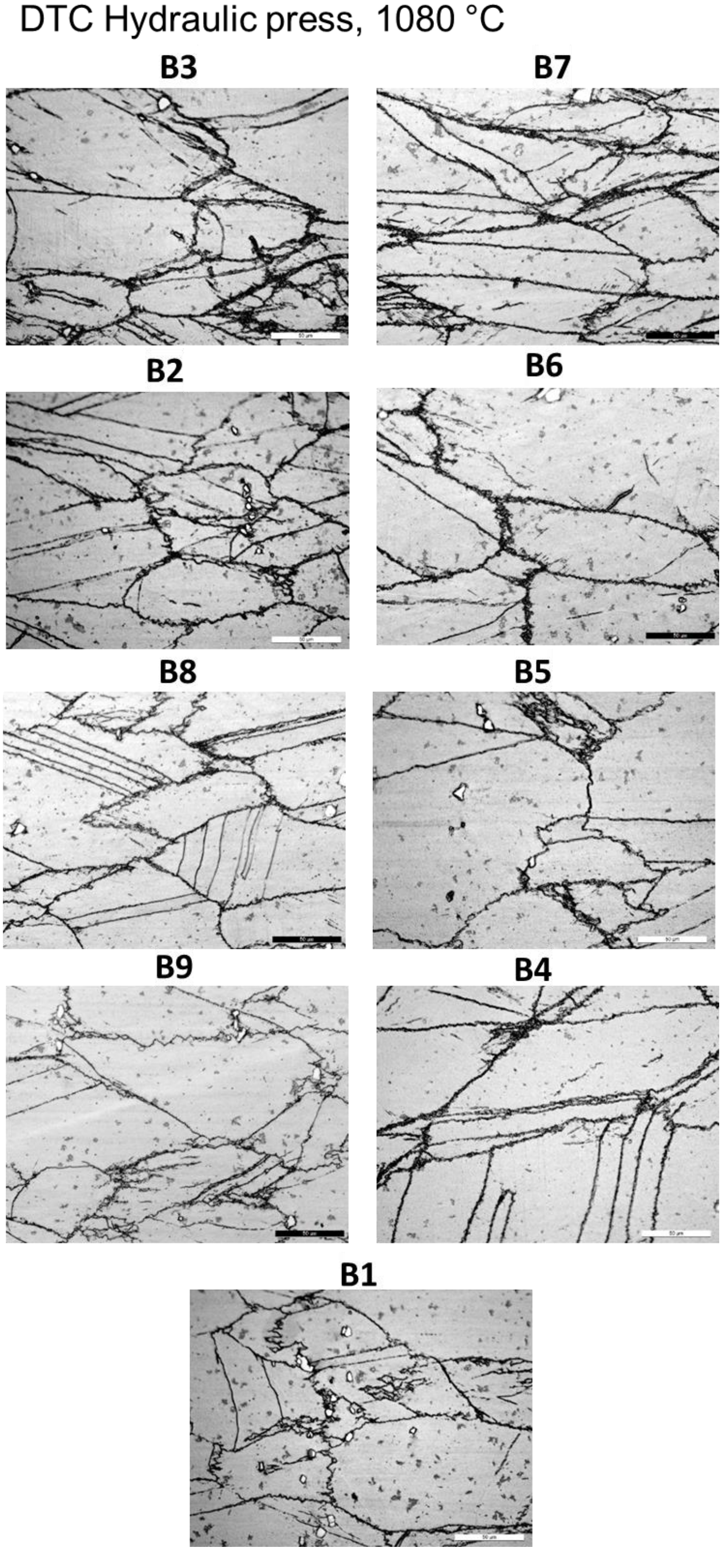

1.6 Figure 4.12

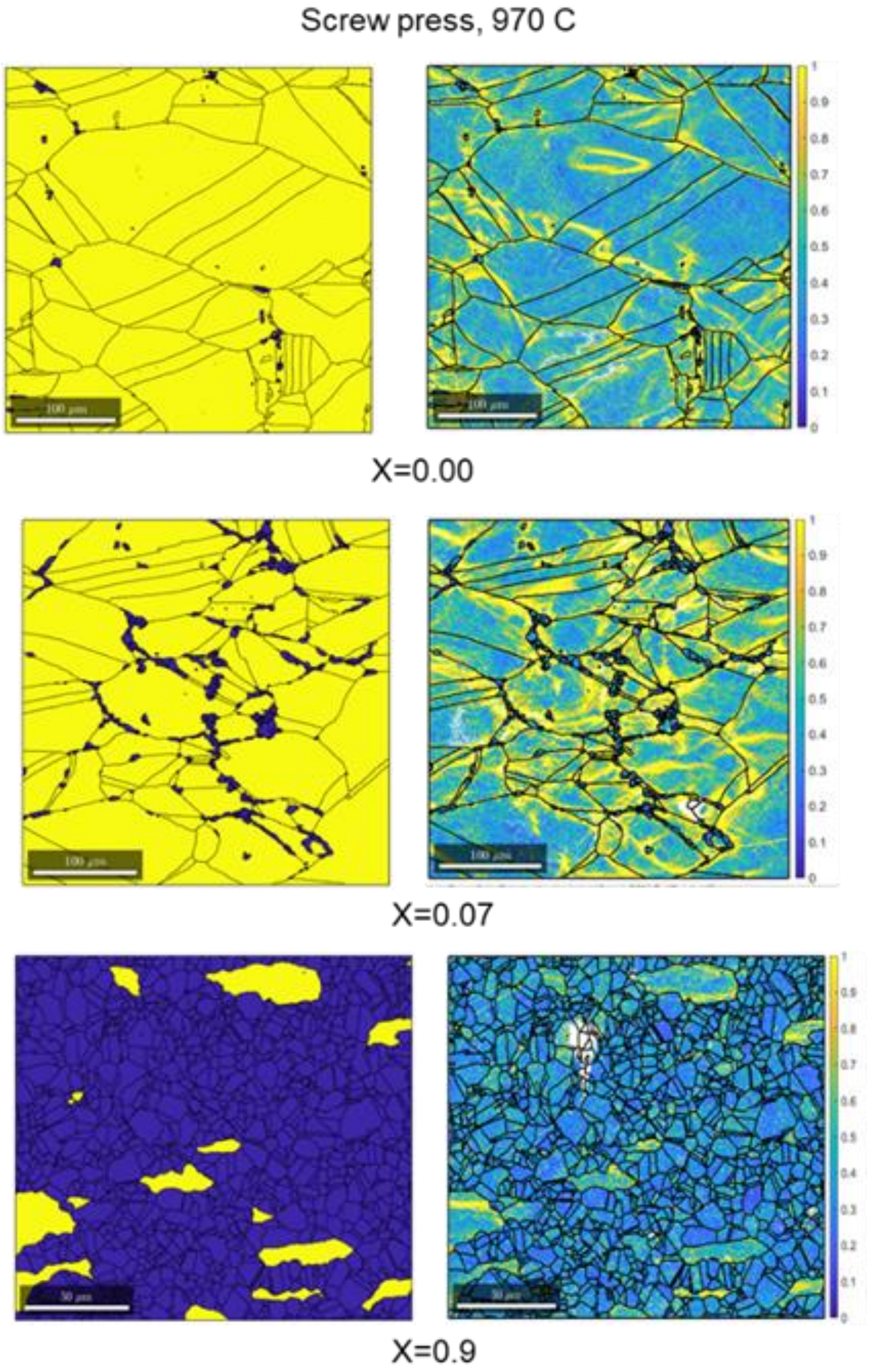

Screw press, 1080 C

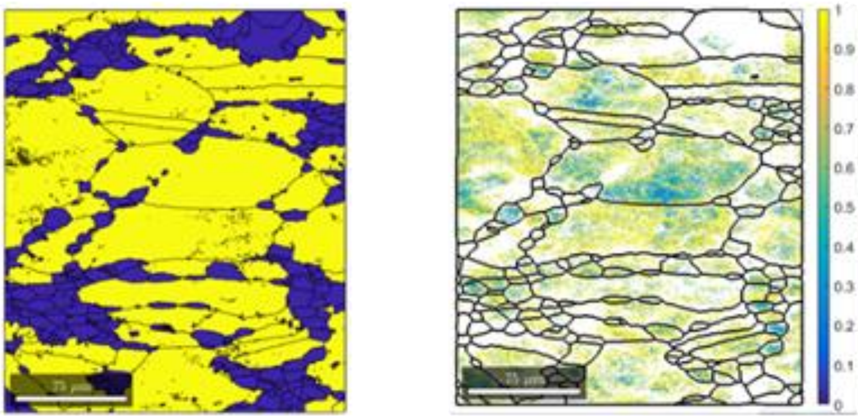

X=0.2

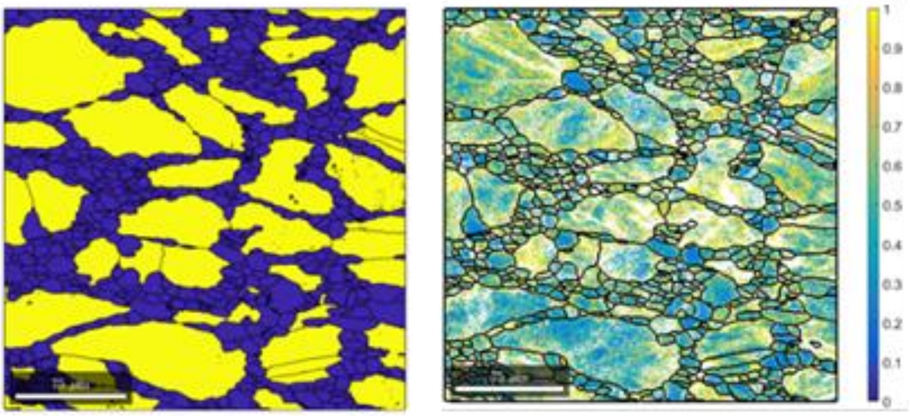

X=0.45

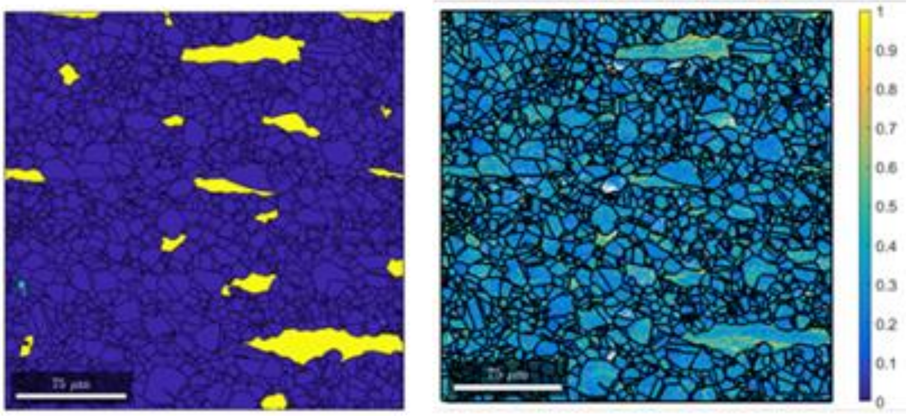

X=0.95

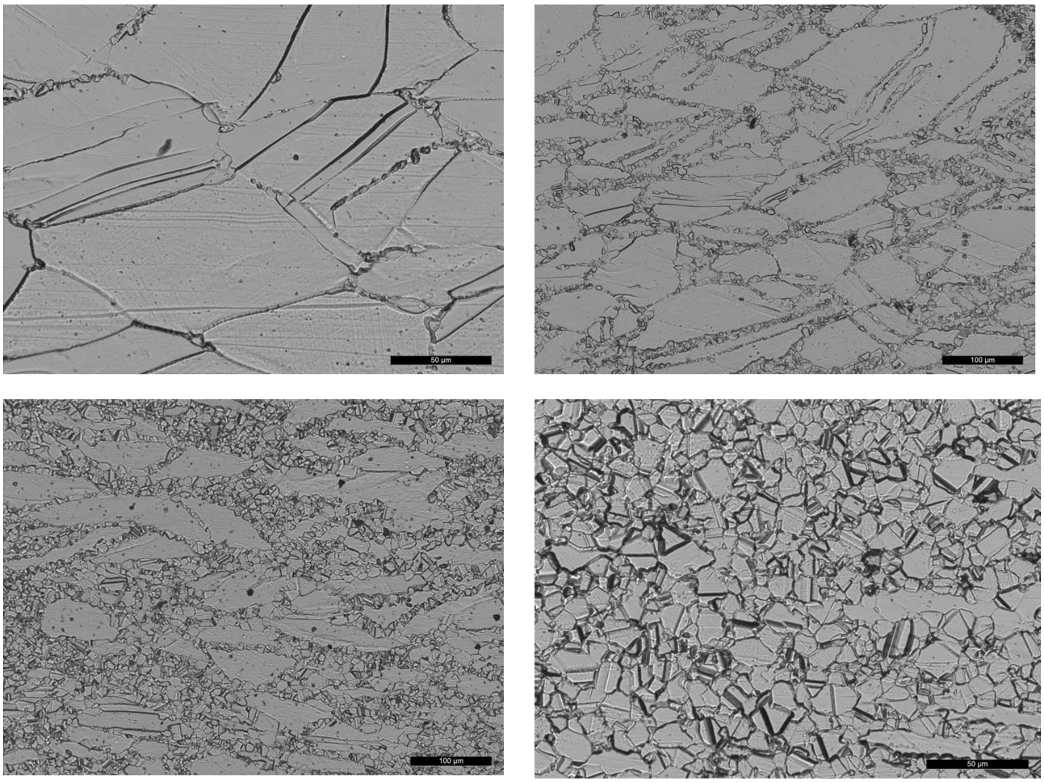

1.7 Figure 4.13

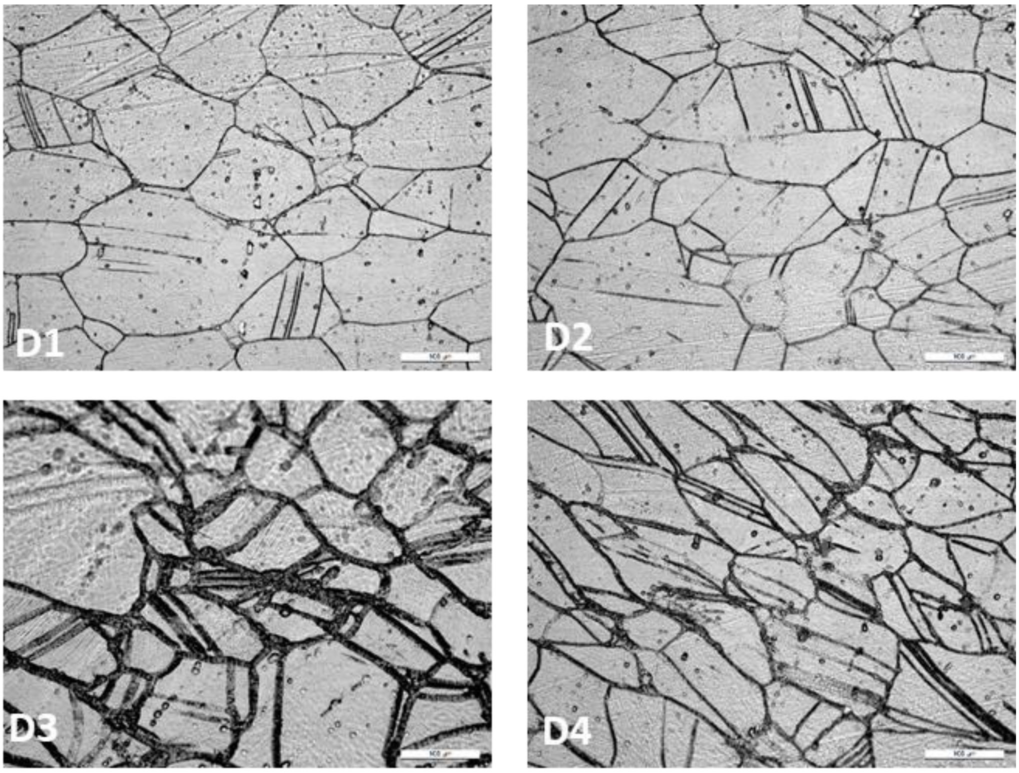

1.8 Figure 4.14

DTC Screw press, 970 C

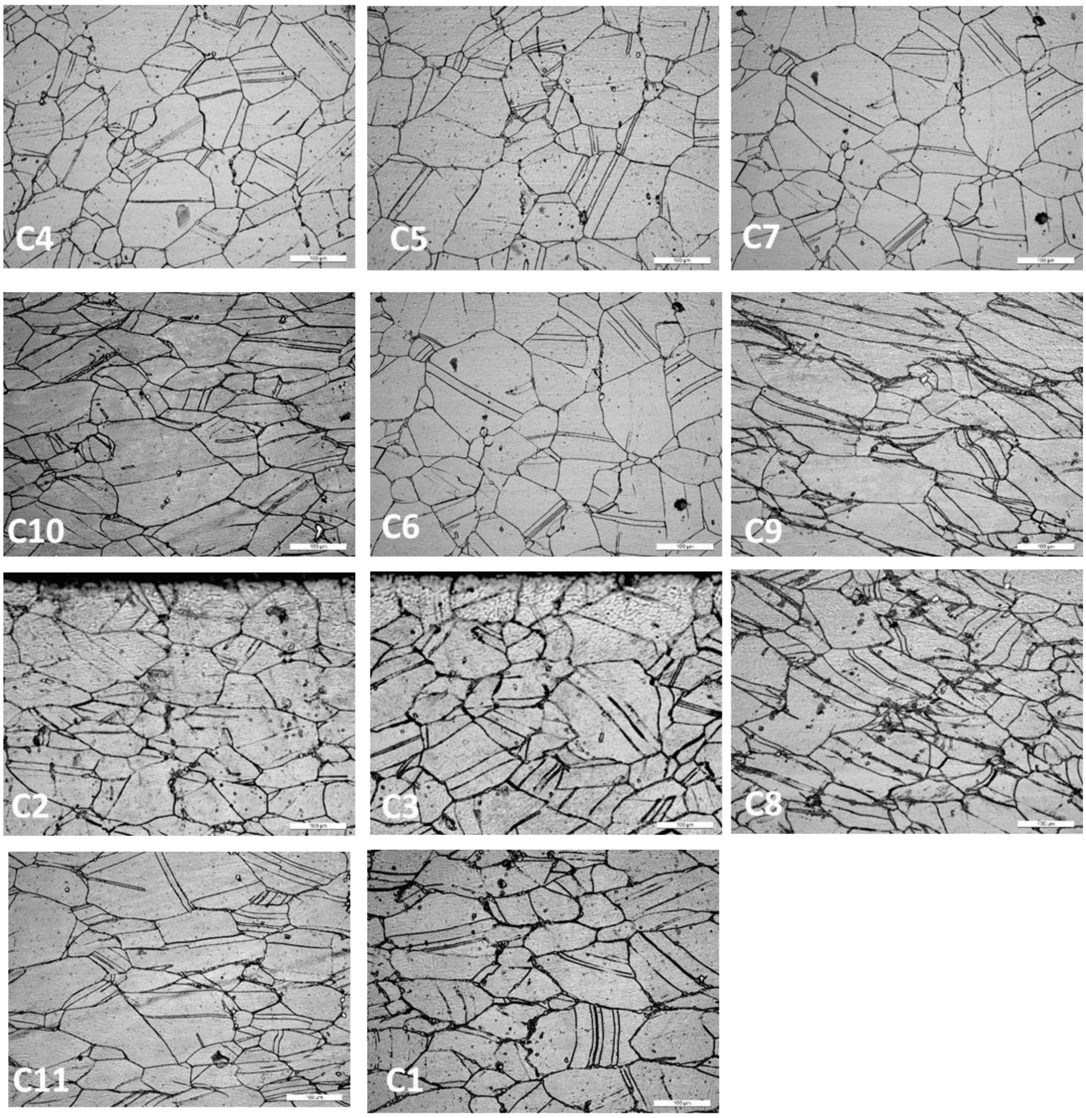

1.9 Figure 4.21

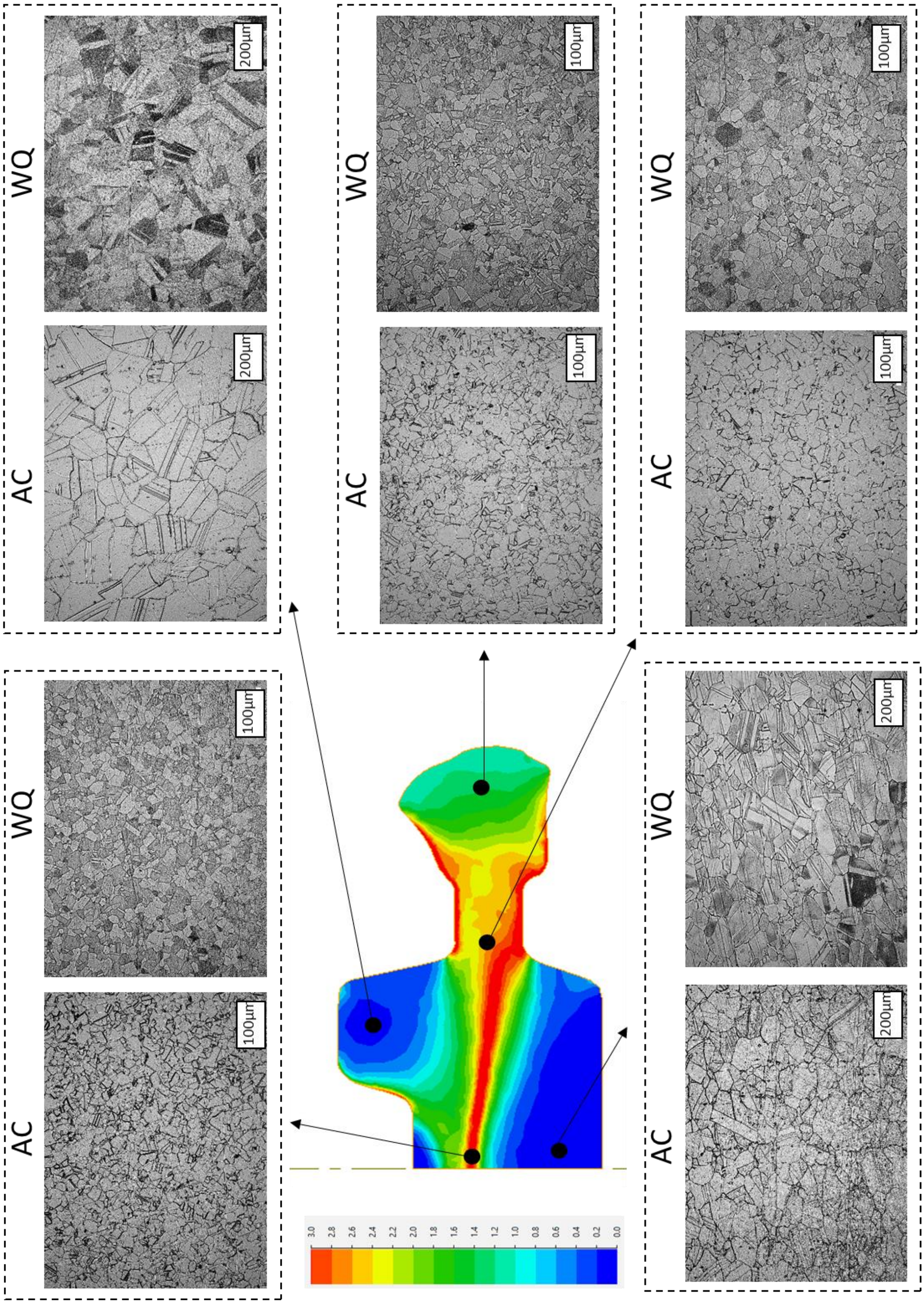

1.10 Figure 5.1

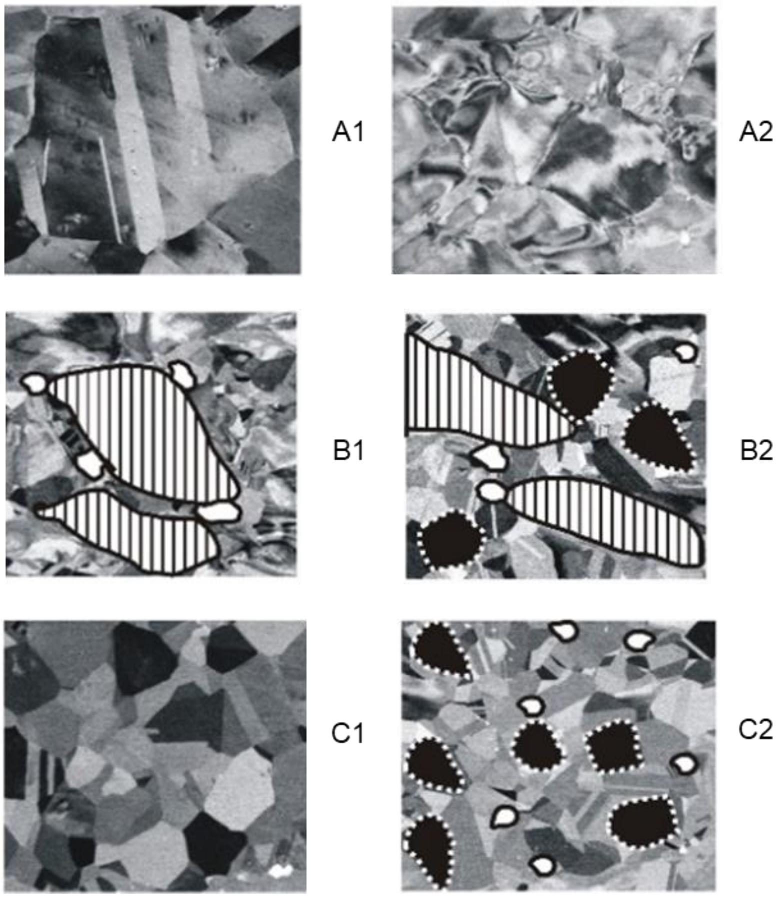

1.11 Figure 6.5

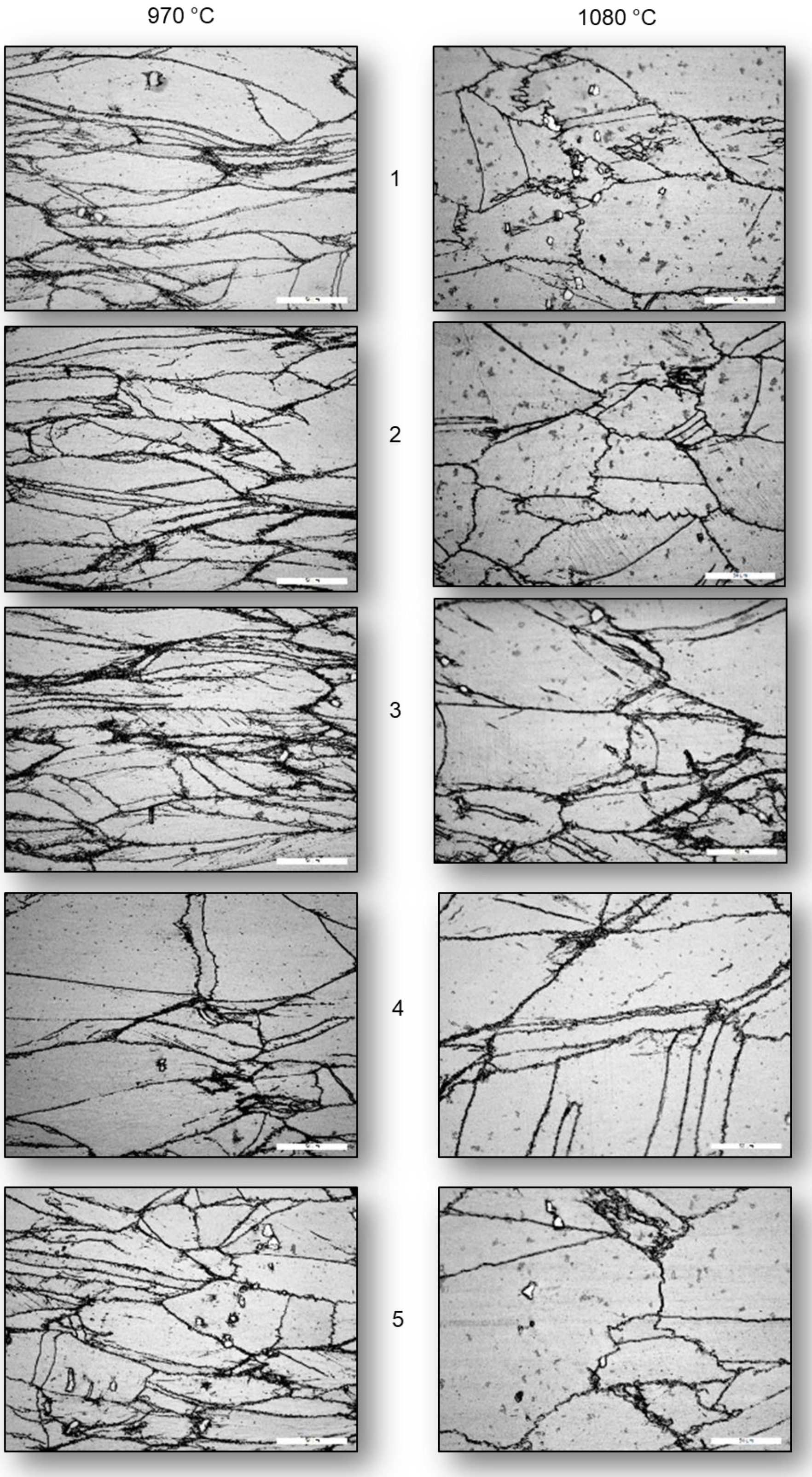

1.12 Figure 6.6

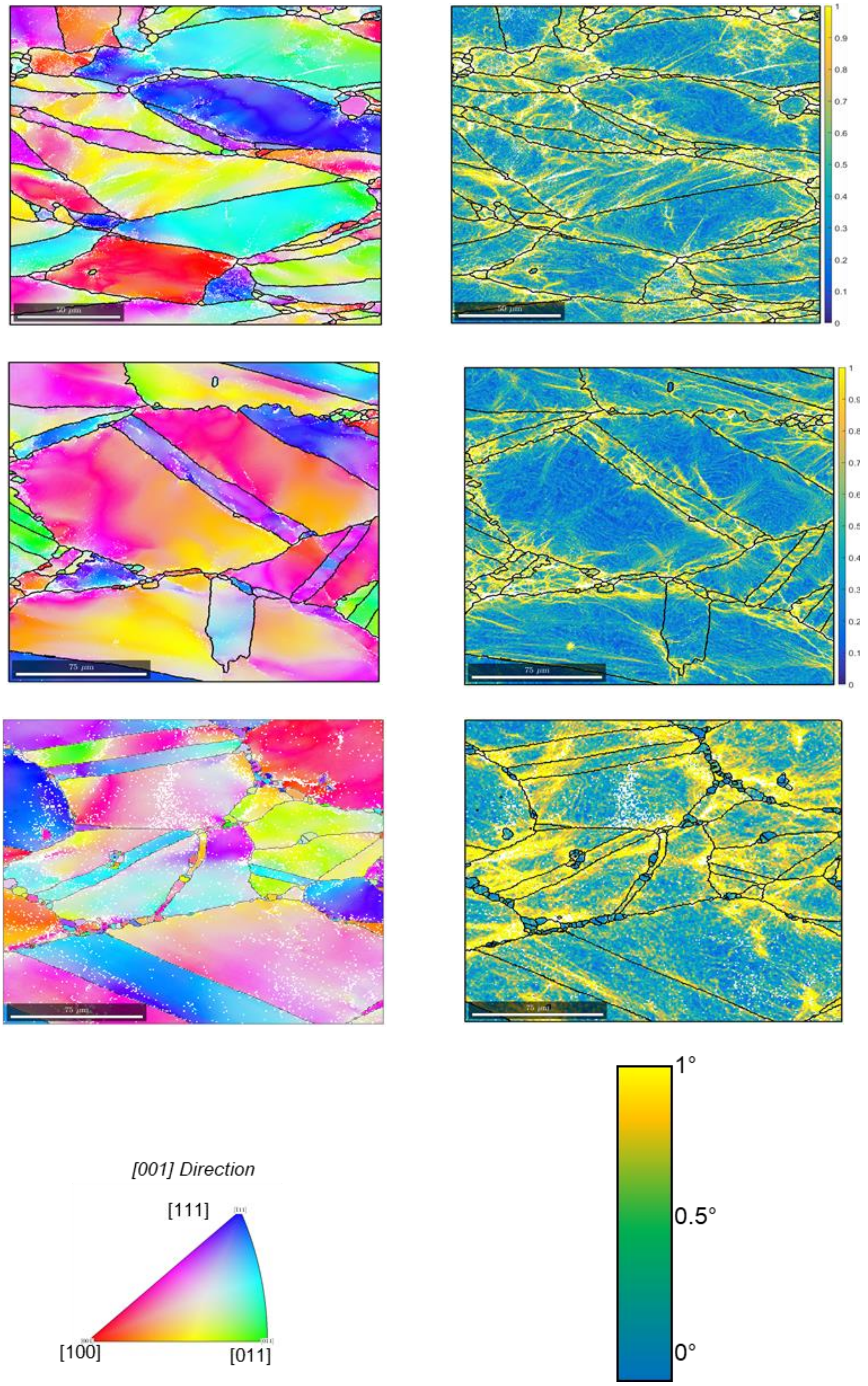

1.13 Figure 7.16

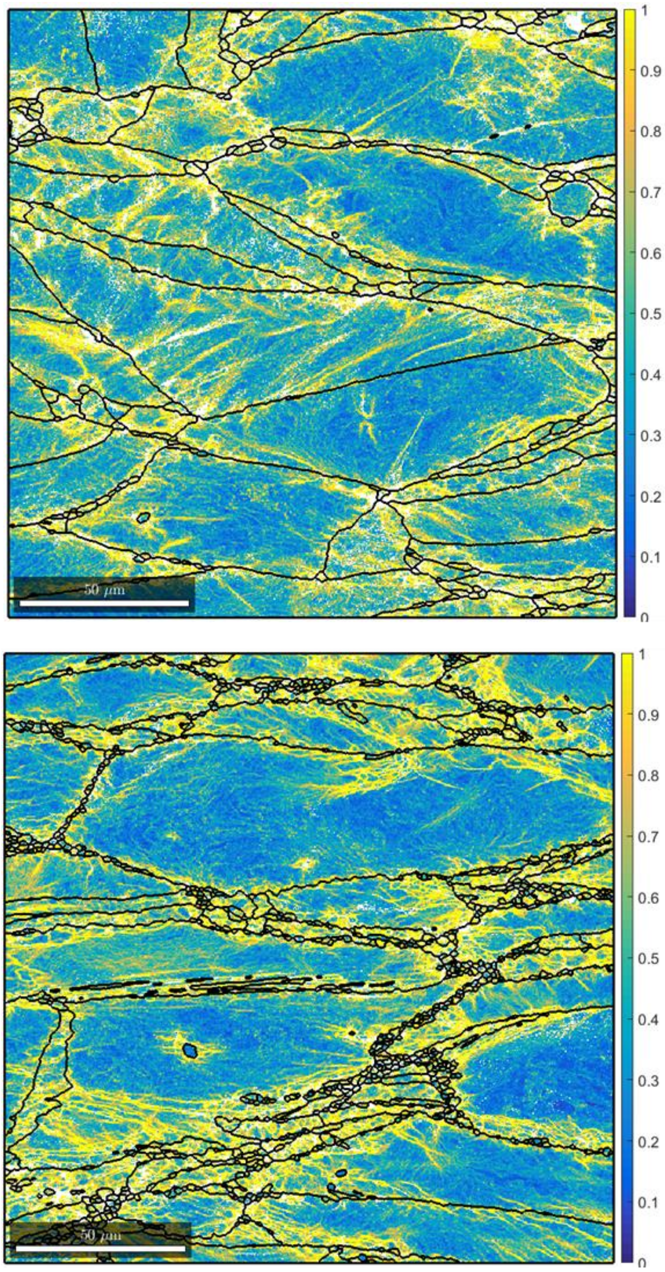

Appendix 2

2.1 QFORM and DEFORM JMAK Model Parameters

DEFORM Microstructure Model Parameters

Parameter	**Q_9**	**T**	**t**	**A**
Description	Activation Energy	Temperature(K)	Time(s)	/
Type	Material Parameter	Process Parameter	Process Parameter	Material Parameter
Value	390753	/	/	0
Parameter	**a1**	**β_m**	**β_s**	**β_d**
Type	Material Parameters			
Value	0.004659	0.693	0.693	0.693
Parameter	**Q_1**	**Q_2**	**Q_3**	**Q_4**
Description	Activation Energies			
Type	Material Parameters			
Value	49520	0	74790	196000
Parameter	**Q_5**	**Q_6**	**Q_7**	**Q_8**
Description	Activation Energies			
Type	Material Parameters			
Value	196000	-31694	-240000	-240000
Parameter	**a_2**	**a_3**	**a_4**	**a_5**
Type	Material Parameters			
Value	0.83	3.16	5.043e-09	5.043e-09
Parameter	**a_6**	**a_7**	**a_8**	**a_9**
Type	Material Parameters			
Value	678	48500000000	48500000000	1.58e+16
Parameter	**a_{10}**	**b_1**	**b_2**	**b_4**
Type	Material Parameters			
Value	0.8	0	0	0
Parameter	**c_1**	**c_5**	**c_6**	**c_7**
Type	Material Parameters			
Value	0	0	0	0
Parameter	**c_8**	**h_3**	**h_4**	**h_5**
Type	Material Parameters			
Value	0	0	0	0
Parameter	**h_6**	**h_7**	**h_8**	**k_s**
Type	Material Parameters			
Value	0	0	0	0.3
Parameter	**k_m**	**k_d**	**n_1**	**n_2**
Type	Material Parameters			
Value	1	1	0	0
Parameter	**n_3**	**n_4**	**n_5**	**n_6**
Type	Material Parameters			
Value	-0.75	-1.42	-1.42	0
Parameter	**n_7**	**n_8**	**m_1**	**m_3**
Type	Material Parameters			
Value	-0.41	-0.41	0.1238	0
Parameter	**m_4**	**m_5**	**m_6**	**m_7**
Type	Material Parameters			
Value	-0.408	-0.408	0	-0.028
Parameter	**m_8**	**m**		
Value	-0.028	2		

QFORM Microstructure Model Parameters

Parameter	**Q_9**	**T**	**t**	**A**
Description	Activation Energy	Temperature(K)	Time(s)	/
Type	Material Parameter	Process Parameter	Process Parameter	Material Parameter
Value	390753	/	/	0
Parameter	**a1**	**β_m**	**β_s**	**β_d**
Type	Material Parameters			
Value	0.004659	0.693	0.693	0.693
Parameter	**Q_1**	**Q_2**	**Q_3**	**Q_4**
Description	Activation Energies			
Type	Material Parameters			
Value	49520	0	74826	196000
Parameter	**Q_5**	**Q_6**	**Q_7**	**Q_8**
Description	Activation Energies			
Type	Material Parameters			
Value	196000	-31710	-240000	-240000
Parameter	**a_2**	**a_3**	**a_4**	**a_5**
Type	Material Parameters			
Value	0.83	3.16	5.043e-09	5.043e-09
Parameter	**a_6**	**a_7**	**a_8**	**a_9**
Type	Material Parameters			
Value	678	48500000000	48500000000	1.58e+16
Parameter	**a_{10}**	**b_1**	**b_2**	**b_4**
Type	Material Parameters			
Value	0.8	0	0	0
Parameter	**c_1**	**c_5**	**c_6**	**c_7**
Type	Material Parameters			
Value	0	0	0	0
Parameter	**c_8**	**h_3**	**h_4**	**h_5**
Type	Material Parameters			
Value	0	0	0	0.2
Parameter	**h_6**	**h_7**	**h_8**	**k_s**
Type	Material Parameters			
Value	0	0	0	0.3
Parameter	**k_m**	**k_d**	**n_1**	**n_2**
Type	Material Parameters			
Value	1	1	0	0
Parameter	**n_3**	**n_4**	**n_5**	**n_6**
Type	Material Parameters			
Value	-0.75	-1.42	-1.42	0
Parameter	**n_7**	**n_8**	**m_1**	**m_3**
Type	Material Parameters			
Value	-0.41	-0.41	0.1238	0
Parameter	**m_4**	**m_5**	**m_6**	**m_7**
Type	Material Parameters			
Value	-0.408	-0.408	0	-0.028
Parameter	**m_8**	**m**		
Type	Material Parameters			
Value	-0.028	2		

Appendix 3

3.1 Geometries

3.1.1 Disk Geometry

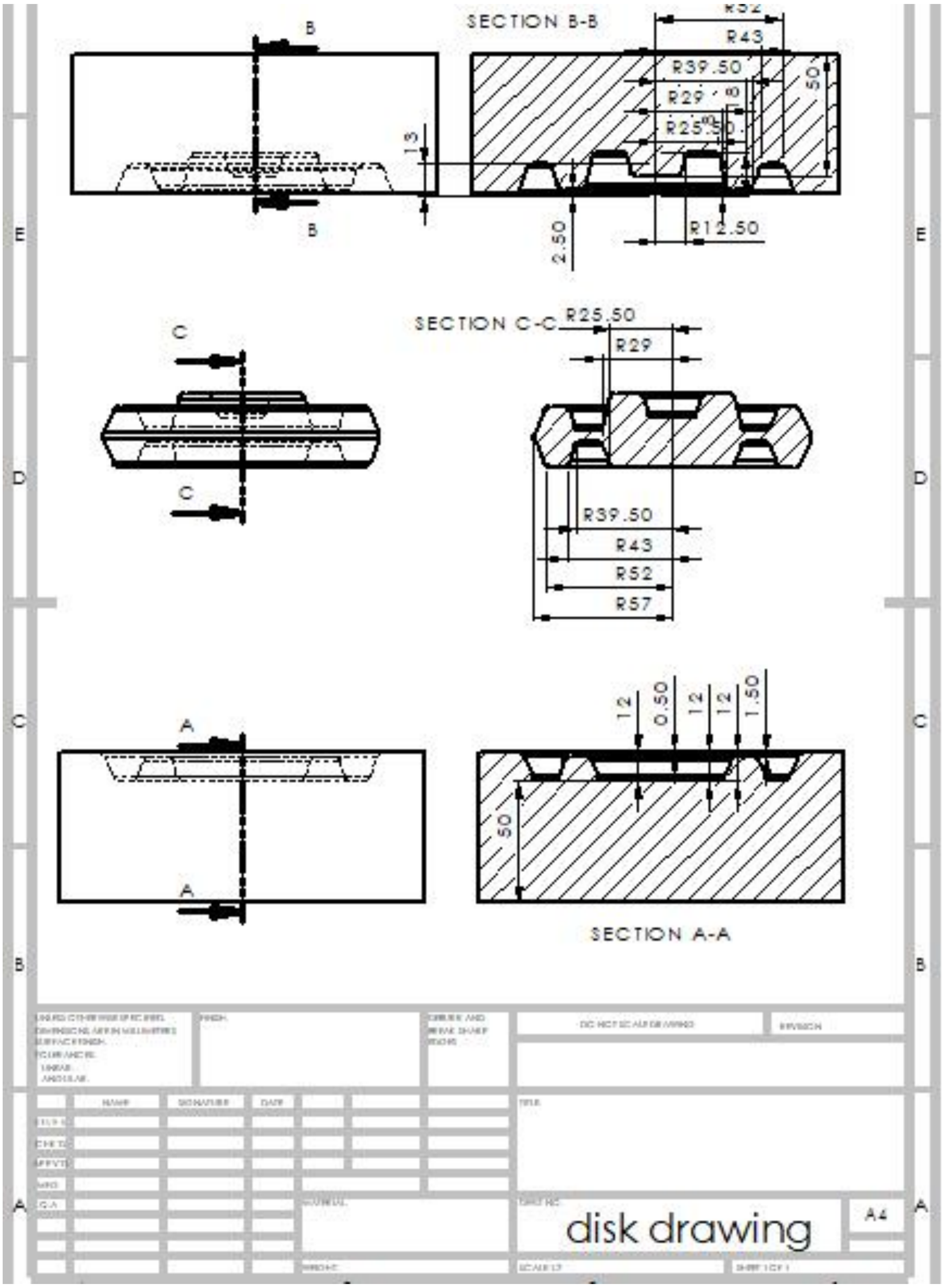

3.1.2 Double Cone Geometry

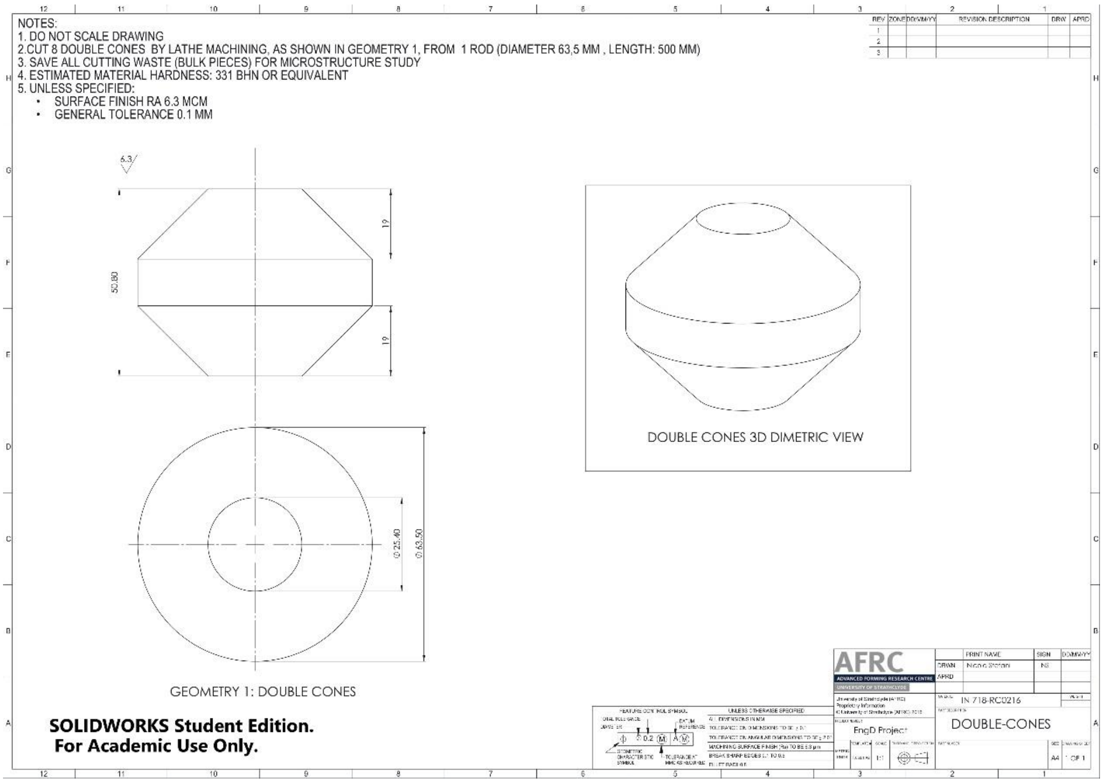

3.1.3 Tensile Specimen Geometry

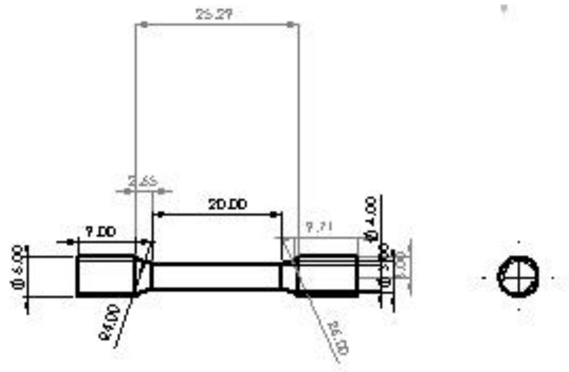

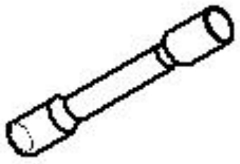

3.2 Metallographic Analysis

3.2.1 Metallographic analysis Template

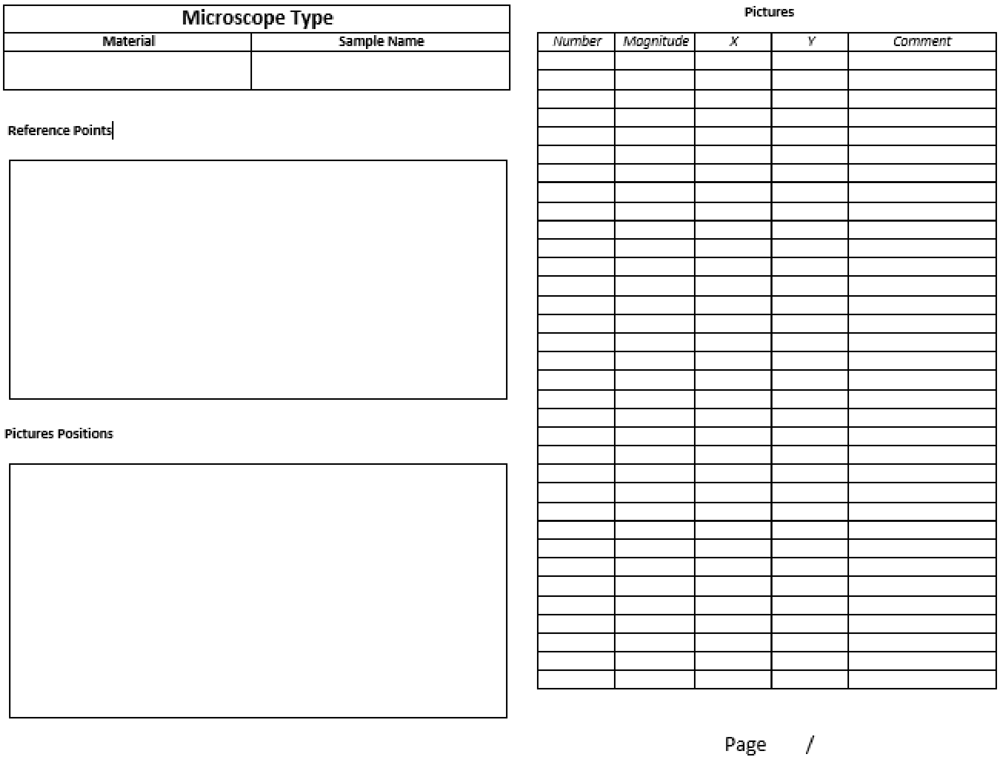

Microscope Type	
Material	Sample Name

Reference Points

Pictures Positions

Pictures

Number	Magnitude	X	Y	Comment

Page /

3.2.2 Metallographic Preparations Procedure

Equipment:

- Buehler EcoMet 300/AutoMet 300 grinder/polisher
- Buehler Vibromet 2 vibratory polisher

Metallographic Procedure:

- Grinding
    - SiC Abrasive Paper P240
        - Until Plane/ 27 N / 240rpm/ Contra
        - Lubricant: Water
    - SiC Abrasive Paper P400
        - Until Plane / 27 N / 240rpm/ Contra
        - Lubricant:Water
    - SiC Abrasive Paper P800
        - Until Plane / 27 N / 240rpm/ Contra
        - Lubricant: Water
    - SiC Abrasive Paper P1200
        - Until Plane / 27 N / 240rpm/ Contra
        - Lubricant: Water
- Polishing
    - Ultra Pol 9 µm
        - 8 minutes/ 25 N / 120rpm/ Contra
        - Lubricant= MetaDi 9 µm Polycrystalline Diamond Suspension
    - SiC Abrasive Paper P4000
        - Until Plane / 27 N / 240rpm/ Contra
        - Lubricant: Water
    - Mastertex 3 µm
        - 8 minutes/ 25 N / 120rpm/ Contra
        - Lubricant= MetaDi 3 µm Polycrystalline Diamond Suspension
    - TexMet 1 µm
        - 8 minutes/ 25 N / 120rpm/ Contra
        - Lubricant= MetaDi 1 µm Polycrystalline Diamond Suspension
    - TexMet 0.25 µm
        - 8 minutes/ 25 N / 120rpm/ Contra
        - Lubricant= MetaDi 0.25 µm Polycrystalline Diamond Suspension
    - MicroCloth 0.05 µm
        - 12 minutes/ 23 N / 120rpm/ Contra
        - Lubricant=Colloidal Silica 0.02
- Cleaning: Clean with cotton wool soaked in methanol to remove silica
- VibroMet: at 20% energy 8 hours or 80% for 3 hours
- Cleaning: Clean with cotton wool soaked in methanol to remove silica

3.3 Forging Recordings Data Collection

3.3.1 Die Temperatures and Characteristic times

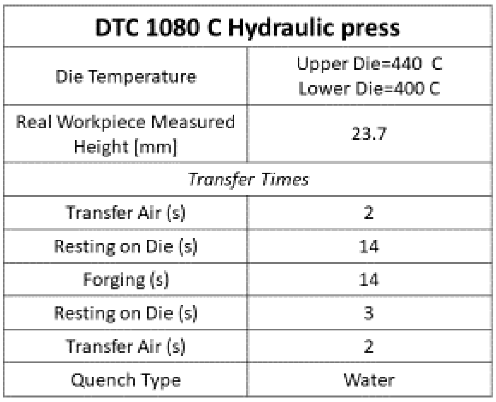

DTC 1080 C Hydraulic press	
Die Temperature	Upper Die=440 C Lower Die=400 C
Real Workpiece Measured Height [mm]	23.7
Transfer Times	
Transfer Air (s)	2
Resting on Die (s)	14
Forging (s)	14
Resting on Die (s)	3
Transfer Air (s)	2
Quench Type	Water

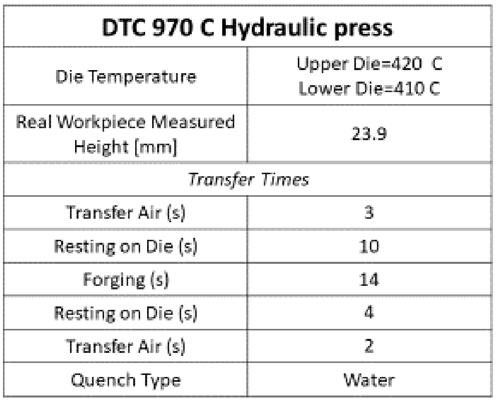

DTC 970 C Hydraulic press	
Die Temperature	Upper Die=420 C Lower Die=410 C
Real Workpiece Measured Height [mm]	23.9
Transfer Times	
Transfer Air (s)	3
Resting on Die (s)	10
Forging (s)	14
Resting on Die (s)	4
Transfer Air (s)	2
Quench Type	Water

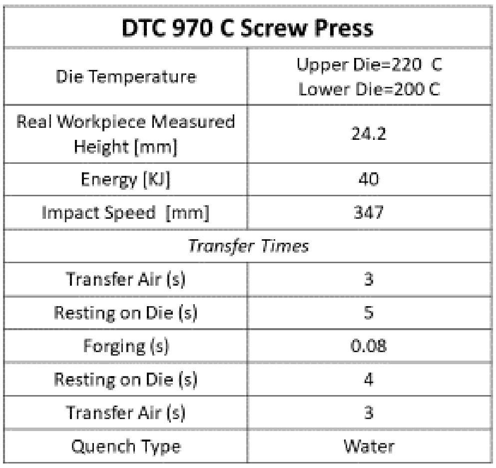

DTC 970 C Screw Press	
Die Temperature	Upper Die=220 C Lower Die=200 C
Real Workpiece Measured Height [mm]	24.2
Energy [KJ]	40
Impact Speed [mm]	347
Transfer Times	
Transfer Air (s)	3
Resting on Die (s)	5
Forging (s)	0.08
Resting on Die (s)	4
Transfer Air (s)	3
Quench Type	Water

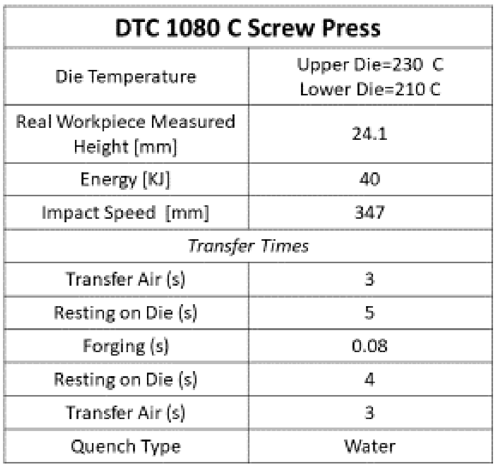

DTC 1080 C Screw Press	
Die Temperature	Upper Die=230 C Lower Die=210 C
Real Workpiece Measured Height [mm]	24.1
Energy [KJ]	40
Impact Speed [mm]	347
Transfer Times	
Transfer Air (s)	3
Resting on Die (s)	5
Forging (s)	0.08
Resting on Die (s)	4
Transfer Air (s)	3
Quench Type	Water

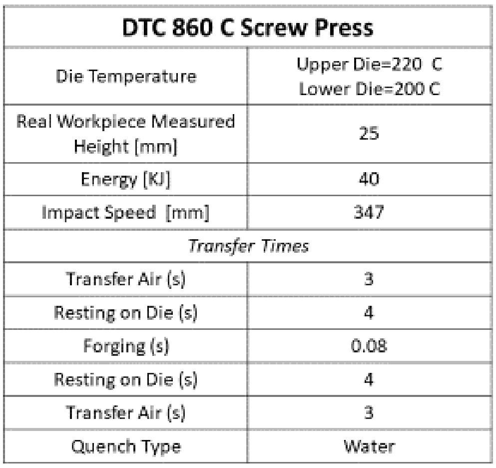

DTC 860 C Screw Press	
Die Temperature	Upper Die=220 C Lower Die=200 C
Real Workpiece Measured Height [mm]	25
Energy [KJ]	40
Impact Speed [mm]	347
Transfer Times	
Transfer Air (s)	3
Resting on Die (s)	4
Forging (s)	0.08
Resting on Die (s)	4
Transfer Air (s)	3
Quench Type	Water

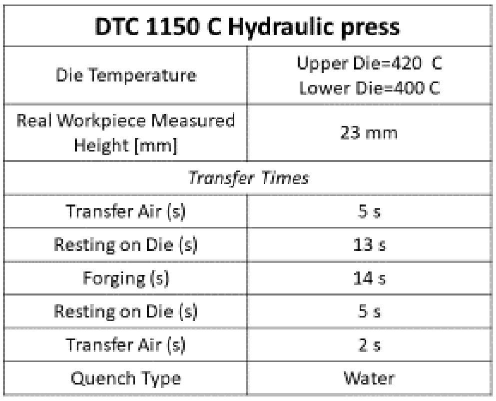

DTC 1150 C Hydraulic press	
Die Temperature	Upper Die=420 C Lower Die=400 C
Real Workpiece Measured Height [mm]	23 mm
Transfer Times	
Transfer Air (s)	5 s
Resting on Die (s)	13 s
Forging (s)	14 s
Resting on Die (s)	5 s
Transfer Air (s)	2 s
Quench Type	Water

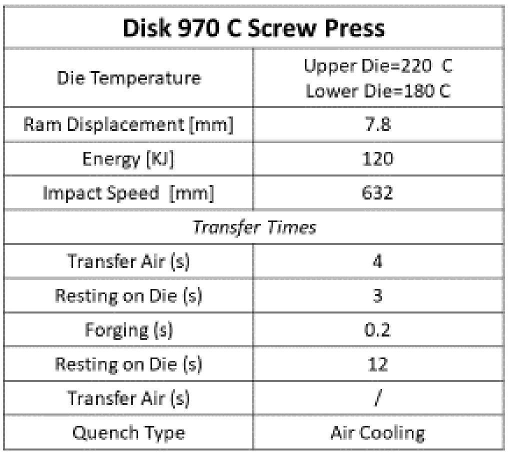

Disk 970 C Screw Press	
Die Temperature	Upper Die=220 C Lower Die=180 C
Ram Displacement [mm]	7.8
Energy [KJ]	120
Impact Speed [mm]	632
Transfer Times	
Transfer Air (s)	4
Resting on Die (s)	3
Forging (s)	0.2
Resting on Die (s)	12
Transfer Air (s)	/
Quench Type	Air Cooling

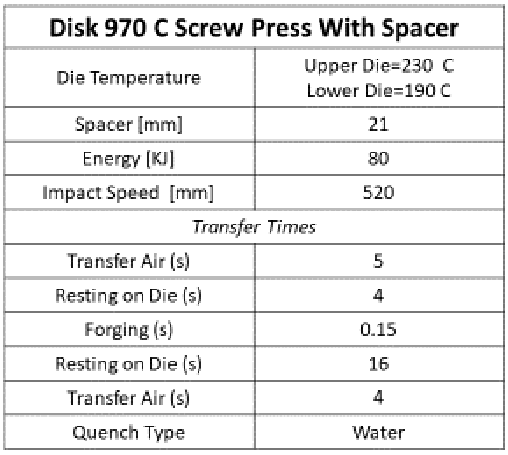

Disk 970 C Screw Press With Spacer	
Die Temperature	Upper Die=230 C Lower Die=190 C
Spacer [mm]	21
Energy [KJ]	80
Impact Speed [mm]	520
Transfer Times	
Transfer Air (s)	5
Resting on Die (s)	4
Forging (s)	0.15
Resting on Die (s)	16
Transfer Air (s)	4
Quench Type	Water

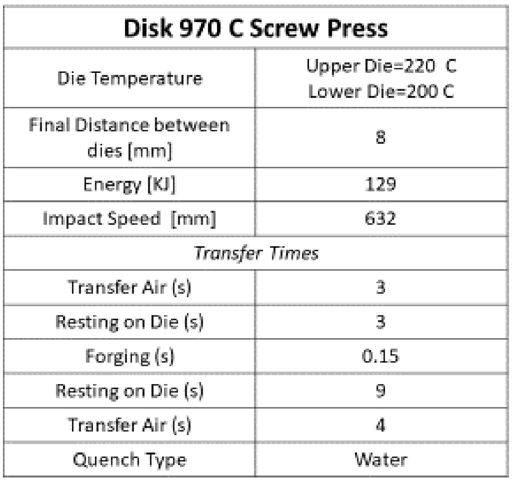

Disk 970 C Screw Press	
Die Temperature	Upper Die=220 C Lower Die=200 C
Final Distance between dies [mm]	8
Energy [KJ]	129
Impact Speed [mm]	632
Transfer Times	
Transfer Air (s)	3
Resting on Die (s)	3
Forging (s)	0.15
Resting on Die (s)	9
Transfer Air (s)	4
Quench Type	Water

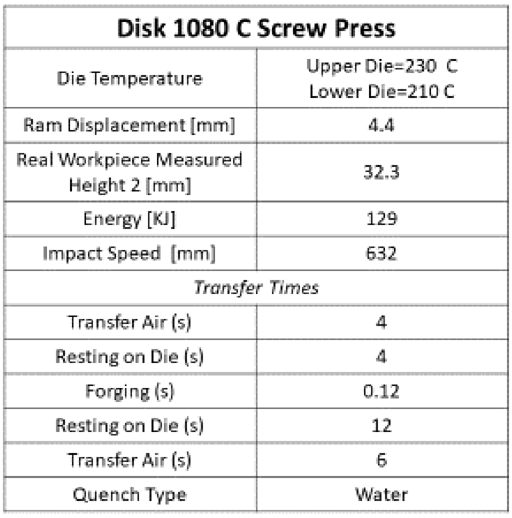

Disk 1080 C Screw Press	
Die Temperature	Upper Die=230 C Lower Die=210 C
Ram Displacement [mm]	4.4
Real Workpiece Measured Height 2 [mm]	32.3
Energy [KJ]	129
Impact Speed [mm]	632
Transfer Times	
Transfer Air (s)	4
Resting on Die (s)	4
Forging (s)	0.12
Resting on Die (s)	12
Transfer Air (s)	6
Quench Type	Water

3.3.2 Raw Data from Screw Press

X0 Position [mm] Y0 Force [KN]					
DTC 970 °C		DTC 860 °C		DTC 1080 °C	
X0	Y0	X0	Y0	X0	Y0
.0	9862.0	.0	2697.0	.0	10902.0
.6	9862.0	.6	2697.0	.6	10902.0
1.2	9862.0	1.2	2697.0	1.2	10902.0
1.8	9862.0	1.8	2697.0	1.8	10902.0
2.4	9862.0	2.4	2697.0	2.4	10902.0
3.0	9862.0	3.0	2697.0	3.0	10902.0
3.6	9862.0	3.6	2697.0	3.6	10902.0
4.2	9862.0	4.2	2697.0	4.2	10902.0
4.8	9862.0	4.8	2697.0	4.8	10902.0
5.4	9862.0	5.4	2697.0	5.4	10902.0
6.0	9862.0	6.0	2697.0	6.0	10902.0
6.6	9862.0	6.6	2697.0	6.6	10902.0
7.2	9862.0	7.2	2697.0	7.2	10902.0
7.8	9862.0	7.8	2697.0	7.8	10902.0
8.4	9862.0	8.4	2697.0	8.4	10902.0

X0 Position [mm] Y0 Force [KN]					
DTC 970 °C		DTC 860 °C		DTC 1080 °C	
9.0	9862.0	9.0	2697.0	9.0	10902.0
9.6	9862.0	9.6	2697.0	9.6	10902.0
10.2	9862.0	10.2	2697.0	10.2	10902.0
10.8	9862.0	10.8	2697.0	10.8	10902.0
11.4	9862.0	11.4	2697.0	11.4	10902.0
12.0	9862.0	12.0	2697.0	12.0	10902.0
12.6	9862.0	12.6	2697.0	12.6	10902.0
13.2	9862.0	13.2	2697.0	13.2	10902.0
13.8	9862.0	13.8	2697.0	13.8	10902.0
14.4	9862.0	14.4	2697.0	14.4	10902.0
15.0	9862.0	15.0	2697.0	15.0	10902.0
15.6	9862.0	15.6	2697.0	15.6	10902.0
16.2	9862.0	16.2	2697.0	16.2	10902.0
16.8	9862.0	16.8	2697.0	16.8	10902.0
17.4	9862.0	17.4	2697.0	17.4	10902.0
18.0	9862.0	18.0	2697.0	18.0	10902.0
18.6	9862.0	18.6	2697.0	18.6	10902.0
19.2	9862.0	19.2	2697.0	19.2	10902.0
19.8	9862.0	19.8	2697.0	19.8	10902.0
20.4	9862.0	20.4	2697.0	20.4	10902.0
21.0	9862.0	21.0	2697.0	21.0	10902.0
21.6	9862.0	21.6	2697.0	21.6	10902.0
22.2	9862.0	22.2	2697.0	22.2	10902.0
22.8	9862.0	22.8	2697.0	22.8	10902.0
23.4	9862.0	23.4	2697.0	23.4	10902.0
24.0	9862.0	24.0	2697.0	24.0	10902.0
24.6	9862.0	24.6	2697.0	24.6	10902.0
25.2	9862.0	25.2	2697.0	25.2	10902.0
25.8	7299.0	25.8	2697.0	25.8	8259.0
26.4	2324.0	26.4	2697.0	26.4	2515.0
27.0	2055.0	27.0	2713.0	27.0	1555.0
27.6	1959.0	27.6	2697.0	27.6	1531.0
28.2	1896.0	28.2	2634.0	28.2	1483.
28.8	1864.0	28.8	2594.0	28.8	1452.
29.4	1761.0	29.4	2507.0	29.4	1428.
30.0	1729.0	30.0	2451.0	30.0	1388.
30.6	1674.0	30.6	2372.0	30.6	1317.0
31.2	1634.0	31.2	2356.	31.2	1301.0
31.8	1578.0	31.8	2253.0	31.8	1269.
32.4	1515.0	32.4	2229.	32.4	1213.
33.0	1531.0	33.0	2142.0	33.0	1213.
33.6	1436.0	33.6	2039.0	33.6	1190.
34.2	1396.0	34.2	2039.0	34.2	1126.
34.8	1372.0	34.8	1991.0	34.8	1102.
35.4	1348.0	35.4	1928.0	35.4	1102.0
36.0	1293.0	36.0	1864.0	36.0	1063.0
36.6	1253.0	36.6	1856.0	36.6	1039.0
37.2	1237.0	37.2	1753.0	37.2	1007.0
37.8	1213.0	37.8	1713.0	37.8	1031.
38.4	1158.0	38.4	1690.	38.4	1007.0
39.0	1126.0	39.0	1721.	39.0	944.0
39.6	1094.0	39.6	1515.0	39.6	952.0
40.2	1087.0	40.2	1610.0	40.2	928.0
40.8	1079.0	40.8	1594.	40.8	975.0
41.4	936.0	41.4	1523.0	41.4	817.0
42.0	1047.0	42.0	1364.0	42.0	912.0
42.6	944.0	42.6	1452.0	42.6	880.0
43.2	928.0	43.2	1475.	43.2	856.0
43.8	928.0	43.8	1372.	43.8	833.0
44.4	825.0	44.4	1253.	44.4	872.0
45.0	833.0	45.0	1174.	45.0	777.0
45.6	852.0	45.6	1388.	45.6	793.0
46.2	872.0	46.2	1317.0	46.2	848.0
46.8	722.0	46.8	1245.0	46.8	745.0
47.4	753.0	47.4	983.0	47.4	729.0
48.0	714.0	48.0	1150.0	48.0	745.0
48.6	706.0	48.6	1134.0	48.6	682.0
49.2	634.0	49.2	1067.0	49.2	674.0

X0 Position [mm] Y0 Force [KN]					
DTC 970 °C		DTC 860 °C		DTC 1080 °C	
49.8	539.0	49.8	999.0	49.8	618.0
50.4	634.0	50.4	714.0	50.4	650.0
51.0	722.0	51.0	999.0	51.0	745.0
51.6	571.0	51.6	1269.	51.6	563.0
52.2	460.0	52.2	666.0	52.2	484.0
52.8	444.0	52.8	571.0	52.8	444.0
53.4	420.0	53.4	245.0	53.4	357.0
54.0	230.0	54.0	238.0	54.0	253.0
54.6	230.0	54.6	245.0	54.6	245.0
55.2	230.0	55.2	245.0	55.2	238.0
55.8	230.0	55.8	245.0	55.8	242.0
56.4	230.0	56.4	245.0	56.4	245.0
57.0	230.0	57.0	245.0	57.0	245.0
57.6	230.0	57.6	253.0	57.6	245.0
58.2	238.0	58.2	238.0	58.2	245.0
58.8	238.0	58.8	245.0	58.8	245.0
59.4	238.0	59.4	245.0	59.4	245.0

X0 Position [mm] Y0 Displacement [mm]					
DTC 970 °C		DTC 860 °C		DTC 1080 °C	
X0	Y0	X0	Y0	X0	Y0
1200.0	86.0	1200.0	82.0	1200.0	83.0
1203.0	85.0	1203.0	81.0	1203.0	82.0
1206.0	84.0	1206.0	80.0	1206.0	81.0
1209.0	83.0	1209.0	79.0	1209.0	80.0
1212.0	81.0	1212.0	78.0	1212.0	79.0
1215.0	80.0	1215.0	77.0	1215.0	78.0
1218.0	80.0	1218.0	76.0	1218.0	77.0
1221.0	79.0	1221.0	75.0	1221.0	76.0
1224.0	77.0	1224.0	74.0	1224.0	75.0
1227.0	76.0	1227.0	72.0	1227.0	74.0
1230.0	75.0	1230.0	72.0	1230.0	73.0
1233.0	74.0	1233.0	71.0	1233.0	72.0
1236.0	73.0	1236.0	70.0	1236.0	71.0
1239.0	72.0	1239.0	68.0	1239.0	70.0
1242.0	71.0	1242.0	67.0	1242.0	69.0
1245.0	70.0	1245.0	66.0	1245.0	68.0
1248.0	69.0	1248.0	65.0	1248.0	67.0
1251.0	68.0	1251.0	64.0	1251.0	66.0
1254.0	67.0	1254.0	63.0	1254.0	64.0
1257.0	66.0	1257.0	62.0	1257.0	64.0
1260.0	65.0	1260.0	61.0	1260.0	63.0
1263.0	64.0	1263.0	60.0	1263.0	62.0
1266.0	63.0	1266.0	59.0	1266.0	60.0
1269.0	62.0	1269.0	58.0	1269.0	59.0
1272.0	61.0	1272.0	57.0	1272.0	58.0
1275.0	60.0	1275.0	56.0	1275.0	57.0
1278.0	58.0	1278.0	55.0	1278.0	56.0
1281.0	57.0	1281.0	54.0	1281.0	55.0
1284.0	56.0	1284.0	53.0	1284.0	54.0
1287.0	55.0	1287.0	52.0	1287.0	53.0
1290.0	54.0	1290.0	52.0	1290.0	52.0
1293.0	53.0	1293.0	51.0	1293.0	51.0
1296.0	52.0	1296.0	50.0	1296.0	51.0
1299.0	51.0	1299.0	49.0	1299.0	50.0
1302.0	51.0	1302.0	48.0	1302.0	49.0
1305.0	49.0	1305.0	47.0	1305.0	48.0
1308.0	48.0	1308.0	46.0	1308.0	47.0
1311.0	48.0	1311.0	45.0	1311.0	46.0
1314.0	47.0	1314.0	44.0	1314.0	45.0
1317.0	46.0	1317.0	43.0	1317.0	44.0
1320.0	45.0	1320.0	42.0	1320.0	43.0
1323.0	44.0	1323.0	41.0	1323.0	42.0
1326.0	43.0	1326.0	40.0	1326.0	41.0

X0 Position [mm] Y0 Displacement [mm]					
DTC 970 °C		DTC 860 °C		DTC 1080 °C	
1329.0	42.0	1329.0	40.0	1329.0	40.0
1332.0	41.0	1332.0	39.0	1332.0	39.0
1335.0	40.0	1335.0	38.0	1335.0	38.0
1338.0	39.0	1338.0	37.0	1338.0	37.0
1341.0	38.0	1341.0	36.0	1341.0	36.0
1344.0	37.0	1344.0	36.0	1344.0	35.0
1347.0	36.0	1347.0	35.0	1347.0	34.0
1350.0	35.0	1350.0	34.0	1350.0	33.0
1353.0	34.0	1353.0	33.0	1353.0	32.0
1356.0	33.0	1356.0	32.0	1356.0	32.0
1359.0	32.0	1359.0	32.0	1359.0	31.0
1362.0	31.0	1362.0	32.0	1362.0	30.0
1365.0	31.0	1365.0	31.0	1365.0	29.0
1368.0	30.0	1368.0	30.0	1368.0	28.0
1371.0	29.0	1371.0	30.0	1371.0	27.0
1374.0	28.0	1374.0	29.0	1374.0	27.0
1377.0	27.0	1377.0	29.0	1377.0	26.0
1380.0	27.0	1380.0	29.0	1380.0	26.0
1383.0	26.0	1383.0	28.0	1383.0	26.0
1386.0	26.0	1386.0	28.0	1386.0	25.0
1389.0	26.0	1389.0	28.0	1389.0	25.0
1392.0	25.0	1392.0	27.0	1392.0	25.0
1395.0	25.0	1395.0	27.0	1395.0	25.0
1398.0	25.0	1398.0	27.0	1398.0	25.0
1401.0	25.0	1401.0	27.0	1401.0	25.0
1404.0	25.0	1404.0	26.0	1404.0	25.0
1407.0	25.0	1407.0	26.0	1407.0	25.0
1410.0	25.0	1410.0	26.0	1410.0	25.0
1413.0	25.0	1413.0	26.0	1413.0	25.0
1416.0	25.0	1416.0	26.0	1416.0	26.0
1419.0	25.0	1419.0	26.0	1419.0	26.0
1422.0	26.0	1422.0	26.0	1422.0	26.0
1425.0	26.0	1425.0	26.0	1425.0	27.0
1428.0	26.0	1428.0	26.0	1428.0	27.0
1431.0	27.0	1431.0	27.0	1431.0	28.0
1434.0	27.0	1434.0	27.0	1434.0	28.0
1437.0	27.0	1437.0	27.0	1437.0	29.0
1440.0	28.0	1440.0	27.0	1440.0	30.0
1443.0	28.0	1443.0	27.0	1443.0	31.0
1446.0	29.0	1446.0	27.0	1446.0	31.0
1449.0	30.0	1449.0	27.0	1449.0	32.0
1452.0	31.0	1452.0	28.0	1452.0	32.0
1455.0	31.0	1455.0	28.0	1455.0	33.0
1458.0	32.0	1458.0	28.0	1458.0	34.0
1461.0	32.0	1461.0	28.0	1461.0	35.0
1464.0	33.0	1464.0	28.0	1464.0	35.0
1467.0	34.0	1467.0	28.0	1467.0	36.0
1470.0	34.0	1470.0	28.0	1470.0	37.0
1473.0	35.0	1473.0	28.0	1473.0	37.0
1476.0	35.0	1476.0	28.0	1476.0	38.0
1479.0	36.0	1479.0	29.0	1479.0	39.0
1482.0	37.0	1482.0	29.0	1482.0	39.0
1485.0	37.0	1485.0	29.0	1485.0	40.0
1488.0	38.0	1488.0	29.0	1488.0	41.0
1491.0	39.0	1491.0	29.0	1491.0	41.0
1494.0	39.0	1494.0	29.0	1494.0	42.0
1497.0	40.0	1497.0	30.0	1497.0	43.0

X0 Position [mm] Y0 Speed [mm/s]					
DTC 970 °C		DTC 860 °C		DTC 1080 °C	
X0	Y0	X0	Y0	X0	Y0
1200.0	-348.0	1200.0	-342.0	1200.0	-343.0
1203.0	-349.0	1203.0	-342.0	1203.0	-343.0
1206.0	-349.0	1206.0	-342.0	1206.0	-343.0

X0 Position [mm] Y0 Speed [mm/s]					
DTC 970 °C		DTC 860 °C		DTC 1080 °C	
1209.0	-349.0	1209.0	-343.0	1209.0	-343.0
1212.0	-349.0	1212.0	-343.0	1212.0	-343.0
1215.0	-350.0	1215.0	-343.0	1215.0	-343.0
1218.0	-350.0	1218.0	-343.0	1218.0	-343.0
1221.0	-350.0	1221.0	-343.0	1221.0	-343.0
1224.0	-350.0	1224.0	-342.0	1224.0	-343.0
1227.0	-350.0	1227.0	-342.0	1227.0	-343.0
1230.0	-350.0	1230.0	-342.0	1230.0	-342.0
1233.0	-350.0	1233.0	-342.0	1233.0	-342.0
1236.0	-350.0	1236.0	-342.0	1236.0	-342.0
1239.0	-349.0	1239.0	-342.0	1239.0	-342.0
1242.0	-349.0	1242.0	-342.0	1242.0	-342.0
1245.0	-349.0	1245.0	-342.0	1245.0	-342.0
1248.0	-349.0	1248.0	-342.0	1248.0	-342.0
1251.0	-349.0	1251.0	-342.0	1251.0	-342.0
1254.0	-349.0	1254.0	-342.0	1254.0	-342.0
1257.0	-349.0	1257.0	-342.0	1257.0	-342.0
1260.0	-349.0	1260.0	-342.0	1260.0	-342.0
1263.0	-349.0	1263.0	-342.0	1263.0	-343.0
1266.0	-349.0	1266.0	-342.0	1266.0	-343.0
1269.0	-349.0	1269.0	-343.0	1269.0	-344.0
1272.0	-349.0	1272.0	-343.0	1272.0	-344.0
1275.0	-350.0	1275.0	-344.0	1275.0	-344.0
1278.0	-350.0	1278.0	-344.0	1278.0	-345.0
1281.0	-350.0	1281.0	-345.0	1281.0	-345.0
1284.0	-351.0	1284.0	-345.0	1284.0	-345.0
1287.0	-351.0	1287.0	-345.0	1287.0	-344.0
1290.0	-352.0	1290.0	-345.0	1290.0	-339.0
1293.0	-352.0	1293.0	-342.0	1293.0	-329.0
1296.0	-352.0	1296.0	-337.0	1296.0	-320.0
1299.0	-349.0	1299.0	-330.0	1299.0	-316.0
1302.0	-344.0	1302.0	-324.0	1302.0	-313.0
1305.0	-337.0	1305.0	-320.0	1305.0	-310.0
1308.0	-332.0	1308.0	-318.0	1308.0	-308.0
1311.0	-329.0	1311.0	-316.0	1311.0	-309.0
1314.0	-327.0	1314.0	-315.0	1314.0	-312.0
1317.0	-326.0	1317.0	-317.0	1317.0	-314.0
1320.0	-325.0	1320.0	-318.0	1320.0	-313.0
1323.0	-325.0	1323.0	-319.0	1323.0	-312.0
1326.0	-325.0	1326.0	-320.0	1326.0	-311.0
1329.0	-325.0	1329.0	-321.0	1329.0	-309.0
1332.0	-325.0	1332.0	-321.0	1332.0	-307.0
1335.0	-326.0	1335.0	-321.0	1335.0	-303.0
1338.0	-327.0	1338.0	-320.0	1338.0	-299.0
1341.0	-327.0	1341.0	-319.0	1341.0	-294.0
1344.0	-325.0	1344.0	-318.0	1344.0	-289.0
1347.0	-323.0	1347.0	-317.0	1347.0	-283.0
1350.0	-320.0	1350.0	-314.0	1350.0	-275.0
1353.0	-317.0	1353.0	-311.0	1353.0	-269.0
1356.0	-314.0	1356.0	-308.0	1356.0	-262.0
1359.0	-311.0	1359.0	-305.0	1359.0	-255.0
1362.0	-308.0	1362.0	-301.0	1362.0	-248.0
1365.0	-304.0	1365.0	-297.0	1365.0	-240.0
1368.0	-299.0	1368.0	-294.0	1368.0	-232.0
1371.0	-295.0	1371.0	-290.0	1371.0	-224.0
1374.0	-289.0	1374.0	-285.0	1374.0	-215.0
1377.0	-284.0	1377.0	-280.0	1377.0	-206.0
1380.0	-277.0	1380.0	-271.0	1380.0	-197.0
1383.0	-271.0	1383.0	-256.0	1383.0	-188.0
1386.0	-262.0	1386.0	-235.0	1386.0	-178.0
1389.0	-248.0	1389.0	-214.0	1389.0	-168.0
1392.0	-229.0	1392.0	-193.0	1392.0	-158.0
1395.0	-209.0	1395.0	-172.0	1395.0	-148.0
1398.0	-188.0	1398.0	-150.0	1398.0	-138.0
1401.0	-167.0	1401.0	-129.0	1401.0	-127.0
1404.0	-147.0	1404.0	-108.0	1404.0	-117.0
1407.0	-125.0	1407.0	-89.0	1407.0	-106.0
1410.0	-105.0	1410.0	-68.0	1410.0	-95.0

X0 Position [mm] Y0 Speed [mm/s]					
DTC 970 °C		DTC 860 °C		DTC 1080 °C	
1413.0	-86.0	1413.0	-48.0	1413.0	-84.0
1416.0	-67.0	1416.0	-28.0	1416.0	-72.0
1419.0	-48.0	1419.0	-9.0	1419.0	-61.0
1422.0	-28.0	1422.0	9.0	1422.0	-51.0
1425.0	-10.0	1425.0	27.0	1425.0	-41.0
1428.0	6.0	1428.0	44.0	1428.0	-31.0
1431.0	22.0	1431.0	59.0	1431.0	-23.0
1434.0	38.0	1434.0	72.0	1434.0	-14.0
1437.0	52.0	1437.0	85.0	1437.0	-6.0
1440.0	64.0	1440.0	102.0	1440.0	.0
1443.0	75.0	1443.0	121.0	1443.0	7.0
1446.0	89.0	1446.0	141.0	1446.0	14.0
1449.0	105.0	1449.0	158.0	1449.0	20.0
1452.0	122.0	1452.0	172.0	1452.0	25.0
1455.0	138.0	1455.0	184.0	1455.0	29.0
1458.0	151.0	1458.0	195.0	1458.0	31.0
1461.0	162.0	1461.0	205.0	1461.0	31.0
1464.0	173.0	1464.0	211.0	1464.0	28.0
1467.0	183.0	1467.0	215.0	1467.0	26.0
1470.0	190.0	1470.0	219.0	1470.0	26.0
1473.0	194.0	1473.0	223.0	1473.0	29.0
1476.0	198.0	1476.0	225.0	1476.0	33.0
1479.0	201.0	1479.0	226.0	1479.0	36.0
1482.0	204.0	1482.0	226.0	1482.0	39.0
1485.0	205.0	1485.0	225.0	1485.0	43.0
1488.0	205.0	1488.0	225.0	1488.0	46.0
1491.0	204.0	1491.0	224.0	1491.0	48.0
1494.0	204.0	1494.0	223.0	1494.0	50.0
1497.0	202.0	1497.0	222.0	1497.0	53.0

X0 Position [mm] Y0 Force [KN]							
Disk 970 °C Quenched		Disk 970 °C Quenched with spacer		Disk 970 °C Air cooled		Disk 1080 °C Quenched	
X0	Y0	X0	Y0	X0	Y0	X0	Y0
.0	5260.0	.0	2277.0	.0	4578.0	.0	8593.0
1.0	5260.0	1.0	2277.0	1.0	4578.0	1.0	8593.0
2.0	5260.0	2.0	2277.0	2.0	4578.0	2.0	8593.0
3.0	5260.0	3.0	2277.0	3.0	4578.0	3.0	8053.0
4.0	5260.0	4.0	2277.0	4.0	4578.0	4.0	5578.0
5.0	5260.0	5.0	2277.0	5.0	4578.0	5.0	5276.0
6.0	5260.0	6.0	2277.0	6.0	4578.0	6.0	5133.0
7.0	5260.0	7.0	2277.0	7.0	5355.0	7.0	4982.0
8.0	5173.0	8.0	2277.0	8.0	5236.0	8.0	5006.0
9.0	3721.0	9.0	2277.0	9.0	3610.0	9.0	2911.0
10.0	3483.0	10.0	2277.0	10.0	3284.0	10.0	2721.0
11.0	3380.0	11.0	2277.0	11.0	3181.0	11.0	2713.0
12.0	3173.0	12.0	2277.0	12.0	3086.0	12.0	2705.0
13.0	3038.0	13.0	2277.0	13.0	2975.0	13.0	2626.0
14.0	2927.0	14.0	2277.0	14.0	2880.0	14.0	2562.0
15.0	2864.0	15.0	2277.0	15.0	2832.0	15.0	2507.0
16.0	2840.0	16.0	2277.0	16.0	2816.0	16.0	2451.0
17.0	2832.0	17.0	2277.0	17.0	2840.0	17.0	2356.0
18.0	2832.0	18.0	2277.0	18.0	2816.0	18.0	2308.0
19.0	2824.0	19.0	2277.0	19.0	2785.0	19.0	2269.0
20.0	2785.0	20.0	2277.0	20.0	2761.0	20.0	2237.0
21.0	2777.0	21.0	2277.0	21.0	2729.0	21.0	2205.0
22.0	2761.0	22.0	2388.0	22.0	2721.0	22.0	2166.0
23.0	2745.0	23.0	2435.0	23.0	2705.0	23.0	2150.0
24.0	2745.0	24.0	2483.0	24.0	2713.0	24.0	2142.0
25.0	2745.0	25.0	2507.0	25.0	2721.0	25.0	2110.0

X0 Position [mm] Y0 Force [KN]							
Disk 970 °C Quenched		Disk 970 °C Quenched with spacer		Disk 970 °C Air cooled		Disk 1080 °C Quenched	
26.0	2753.0	26.0	2499.0	26.0	2713.0	26.0	2055.0
27.0	2681.0	27.0	2475.0	27.0	2658.0	27.0	2007.0
28.0	2618.0	28.0	2435.0	28.0	2546.0	28.0	1943.0
29.0	2570.0	29.0	2388.0	29.0	2499.0	29.0	1888.0
30.0	2515.0	30.0	2332.0	30.0	2451.0	30.0	1848.0
31.0	2467.0	31.0	2301.0	31.0	2396.0	31.0	1793.0
32.0	2412.0	32.0	2261.0	32.0	2356.0	32.0	1761.0
33.0	2372.0	33.0	2245.0	33.0	2316.0	33.0	1713.0
34.0	2285.0	34.0	2205.0	34.0	2261.0	34.0	1682.0
35.0	2245.0	35.0	2174.0	35.0	2221.0	35.0	1650.0
36.0	2221.0	36.0	2142.0	36.0	2205.0	36.0	1618.0
37.0	2182.0	37.0	2118.0	37.0	2166.0	37.0	1594.0
38.0	2150.0	38.0	2102.0	38.0	2134.0	38.0	1578.0
39.0	2134.0	39.0	2086.0	39.0	2110.0	39.0	1563.0
40.0	2110.0	40.0	2062.0	40.0	2086.0	40.0	1539.0
41.0	2086.0	41.0	2047.0	41.0	2062.0	41.0	1531.0
42.0	2074.0	42.0	2039.0	42.0	2039.0	42.0	1499.0
43.0	2062.0	43.0	2007.0	43.0	2007.0	43.0	1483.0
44.0	2039.0	44.0	1983.0	44.0	1999.0	44.0	1467.0
45.0	1991.0	45.0	1959.0	45.0	1951.0	45.0	1444.0
46.0	1975.0	46.0	1936.0	46.0	1936.0	46.0	1436.0
47.0	1951.0	47.0	1920.0	47.0	1920.0	47.0	1420.0
48.0	1912.0	48.0	1896.0	48.0	1880.0	48.0	1388.0
49.0	1856.0	49.0	1840.0	49.0	1817.0	49.0	1380.0
50.0	1809.0	50.0	1817.0	50.0	1801.0	50.0	1372.0
51.0	1769.0	51.0	1785.0	51.0	1781.0	51.0	1356.0
52.0	1745.0	52.0	1745.0	52.0	1761.0	52.0	1333.0
53.0	1701.0	53.0	1697.0	53.0	1705.0	53.0	1293.0
54.0	1658.0	54.0	1634.0	54.0	1642.0	54.0	1285.0
55.0	1618.0	55.0	1586.0	55.0	1602.0	55.0	1269.0
56.0	1555.0	56.0	1507.0	56.0	1555.0	56.0	1265.0
57.0	1483.0	57.0	1491.0	57.0	1483.0	57.0	1261.0
58.0	1420.0	58.0	1436.0	58.0	1428.0	58.0	1245.0
59.0	1340.0	59.0	1396.0	59.0	1372.0	59.0	1198.0
60.0	1313.0	60.0	1325.0	60.0	1348.0	60.0	1213.0
61.0	1285.0	61.0	1293.0	61.0	1309.0	61.0	1182.0
62.0	1245.0	62.0	1253.0	62.0	1182.0	62.0	1150.0
63.0	1087.0	63.0	1102.0	63.0	1126.0	63.0	1118.0
64.0	1118.0	64.0	1118.0	64.0	1102.0	64.0	1126.0
65.0	1007.0	65.0	1023.0	65.0	1079.0	65.0	1071.0
66.0	983.0	66.0	968.0	66.0	999.0	66.0	1039.0
67.0	960.0	67.0	904.0	67.0	952.0	67.0	1003.0
68.0	912.0	68.0	841.0	68.0	801.0	68.0	968.0
69.0	729.0	69.0	848.0	69.0	769.0	69.0	793.0
70.0	722.0	70.0	777.0	70.0	781.0	70.0	777.0
71.0	817.0	71.0	722.0	71.0	793.0	71.0	753.0
72.0	765.0	72.0	722.0	72.0	737.0	72.0	706.0
73.0	714.0	73.0	698.0	73.0	698.0	73.0	678.0
74.0	658.0	74.0	706.0	74.0	618.0	74.0	650.0
75.0	587.0	75.0	690.0	75.0	603.0	75.0	563.0
76.0	690.0	76.0	618.0	76.0	587.0	76.0	595.0
77.0	773.0	77.0	603.0	77.0	745.0	77.0	793.0
78.0	856.0	78.0	698.0	78.0	841.0	78.0	722.0
79.0	674.0	79.0	777.0	79.0	618.0	79.0	539.0
80.0	499.0	80.0	610.0	80.0	484.0	80.0	495.0
81.0	452.0	81.0	452.0	81.0	436.0	81.0	452.0
82.0	380.0	82.0	380.0	82.0	333.0	82.0	412.0
83.0	245.0	83.0	245.0	83.0	289.0	83.0	269.0
84.0	242.0	84.0	238.0	84.0	245.0	84.0	245.0
85.0	238.0	85.0	238.0	85.0	245.0	85.0	249.0
86.0	245.0	86.0	238.0	86.0	245.0	86.0	253.0
87.0	238.0	87.0	238.0	87.0	238.0	87.0	245.0
88.0	242.0	88.0	238.0	88.0	238.0	88.0	253.0

X0 Position [mm] Y0 Force [KN]							
Disk 970 °C Quenched		Disk 970 °C Quenched with spacer		Disk 970 °C Air cooled		Disk 1080 °C Quenched	
89.0	245.0	89.0	238.0	89.0	238.0	89.0	253.0
90.0	238.0	90.0	238.0	90.0	238.0	90.0	253.0
91.0	238.0	91.0	245.0	91.0	245.0	91.0	253.0
92.0	245.0	92.0	238.0	92.0	242.0	92.0	245.0
93.0	245.0	93.0	245.0	93.0	238.0	93.0	245.0
94.0	245.0	94.0	238.0	94.0	238.0	94.0	245.0
95.0	245.0	95.0	245.0	95.0	245.0	95.0	245.0
96.0	245.0	96.0	245.0	96.0	245.0	96.0	245.0
97.0	245.0	97.0	245.0	97.0	245.0	97.0	245.0
98.0	245.0	98.0	245.0	98.0	245.0	98.0	253.0
99.0	245.0	99.0	245.0	99.0	238.0	99.0	253.0

X0 Position [mm] Y0 Displacement [mm]							
Disk 970 °C Quenched		Disk 970 °C Quenched with spacer		Disk 970 °C Air cooled		Disk 1080 °C Quenched	
X0	Y0	X0	Y0	X0	Y0	X0	Y0
.0	401.0	.0	401.0	.0	401.0	.0	401.0
40.0	401.0	40.0	401.0	40.0	401.0	40.0	401.0
80.0	401.0	80.0	401.0	80.0	401.0	80.0	401.0
120.0	400.0	120.0	400.0	120.0	400.0	120.0	400.0
160.0	398.0	160.0	398.0	160.0	399.0	160.0	399.0
200.0	395.0	200.0	395.0	200.0	396.0	200.0	396.0
240.0	392.0	240.0	392.0	240.0	392.0	240.0	392.0
280.0	387.0	280.0	387.0	280.0	388.0	280.0	387.0
320.0	381.0	320.0	381.0	320.0	382.0	320.0	381.0
360.0	373.0	360.0	373.0	360.0	375.0	360.0	374.0
400.0	365.0	400.0	365.0	400.0	367.0	400.0	366.0
440.0	355.0	440.0	355.0	440.0	357.0	440.0	356.0
480.0	344.0	480.0	344.0	480.0	347.0	480.0	345.0
520.0	332.0	520.0	332.0	520.0	335.0	520.0	333.0
560.0	318.0	560.0	318.0	560.0	321.0	560.0	320.0
600.0	303.0	600.0	303.0	600.0	307.0	600.0	305.0
640.0	287.0	640.0	287.0	640.0	291.0	640.0	289.0
680.0	270.0	680.0	270.0	680.0	274.0	680.0	272.0
720.0	251.0	720.0	251.0	720.0	256.0	720.0	253.0
760.0	232.0	760.0	231.0	760.0	236.0	760.0	233.0
800.0	211.0	800.0	211.0	800.0	216.0	800.0	213.0
840.0	189.0	840.0	190.0	840.0	194.0	840.0	191.0
880.0	165.0	880.0	170.0	880.0	171.0	880.0	168.0
920.0	141.0	920.0	149.0	920.0	147.0	920.0	143.0
960.0	116.0	960.0	129.0	960.0	123.0	960.0	118.0
1000.0	91.0	1000.0	109.0	1000.0	97.0	1000.0	93.0
1040.0	66.0	1040.0	89.0	1040.0	72.0	1040.0	68.0
1080.0	43.0	1080.0	70.0	1080.0	49.0	1080.0	45.0
1120.0	24.0	1120.0	52.0	1120.0	29.0	1120.0	24.0
1160.0	12.0	1160.0	37.0	1160.0	14.0	1160.0	8.0
1200.0	7.0	1200.0	26.0	1200.0	7.0	1200.0	3.0
1240.0	9.0	1240.0	21.0	1240.0	8.0	1240.0	7.0
1280.0	13.0	1280.0	21.0	1280.0	11.0	1280.0	15.0
1320.0	18.0	1320.0	22.0	1320.0	16.0	1320.0	23.0
1360.0	22.0	1360.0	23.0	1360.0	20.0	1360.0	32.0
1400.0	28.0	1400.0	24.0	1400.0	25.0	1400.0	40.0
1440.0	33.0	1440.0	26.0	1440.0	31.0	1440.0	50.0
1480.0	40.0	1480.0	29.0	1480.0	38.0	1480.0	61.0
1520.0	47.0	1520.0	32.0	1520.0	45.0	1520.0	72.0
1560.0	55.0	1560.0	36.0	1560.0	52.0	1560.0	84.0

X0 Position [mm] Y0 Displacement [mm]							
Disk 970 °C Quenched		Disk 970 °C Quenched with spacer		Disk 970 °C Air cooled		Disk 1080 °C Quenched	
1600.0	64.0	1600.0	40.0	1600.0	61.0	1600.0	97.0
1640.0	73.0	1640.0	45.0	1640.0	70.0	1640.0	111.0
1680.0	83.0	1680.0	51.0	1680.0	80.0	1680.0	125.0
1720.0	94.0	1720.0	57.0	1720.0	91.0	1720.0	140.0
1760.0	105.0	1760.0	64.0	1760.0	103.0	1760.0	156.0
1800.0	118.0	1800.0	72.0	1800.0	115.0	1800.0	173.0
1840.0	131.0	1840.0	81.0	1840.0	128.0	1840.0	190.0
1880.0	145.0	1880.0	90.0	1880.0	142.0	1880.0	208.0
1920.0	160.0	1920.0	100.0	1920.0	157.0	1920.0	227.0
1960.0	176.0	1960.0	111.0	1960.0	172.0	1960.0	247.0
2000.0	192.0	2000.0	123.0	2000.0	188.0	2000.0	267.0
2040.0	209.0	2040.0	135.0	2040.0	205.0	2040.0	285.0
2080.0	227.0	2080.0	148.0	2080.0	223.0	2080.0	302.0
2120.0	246.0	2120.0	162.0	2120.0	242.0	2120.0	317.0
2160.0	265.0	2160.0	177.0	2160.0	261.0	2160.0	332.0
2200.0	283.0	2200.0	193.0	2200.0	280.0	2200.0	345.0
2240.0	301.0	2240.0	209.0	2240.0	297.0	2240.0	357.0
2280.0	317.0	2280.0	226.0	2280.0	314.0	2280.0	368.0
2320.0	331.0	2320.0	244.0	2320.0	329.0	2320.0	378.0
2360.0	345.0	2360.0	263.0	2360.0	343.0	2360.0	387.0
2400.0	358.0	2400.0	281.0	2400.0	355.0	2400.0	394.0
2440.0	369.0	2440.0	299.0	2440.0	367.0	2440.0	400.0
2480.0	379.0	2480.0	315.0	2480.0	377.0	2480.0	401.0
2520.0	388.0	2520.0	330.0	2520.0	386.0	2520.0	401.0
2560.0	395.0	2560.0	344.0	2560.0	394.0	2560.0	401.0
2600.0	400.0	2600.0	357.0	2600.0	400.0	2600.0	401.0
2640.0	401.0	2640.0	368.0	2640.0	401.0	2640.0	401.0
2680.0	401.0	2680.0	379.0	2680.0	401.0	2680.0	401.0
2720.0	401.0	2720.0	388.0	2720.0	401.0	2720.0	401.0
2760.0	401.0	2760.0	396.0	2760.0	401.0	2760.0	401.0
2800.0	401.0	2800.0	400.0	2800.0	401.0	2800.0	401.0
2840.0	401.0	2840.0	401.0	2840.0	401.0	2840.0	401.0
2880.0	401.0	2880.0	401.0	2880.0	401.0	2880.0	401.0
2920.0	401.0	2920.0	401.0	2920.0	401.0	2920.0	401.0
2960.0	401.0	2960.0	401.0	2960.0	401.0	2960.0	401.0
3000.0	401.0	3000.0	401.0	3000.0	401.0	3000.0	401.0
3040.0	401.0	3040.0	401.0	3040.0	401.0	3040.0	401.0
3080.0	401.0	3080.0	401.0	3080.0	401.0	3080.0	401.0
3120.0	401.0	3120.0	401.0	3120.0	401.0	3120.0	401.0
3160.0	401.0	3160.0	401.0	3160.0	401.0	3160.0	401.0
3200.0	401.0	3200.0	401.0	3200.0	401.0	3200.0	401.0
3240.0	401.0	3240.0	401.0	3240.0	401.0	3240.0	401.0
3280.0	401.0	3280.0	401.0	3280.0	401.0	3280.0	401.0
3320.0	401.0	3320.0	401.0	3320.0	401.0	3320.0	401.0
3360.0	401.0	3360.0	401.0	3360.0	401.0	3360.0	401.0
3400.0	401.0	3400.0	401.0	3400.0	401.0	3400.0	401.0
3440.0	401.0	3440.0	401.0	3440.0	401.0	3440.0	401.0
3480.0	401.0	3480.0	401.0	3480.0	401.0	3480.0	401.0
3520.0	401.0	3520.0	401.0	3520.0	401.0	3520.0	401.0
3560.0	401.0	3560.0	401.0	3560.0	401.0	3560.0	401.0
3600.0	401.0	3600.0	401.0	3600.0	401.0	3600.0	401.0
3640.0	401.0	3640.0	401.0	3640.0	401.0	3640.0	401.0
3680.0	401.0	3680.0	401.0	3680.0	401.0	3680.0	401.0
3720.0	401.0	3720.0	401.0	3720.0	401.0	3720.0	401.0
3760.0	401.0	3760.0	401.0	3760.0	401.0	3760.0	401.0
3800.0	401.0	3800.0	401.0	3800.0	401.0	3800.0	401.0
3840.0	401.0	3840.0	401.0	3840.0	401.0	3840.0	401.0
3880.0	401.0	3880.0	401.0	3880.0	401.0	3880.0	401.0
3920.0	401.0	3920.0	401.0	3920.0	401.0	3920.0	401.0
3960.0	401.0	3960.0	401.0	3960.0	401.0	3960.0	401.0

X0 Position [mm] Y0 Velocity [mm/s]							
Disk 970 °C Quenched		Disk 970 °C Quenched with spacer		Disk 970 °C Air cooled		Disk 1080 °C Quenched	
X0	Y0	X0	Y0	X0	Y0	X0	Y0
.0	.0	.0	.0	.0	.0	.0	.0
40.0	.0	40.0	.0	40.0	.0	40.0	.0
80.0	-3.0	80.0	-3.0	80.0	-1.0	80.0	-2.0
120.0	-21.0	120.0	-22.0	120.0	-17.0	120.0	-20.0
160.0	-44.0	160.0	-45.0	160.0	-39.0	160.0	-43.0
200.0	-69.0	200.0	-70.0	200.0	-64.0	200.0	-67.0
240.0	-95.0	240.0	-96.0	240.0	-89.0	240.0	-93.0
280.0	-122.0	280.0	-123.0	280.0	-116.0	280.0	-120.0
320.0	-150.0	320.0	-151.0	320.0	-144.0	320.0	-148.0
360.0	-179.0	360.0	-180.0	360.0	-173.0	360.0	-177.0
400.0	-210.0	400.0	-211.0	400.0	-203.0	400.0	-208.0
440.0	-242.0	440.0	-243.0	440.0	-235.0	440.0	-239.0
480.0	-275.0	480.0	-275.0	480.0	-267.0	480.0	-272.0
520.0	-308.0	520.0	-308.0	520.0	-300.0	520.0	-304.0
560.0	-339.0	560.0	-340.0	560.0	-331.0	560.0	-336.0
600.0	-370.0	600.0	-371.0	600.0	-363.0	600.0	-368.0
640.0	-399.0	640.0	-400.0	640.0	-392.0	640.0	-398.0
680.0	-431.0	680.0	-432.0	680.0	-422.0	680.0	-429.0
720.0	-461.0	720.0	-462.0	720.0	-452.0	720.0	-459.0
760.0	-492.0	760.0	-492.0	760.0	-482.0	760.0	-489.0
800.0	-521.0	800.0	-511.0	800.0	-511.0	800.0	-519.0
840.0	-550.0	840.0	-516.0	840.0	-540.0	840.0	-548.0
880.0	-579.0	880.0	-511.0	880.0	-569.0	880.0	-577.0
920.0	-607.0	920.0	-506.0	920.0	-598.0	920.0	-605.0
960.0	-626.0	960.0	-502.0	960.0	-622.0	960.0	-626.0
1000.0	-632.0	1000.0	-500.0	1000.0	-631.0	1000.0	-632.0
1040.0	-612.0	1040.0	-503.0	1040.0	-618.0	1040.0	-615.0
1080.0	-576.0	1080.0	-483.0	1080.0	-591.0	1080.0	-590.0
1120.0	-472.0	1120.0	-457.0	1120.0	-506.0	1120.0	-520.0
1160.0	-323.0	1160.0	-376.0	1160.0	-370.0	1160.0	-400.0
1200.0	-122.0	1200.0	-261.0	1200.0	-185.0	1200.0	-150.0
1240.0	44.0	1240.0	-129.0	1240.0	12.0	1240.0	103.0
1280.0	99.0	1280.0	-18.0	1280.0	85.0	1280.0	194.0
1320.0	108.0	1320.0	17.0	1320.0	106.0	1320.0	199.0
1360.0	116.0	1360.0	31.0	1360.0	114.0	1360.0	211.0
1400.0	130.0	1400.0	39.0	1400.0	128.0	1400.0	227.0
1440.0	146.0	1440.0	51.0	1440.0	143.0	1440.0	244.0
1480.0	161.0	1480.0	65.0	1480.0	159.0	1480.0	262.0
1520.0	177.0	1520.0	79.0	1520.0	175.0	1520.0	280.0
1560.0	195.0	1560.0	93.0	1560.0	193.0	1560.0	299.0
1600.0	213.0	1600.0	108.0	1600.0	211.0	1600.0	318.0
1640.0	231.0	1640.0	123.0	1640.0	229.0	1640.0	338.0
1680.0	251.0	1680.0	140.0	1680.0	248.0	1680.0	357.0
1720.0	271.0	1720.0	157.0	1720.0	269.0	1720.0	378.0
1760.0	291.0	1760.0	176.0	1760.0	288.0	1760.0	397.0
1800.0	308.0	1800.0	194.0	1800.0	307.0	1800.0	416.0
1840.0	330.0	1840.0	212.0	1840.0	327.0	1840.0	436.0
1880.0	349.0	1880.0	232.0	1880.0	347.0	1880.0	456.0
1920.0	369.0	1920.0	251.0	1920.0	366.0	1920.0	475.0
1960.0	388.0	1960.0	270.0	1960.0	386.0	1960.0	494.0
2000.0	408.0	2000.0	288.0	2000.0	405.0	2000.0	482.0
2040.0	427.0	2040.0	311.0	2040.0	425.0	2040.0	454.0
2080.0	447.0	2080.0	329.0	2080.0	445.0	2080.0	423.0
2120.0	467.0	2120.0	348.0	2120.0	464.0	2120.0	394.0
2160.0	480.0	2160.0	368.0	2160.0	481.0	2160.0	364.0
2200.0	461.0	2200.0	388.0	2200.0	467.0	2200.0	335.0
2240.0	431.0	2240.0	407.0	2240.0	438.0	2240.0	305.0
2280.0	402.0	2280.0	427.0	2280.0	408.0	2280.0	275.0
2320.0	372.0	2320.0	447.0	2320.0	379.0	2320.0	245.0
2360.0	343.0	2360.0	466.0	2360.0	349.0	2360.0	214.0
2400.0	313.0	2400.0	465.0	2400.0	319.0	2400.0	184.0
2440.0	283.0	2440.0	438.0	2440.0	289.0	2440.0	136.0

X0 Position [mm] Y0 Velocity [mm/s]			
Disk 970 °C Quenched	Disk 970 °C Quenched with spacer	Disk 970 °C Air cooled	Disk 1080 °C Quenched
2480.0 253.0	2480.0 408.0	2480.0 259.0	2480.0 44.0
2520.0 222.0	2520.0 378.0	2520.0 229.0	2520.0 .0
2560.0 192.0	2560.0 349.0	2560.0 199.0	2560.0 .0
2600.0 120.0	2600.0 319.0	2600.0 135.0	2600.0 .0
2640.0 25.0	2640.0 289.0	2640.0 37.0	2640.0 .0
2680.0 .0	2680.0 259.0	2680.0 .0	2680.0 .0
2720.0 .0	2720.0 229.0	2720.0 .0	2720.0 .0
2760.0 .0	2760.0 196.0	2760.0 .0	2760.0 .0
2800.0 .0	2800.0 115.0	2800.0 .0	2800.0 .0
2840.0 .0	2840.0 20.0	2840.0 .0	2840.0 .0
2880.0 .0	2880.0 .0	2880.0 .0	2880.0 .0
2920.0 .0	2920.0 .0	2920.0 .0	2920.0 .0
2960.0 .0	2960.0 .0	2960.0 .0	2960.0 .0
3000.0 .0	3000.0 .0	3000.0 .0	3000.0 .0
3040.0 .0	3040.0 .0	3040.0 .0	3040.0 .0
3080.0 .0	3080.0 .0	3080.0 .0	3080.0 .0
3120.0 .0	3120.0 .0	3120.0 .0	3120.0 .0
3160.0 .0	3160.0 .0	3160.0 .0	3160.0 .0
3200.0 .0	3200.0 .0	3200.0 .0	3200.0 .0
3240.0 .0	3240.0 .0	3240.0 .0	3240.0 .0
3280.0 .0	3280.0 .0	3280.0 .0	3280.0 .0
3320.0 .0	3320.0 .0	3320.0 .0	3320.0 .0
3360.0 .0	3360.0 .0	3360.0 .0	3360.0 .0
3400.0 .0	3400.0 .0	3400.0 .0	3400.0 .0
3440.0 .0	3440.0 .0	3440.0 .0	3440.0 .0
3480.0 .0	3480.0 .0	3480.0 .0	3480.0 .0
3520.0 .0	3520.0 .0	3520.0 .0	3520.0 .0
3560.0 .0	3560.0 .0	3560.0 .0	3560.0 .0
3600.0 .0	3600.0 .0	3600.0 .0	3600.0 .0
3640.0 .0	3640.0 .0	3640.0 .0	3640.0 .0
3680.0 .0	3680.0 .0	3680.0 .0	3680.0 .0
3720.0 .0	3720.0 .0	3720.0 .0	3720.0 .0
3760.0 .0	3760.0 .0	3760.0 .0	3760.0 .0
3800.0 .0	3800.0 .0	3800.0 .0	3800.0 .0
3840.0 .0	3840.0 .0	3840.0 .0	3840.0 .0
3880.0 .0	3880.0 .0	3880.0 .0	3880.0 .0
3920.0 .0	3920.0 .0	3920.0 .0	3920.0 .0
3960.0 .0	3960.0 .0	3960.0 .0	3960.0 .0

3.3.3 Raw Data from Hydraulic Press

Top Die [mm], Bottom Die [mm], Position [mm], Speed [mm/s], Load [Tons]						
DTC 1080 °C	DTC 970 °C	DTC 915 °C				
397.0,397.3,169.0, 0.0, -1	397.2,397.3,194.0, 0.0, -1	397.2	397.8	180.8	0	-1
397.0,397.3,148.8, 0.0, -0	397.2,397.3,174.0, 0.0, -0	397.2	397.8	158.4	0	0
397.0,397.3,122.1, 0.0, -0	397.2,397.3,152.9, 0.0, -1	397.2	397.8	135.4	0	0
397.0,397.3, 99.9, 0.0, -0	397.2,397.3,131.5, 0.0, -0	397.2	397.8	112	0	0
397.0,397.3, 80.1, 0.0, -0	397.2,397.3,108.8, 0.0, -1	397.2	397.8	93.9	0	0
397.0,397.3, 62.5, 5.2, -0	397.2,397.3, 89.1, 0.0, -0	397.2	397.8	69.6	0	0
397.0,397.3, 62.6, 11.0, -1	397.2,397.3, 66.8, 5.0, -0	397.1	397.8	63.8	5.2	0
397.0,397.3, 64.7, 11.3, -0	397.2,397.3, 69.7, 10.5, -1	397.1	397.8	64.2	7.9	0
397.0,397.3, 64.8, 10.6, -0	397.2,397.3, 69.3, 12.1, -1	397.1	397.8	62.5	8.2	0
397.0,397.3, 64.9, 11.0, -0	397.2,397.3, 69.4, 11.4, -0	397.1	397.8	62.6	8.2	0
397.0,397.3, 64.5, 10.4, -0	397.2,397.3, 69.0, 11.0, 1	397.1	397.8	63.1	8.3	1
397.0,397.3, 64.6, 9.8, 0	397.2,397.3, 68.7, 10.2, -1	397.1	397.8	63	8	-1

Top Die [mm], Bottom Die [mm], Position [mm], Speed [mm/s], Load [Tons]		
DTC 1080 °C	DTC 970 °C	DTC 915 °C
397.0,397.3, 64.4, 9.3, 0	397.2,397.3, 68.7, 9.6, -1	397.1 397.8 63 7.4 0
397.0,397.3, 64.2, 9.3, 1	397.2,397.3, 68.5, 9.1, 1	397.1 397.8 62.8 7 1
397.0,397.3, 64.0, 8.9, 1	397.2,397.3, 68.4, 8.6, 1	397.1 397.8 62.6 6.6 1
397.0,397.3, 63.8, 8.5, 1	397.2,397.3, 68.2, 8.4, 1	397.1 397.8 62.5 6.2 1
397.0,397.3, 63.6, 8.7, 1	397.2,397.3, 68.0, 8.6, 1	397.1 397.8 62.3 6.2 1
397.0,397.3, 63.5, 2.5, 1	397.2,397.3, 67.8, 2.7, 1	397.1 397.8 62.1 6.4 1
397.0,397.3, 63.2, 1.8, 2	397.2,397.3, 67.6, 2.7, 1	397.1 397.8 61.9 3.4 1
397.0,397.3, 63.1, 2.1, 2	397.2,397.3, 67.4, 0.8, 1	397.1 397.8 61.7 2.7 1
397.0,397.3, 62.9, 1.4, 2	397.2,397.3, 67.2, 1.1, 2	397.1 397.8 61.5 2.2 2
397.0,397.3, 62.7, 1.6, 2	397.2,397.3, 67.0, 1.1, 2	397.1 397.8 61.3 1.8 2
397.0,397.3, 62.5, 1.8, 2	397.2,397.3, 66.9, 1.6, 2	397.1 397.8 61.1 1.7 2
396.9,397.2, 62.3, 1.8, 2	397.2,397.3, 66.6, 1.7, 2	397.1 397.8 60.9 1.9 2
396.9,397.2, 62.1, 1.9, 2	397.2,397.3, 66.5, 1.9, 2	397.1 397.8 60.7 1.9 2
396.9,397.2, 61.9, 1.9, 2	397.2,397.3, 66.3, 2.0, 2	397.1 397.8 60.6 1.9 2
396.9,397.2, 61.7, 1.9, 3	397.2,397.3, 66.1, 1.9, 2	397.1 397.8 60.4 1.9 2
396.9,397.2, 61.6, 1.9, 3	397.2,397.3, 65.9, 1.9, 2	397.1 397.8 60.2 1.9 2
396.9,397.2, 61.3, 1.9, 3	397.2,397.3, 65.7, 1.9, 3	397.1 397.8 59.9 1.8 3
396.9,397.2, 61.2, 1.9, 3	397.2,397.3, 65.5, 1.9, 3	397.1 397.8 59.8 1.9 3
396.9,397.2, 61.0, 1.9, 3	397.2,397.2, 65.3, 1.9, 3	397.1 397.8 59.6 1.9 3
396.9,397.2, 60.8, 1.9, 3	397.2,397.2, 65.1, 2.0, 3	397.1 397.8 59.4 1.9 3
396.9,397.2, 60.6, 1.9, 3	397.2,397.2, 64.9, 1.9, 3	397.1 397.8 59.2 1.9 3
396.9,397.2, 60.4, 1.9, 3	397.2,397.2, 64.7, 1.9, 3	397.1 397.8 59 1.9 3
396.9,397.2, 60.2, 1.9, 3	397.2,397.2, 64.5, 2.0, 3	397.1 397.8 58.8 1.9 3
396.9,397.2, 60.0, 1.9, 3	397.2,397.2, 64.3, 1.8, 3	397.1 397.8 58.6 1.9 3
396.9,397.2, 59.8, 1.9, 3	397.2,397.2, 64.1, 1.9, 3	397.1 397.8 58.4 1.9 3
396.9,397.2, 59.6, 1.9, 3	397.2,397.2, 63.9, 1.9, 3	397.1 397.8 58.3 1.9 3
396.9,397.2, 59.4, 1.9, 3	397.2,397.2, 63.7, 1.9, 3	397.1 397.8 58 2 3
396.9,397.2, 59.2, 1.9, 3	397.2,397.2, 63.5, 2.0, 3	397.1 397.8 57.8 1.9 3
396.9,397.2, 59.0, 1.9, 3	397.2,397.2, 63.3, 2.0, 3	397.1 397.8 57.6 1.9 3
396.9,397.2, 58.8, 1.9, 3	397.2,397.2, 63.2, 1.8, 3	397.1 397.8 57.4 1.9 3
396.9,397.2, 58.6, 2.0, 3	397.2,397.2, 62.9, 2.0, 3	397.1 397.8 57.2 1.9 3
396.9,397.2, 58.4, 1.9, 3	397.2,397.2, 62.7, 2.0, 3	397.1 397.8 57 1.9 3
396.9,397.2, 58.2, 2.0, 3	397.2,397.2, 62.5, 1.9, 3	397.1 397.8 56.8 1.9 3
396.9,397.2, 58.0, 2.0, 3	397.2,397.2, 62.3, 1.9, 3	397.1 397.8 56.6 2 3
396.9,397.2, 57.8, 2.0, 3	397.2,397.2, 62.1, 2.0, 3	397.1 397.8 56.4 2 3
396.9,397.2, 57.6, 2.0, 3	397.2,397.2, 62.0, 1.9, 3	397.1 397.8 56.2 2 3
396.9,397.2, 57.4, 2.0, 3	397.2,397.2, 61.7, 1.9, 3	397.1 397.8 56 2 3
396.9,397.2, 57.2, 1.9, 3	397.2,397.2, 61.5, 2.0, 3	397.1 397.8 55.8 1.9 3
396.9,397.2, 57.0, 1.9, 3	397.2,397.2, 61.3, 1.9, 3	397.1 397.8 55.6 2 3
396.9,397.2, 56.8, 1.9, 3	397.2,397.2, 61.1, 1.9, 3	397.1 397.8 55.4 2 3
396.9,397.2, 56.6, 2.0, 3	397.2,397.2, 60.9, 2.1, 3	397.1 397.8 55.2 2 3
396.9,397.2, 56.4, 1.9, 3	397.2,397.2, 60.8, 2.1, 3	397.1 397.8 55 2 3
396.9,397.2, 56.2, 2.0, 3	397.2,397.2, 60.6, 2.0, 3	397.1 397.8 54.8 2 3
396.9,397.2, 56.0, 2.0, 3	397.2,397.2, 60.3, 2.0, 3	397.1 397.8 54.6 1.9 3
396.9,397.2, 55.8, 2.0, 3	397.2,397.2, 60.1, 2.0, 3	397.1 397.8 54.4 2 3
396.9,397.2, 55.6, 2.0, 3	397.2,397.2, 59.9, 2.0, 3	397.1 397.8 54.3 1.9 3
396.9,397.2, 55.4, 2.0, 3	397.2,397.2, 59.7, 2.0, 3	397.1 397.8 54.1 1.9 3
396.9,397.2, 55.2, 1.9, 3	397.2,397.2, 59.6, 2.0, 3	397.1 397.8 53.9 1.9 3
396.9,397.2, 55.0, 1.9, 3	397.2,397.2, 59.3, 1.9, 3	397.1 397.8 53.7 1.9 3
396.9,397.2, 54.8, 1.9, 3	397.2,397.2, 59.2, 2.0, 3	397.1 397.8 53.4 1.9 3
396.9,397.2, 54.6, 2.0, 3	397.2,397.2, 58.9, 2.0, 3	397.1 397.8 53.2 1.9 3
396.9,397.2, 54.4, 2.0, 3	397.2,397.2, 58.7, 1.9, 3	397.1 397.8 53 1.9 5
396.9,397.2, 54.2, 2.0, 3	397.2,397.2, 58.5, 1.9, 3	397.1 397.8 52.9 1.9 8
396.9,397.2, 54.1, 1.9, 3	397.2,397.2, 58.3, 2.0, 3	397.1 397.8 52.8 1.9 10
396.9,397.2, 53.8, 1.9, 3	397.2,397.2, 58.1, 2.0, 3	397.1 397.8 52.6 1.8 16
396.9,397.2, 53.6, 2.0, 3	397.2,397.2, 57.9, 2.0, 3	397.1 397.8 52.5 1.7 22
396.9,397.2, 53.4, 2.0, 4	397.2,397.2, 57.7, 2.0, 3	397.1 397.8 52.3 1.8 25
396.9,397.2, 53.3, 2.0, 5	397.2,397.2, 57.5, 2.0, 3	397.1 397.8 52.1 1.7 28
396.9,397.2, 53.1, 2.0, 8	397.2,397.2, 57.3, 2.0, 3	397.1 397.8 51.9 1.7 30
396.9,397.2, 52.9, 1.9, 13	397.2,397.2, 57.1, 2.0, 3	397.1 397.8 51.7 1.7 31
396.9,397.2, 52.8, 1.9, 18	397.2,397.2, 56.9, 2.0, 3	397.1 397.8 51.5 1.7 32
396.9,397.2, 52.6, 1.7, 22	397.2,397.2, 56.7, 2.0, 3	397.1 397.8 51.3 1.7 33
396.9,397.2, 52.5, 1.7, 24	397.2,397.2, 56.5, 2.1, 3	397.1 397.8 51.1 1.7 34
396.9,397.2, 52.2, 1.8, 25	397.2,397.2, 56.3, 2.1, 3	397.1 397.8 50.9 1.7 35
396.9,397.2, 52.0, 1.8, 25	397.2,397.2, 56.1, 2.0, 3	397.1 397.8 50.7 1.8 36
396.9,397.2, 51.8, 1.8, 26	397.2,397.2, 55.9, 2.0, 3	397.1 397.8 50.5 1.9 37
396.9,397.2, 51.6, 1.8, 26	397.2,397.2, 55.8, 2.0, 3	397.1 397.8 50.3 2 38
396.9,397.2, 51.4, 1.8, 26	397.2,397.2, 55.6, 2.0, 3	397.1 397.8 50.1 1.9 39

Top Die [mm], Bottom Die [mm], Position [mm], Speed [mm/s], Load [Tons]		
DTC 1080 °C	DTC 970 °C	DTC 915 °C
396.9,397.2, 51.2, 1.9, 26	397.2,397.2, 55.3, 2.0, 3	397.1 397.8 49.8 2 40
396.9,397.2, 51.0, 1.9, 27	397.2,397.2, 55.1, 2.0, 3	397.1 397.8 49.7 2 41
396.9,397.2, 50.8, 1.9, 27	397.2,397.2, 54.9, 1.9, 3	397.1 397.8 49.4 2 42
396.9,397.2, 50.6, 1.9, 27	397.2,397.2, 54.8, 1.9, 3	397.1 397.8 49.2 2 43
396.9,397.2, 50.4, 2.0, 27	397.2,397.2, 54.6, 1.9, 3	397.1 397.8 49 2 44
396.9,397.2, 50.2, 2.0, 28	397.2,397.2, 54.4, 1.9, 3	397.1 397.8 48.9 2 45
396.9,397.2, 50.0, 2.0, 28	397.2,397.2, 54.2, 2.0, 3	397.1 397.8 48.6 2 46
396.9,397.2, 49.8, 2.1, 28	397.2,397.2, 54.0, 2.0, 3	397.1 397.8 48.4 2 47
396.9,397.2, 49.6, 2.0, 29	397.2,397.2, 53.8, 2.0, 3	397.1 397.8 48.2 2 48
396.9,397.2, 49.4, 2.1, 29	397.2,397.2, 53.6, 2.0, 3	397.1 397.8 48 2 49
396.9,397.2, 49.2, 2.1, 29	397.2,397.2, 53.4, 2.0, 3	397.1 397.8 47.8 2 50
396.9,397.2, 49.0, 2.0, 29	397.2,397.2, 53.2, 2.0, 5	397.1 397.8 47.6 2 51
396.9,397.2, 48.8, 2.0, 30	397.2,397.2, 53.0, 1.9, 8	397.1 397.8 47.4 1.9 52
396.9,397.2, 48.6, 2.0, 30	397.2,397.2, 52.9, 1.9, 12	397.1 397.8 47.2 2 53
396.9,397.2, 48.4, 2.0, 30	397.2,397.2, 52.8, 1.8, 17	397.1 397.7 47 2 54
396.9,397.2, 48.1, 2.0, 31	397.2,397.2, 52.7, 1.8, 22	397.1 397.7 46.9 2 55
396.9,397.2, 47.9, 2.0, 31	397.2,397.2, 52.5, 1.6, 26	397.1 397.7 46.6 2 56
396.9,397.2, 47.8, 2.1, 31	397.2,397.2, 52.3, 1.6, 28	397.1 397.7 46.4 2 57
396.9,397.2, 47.6, 2.0, 31	397.2,397.2, 52.1, 1.6, 30	397.1 397.7 46.2 1.9 58
396.9,397.2, 47.4, 2.1, 32	397.2,397.2, 51.9, 1.6, 31	397.1 397.7 46 2 59
396.9,397.2, 47.1, 2.0, 32	397.2,397.2, 51.7, 1.6, 32	397.1 397.7 45.8 2 60
396.9,397.2, 47.0, 2.0, 32	397.2,397.2, 51.5, 1.6, 34	397.1 397.7 45.6 2 60
396.9,397.2, 46.8, 2.0, 32	397.2,397.2, 51.3, 1.8, 35	397.1 397.7 45.4 2 61
396.9,397.2, 46.6, 2.0, 32	397.2,397.2, 51.1, 1.8, 36	397.1 397.7 45.2 2 62
396.9,397.2, 46.3, 2.0, 33	397.2,397.2, 50.9, 1.9, 37	397.1 397.7 45 2 63
396.9,397.2, 46.1, 2.0, 33	397.2,397.2, 50.7, 1.9, 38	397.1 397.7 44.8 2 64
396.9,397.2, 46.0, 2.0, 33	397.2,397.2, 50.5, 1.9, 39	397.1 397.7 44.6 2 65
396.9,397.2, 45.8, 2.0, 33	397.2,397.2, 50.3, 1.9, 40	397.1 397.7 44.4 2 66
396.9,397.2, 45.5, 2.0, 34	397.2,397.2, 50.1, 2.0, 41	397.1 397.7 44.2 2 66
396.9,397.2, 45.3, 2.0, 34	397.2,397.2, 49.9, 2.0, 42	397.1 397.7 44.1 2 67
396.9,397.2, 45.1, 2.0, 34	397.2,397.2, 49.7, 2.0, 43	397.1 397.7 43.9 1.8 68
396.9,397.2, 44.9, 2.0, 34	397.2,397.2, 49.5, 2.1, 44	397.1 397.7 43.7 1.8 69
396.9,397.2, 44.7, 2.0, 35	397.2,397.2, 49.3, 2.1, 44	397.1 397.7 43.5 1.8 70
396.9,397.2, 44.6, 2.0, 35	397.2,397.2, 49.1, 2.0, 45	397.1 397.7 43.3 1.9 70
396.9,397.2, 44.3, 2.0, 35	397.2,397.2, 48.9, 1.9, 46	397.1 397.7 43.1 1.9 71
396.9,397.2, 44.2, 2.0, 36	397.2,397.2, 48.7, 1.9, 46	397.1 397.7 42.9 1.9 72
396.9,397.2, 44.0, 1.9, 36	397.2,397.2, 48.5, 2.0, 47	397.1 397.7 42.7 1.8 73
396.9,397.2, 43.9, 1.9, 36	397.2,397.2, 48.3, 2.0, 48	397.1 397.7 42.6 1.8 74
396.9,397.2, 43.7, 1.9, 36	397.1,397.2, 48.1, 2.0, 49	397.1 397.7 42.3 1.9 75
396.9,397.2, 43.4, 1.9, 37	397.1,397.2, 47.9, 2.0, 49	397.1 397.7 42.1 1.9 75
396.9,397.2, 43.2, 1.9, 37	397.1,397.2, 47.7, 2.0, 50	397.1 397.7 41.9 2 76
396.9,397.2, 43.1, 1.9, 37	397.1,397.2, 47.4, 2.0, 50	397.1 397.7 41.7 2 77
396.9,397.2, 42.8, 1.9, 38	397.1,397.2, 47.3, 2.0, 51	397.1 397.7 41.5 2 78
396.9,397.2, 42.6, 1.9, 38	397.1,397.2, 47.1, 2.0, 52	397.1 397.7 41.3 2 79
396.9,397.2, 42.4, 1.9, 38	397.1,397.2, 46.9, 2.0, 52	397.1 397.7 41.1 2 80
396.9,397.2, 42.2, 1.9, 39	397.1,397.2, 46.6, 2.0, 53	397.1 397.7 40.9 1.9 81
396.9,397.2, 42.0, 2.0, 39	397.1,397.2, 46.4, 2.1, 53	397.1 397.7 40.7 2 81
396.9,397.2, 41.8, 2.0, 39	397.1,397.2, 46.2, 2.1, 54	397.1 397.7 40.5 2.1 82
396.9,397.2, 41.6, 2.1, 40	397.1,397.2, 46.0, 2.0, 54	397.1 397.7 40.3 2.1 83
396.9,397.2, 41.5, 1.9, 40	397.1,397.2, 45.8, 2.0, 55	397.1 397.7 40.1 2 84
396.9,397.2, 41.2, 1.9, 40	397.1,397.2, 45.6, 2.0, 56	397.1 397.7 39.9 2 85
396.9,397.2, 41.0, 2.0, 41	397.1,397.2, 45.4, 2.0, 56	397.1 397.7 39.7 2 86
396.9,397.2, 40.8, 2.0, 41	397.1,397.2, 45.2, 2.1, 57	397.1 397.7 39.5 2 87
396.9,397.2, 40.6, 2.0, 42	397.1,397.2, 45.0, 2.0, 57	397.1 397.7 39.3 2.1 88
396.9,397.2, 40.4, 2.0, 42	397.1,397.2, 44.8, 2.1, 58	397.1 397.7 39.1 2 89
396.9,397.2, 40.3, 2.0, 42	397.1,397.2, 44.6, 2.1, 58	397.1 397.7 38.9 2 90
396.9,397.2, 40.1, 2.0, 43	397.1,397.2, 44.4, 2.1, 59	397.1 397.7 38.7 1.9 91
396.9,397.2, 39.8, 2.0, 43	397.1,397.2, 44.2, 2.0, 59	397.1 397.7 38.5 1.9 92
396.9,397.2, 39.6, 2.0, 44	397.1,397.2, 44.1, 2.0, 60	397.1 397.7 38.3 1.9 93
396.9,397.2, 39.4, 1.9, 44	397.1,397.2, 43.9, 1.9, 60	397.1 397.6 38.1 2 94
396.9,397.2, 39.2, 2.0, 45	397.1,397.2, 43.7, 1.9, 61	397.1 397.6 37.9 1.9 95
396.9,397.2, 39.0, 2.0, 45	397.1,397.2, 43.5, 1.9, 62	397.1 397.6 37.7 1.9 96
396.9,397.2, 38.9, 2.0, 46	397.1,397.2, 43.3, 2.0, 62	397.1 397.6 37.5 2 97
396.9,397.2, 38.6, 2.0, 46	397.1,397.1, 43.1, 1.9, 63	397.1 397.6 37.3 2 98
396.9,397.2, 38.5, 2.0, 47	397.1,397.1, 42.9, 1.9, 63	397.1 397.6 37.1 1.9 99
396.9,397.2, 38.2, 2.0, 48	397.1,397.1, 42.7, 1.9, 64	397.1 397.6 36.8 2 101
396.9,397.2, 38.1, 2.0, 48	397.1,397.1, 42.5, 1.9, 64	397.1 397.6 36.6 1.9 102
396.9,397.2, 37.9, 2.0, 49	397.1,397.1, 42.3, 1.9, 65	397.1 397.6 36.5 2 103

Top Die [mm], Bottom Die [mm], Position [mm], Speed [mm/s], Load [Tons]						
DTC 1080 °C	DTC 970 °C	DTC 915 °C				
396.9,397.2, 37.7, 2.0, 50	397.1,397.1, 42.1, 1.9, 66	397.1	397.6	36.3	2	104
396.9,397.2, 37.4, 2.0, 50	397.1,397.1, 41.9, 2.0, 66	397.1	397.6	36.1	1.9	106
396.9,397.2, 37.2, 2.1, 51	397.1,397.1, 41.6, 2.0, 67	397.1	397.6	35.9	1.9	106
396.9,397.2, 37.1, 2.1, 52	397.1,397.1, 41.4, 2.0, 68	397.1	397.6	35.6	2	108
396.9,397.2, 36.8, 2.0, 52	397.1,397.1, 41.3, 2.0, 68	397.1	397.6	35.5	2.1	110
396.9,397.2, 36.6, 2.0, 53	397.1,397.1, 41.1, 2.0, 69	397.1	397.6	35.3	2	111
396.9,397.2, 36.5, 2.0, 54	397.1,397.1, 40.9, 2.0, 69	397.1	397.6	35.1	2	112
396.9,397.2, 36.2, 2.0, 54	397.1,397.1, 40.7, 2.0, 70	397.1	397.6	34.9	2.1	113
396.9,397.2, 36.1, 2.0, 55	397.1,397.1, 40.4, 2.0, 71	397.1	397.6	34.6	2	115
396.9,397.2, 35.8, 2.0, 56	397.1,397.1, 40.2, 2.0, 71	397.1	397.6	34.5	2.1	116
396.9,397.2, 35.6, 2.0, 57	397.1,397.1, 40.0, 2.1, 72	397.1	397.6	34.2	2	117
396.9,397.2, 35.4, 2.0, 58	397.1,397.1, 39.9, 2.0, 73	397.1	397.6	34.1	2	119
396.9,397.2, 35.3, 2.0, 58	397.1,397.1, 39.6, 2.0, 74	397.1	397.6	33.8	2	120
396.9,397.2, 35.0, 2.0, 59	397.1,397.1, 39.4, 2.1, 74	397.1	397.6	33.6	2	122
396.9,397.2, 34.9, 2.0, 60	397.1,397.1, 39.2, 2.1, 75	397.1	397.6	33.5	1.9	123
396.9,397.2, 34.6, 2.0, 61	397.1,397.1, 39.0, 1.9, 76	397.1	397.6	33.3	1.9	125
396.9,397.2, 34.4, 2.0, 62	397.1,397.1, 38.8, 1.9, 77	397.1	397.6	33	2	127
396.9,397.2, 34.2, 2.0, 63	397.1,397.1, 38.6, 1.9, 77	397.1	397.6	32.9	2	128
396.9,397.2, 34.0, 2.0, 64	397.1,397.1, 38.4, 1.9, 78	397.1	397.6	32.7	2	130
396.9,397.2, 33.8, 2.0, 65	397.1,397.1, 38.2, 2.0, 79	397.1	397.6	32.5	2	131
396.9,397.2, 33.7, 2.0, 66	397.1,397.1, 38.0, 2.0, 80	397.1	397.6	32.3	2	133
396.9,397.2, 33.4, 2.0, 67	397.1,397.1, 37.8, 1.9, 81	397.1	397.6	32.1	2	135
396.9,397.2, 33.2, 1.9, 68	397.1,397.1, 37.6, 2.0, 82	397.1	397.6	31.9	2	137
396.9,397.2, 33.1, 1.9, 69	397.1,397.1, 37.4, 2.0, 82	397.1	397.6	31.7	2	139
396.9,397.2, 32.9, 1.9, 70	397.1,397.1, 37.2, 2.0, 83	397.1	397.6	31.5	2	140
396.9,397.2, 32.7, 1.9, 71	397.1,397.1, 37.0, 2.0, 84	397.1	397.6	31.3	2	143
396.9,397.2, 32.4, 1.9, 72	397.1,397.1, 36.8, 2.1, 85	397.1	397.6	31.1	2	144
396.9,397.2, 32.2, 2.0, 74	397.1,397.1, 36.6, 2.1, 86	397.1	397.6	30.9	1.9	146
396.9,397.2, 32.0, 2.0, 75	397.1,397.1, 36.4, 2.1, 87	397.1	397.6	30.7	1.9	148
396.9,397.2, 31.9, 2.0, 76	397.1,397.1, 36.2, 2.1, 88	397.1	397.6	30.5	1.9	150
396.9,397.2, 31.7, 2.0, 77	397.1,397.1, 36.0, 2.0, 89	397.1	397.6	30.3	1.9	152
396.9,397.2, 31.5, 2.0, 79	397.1,397.1, 35.8, 1.9, 91	397.1	397.6	30.1	1.9	154
396.9,397.2, 31.3, 2.0, 80	397.1,397.1, 35.6, 1.9, 91	397.1	397.6	29.9	1.9	157
396.9,397.2, 31.1, 2.0, 81	397.1,397.1, 35.4, 2.0, 93	397.1	397.6	29.7	1.9	159
396.9,397.2, 30.9, 2.0, 82	397.0,397.1, 35.2, 2.0, 94	397.1	397.6	29.5	2	161
396.9,397.2, 30.7, 2.0, 84	397.0,397.1, 35.0, 2.0, 95	397.1	397.6	29.3	1.9	163
396.9,397.2, 30.5, 2.0, 85	397.0,397.1, 34.8, 2.0, 96	397.1	397.6	29	2	166
396.9,397.2, 30.3, 2.0, 87	397.0,397.1, 34.6, 1.9, 97	397.1	397.6	28.9	2	168
396.9,397.2, 30.1, 2.0, 88	397.0,397.1, 34.4, 2.0, 99	397.1	397.6	28.7	1.9	170
396.9,397.2, 29.9, 1.9, 90	397.0,397.1, 34.2, 2.0,100	397.1	397.6	28.5	1.9	173
396.9,397.2, 29.7, 2.0, 92	397.0,397.1, 34.0, 2.0,101	397.1	397.6	28.3	1.9	175
396.9,397.2, 29.5, 2.0, 93	397.0,397.1, 33.8, 2.0,103	397.1	397.6	28.1	2	178
396.9,397.2, 29.3, 2.0, 95	397.0,397.1, 33.6, 2.0,104	397.1	397.6	27.9	2	180
396.9,397.2, 29.1, 2.0, 96	397.0,397.1, 33.4, 2.0,105	397.1	397.6	27.7	2	183
396.9,397.2, 28.9, 1.9, 98	397.0,397.1, 33.2, 2.0,107	397.1	397.6	27.5	2	185
396.9,397.2, 28.7, 2.0,100	397.0,397.1, 33.0, 2.0,108	397.2	397.6	27.3	2	188
396.9,397.2, 28.5, 2.0,101	397.0,397.1, 32.8, 2.0,110	397.2	397.6	27.1	2	191
396.9,397.2, 28.3, 2.0,103	397.0,397.1, 32.6, 2.0,111	397.2	397.6	26.9	2.1	193
396.9,397.2, 28.1, 1.9,106	397.0,397.1, 32.4, 1.9,113	397.2	397.6	26.7	1.9	196
396.9,397.2, 27.9, 1.9,107	397.0,397.1, 32.2, 1.9,114	397.2	397.6	26.5	2	199
396.9,397.2, 27.7, 2.0,110	397.0,397.1, 32.0, 1.9,116	397.1	397.6	26.3	1.9	202
396.9,397.2, 27.5, 1.9,111	397.0,397.1, 31.8, 1.9,118	397.1	397.6	26.1	1.9	205
396.9,397.2, 27.3, 2.0,113	397.0,397.1, 31.6, 1.9,119	397.1	397.6	25.9	1.9	208
396.9,397.2, 27.1, 2.0,115	397.0,397.1, 31.4, 1.9,121	397.1	397.6	25.8	1.9	211
396.9,397.2, 26.9, 2.0,117	397.0,397.1, 31.2, 1.9,123	397.2	397.6	25.6	1.9	214
396.9,397.2, 26.7, 2.0,120	397.0,397.1, 31.0, 1.9,125	397.2	397.6	25.4	0	160
396.9,397.2, 26.5, 2.0,121	397.0,397.1, 30.8, 1.9,126	397.2	397.6	25.6	0	166
396.9,397.1, 26.3, 1.9,124	397.0,397.1, 30.6, 1.9,129	397.2	397.6	25.9	0	110
396.9,397.1, 26.1, 1.9,126	397.0,397.1, 30.4, 1.9,130	397.2	397.6	26.1	0	81
396.9,397.1, 25.9, 2.0,129	397.0,397.1, 30.3, 1.9,132	397.2	397.6	26.3	0	58
396.9,397.1, 25.7, 1.9,131	397.0,397.1, 30.1, 1.9,135	397.2	397.6	26.5	0	40
396.9,397.1, 25.5, 1.9,134	397.0,397.1, 29.9, 1.9,136	397.2	397.6	26.6	0	26
396.9,397.1, 25.3, 2.0,135	397.0,397.1, 29.7, 1.9,138	397.2	397.6	26.8	0	18
396.9,397.1, 25.1, 1.9,139	397.0,397.1, 29.5, 1.9,140	397.2	397.6	27.8	0	4
396.9,397.1, 24.9, 1.9,141	397.0,397.1, 29.3, 2.0,143	397.2	397.6	28	0	-2
396.9,397.1, 24.7, 1.9,144	397.0,397.1, 29.0, 2.0,145	397.2	397.6	28	0	0
396.9,397.1, 24.5, 0.0,147	397.0,397.1, 28.9, 2.0,147	397.2	397.6	28	0	2
396.9,397.1, 24.5, 0.0,119	397.0,397.1, 28.7, 2.0,149	397.2	397.6	28	0	0

Top Die [mm], Bottom Die [mm], Position [mm], Speed [mm/s], Load [Tons]						
DTC 1080 °C	DTC 970 °C	DTC 915 °C				
396.9,397.1, 24.7, 0.0, 84	397.0,397.1, 28.4, 1.9,152	397.2	397.6	28	0	-1
396.9,397.1, 24.9, 0.0, 55	397.0,397.1, 28.2, 2.0,154	397.2	397.6	28	0	0
396.9,397.1, 25.1, 0.0, 38	397.0,397.1, 28.0, 2.0,157	397.2	397.6	28	0	-1
396.9,397.1, 25.2, 0.0, 23	397.0,397.1, 27.9, 2.0,159	397.2	397.6	28	0	-2
396.9,397.2, 25.3, 0.0, 15	397.0,397.1, 27.7, 2.0,162	397.2	397.6	37.3	0	0
396.9,397.2, 26.5, 0.0, -2	397.0,397.1, 27.5, 2.0,164	397.2	397.6	43.4	0	0
396.9,397.2, 26.5, 0.0, 3	397.0,397.1, 27.3, 1.9,167	397.2	397.6	51.7	0	0
396.9,397.2, 26.5, 0.0, 1	397.0,397.1, 27.1, 1.9,169	397.2	397.6	62.2	0	0
396.9,397.2, 26.5, 0.0, -1	397.0,397.1, 26.9, 1.9,172	397.2	397.6	68.7	0	0
396.9,397.2, 26.5, 0.0, -1	397.0,397.1, 26.7, 1.9,175	397.2	397.6	77.4	0	0
396.9,397.2, 26.5, 0.0, -1	397.0,397.1, 26.5, 2.0,177	397.2	397.6	87.4	0	0
396.9,397.2, 26.5, 0.0, -2	397.0,397.1, 26.3, 2.0,180	397.2	397.6	95.6	0	0
396.9,397.2, 26.5, 0.0, -1	397.0,397.1, 26.1, 1.9,184	397.2	397.6	103.6	0	0
396.9,397.2, 27.4, 0.0, 2	397.0,397.1, 25.9, 1.9,186	397.2	397.6	112.1	0	0
396.9,397.2, 38.2, 0.0, -0	397.0,397.1, 25.7, 1.9,190	397.2	397.6	121.1	0	0
396.9,397.2, 46.6, 0.0, -0	397.0,397.1, 25.6, 1.9,192	397.2	397.6	128.8	0	0
396.9,397.2, 54.1, 0.0, 0	397.0,397.1, 25.3, 2.0,196	397.2	397.6	137.8	0	0
396.9,397.2, 62.1, 0.0, -0	397.0,397.1, 25.1, 2.0,199	397.2	397.6	146.1	0	0
396.9,397.2, 72.0, 0.0, -0	397.0,397.1, 24.9, 2.0,202	397.2	397.6	154.2	0	0
396.9,397.2, 80.6, 0.0, -0	397.0,397.1, 24.7, 2.0,205					
396.9,397.2, 88.1, 0.0, 0	397.0,397.1, 24.5, 2.0,209					
396.9,397.2, 97.3, 0.0, -0	397.0,397.1, 24.4, 0.0,173					
396.9,397.2,105.5, 0.0, -0	397.0,397.1, 24.7, 0.0,131					
396.9,397.2,112.7, 0.0, 0	397.0,397.1, 24.9, 0.0, 97					
396.9,397.2,121.5, 0.0, -0	397.0,397.1, 25.1, 0.0, 66					
396.9,397.2,129.8, 0.0, -0	397.0,397.1, 25.3, 0.0, 46					
396.9,397.2,138.5, 0.0, -0	397.0,397.1, 25.5, 0.0, 32					
396.9,397.2,147.0, 0.0, -0	397.0,397.1, 25.6, 0.0, 20					
396.9,397.2,155.6, 0.0, -0	397.0,397.1, 25.7, 0.0, 15					
	397.0,397.1, 26.8, 0.0, -2					
	397.0,397.1, 26.9, 0.0, 4					
	397.0,397.1, 26.9, 0.0, -1					
	397.0,397.1, 26.9, 0.0, -1					
	397.0,397.1, 26.9, 0.0, -1					
	397.0,397.1, 26.9, 0.0, 0					
	397.0,397.1, 26.9, 0.0, 2					
	397.0,397.1, 26.8, 0.0, 2					
	397.0,397.1, 28.1, 0.0, 1					
	397.0,397.1, 38.7, 0.0, -0					
	397.0,397.1, 48.3, 0.0, -0					
	397.0,397.1, 54.5, 0.0, -0					
	397.0,397.1, 62.6, 0.0, -0					
	397.0,397.1, 71.9, 0.0, -0					
	397.0,397.1, 80.6, 0.0, -0					
	397.0,397.1, 89.6, 0.0, -0					
	397.0,397.1, 98.0, 0.0, -0					
	397.0,397.1,106.9, 0.0, -0					
	397.0,397.1,114.8, 0.0, -0					
	397.0,397.1,122.8, 0.0, -0					
	397.0,397.1,131.6, 0.0, -0					
	397.0,397.1,140.2, 0.0, -0					
	397.0,397.1,149.1, 0.0, -0					
	397.0,397.1,157.0, 0.0, -0					

Top Die [mm], Bottom Die [mm], Position [mm], Speed [mm/s], Load [Tons]		
DTC 1150 °C		
377.3,446.8,158.2, 0.0, -1	377.3,446.8, 63.3, 2.5, 3	377.3,446.8, 41.9, 2.0, 32
377.3,446.8,138.4, 0.0, -0	377.3,446.8, 63.0, 2.4, 3	377.3,446.8, 41.7, 2.0, 32
377.3,446.8,117.8, 0.0, -1	377.3,446.8, 62.8, 2.4, 3	377.3,446.8, 41.5, 2.0, 32
377.3,446.8, 98.0, 0.0, -1	377.3,446.8, 62.6, 2.5, 3	377.3,446.8, 41.3, 2.0, 33
377.3,446.8, 76.1, 1.8, -1	377.3,446.8, 62.3, 2.4, 3	377.3,446.8, 41.1, 2.0, 33
377.3,446.8, 75.5, 7.2, -1	377.3,446.8, 62.1, 2.5, 3	377.3,446.8, 40.9, 2.0, 33
377.3,446.8, 74.5, 8.7, -0	377.3,446.8, 61.9, 2.4, 3	377.3,446.8, 40.7, 2.0, 34
377.3,446.8, 72.9, 9.3, -0	377.3,446.8, 61.7, 2.3, 3	377.3,446.8, 40.5, 2.0, 34

Top Die [mm], Bottom Die [mm], Position [mm], Speed [mm/s], Load [Tons]
DTC 1150 °C
377.3,446.8, 73.1, 9.3, -0
377.3,446.8, 73.1, 9.0, -0
377.3,446.8, 73.1, 8.7, -0
377.3,446.8, 73.2, 8.6, -0
377.3,446.8, 73.2, 8.3, -0
377.3,446.8, 73.2, 8.1, -0
377.3,446.8, 73.2, 7.9, -0
377.3,446.8, 73.2, 7.9, -0
377.3,446.8, 73.2, 2.3, -0
377.3,446.8, 73.2, 0.7, -0
377.3,446.8, 73.2, -0.3, -0
377.3,446.8, 73.2, -0.1, -0
377.3,446.8, 73.2, 0.0, -0
377.3,446.8, 73.2, -0.1, -0
377.3,446.8, 73.2, 0.0, -0
377.3,446.8, 73.2, 0.0, -0
377.3,446.8, 73.2, 0.0, -0
377.3,446.8, 73.2, 0.0, -0
377.3,446.8, 73.2, 0.0, -0
377.3,446.8, 73.2, 0.0, -0
377.3,446.8, 73.2, 0.0, -0
377.3,446.8, 73.2, 0.0, -0
377.3,446.8, 73.2, 0.0, -0
377.3,446.8, 73.2, 0.0, -0
377.3,446.8, 73.2, 0.0, -0
377.3,446.8, 73.2, 0.0, -0
377.3,446.8, 73.2, 0.0, 5
377.3,446.8, 73.0, 0.1, 1
377.3,446.8, 72.7, 0.3, 1
377.3,446.8, 72.5, 0.6, 1
377.3,446.8, 72.2, 0.8, 1
377.3,446.8, 71.9, 1.1, 2
377.3,446.8, 71.7, 1.4, 2
377.3,446.8, 71.4, 1.7, 2
377.3,446.8, 71.1, 1.9, 2
377.3,446.8, 70.8, 2.2, 2
377.3,446.8, 70.6, 2.2, 2
377.3,446.8, 70.3, 2.5, 3
377.3,446.8, 70.0, 2.7, 3
377.3,446.8, 69.7, 2.8, 3
377.3,446.8, 69.4, 2.8, 3
377.3,446.8, 69.1, 2.8, 3
377.3,446.8, 68.9, 2.8, 3
377.3,446.8, 68.6, 2.8, 3
377.3,446.8, 68.3, 2.8, 3
377.3,446.8, 68.1, 2.7, 3
377.3,446.8, 67.8, 2.7, 3
377.3,446.8, 67.6, 2.7, 3
377.3,446.8, 67.3, 2.7, 3
377.3,446.8, 67.0, 2.7, 3
377.3,446.8, 66.7, 2.7, 3
377.3,446.8, 66.5, 2.6, 3
377.3,446.8, 66.2, 2.7, 3
377.3,446.8, 66.0, 2.6, 3
377.3,446.8, 65.7, 2.6, 3
377.3,446.8, 65.5, 2.6, 3
377.3,446.8, 65.2, 2.6, 3
377.3,446.8, 65.0, 2.6, 3
377.3,446.8, 64.8, 2.5, 3
377.3,446.8, 64.5, 2.5, 3
377.3,446.8, 64.3, 2.5, 3
377.3,446.8, 64.0, 2.5, 3
377.3,446.8, 63.8, 2.4, 3
377.3,446.8, 63.5, 2.4, 3
377.3,446.8, 57.7, 2.1, 3
377.3,446.8, 57.4, 2.1, 3
377.3,446.8, 57.2, 2.1, 3
377.3,446.8, 57.0, 2.1, 4
377.3,446.8, 56.8, 2.1, 3
377.3,446.8, 56.6, 2.2, 3
377.3,446.8, 61.4, 2.3, 3
377.3,446.8, 61.2, 2.4, 3
377.3,446.8, 61.0, 2.4, 3
377.3,446.8, 60.8, 2.3, 3
377.3,446.8, 60.5, 2.3, 3
377.3,446.8, 60.3, 2.2, 3
377.3,446.8, 60.1, 2.2, 4
377.3,446.8, 59.8, 2.3, 3
377.3,446.8, 59.6, 2.2, 4
377.3,446.8, 59.4, 2.2, 3
377.3,446.8, 59.2, 2.3, 3
377.3,446.8, 59.0, 2.2, 4
377.3,446.8, 58.8, 2.2, 3
377.3,446.8, 58.5, 2.2, 3
377.3,446.8, 58.3, 2.2, 3
377.3,446.8, 58.1, 2.2, 4
377.3,446.8, 52.4, 1.9, 20
377.3,446.8, 52.2, 1.8, 20
377.3,446.8, 52.0, 1.9, 20
377.3,446.8, 51.8, 1.8, 21
377.3,446.8, 51.6, 1.8, 21
377.3,446.8, 51.4, 1.8, 21
377.3,446.8, 51.2, 1.9, 21
377.3,446.8, 51.0, 1.9, 22
377.3,446.8, 50.8, 1.9, 22
377.3,446.8, 50.6, 1.9, 22
377.3,446.8, 50.4, 2.0, 23
377.3,446.8, 50.2, 2.0, 23
377.3,446.8, 50.0, 2.0, 23
377.3,446.8, 49.8, 2.0, 23
377.3,446.8, 49.5, 2.0, 24
377.3,446.8, 49.3, 2.1, 24
377.3,446.8, 49.1, 2.1, 24
377.3,446.8, 48.9, 2.0, 24
377.3,446.8, 48.7, 2.0, 24
377.3,446.8, 48.5, 2.0, 25
377.3,446.8, 48.3, 2.0, 25
377.3,446.8, 48.1, 2.1, 25
377.3,446.8, 47.9, 2.1, 25
377.3,446.8, 47.7, 2.1, 25
377.3,446.8, 47.5, 2.1, 26
377.3,446.8, 47.2, 2.0, 26
377.3,446.8, 47.1, 2.0, 26
377.3,446.8, 46.9, 2.0, 26
377.3,446.8, 46.7, 2.0, 26
377.3,446.8, 46.5, 2.0, 26
377.3,446.8, 46.3, 2.1, 26
377.3,446.8, 46.1, 2.1, 27
377.3,446.8, 45.8, 2.0, 27
377.3,446.8, 45.7, 2.1, 27
377.3,446.8, 45.4, 2.0, 27
377.3,446.8, 45.2, 2.0, 27
377.3,446.8, 45.0, 2.0, 28
377.3,446.8, 44.8, 2.0, 28
377.3,446.8, 44.6, 2.0, 28
377.3,446.8, 44.5, 2.0, 28
377.3,446.8, 44.4, 1.8, 28
377.3,446.8, 44.2, 1.8, 29
377.3,446.8, 44.0, 1.8, 29
377.3,446.8, 43.8, 1.8, 29
377.3,446.8, 43.5, 1.9, 29
377.3,446.8, 43.3, 1.9, 30
377.3,446.8, 43.1, 1.9, 30
377.3,446.8, 43.0, 1.9, 30
377.3,446.8, 42.8, 1.9, 30
377.3,446.8, 42.5, 1.9, 31
377.3,446.8, 42.3, 1.9, 31
377.3,446.8, 42.1, 2.0, 31
377.3,446.8, 36.9, 2.0, 43
377.3,446.8, 36.7, 2.0, 43
377.3,446.8, 40.3, 2.1, 34
377.3,446.8, 40.1, 2.0, 35
377.3,446.8, 39.9, 2.0, 35
377.3,446.8, 39.7, 2.0, 36
377.3,446.8, 39.5, 2.0, 36
377.3,446.8, 39.3, 1.9, 36
377.3,446.8, 39.1, 2.0, 37
377.3,446.8, 38.9, 2.0, 37
377.3,446.8, 38.7, 2.0, 38
377.3,446.8, 38.5, 2.1, 38
377.3,446.8, 38.3, 2.0, 39
377.3,446.8, 38.1, 2.0, 39
377.3,446.8, 37.8, 2.0, 40
377.3,446.8, 37.7, 2.0, 40
377.3,446.8, 37.5, 1.9, 41
377.3,446.8, 37.2, 2.0, 42
377.3,446.8, 37.1, 2.0, 42
377.3,446.8, 32.3, 1.9, 61
377.3,446.8, 32.1, 2.0, 62
377.3,446.8, 31.9, 2.0, 63
377.3,446.8, 31.7, 2.0, 64
377.3,446.8, 31.4, 2.0, 66
377.3,446.8, 31.3, 2.0, 67
377.3,446.8, 31.1, 1.9, 68
377.3,446.8, 30.9, 1.9, 69
377.3,446.8, 30.7, 1.9, 71
377.3,446.8, 30.4, 1.9, 71
377.3,446.8, 30.2, 2.0, 73
377.3,446.8, 30.1, 2.0, 74
377.3,446.8, 29.9, 2.0, 76
377.3,446.8, 29.7, 2.0, 77
377.3,446.8, 29.5, 2.0, 78
377.3,446.8, 29.3, 2.0, 80
377.3,446.8, 29.1, 2.0, 81
377.3,446.8, 28.9, 2.0, 83
377.3,446.8, 28.7, 2.0, 85
377.3,446.8, 28.5, 2.0, 86
377.3,446.8, 28.3, 1.9, 88
377.3,446.8, 28.1, 1.9, 90
377.3,446.8, 27.9, 1.9, 91
377.3,446.8, 27.7, 1.9, 93
377.3,446.8, 27.5, 1.9, 95
377.3,446.8, 27.3, 1.9, 97
377.3,446.8, 27.2, 1.9, 99
377.3,446.8, 26.9, 2.0, 100
377.3,446.8, 26.7, 1.9, 103
377.3,446.8, 26.5, 2.0, 105
377.3,446.8, 26.3, 2.0, 107
377.3,446.8, 26.1, 1.9, 109
377.3,446.8, 25.9, 1.9, 111
377.3,446.8, 25.7, 1.9, 113
377.3,446.8, 25.6, 1.9, 116
377.3,446.8, 25.4, 1.9, 118
377.3,446.8, 25.1, 1.9, 120
377.3,446.8, 24.9, 2.0, 123
377.3,446.8, 24.8, 1.9, 125
377.3,446.8, 24.5, 2.0, 128
377.3,446.8, 24.4, 1.9, 130
377.3,446.8, 24.1, 2.0, 133
377.3,446.8, 23.9, 0.0, 136
377.3,446.8, 24.0, 0.0, 101
377.3,446.8, 24.2, 0.0, 66
377.3,446.8, 24.3, 0.0, 46
377.3,446.8, 24.5, 0.0, 30
377.3,446.8, 24.6, 0.0, 18
377.3,446.8, 24.9, 0.0, 13
377.3,446.8, 25.7, 0.0, 8
377.3,446.8, 25.7, 0.0, -0
377.3,446.8, 25.7, 0.0, -1
377.3,446.8, 25.7, 0.0, 3

Top Die [mm], Bottom Die [mm], Position [mm], Speed [mm/s], Load [Tons]		
DTC 1150 °C		
377.3,446.8, 56.4, 2.2, 4	377.3,446.8, 36.5, 2.0, 44	377.3,446.8, 25.7, 0.0, 0
377.3,446.8, 56.2, 2.2, 3	377.3,446.8, 36.3, 1.9, 45	377.3,446.8, 25.8, 0.0, -1
377.3,446.8, 55.9, 2.1, 4	377.3,446.8, 36.1, 2.0, 45	377.3,446.8, 25.7, 0.0, -2
377.3,446.8, 55.7, 2.1, 3	377.3,446.8, 35.8, 1.9, 46	377.3,446.8, 25.8, 0.0, 3
377.3,446.8, 55.5, 2.1, 3	377.3,446.8, 35.6, 1.9, 47	377.3,446.8, 35.6, 0.0, -0
377.3,446.8, 55.3, 2.1, 4	377.3,446.8, 35.5, 2.0, 47	377.3,446.8, 40.7, 0.0, -0
377.3,446.8, 55.1, 2.1, 4	377.3,446.8, 35.2, 1.9, 48	377.3,446.8, 49.7, 0.0, -0
377.3,446.8, 54.9, 2.1, 4	377.3,446.8, 35.0, 2.0, 49	377.3,446.8, 59.6, 0.0, -0
377.3,446.8, 54.7, 2.1, 3	377.3,446.8, 34.9, 2.0, 50	377.3,446.8, 67.3, 0.0, -0
377.3,446.8, 54.5, 2.0, 3	377.3,446.8, 34.6, 2.1, 50	377.3,446.8, 75.6, 0.0, -0
377.3,446.8, 54.3, 2.0, 4	377.3,446.8, 34.5, 2.1, 51	377.3,446.8, 85.5, 0.0, -0
377.3,446.8, 54.1, 2.0, 4	377.3,446.8, 34.3, 2.0, 52	377.3,446.8, 93.9, 0.0, -0
377.3,446.8, 53.9, 2.0, 3	377.3,446.8, 34.1, 2.0, 53	377.3,446.8,101.3, 0.0, -0
377.3,446.8, 53.7, 2.1, 4	377.3,446.8, 33.9, 2.0, 54	377.3,446.8,110.1, 0.0, -0
377.3,446.8, 53.5, 2.1, 4	377.3,446.8, 33.7, 2.0, 54	377.3,446.8,119.2, 0.0, -0
377.3,446.8, 53.2, 2.1, 4	377.3,446.8, 33.4, 2.0, 55	377.3,446.8,127.0, 0.0, -0
377.3,446.8, 57.9, 2.1, 3	377.3,446.8, 33.3, 2.0, 56	377.3,446.8,134.8, 0.0, -0
377.3,446.8, 53.1, 2.1, 5	377.3,446.8, 33.1, 2.0, 57	377.3,446.8,144.2, 0.0, -0
377.3,446.8, 52.9, 2.0, 9	377.3,446.8, 32.8, 2.0, 58	377.3,446.8,152.7, 0.0, -0
377.3,446.8, 52.8, 2.0, 15	377.3,446.8, 32.6, 2.0, 59	
377.3,446.8, 52.6, 1.9, 19	377.3,446.8, 32.4, 1.9, 60	

3.4 FE Modelling Data

3.4.1 QFORM and DEFORM Comparison

No significant difference was found between Qform and Deform simulations. The Table below shows a back-to-back comparison of the three main state variables taken from simulation.

VARIABLES	QFORM	DEFORM
TEMPERATURE (℃)	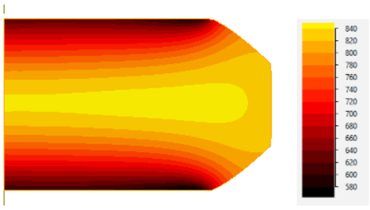	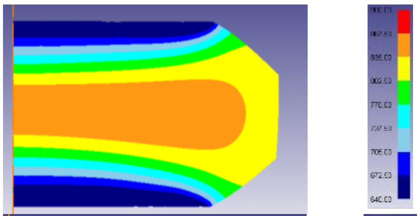
STRAIN	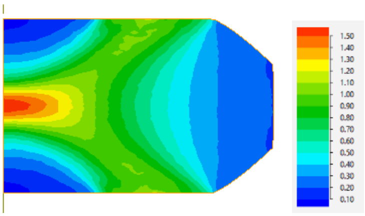	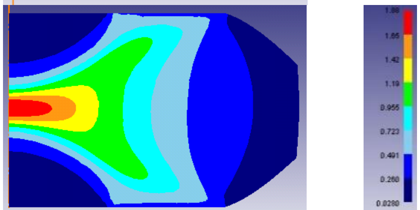
STRAIN RATE (1/S)	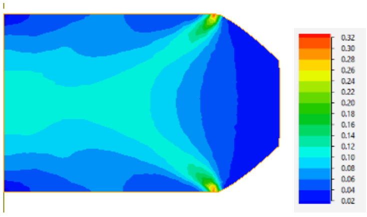	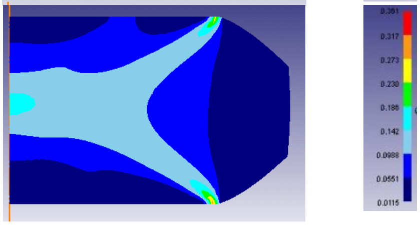

3.4.2 Preliminary Simulation Flow Stress Data

The material data used in both QForm and DEFORM were taken from 'Hot Working Guide' published by Prasad [Y. V. R. K. Prasad, S. Sasidhara, Hot Working Guide: a compendium of processing maps]. In the figures below are shown the flow stress curves for the range of temperatures 900–1200°C and strain-rates 0.001–100 1/s.

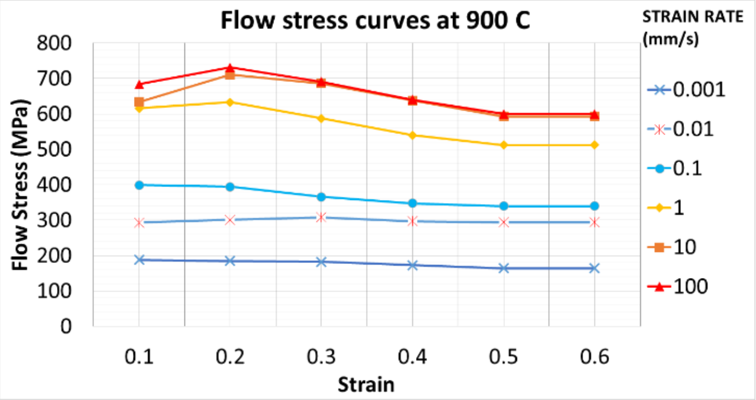
Flow stress curves at 900 C
Flow Stress (MPa)
800
700
600
500
400
300
200
100
0
0.1
0.2
0.3
0.4
0.5
0.6
Strain
STRAIN RATE (mm/s)
0.001
0.01
0.1
1
10
100

a)

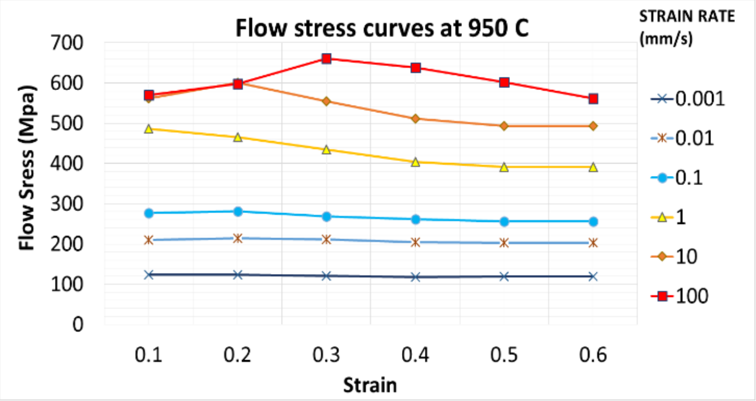
Flow stress curves at 950 C
Flow Sress (Mpa)
700
600
500
400
300
200
100
0
0.1
0.2
0.3
0.4
0.5
0.6
Strain
STRAIN RATE (mm/s)
0.001
0.01
0.1
1
10
100

b)

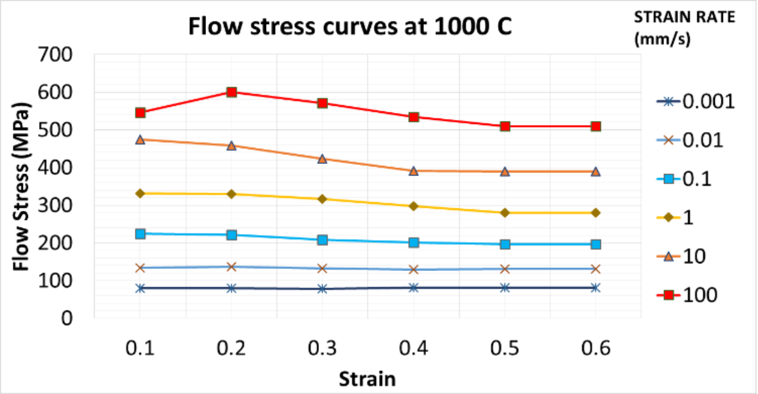
Flow stress curves at 1000 C
Flow Stress (MPa)
700
600
500
400
300
200
100
0
0.1
0.2
0.3
0.4
0.5
0.6
Strain
STRAIN RATE (mm/s)
0.001
0.01
0.1
1
10
100

c)

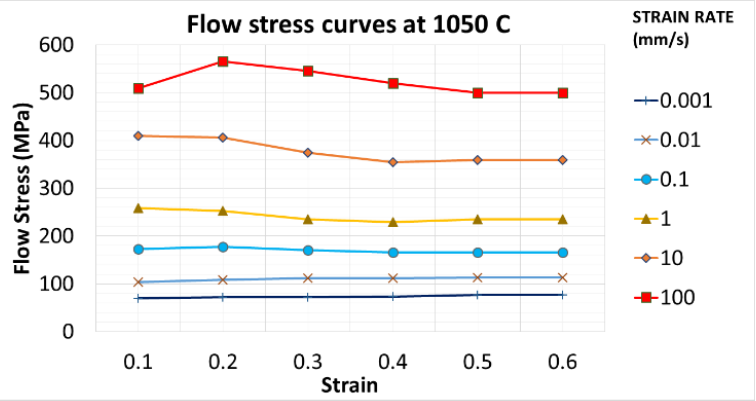
Flow stress curves at 1050 C
Flow Stress (MPa)
600
500
400
300
200
100
0
0.1
0.2
0.3
0.4
0.5
0.6
Strain
STRAIN RATE (mm/s)
0.001
0.01
0.1
1
10
100

d)

e)

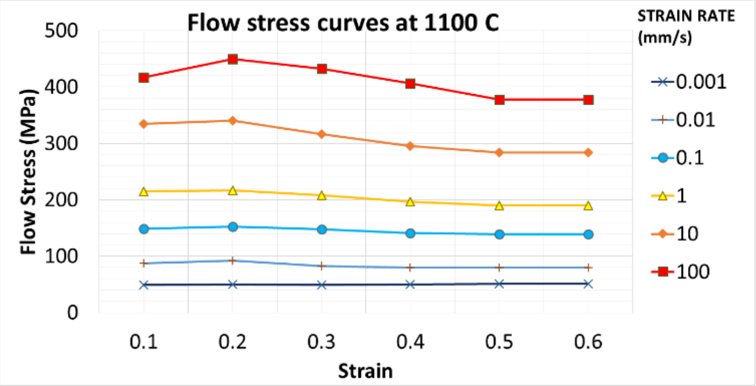
Flow stress curves at 1100 C
Flow Stress (MPa)
500
400
300
200
100
0
0.1
0.2
0.3
0.4
0.5
0.6
Strain
STRAIN RATE (mm/s)
0.001
0.01
0.1
1
10
100

f)

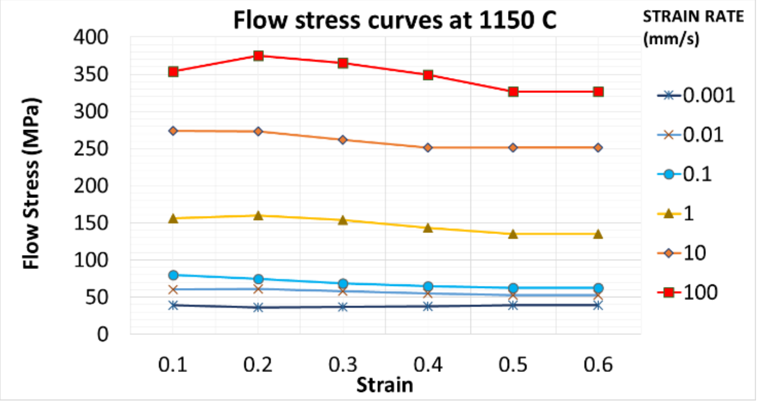
Flow stress curves at 1150 C
Flow Stress (MPa)
400
350
300
250
200
150
100
50
0
0.1
0.2
0.3
0.4
0.5
0.6
Strain
STRAIN RATE (mm/s)
0.001
0.01
0.1
1
10
100

g)

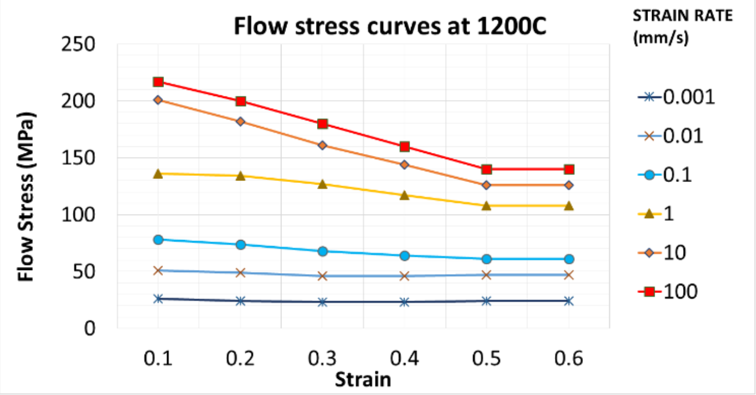
Flow stress curves at 1200C
Flow Stress (MPa)
250
200
150
100
50
0
0.1
0.2
0.3
0.4
0.5
0.6
Strain
STRAIN RATE (mm/s)
0.001
0.01
0.1
1
10
100

3.4.3 Digital Twin FE Simulation Flow Stress Data

600 °C	**0.001**	**0.01**	**0.1**	**1**	**10**	**100**
0	1004	1004	1004	1004	1004	1004
0.05	1185.401	1185.401	1185.401	1185.401	1185.401	1185.401
0.1	1305.342	1305.342	1305.342	1305.342	1305.342	1305.342
0.2	1392.799	1392.799	1392.799	1392.799	1392.799	1392.799
0.3	1392.799	1392.799	1392.799	1392.799	1392.799	1392.799
0.4	1392.799	1392.799	1392.799	1392.799	1392.799	1392.799
0.5	1392.799	1392.799	1392.799	1392.799	1392.799	1392.799
0.6	1392.799	1392.799	1392.799	1392.799	1392.799	1392.799
0.7	1392.799	1392.799	1392.799	1392.799	1392.799	1392.799

750 °C	**0.001**	**0.01**	**0.1**	**1**	**10**	**100**
0	900	900	900	900	900	900
0.05	955	955	955	955	955	955
0.1	1001	1001	1001	1001	1001	1001
0.2	1050	1050	1050	1050	1050	1050
0.3	1010	1010	1010	1010	1010	1010
0.4	1001	1001	1001	1001	1001	1001
0.5	1001	1001	1001	1001	1001	1001
0.6	1001	1001	1001	1001	1001	1001
0.7	1001	1001	1001	1001	1001	1001

800 °C	**0.001**	**0.01**	**0.1**	**1**	**10**	**100**
0	700	700	700	700	700	700
0.05	755	755	755	755	755	755
0.1	801	801	801	801	801	801
0.2	850	850	850	850	850	850
0.3	810	810	810	810	810	810
0.4	801	801	801	801	801	801
0.5	801	801	801	801	801	801
0.6	801	801	801	801	801	801
0.7	801	801	801	801	801	801

850 °C	**0.001**	**0.01**	**0.1**	**1**	**10**	**100**
0	348	348	348	348	348	348
0.05	450	450	450	450	450	450
0.1	531	531	531	531	531	531
0.2	580	580	580	580	580	580
0.3	595	595	595	595	595	595
0.4	599	599	599	599	599	599
0.5	595	595	595	595	595	595
0.6	580	580	580	580	580	580
0.7	536	536	536	536	536	536

900 °C	**0.001**	**0.01**	**0.1**	**1**	**10**	**100**
0	300	350	400	450	480	530
0.05	400	450	500	550	570	620
0.1	466	516	566	616	634	684
0.2	483	533	583	633	711	731
0.3	437	487	537	587	686	691
0.4	390	440	490	540	638	640
0.5	362	412	462	512	593	600
0.6	362	412	462	512	593	600
0.7	362	412	462	512	593	600

950 °C	**0.001**	**0.01**	**0.1**	**1**	**10**	**100**
0	120	140	130	160	176.6517	190
0.05	263.477	283.477	303.477	333.477	371.3215	447.6156
0.1	312.3892	332.3892	352.3892	382.3892	421.6812	498.2457
0.2	362.446	382.446	402.446	432.446	473.0295	556.9449
0.3	379.9659	399.9659	419.9659	449.9659	491.6904	577.8157
0.4	360.7775	380.7775	400.7775	430.7775	503.7428	589.5556
0.5	340.7547	360.7547	380.7547	410.7547	504.8627	597.3821
0.6	329.9091	349.9091	369.9091	399.9091	507.0581	599.991
0.7	328.4537	348.4537	368.4537	398.4537	509.2535	601.5173

1000 °C	**0.001**	**0.01**	**0.1**	**1**	**10**	**100**
0	79.3434	122.9837	141.1468	160	176.6517	185
0.05	95.101	155	170	250.2953	330.0552	390.1734
0.1	95.1924	159.7374	190.4353	291.4527	381.9208	443.4598
0.2	89.1706	150.9401	214.2075	325.6581	431.6169	503.4634
0.3	85.8587	135.2346	218.1583	328.161	441.1964	532.1608
0.4	83.1489	128.6377	208.7389	315.6468	441.3974	537.3785
0.5	83.1489	127.6953	201.875	312.3097	439.001	541.2918
0.6	83.1489	128.5014	200.3791	311.4754	436.8056	541.2918
0.7	83.1489	127.2241	199.3924	311.181	434.6102	544.075

1050 °C	**0.001**	**0.01**	**0.1**	**1**	**10**	**100**
0	59.7475	89.5274	100.01	124.7767	143.7209	155
0.05	73.8889	122.248	130	195.069	272.2822	342.4855
0.1	73.213	122.512	134.38	215.5331	309.4729	399
0.2	67.4923	114.523	149.25	225.5445	344.5992	453.8952
0.3	65.6858	104.1349	149.46	223.8759	353.3807	469.5483
0.4	65.9869	97.538	146.96	215.5331	346.9444	476.0705
0.5	65.9869	97.97	147.04	217.2017	327.036	476.0705
0.6	65.9869	98.3379	146.5	215.5331	320.4499	476.0705
0.7	66.288	96.5955	146.41	217.7729	320.4499	476.8786

1100 °C	**0.001**	**0.01**	**0.1**	**1**	**10**	**100**
0	57.1212	78.6897	92	118.6404	143.7209	159.0949
0.05	69.4444	102	111.077	176.6589	247.5224	320.8092
0.1	68.0945	106.0197	125.2288	193.8419	281.3732	362.5854
0.2	63.8793	98.4804	138.7774	202.1847	311.6683	401.7182
0.3	62.3739	91.4123	133.2366	198.8475	320.5033	413.458
0.4	62.3739	85.4632	123.5129	191.339	311.6683	413.458
0.5	62.3739	81.5169	120.6529	188.0019	299.5936	417.3713
0.6	62.3739	81.5169	120.6529	188.8362	288.8646	416.0669
0.7	62.3739	81.5169	120.3724	187.0901	287.519	419.4364

1150 °C	**0.001**	**0.01**	**0.1**	**1**	**10**	**100**
0	41.5657	59.3701	62	64.7767	143.7209	190.7514
0.05	56.9192	80	89.0769	100.9781	179.6621	235.1879
0.1	57.8576	81.5169	98.9175	108.7453	190.922	253.014
0.2	58.7608	79.6321	103.7582	115.4195	199	263.449
0.3	58.1586	76.8048	98.9175	114.5852	199	268.667
0.4	58.1586	76	94.3416	111.2481	200	270
0.5	58.4597	76	90.9096	109.5795	201	273.8844
0.6	58.7608	75.5	88.6217	111.2481	202	274
0.7	58.9394	75	88.0458	111.4093	203	274.2052

3.4.4 Digital Twin FE Simulation Thermal Properties Settings

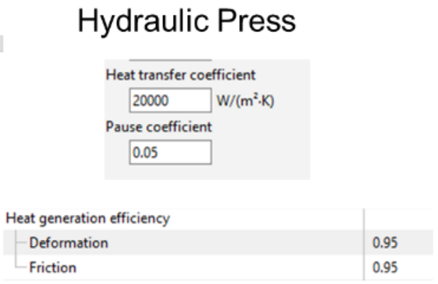

Hydraulic Press

Heat transfer coefficient: 20000 W/(m²·K)

Pause coefficient: 0.05

Heat generation efficiency	
Deformation	0.95
Friction	0.95

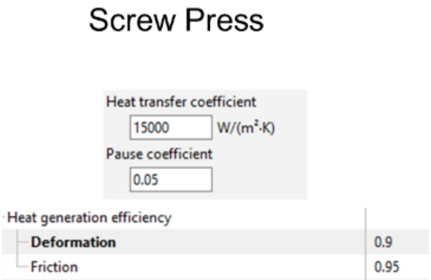

Screw Press

Heat transfer coefficient: 15000 W/(m²·K)

Pause coefficient: 0.05

Heat generation efficiency	
Deformation	0.9
Friction	0.95

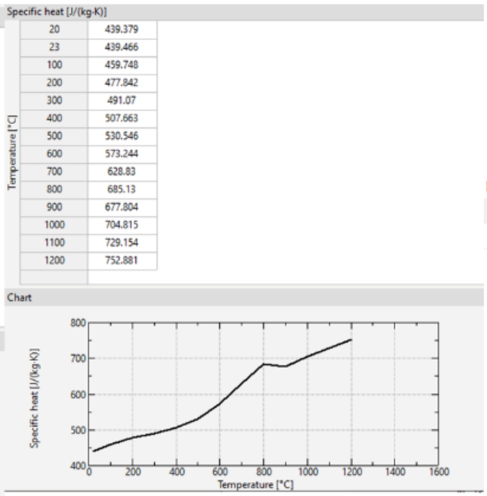

Specific heat [J/(kg·K)]

Temperature [°C]	Specific heat [J/(kg·K)]
20	439.379
23	439.466
100	459.748
200	477.842
300	491.07
400	507.663
500	530.546
600	573.244
700	628.83
800	685.13
900	677.804
1000	704.815
1100	729.154
1200	752.881

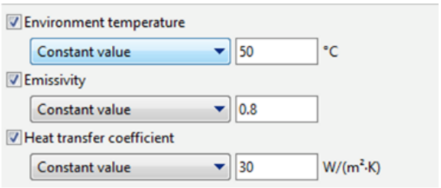

☑ Environment temperature

Constant value: 50 °C

☑ Emissivity

Constant value: 0.8

☑ Heat transfer coefficient

Constant value: 30 W/(m²·K)

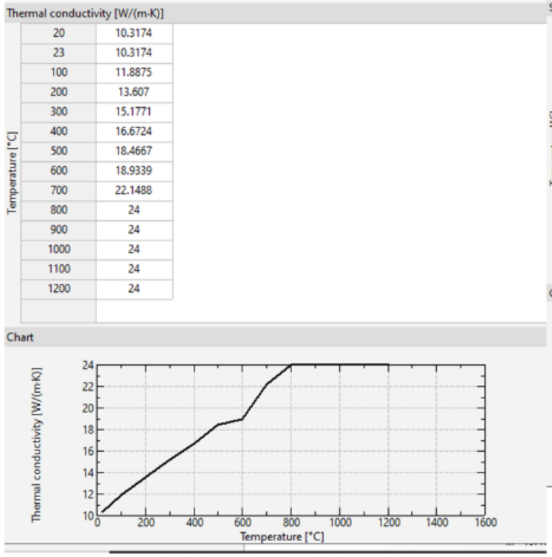

Thermal conductivity [W/(m·K)]

Temperature [°C]	Thermal conductivity [W/(m·K)]
20	10.3174
23	10.3174
100	11.8875
200	13.607
300	15.1771
400	16.6724
500	18.4667
600	18.9339
700	22.1488
800	24
900	24
1000	24
1100	24
1200	24

3.4.5 Main FE Simulations Summary

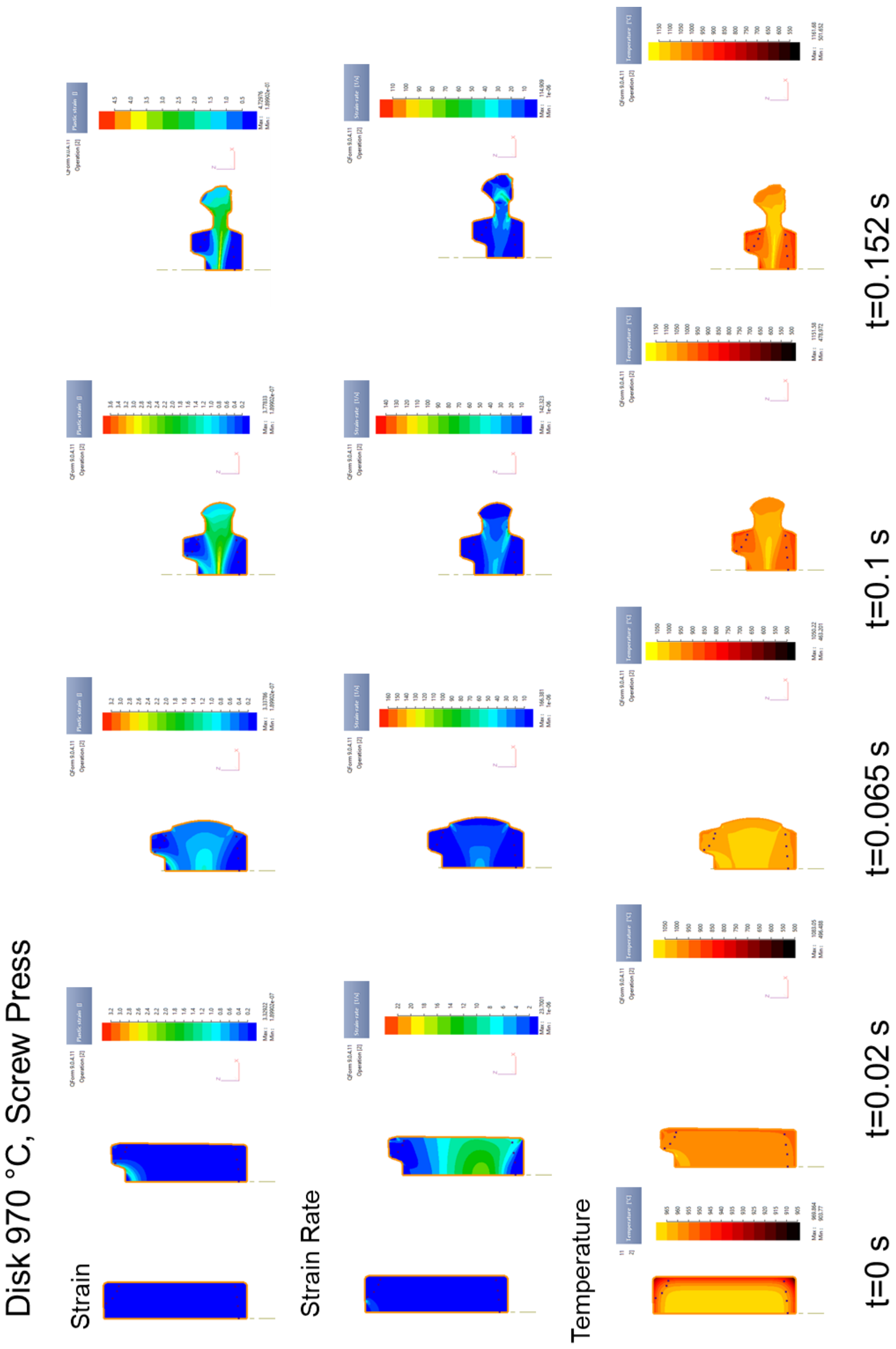

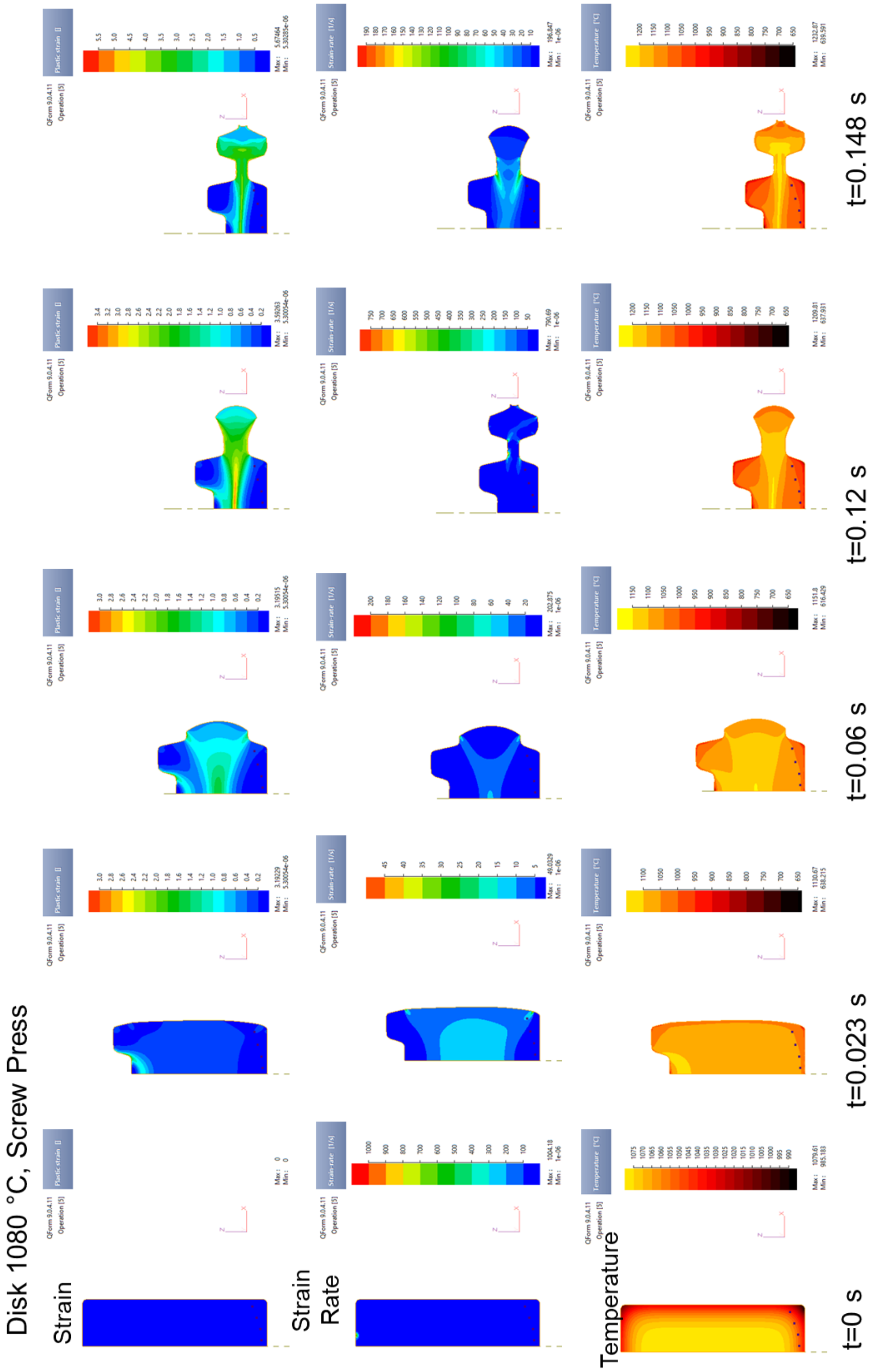
Disk 1080 °C, Screw Press
Strain
Strain Rate
Temperature
t=0 s
t=0.023 s
t=0.06 s
t=0.12 s
t=0.148 s

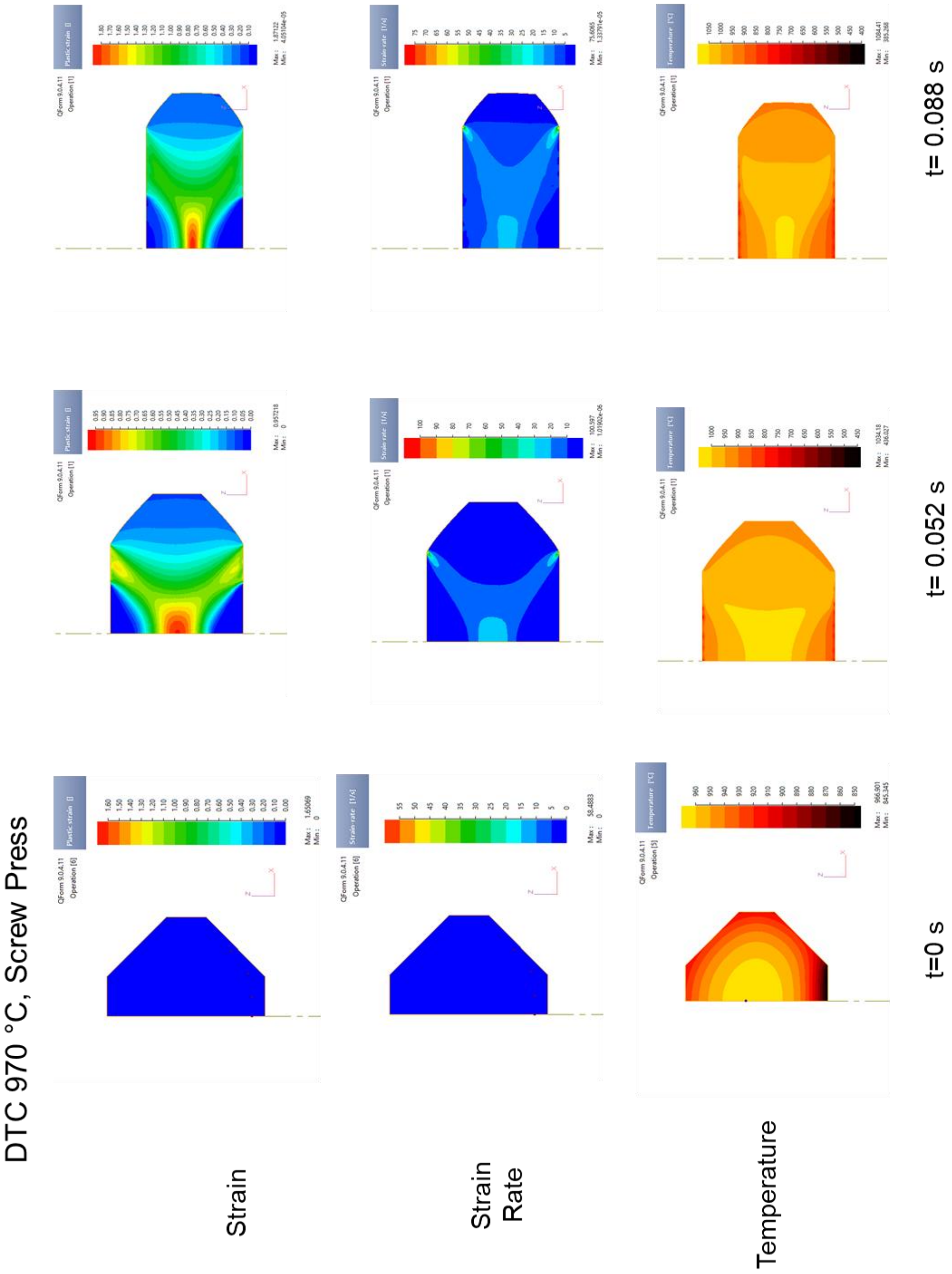
DTC 970 °C, Screw Press
Strain
Strain Rate
Temperature
t=0 s
t= 0.052 s
t= 0.088 s

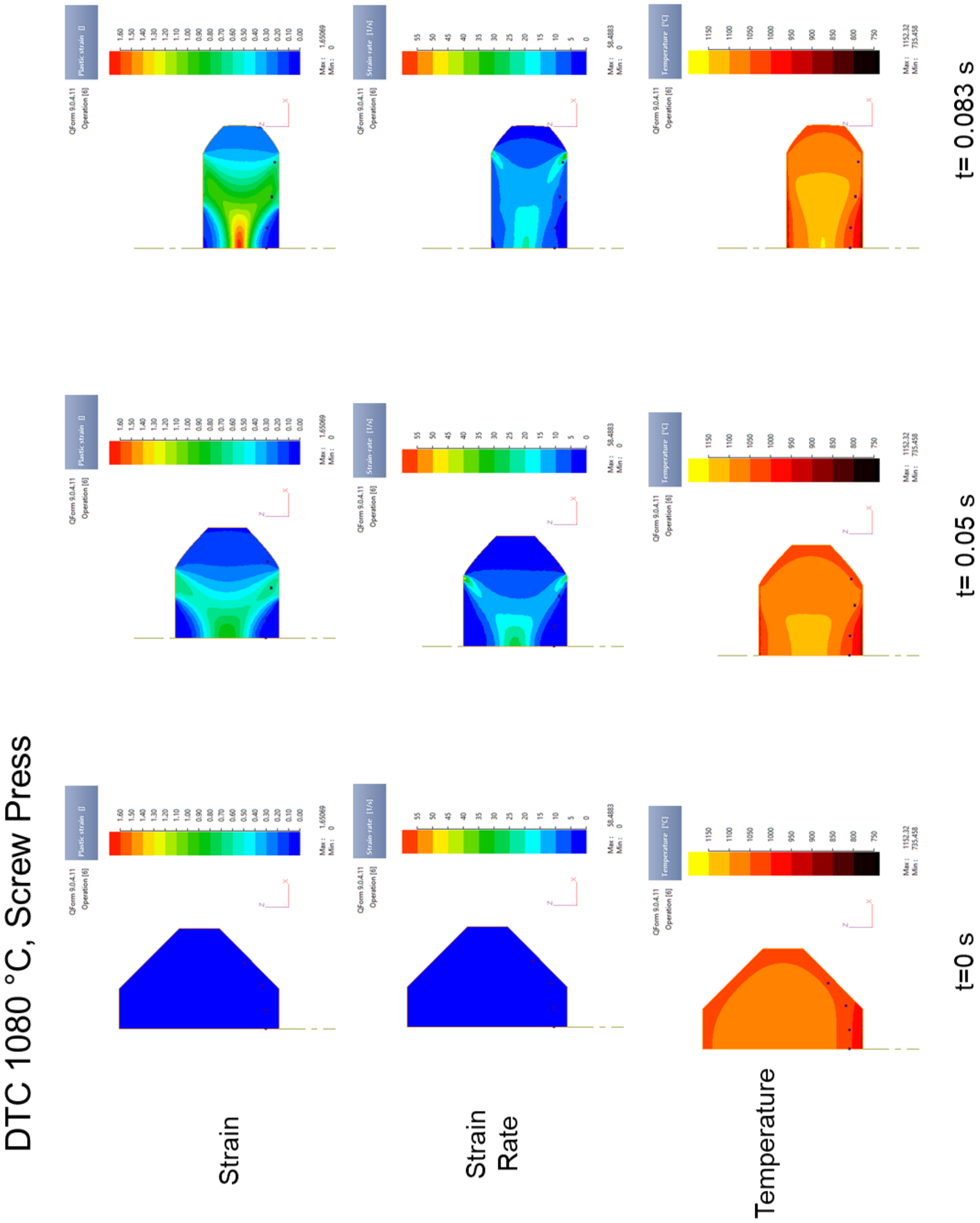
DTC 1080 °C, Screw Press
Strain
Strain Rate
Temperature
t=0 s
t= 0.05 s
t= 0.083 s
QForm 9.0.4.11
Operation [6]
Plastic strain []
1.60
1.50
1.40
1.30
1.20
1.10
1.00
0.90
0.80
0.70
0.60
0.50
0.40
0.30
0.20
0.10
0.00
Max : 1.65069
Min : 0
Strain rate [1/s]
55
50
45
40
35
30
25
20
15
10
5
0
Max : 58.4883
Min : 0
Temperature [°C]
1150
1100
1050
1000
950
900
850
800
750
Max : 1152.32
Min : 735.458
Z
X

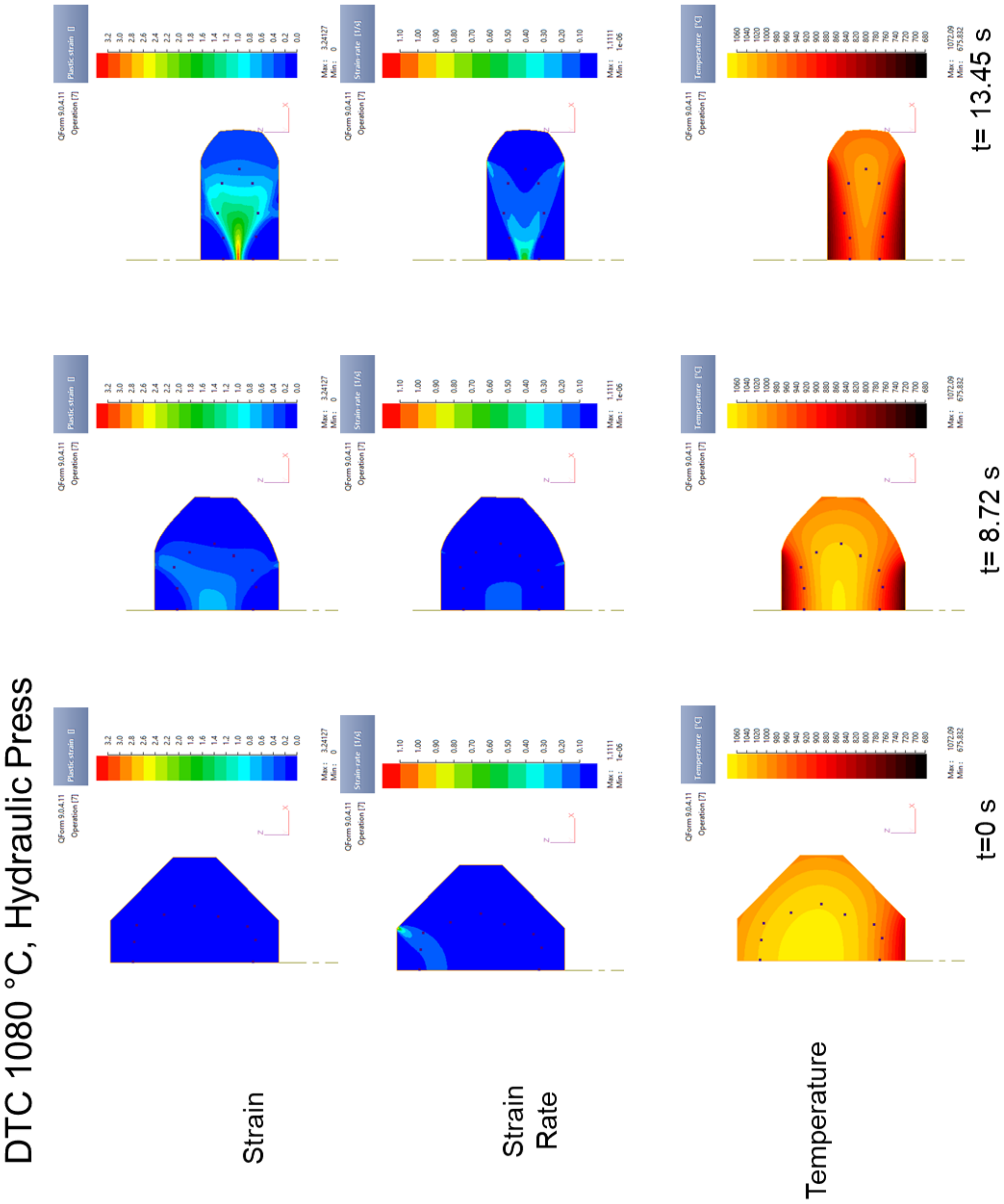
DTC 1080 °C, Hydraulic Press
Strain
Strain Rate
Temperature
t=0 s
t= 8.72 s
t= 13.45 s
QForm 9.0.4.11
Operation [7]
Plastic strain []
3.2
3.0
2.8
2.6
2.4
2.2
2.0
1.8
1.6
1.4
1.2
1.0
0.8
0.6
0.4
0.2
0.0
Max : 3.24127
Min : 0
Strain-rate [1/s]
1.10
1.00
0.90
0.80
0.70
0.60
0.50
0.40
0.30
0.20
0.10
Max : 1.1111
Min : 1e-06
Temperature [°C]
1060
1040
1020
1000
980
960
940
920
900
880
860
840
820
800
780
760
740
720
700
680
Max : 1072.09
Min : 675.832
Z
X

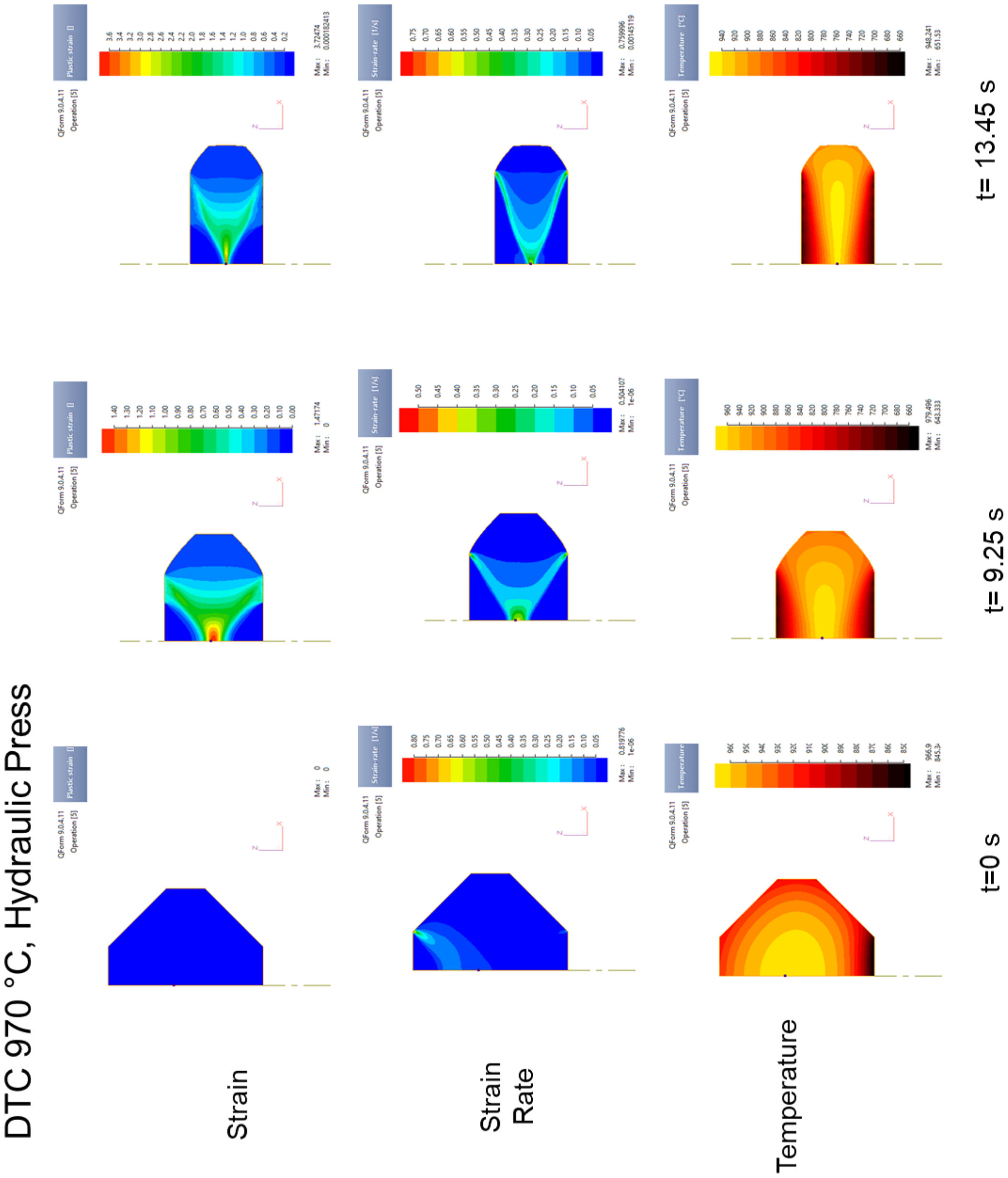

DTC 970 °C, Hydraulic Press

3.5 MATLAB Codes

3.5.1 MATLAB Code to calculate Average Grain size

```
%START OF THE CODE

load('GS_IN_TDC_processed.mat')

%DATA STRUCTURE AT THIS POINT
% Columns: 1- Grain Number ; 2 - Smaller Length ; 3 - Bigger Length;


%Calculate and add Aspect ration in column 4, average length in column 5, area in
%column 6
data=GS_IN_TDC_processed;
for i=1:max(data(:,1))
data(i,4)=data(i,3)/data(i,2); %Calculate Aspect ration in column 4
data(i,5)=(data(i,3)+data(i,2))/2; %Calculate average length in column 5
data(i,6)=((data(i,5)/2)^2)*pi; %Calculate area in column 6
end

%Total Area
TOTAREA=sum(data(:,6)); %Calculate total area of the grains

%Create Baskets adn assign 1 basket to each row
x=linspace(min(data(:,5)),max(data(:,5)),10); %Calculate baskets edges based on min and max average length of grains - e.g. 10 edges makes 9 baskets
 for i=1:max(data(:,1))
 for j=2:(size(x,2))
     if (data(i,5))<=x(j) && (data(i,5))>=x(j-1)
   data(i,7)=j; % If average diameter falls in basket, the number of the bigger boundary of the basket is assigned to the grain
   % e.g. if we take basket boundaries 1 and 2 and grain falls in, it is assigned the number 2 to the grain
     else
    end
 end
 end

%Create y Vector with total area and grain frequency for each basket
y=[];
freq=[];
for i=2:(size(x,2))
 [r,~]=(find(data(:,7)==i)); % find rows belonging to 1 basket each basket
  AreaBasket=sum(data(r,6)); % calculate total basket area
  y=[y AreaBasket]; % creating vector with basket areas
  freq=[freq size(r,1)]; % creating vector with basket frequency
end

 %Create x Vector indicating actual basket grain size (average between
 %basket edges)
 x2=[];
```

```
 for i=2:(size(x,2))
 x2=[x2 ((x(i)+x(i-1))/2)]
end


%Plotting Figure with AREA
figure
xlabel('Grain Diameter Size [Microns]')
ylabel('Area Vol Fraction %')
pbaspect([1 1 1])
set(gcf,'color','w');
grid on
hold all
xticks([round(x2)])
bar(x2,y/TOTAREA) % Plotting

avg=mean(data(:,5));
AR=mean(data(:,4));
num=max(data(:,1));
%calculate weighted average based on Area
avg2=sum((data(:,5).*data(:,6)))/TOTAREA;

% Plotting a text box with Q1, m1 and k1
        dim = [0.6 0.6 0.3 0.3];
        str = {['\bf Average GrainSize= ' num2str(round(avg))],['Weighted Average
GrainSize(area)= ' num2str(round(avg2))],['Aspect Ratio= ' num2str(round(AR,2))],['Number
of grains= ' num2str(round(num))]};
        annotation('textbox',dim,'String',str,'FitBoxToText','on','FontSize',9);
        hold on


%Plotting Figure with frequency
figure
xlabel('Grain Diameter Size [Microns]')
ylabel('Frequency')
pbaspect([1 1 1])
set(gcf,'color','w');
grid on
hold all
bar(x2,freq)
xticks([round(x2)])

avg=mean(data(:,5));
AR=mean(data(:,4));
num=max(data(:,1));
% Plotting a text box with Avg Grain Size, Aspect Ration, Number of grains
      dim = [0.6 0.6 0.3 0.3];
        str = {['\bf Average GrainSize= ' num2str(round(avg))],['Weighted Average
GrainSize(area)= ' num2str(round(avg2))],['Aspect Ratio= ' num2str(round(AR,2))],['Number
of grains= ' num2str(round(num))]};
        annotation('textbox',dim,'String',str,'FitBoxToText','on','FontSize',9);
        hold on
```

Appendix 4

4.1 Comparison between fully forged and half forged Disk (970 °C on Screw Press).

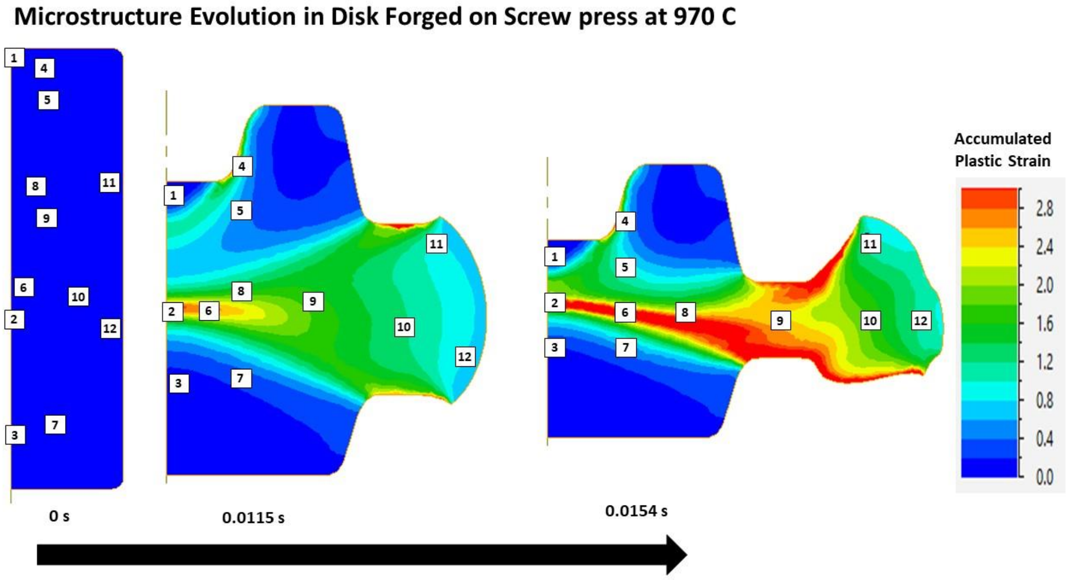

Microstructure Evolution in Disk Forged on Screw press at 970 C

Microstructure Evolution in Disk Forged on Screw press at 970 C - Location 1 and 2

- ◆ Intermediate Microstructure
- ● Final Microstructure

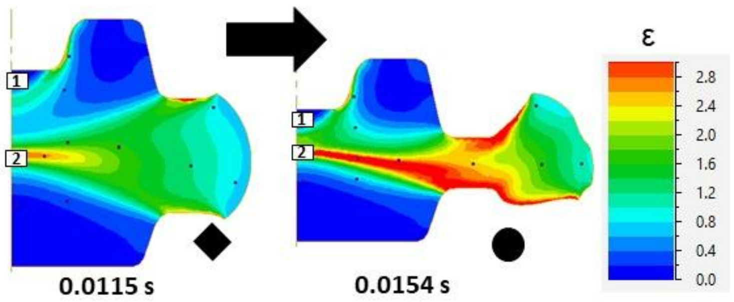

Point 1.

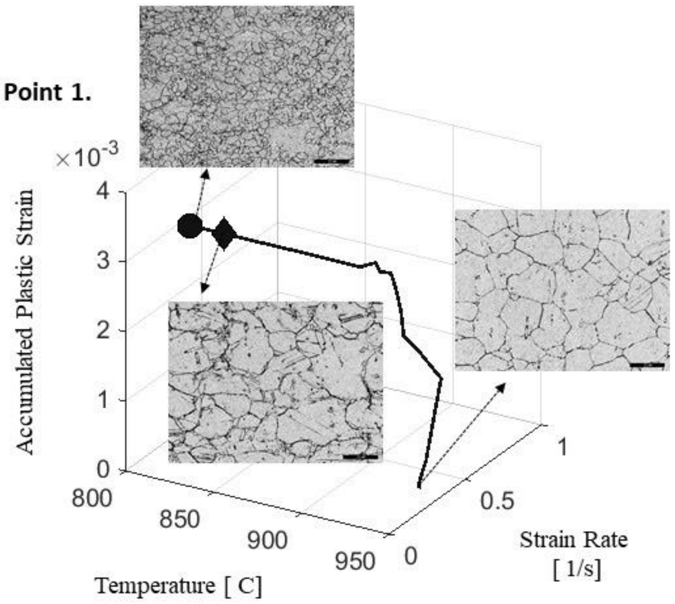

Point 2.

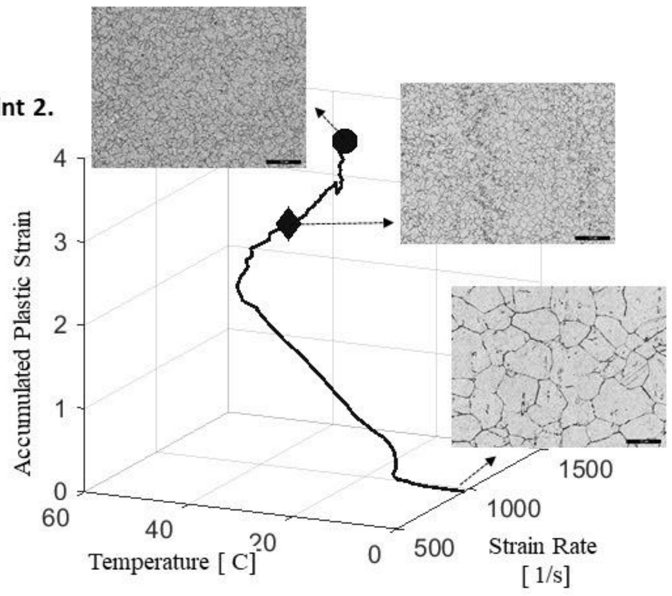

Microstructure Evolution in Disk Forged on Screw press at 970 C - Location 3 and 4

◆ **Intermediate Microstructure**

● **Final Microstructure**

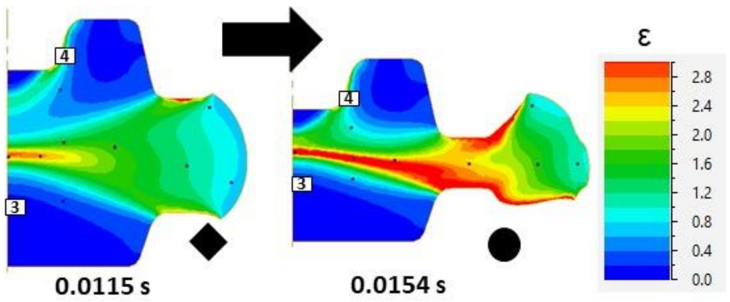

Point 3.

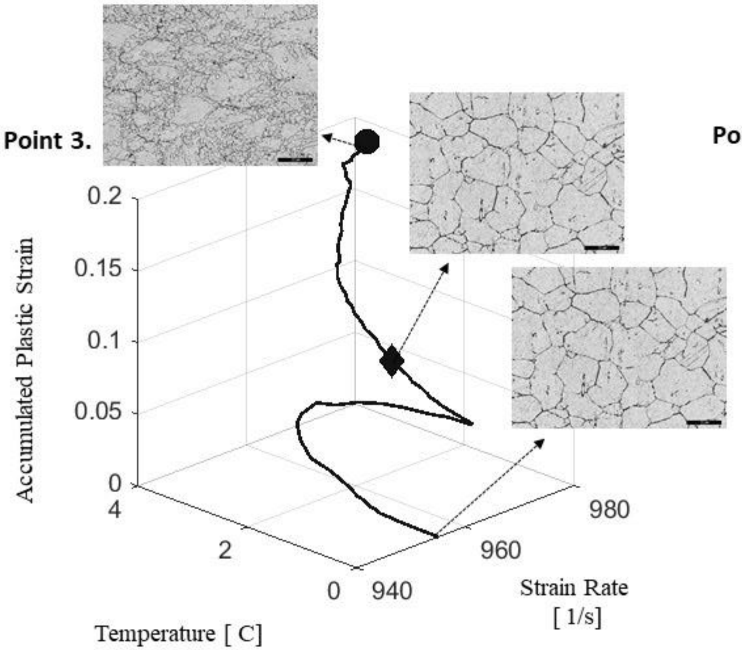

Point 4.

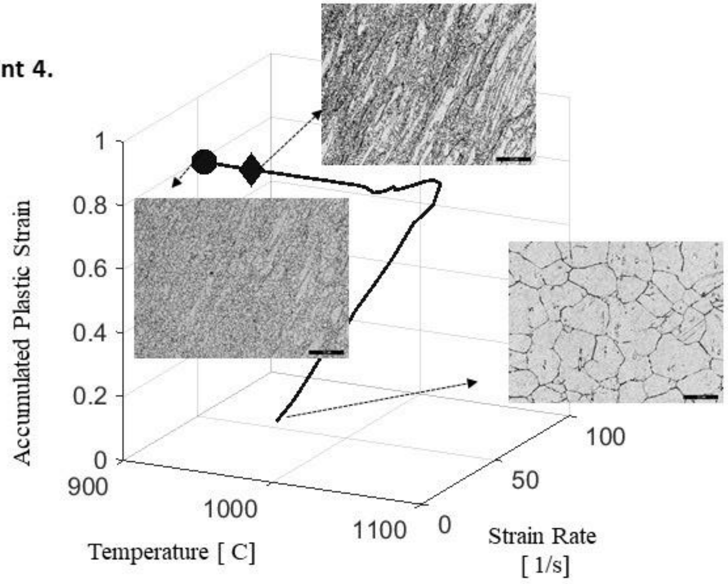

Microstructure Evolution in Disk Forged on Screw press at 970 C - Location 5 and 6

- ◆ Intermediate Microstructure
- ● Final Microstructure

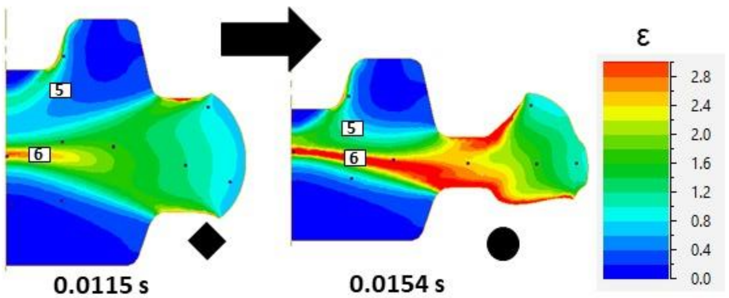

Point 5.

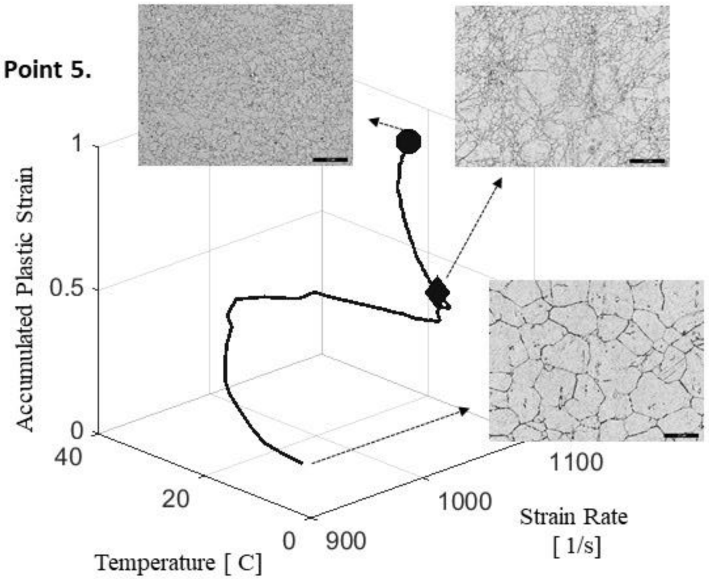

Point 6.

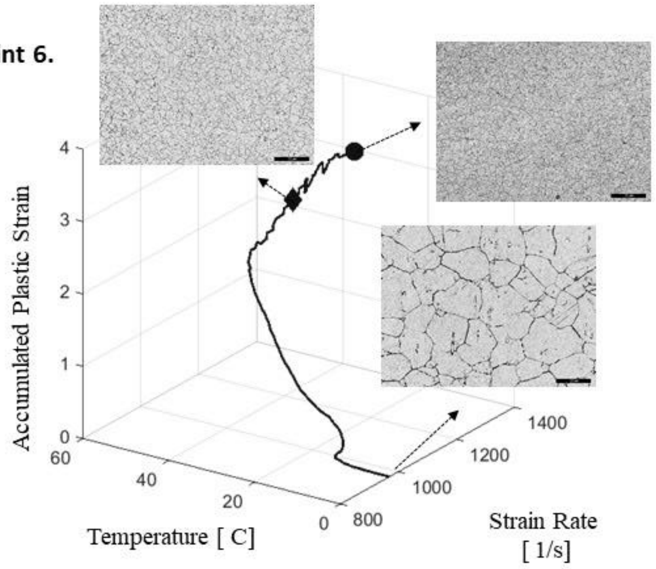

Microstructure Evolution in Disk Forged on Screw press at 970 C - Location 7 and 8

◆ Intermediate Microstructure

● Final Microstructure

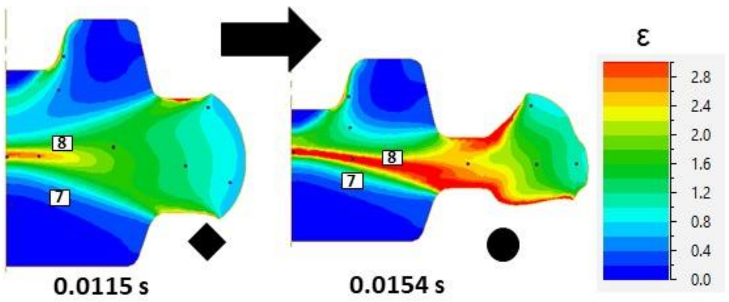

Point 7.

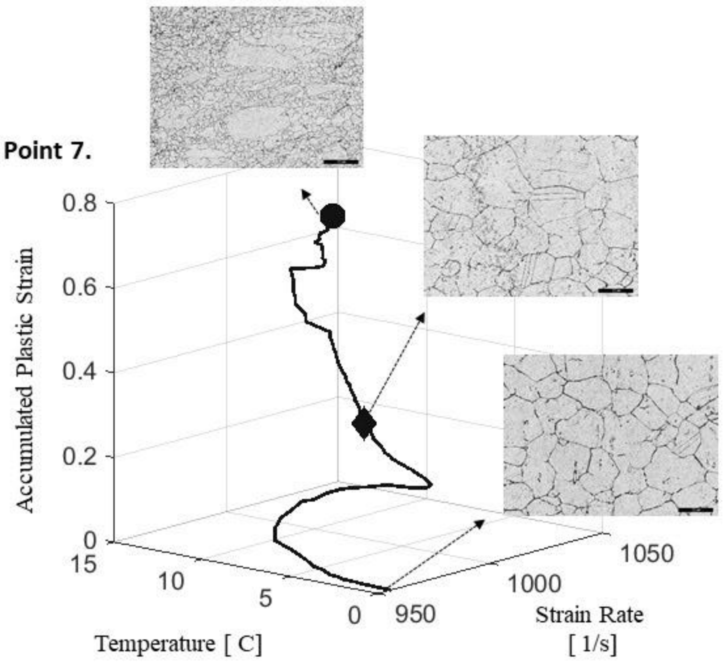

Point 8.

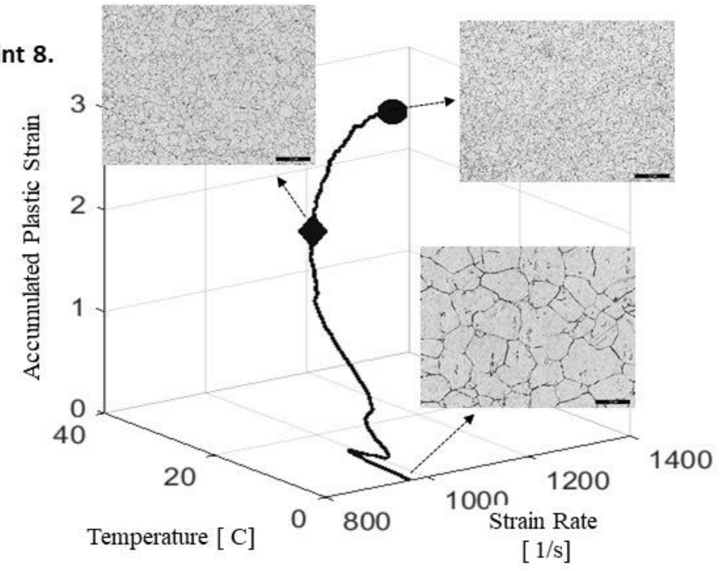

Microstructure Evolution in Disk Forged on Screw press at 970 C- Location 9 and 10

◆ Intermediate Microstructure

● Final Microstructure

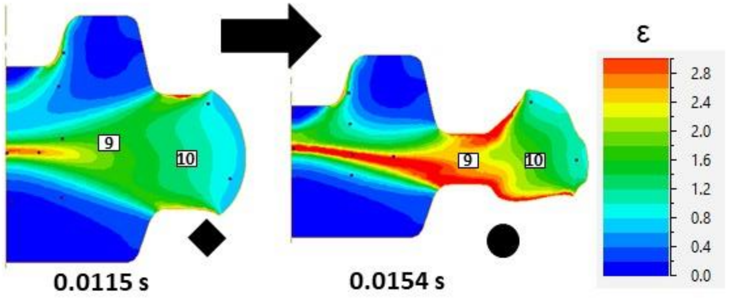

Point 9.

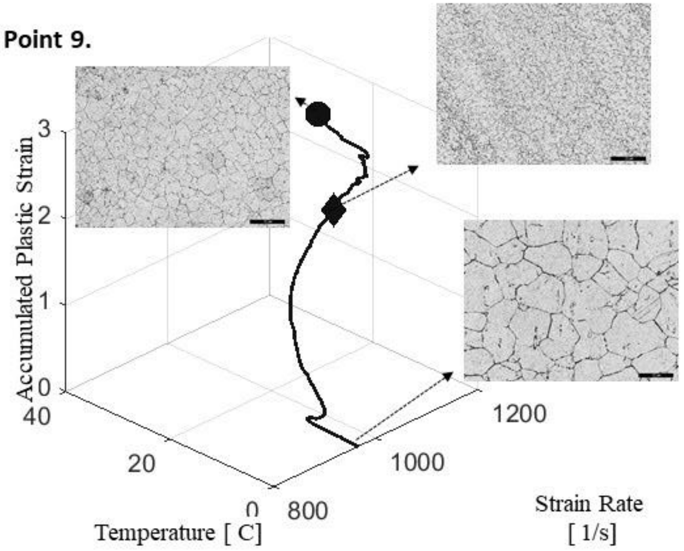

Point 10.

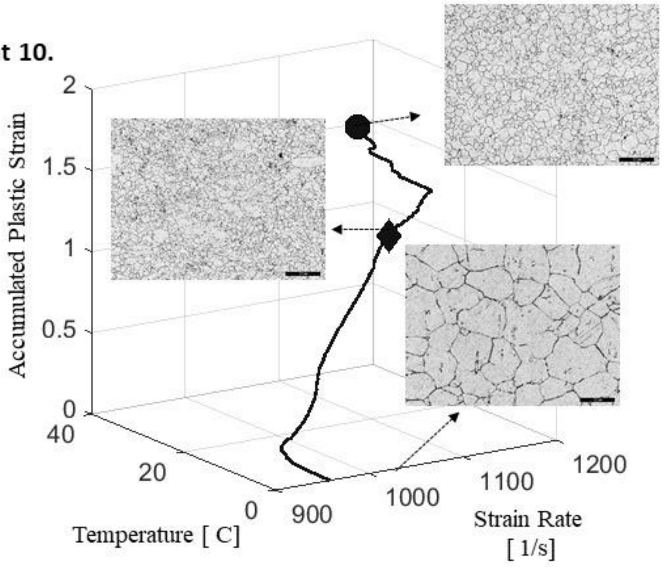

Microstructure Evolution in Disk Forged on Screw press at 970 C - Location 11 and 12

- ◆ **Intermediate Microstructure**
- ● **Final Microstructure**

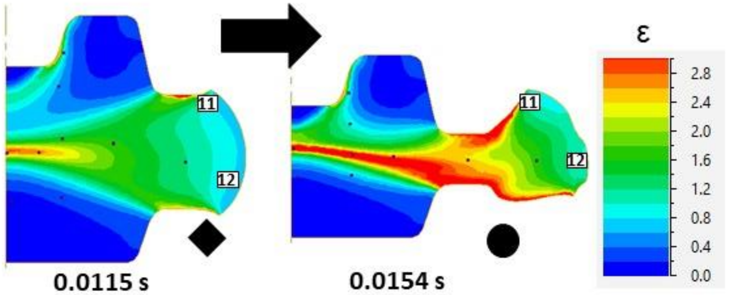

Point 11.

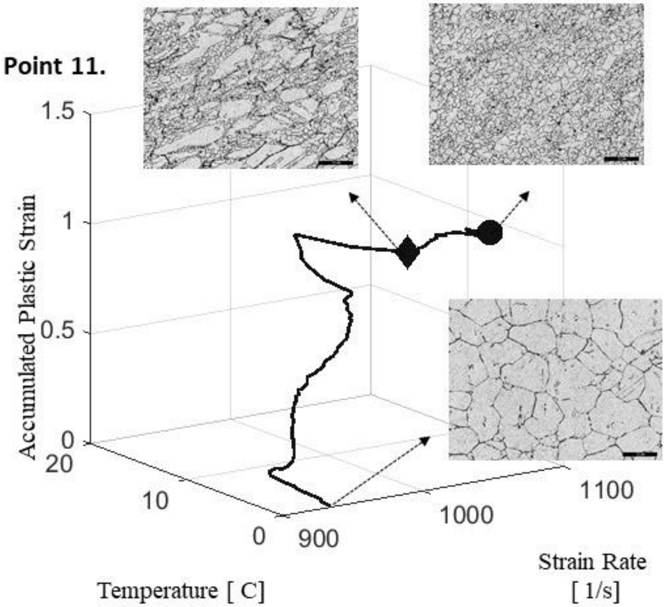

Point 12.

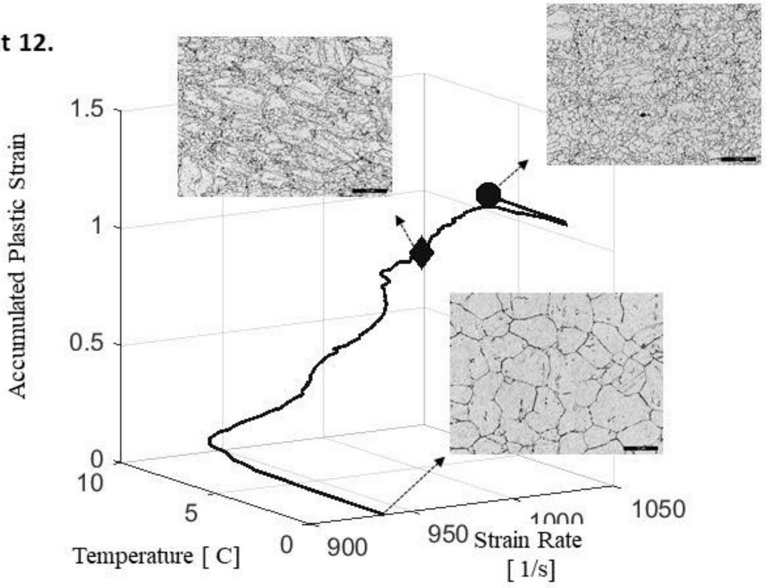

4.2 Microstructure Collection

During this project a vast number of microstructural pictures were taken and not included in the main text. However, this could be useful for other researchers who wish to use the data developed in this project.

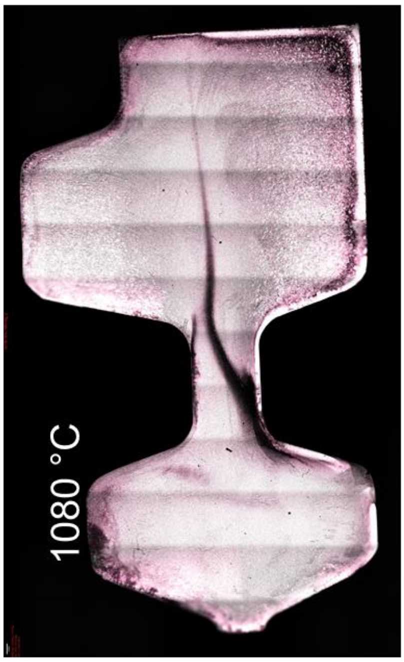

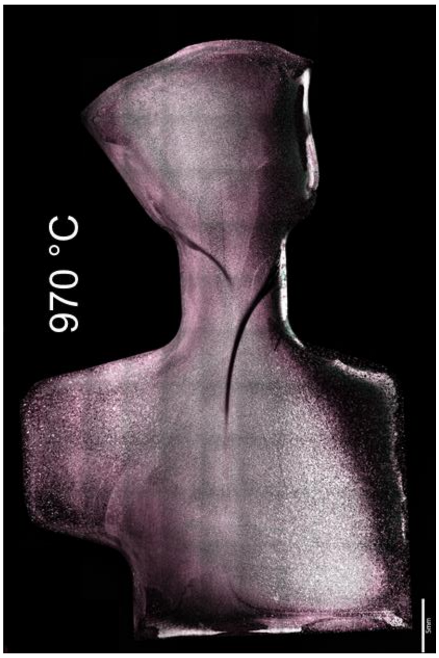

Disk- Screw Press Forgings
-
Alicona Microscope

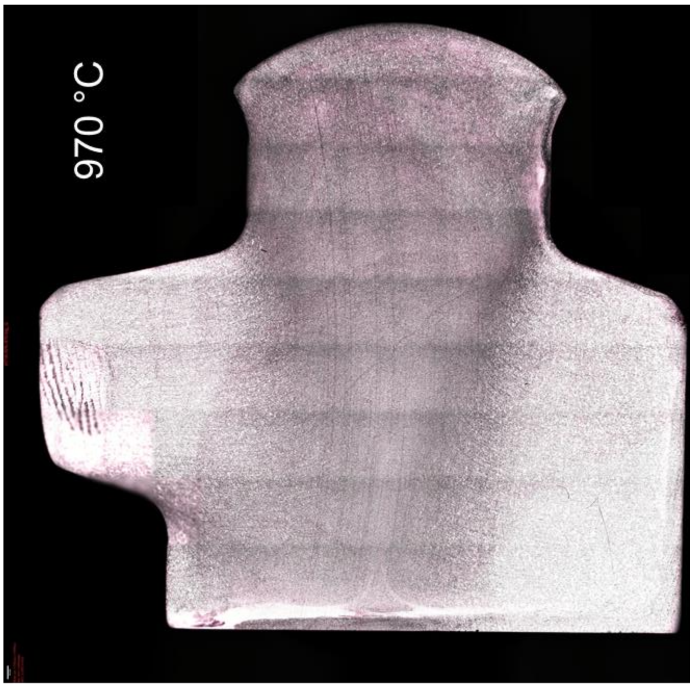

DTC- Screw Press Forgings
-
Alicona Microscope

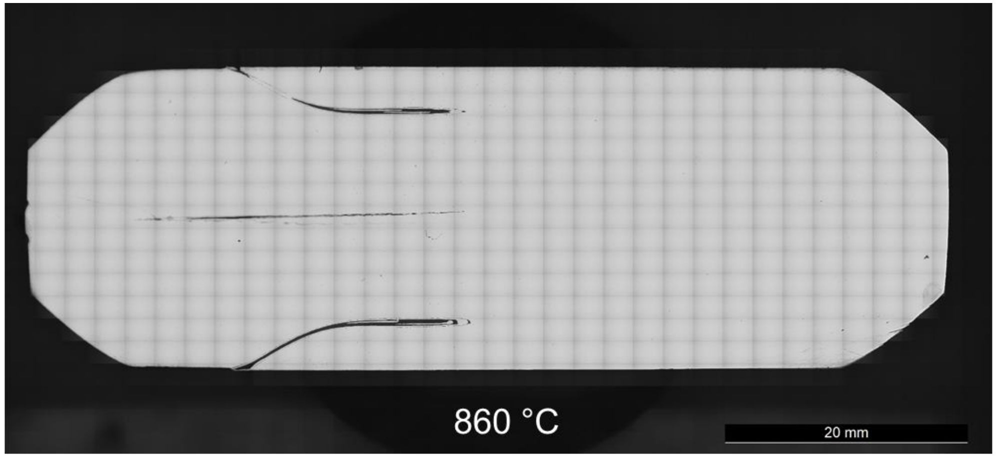

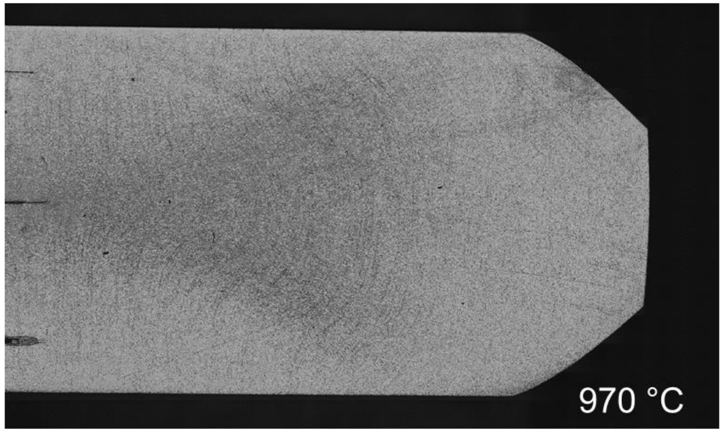

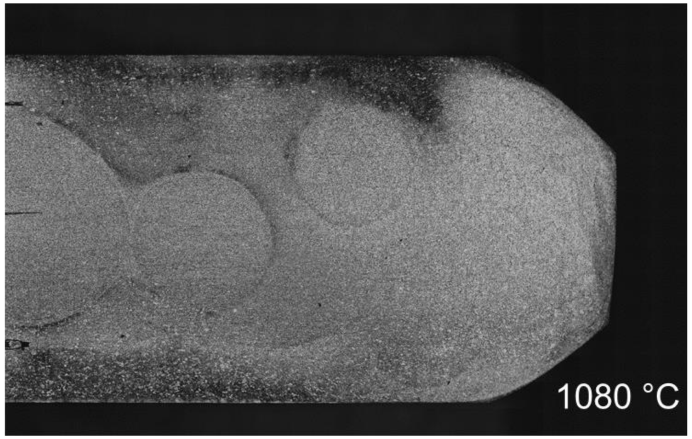

DTC- Hydraulic Press Forgings - Alicona Microscope

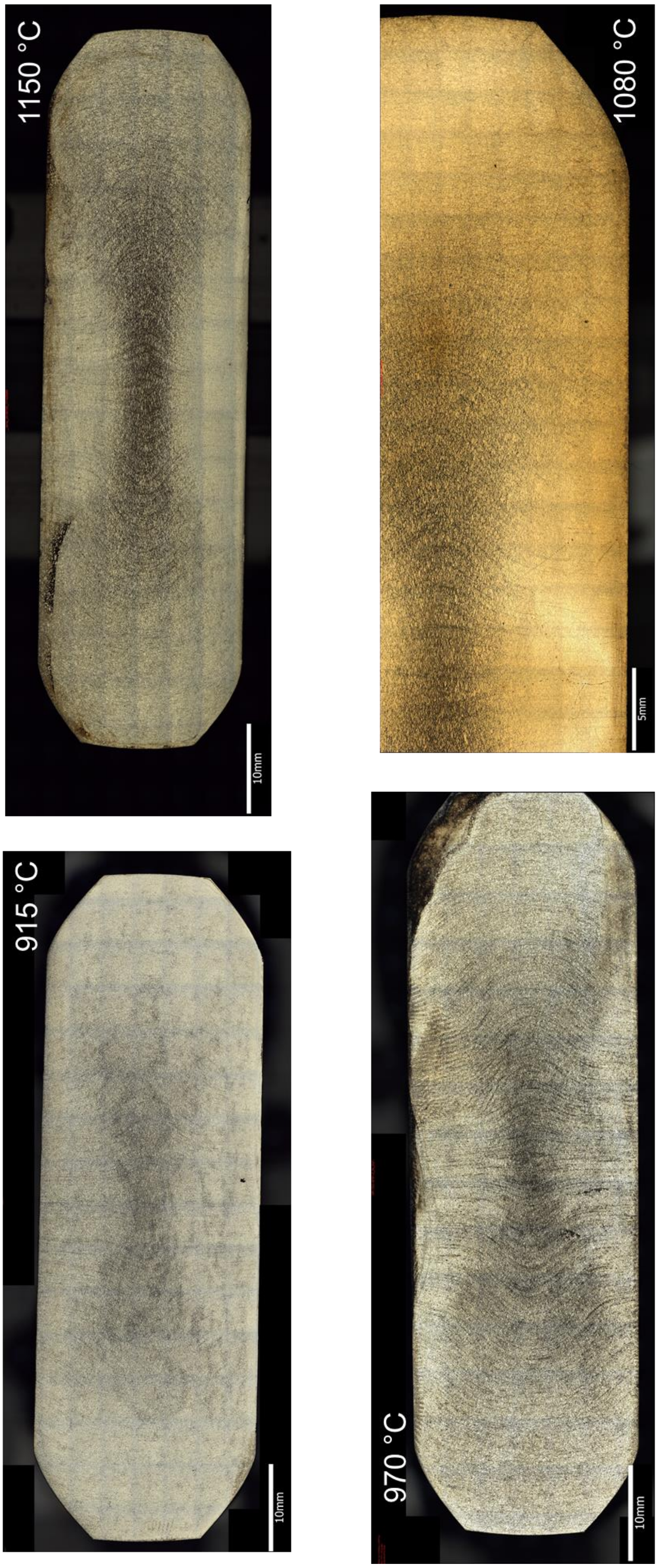

DTC 1080 °C, Hydraulic Press

Point N	X	Y	Mag 1
1	0	23	20x
2	0	22	20x
3	0	21	20x
4	0	20	20x
5	0	19	20x
6	0	18	20x
7	0	17	20x
8	0	16	20x
9	0	15	20x
10	0	14	20x
11	0	13	20x
12	0	12	20x
13	0	11	20x
14	0	10	20x
15	0	9	20x
16	0	8	20x
17	0	7	20x
18	0	6	20x
19	0	5	20x
20	0	4	20x
21	0	3	20x
22	0	2	20x
23	0	1	20x

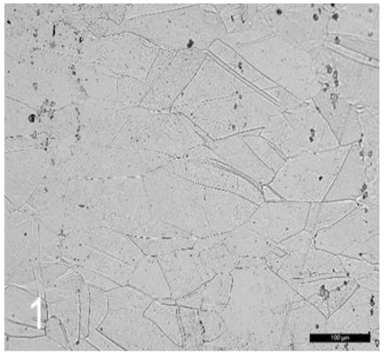

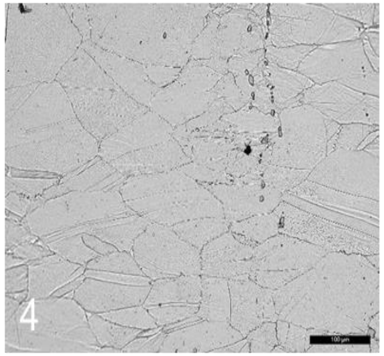

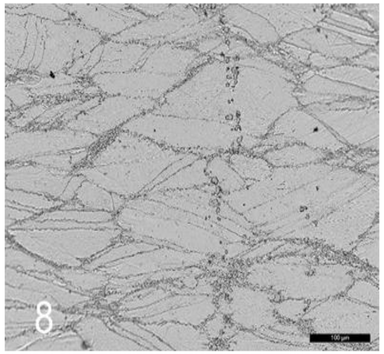

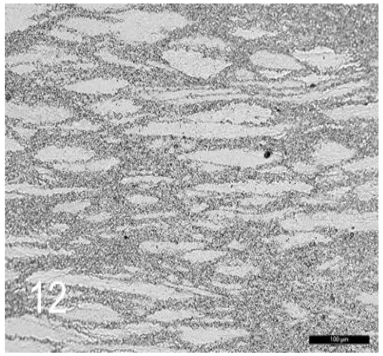

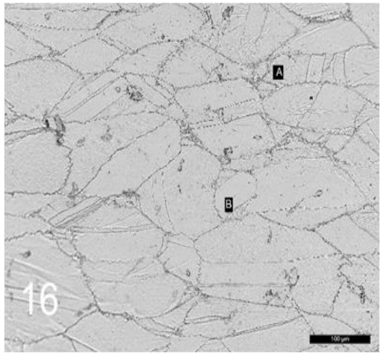

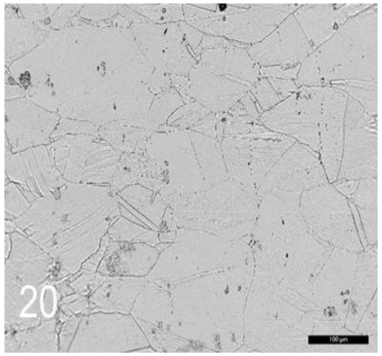

DTC 1080 °C, Hydraulic Press

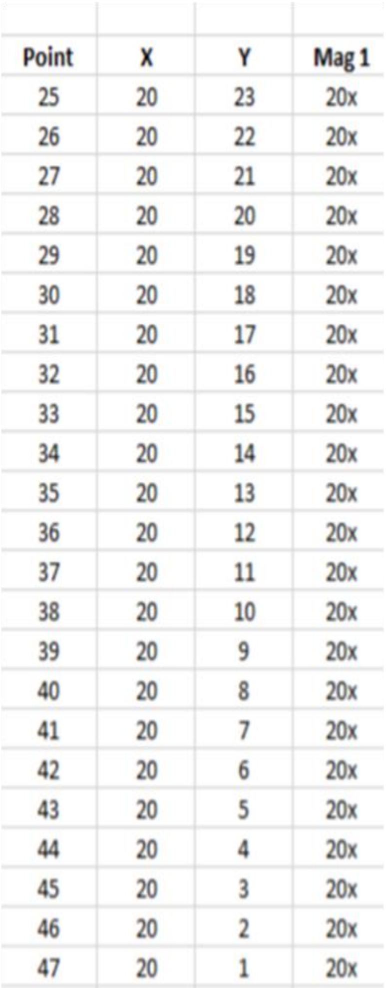

Point	X	Y	Mag 1
25	20	23	20x
26	20	22	20x
27	20	21	20x
28	20	20	20x
29	20	19	20x
30	20	18	20x
31	20	17	20x
32	20	16	20x
33	20	15	20x
34	20	14	20x
35	20	13	20x
36	20	12	20x
37	20	11	20x
38	20	10	20x
39	20	9	20x
40	20	8	20x
41	20	7	20x
42	20	6	20x
43	20	5	20x
44	20	4	20x
45	20	3	20x
46	20	2	20x
47	20	1	20x

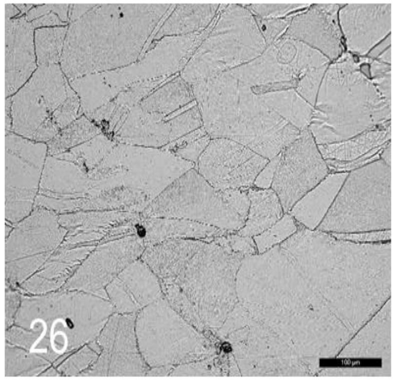

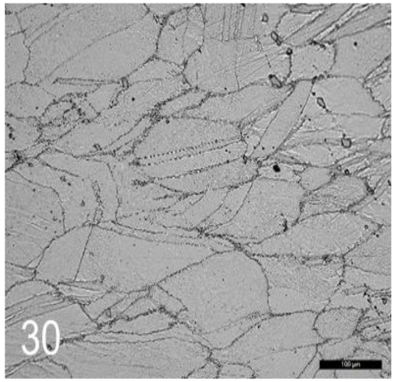

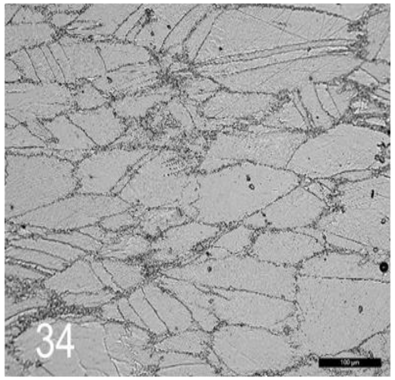

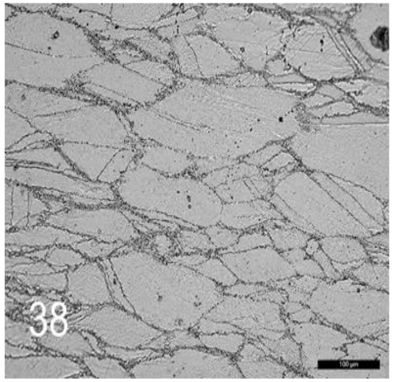

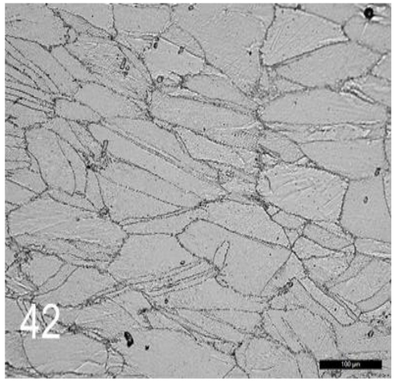

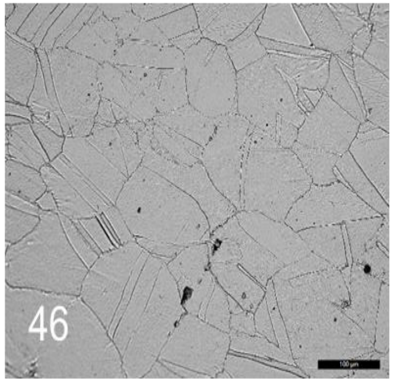

DTC 970 °C, Hydraulic Press

Point N	X	Y	Mag 1
1	0	23	20x
2	0	22	20x
3	0	21	20x
4	0	20	20x
5	0	19	20x
6	0	18	20x
7	0	17	20x
8	0	16	20x
9	0	15	20x
10	0	14	20x
11	0	13	20x
12	0	12	20x
13	0	11	20x
14	0	10	20x
15	0	9	20x
16	0	8	20x
17	0	7	20x
18	0	6	20x
19	0	5	20x
20	0	4	20x
21	0	3	20x
22	0	2	20x
23	0	1	20x

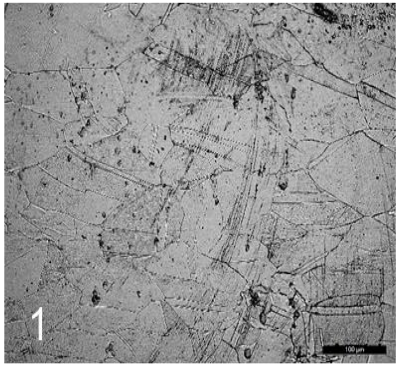

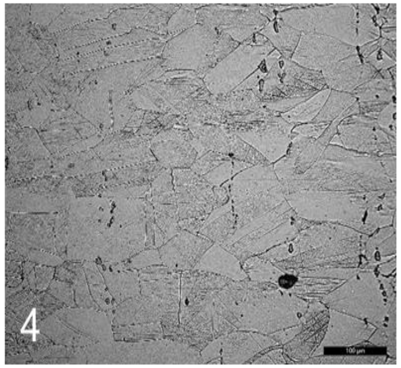

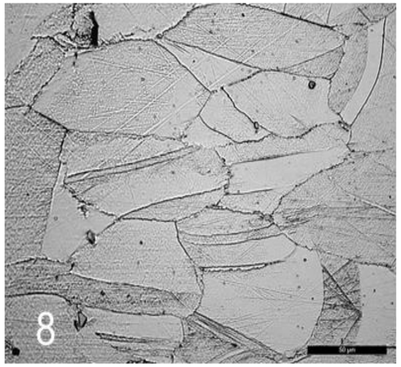

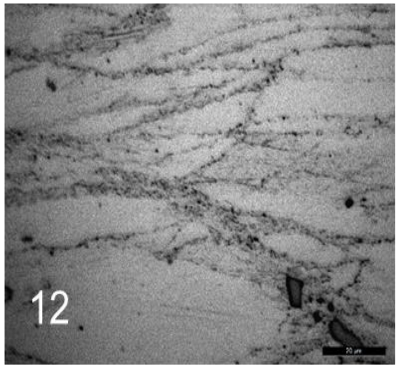

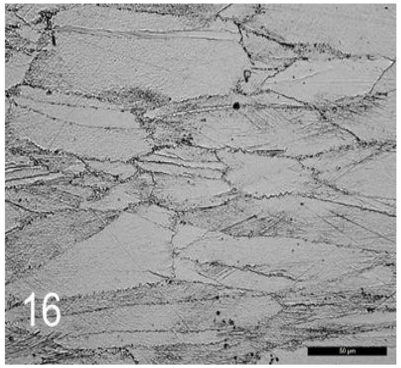

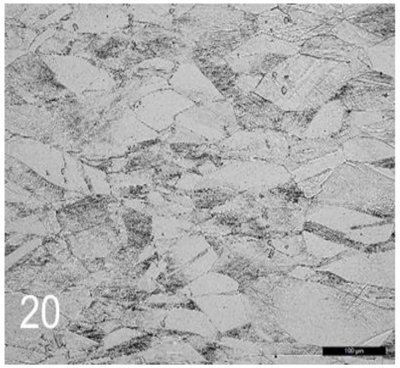

DTC 970 °C, Hydraulic Press

Point	X	Y	Mag 1
25	20	23	20x
26	20	22	20x
27	20	21	20x
28	20	20	20x
29	20	19	20x
30	20	18	20x
31	20	17	20x
32	20	16	20x
33	20	15	20x
34	20	14	20x
35	20	13	20x
36	20	12	20x
37	20	11	20x
38	20	10	20x
39	20	9	20x
40	20	8	20x
41	20	7	20x
42	20	6	20x
43	20	5	20x
44	20	4	20x
45	20	3	20x
46	20	2	20x
47	20	1	20x

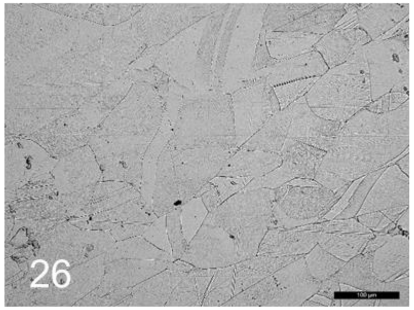

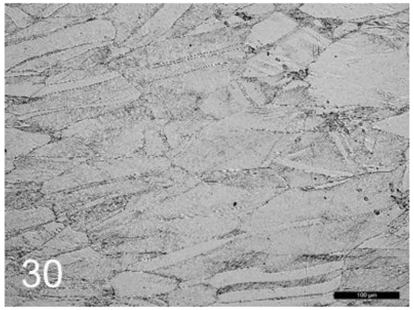

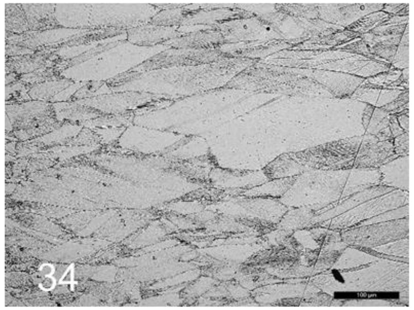

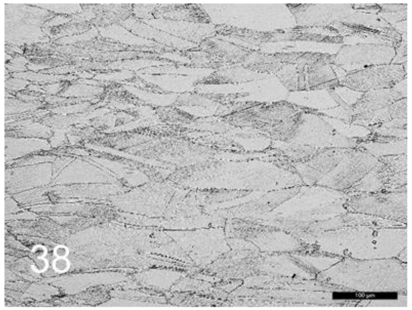

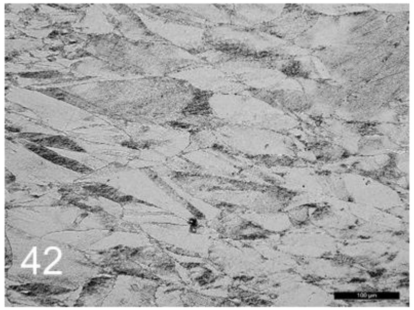

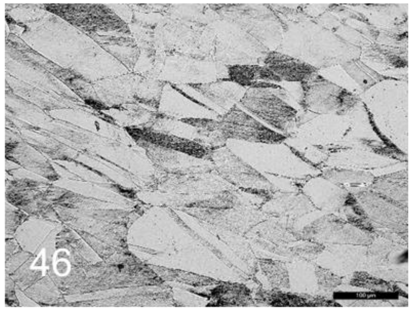

Disk 970 °C, Screw Press, Zero Boundary

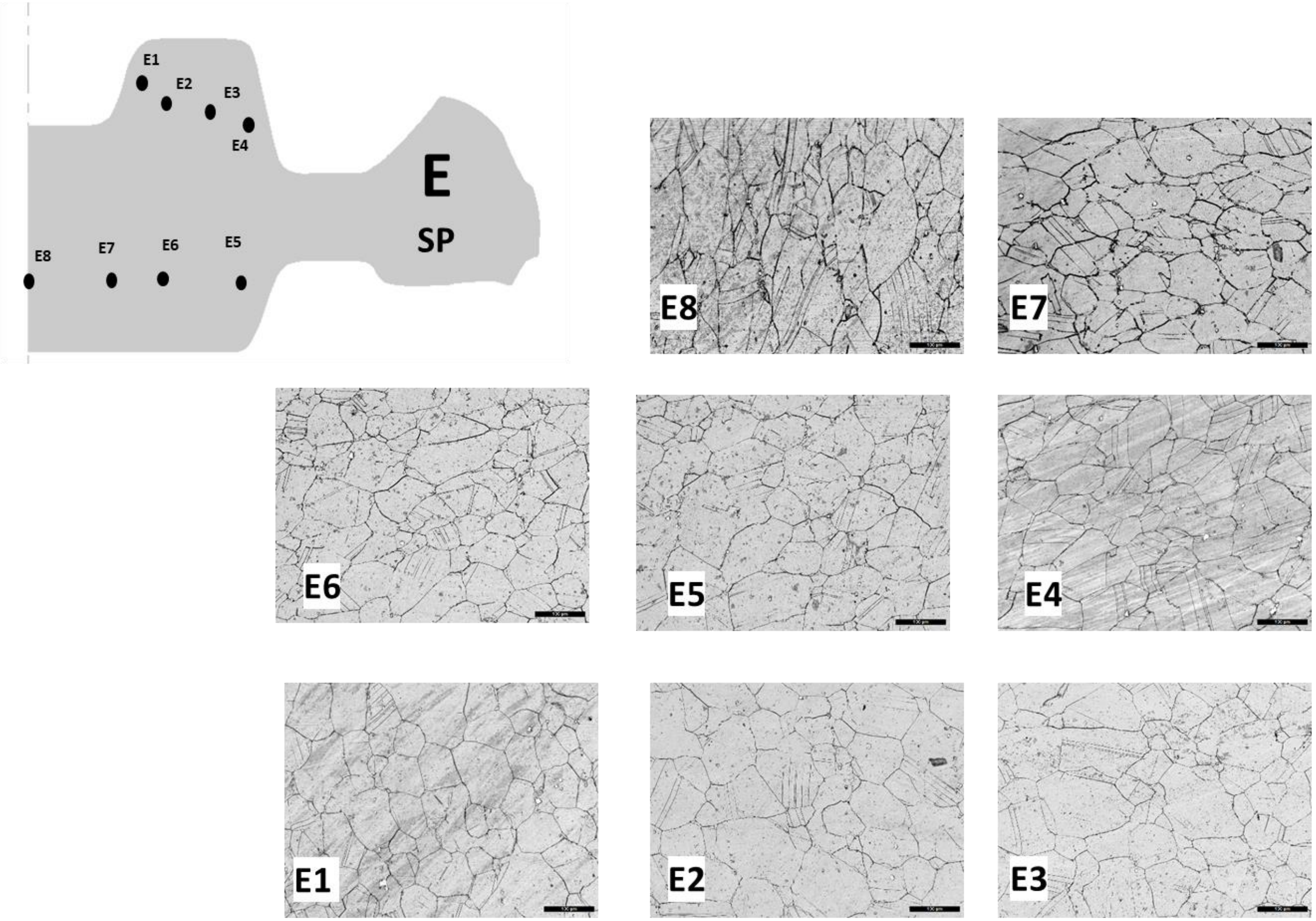

Disk 1080 °C, Screw Press, Zero Boundary

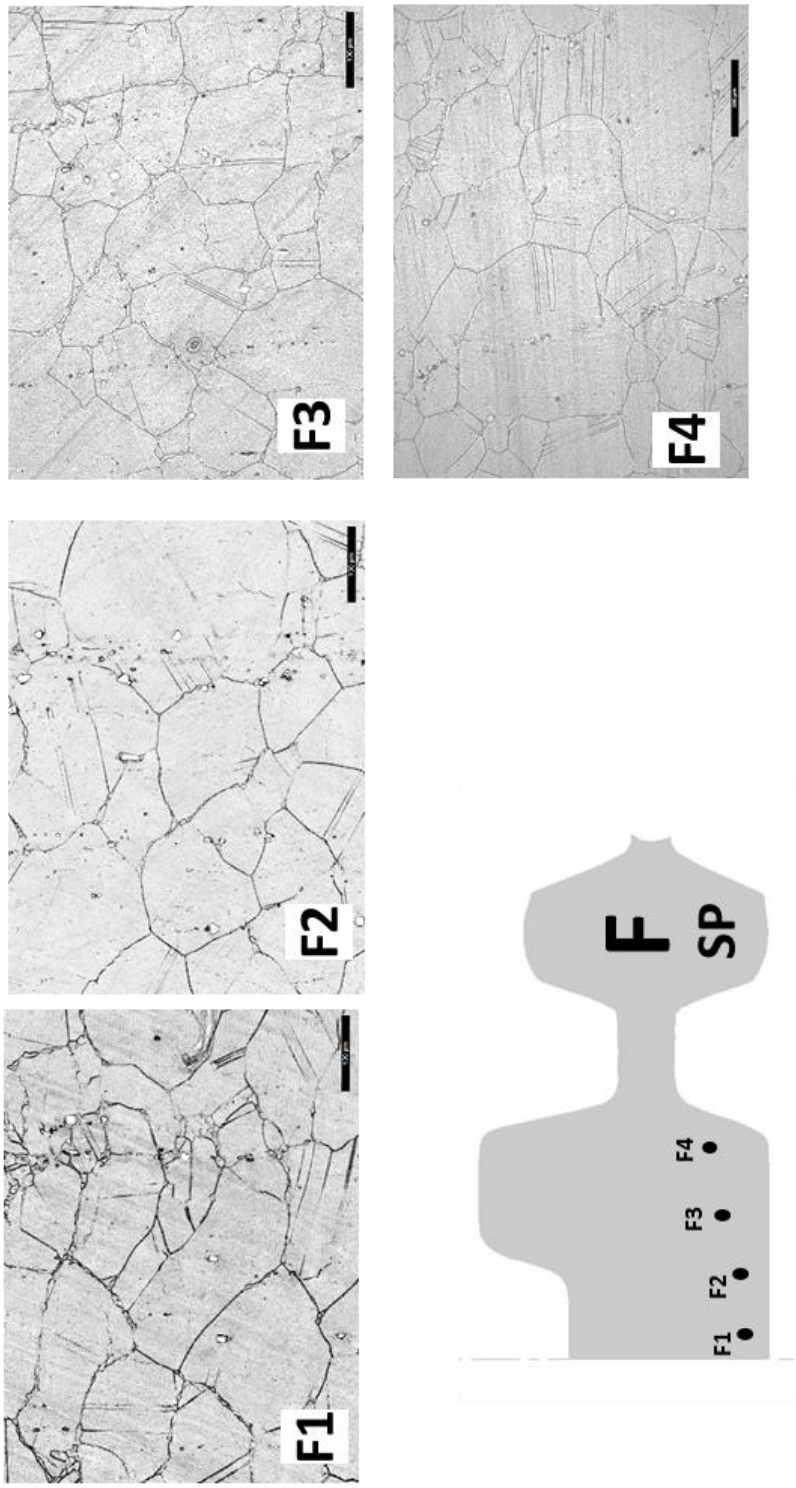

Appendix 5

5.1 Lua Subroutine

```
set_target_workpiece() -- What this subroutine is going to act on

-- a1       a2  n1  m1  c1  Q1 [J/mol]  R [J/(K*mol)    --Critical
Strain Constants
-- 0.0046590    0.83    0.00    0.1238  0.00    49520.00    8.31

--a5            h5  n5  m5  C5  Q5 [J/mol]  R [J/(K*mol)    -- 0.5
Strain Constants
--0.000000005043    0.00    -1.42   -0.41   0.00    196000.00   8.31


--a10   Bd  kd --  DRX Volume Fraction Constants
--0.8   0.69    1.00


Mat_con_a1=parameter("Mat_con_a1", 0.0046590)  -- Material constant
a1
Mat_con_a2=parameter("Mat_con_a2", 0.83)  -- Material constant a2
Mat_con_a5=parameter("Mat_con_a5", 0.000000005043)  -- Material
constant a5
Mat_con_a10=parameter("Mat_con_a10", 0.8)  -- Material constant a10
Mat_con_n1=parameter("Mat_con_n1", 0)  -- Material constant n1
Mat_con_m1=parameter("Mat_con_m1", 0.1238)  -- Material constant m1
Mat_con_c1=parameter("Mat_con_c1", 0)  -- Material constant c1
Mat_con_Q1=parameter("Mat_con_Q1", 49520)  -- Material constant Q1
Mat_con_h5=parameter("Mat_con_h5", 0)  -- Material constant h5
Mat_con_n5=parameter("Mat_con_n5", -1.42)  -- Material constant n5
Mat_con_m5=parameter("Mat_con_m5", -0.41)  -- Material constant m5
Mat_con_c5=parameter("Mat_con_c5", 0)  -- Material constant c5
Mat_con_Q5=parameter("Mat_con_Q5", 196000)  -- Material constant Q5
Mat_con_bd=parameter("Mat_con_bd", 0.69)  -- Material constant bd
Mat_con_kd=parameter("Mat_con_kd", 1)  -- Material constant kd
Gas_constant=parameter("Gas_constant", 8.31)-- Universal Gas
Constant R
initial_grain_size=parameter("initial_grain_size",100) --
initial_grain_size

Recrystallisation=result("Recrystallisation",0) -- DRX Volume
Fraction
CriticalStrain=result("CriticalStrain",0) -- Critical Strain
PeakStrain=result("PeakStrain",0) -- Peak Strain
Strain_zero_point_five=result("Strain_zero_point-five",0) -- Strain
to achieve 50% DRX
DRX_vol_fraction=result("DRX_vol_fraction",0) -- DRX Volume Fraction
PossRX=result("PossRX",0) -- Where Strain is more than Critical
Strain

function UserFields (T, dt, strain,
strain_rate,prev_DRX_vol_fraction)  --we select the parameters that
we will be calling from the software so as to use them in our
function
```

```
TK=T+273

PK=((Mat_con_a1*(initial_grain_size^Mat_con_n1)*(strain_rate^Mat_con
_m1)*2.71^(Mat_con_Q1/(Gas_constant*TK))))+Mat_con_c1 --PeakStrain

CR=PK*Mat_con_a2 -- Critical Strain

ST_ZE_FI=(Mat_con_a5*(initial_grain_size^Mat_con_h5)*(strain^Mat_con
_n5)*(strain_rate^Mat_con_m5)*2.71^(Mat_con_Q5/(Gas_constant*TK)))+M
at_con_c5 -- Strain to achieve 50% RX

Vol=1-2.71^(-Mat_con_bd*((strain-
PK*Mat_con_a10)/ST_ZE_FI)^Mat_con_kd) -- VOL fraction RX

if Vol<prev_DRX_vol_fraction then

Vol=prev_DRX_vol_fraction

end

if strain>CR then
PRX=1
else
end

if strain>CR and prev_Recrystallisation==0 and strain_rate>0.01 then

    RX=1

    else

    end


store (PeakStrain, PK) -- Association of the displaying result
Critical Strain with CR
store (CriticalStrain, CR) -- Association of the displaying result
Critical Strain with CR
store (Strain_zero_point_five, ST_ZE_FI) -- Association of the
displaying result Strain to achieve 50% DRX
store (DRX_vol_fraction, Vol) -- volume fraction
store (Recrystallisation, RX) -- volume fraction
store (PossRX, PRX) -- Where Strain is more than Critical Strain

end -- exit subroutine
```

5.2 MATLAB Codes

5.2.1 Plot trajectories as Points

```
%Plot trajectories as cloud of points

f=figure
load('cone_data.mat')
points=cone_data;

scatter3(points(:,2),log10(points(:,4)),points(:,3),'filled','Mar
kerEdgeColor','k','MarkerFaceColor','g');
hold on

set(gca,'FontSize',15)
set(f,'color','w')
```

5.2.2 Plot trajectories as Lines

```
%Plot trajectories as lines

f=figure
load('cone_data.mat')
points=cone_data;

SN=Insert_here_number_of_Steps; %Step Number
points=cone_data;
x=1;
for j=1:(length(points(:,1))/SN) % plot trajectories
    y=x+(SN-1);

p=plot3(points(x:y,2),points(x:y,4),points(x:y,3),'color','k'); %
plot trajectory of each j point
    hold on
 x=x+SN;
end
set(gca,'FontSize',15)
set(f,'color','w')
```

5.2.3 Find Top Points from Clout of Points

```
N.B. The results of this code are greatly influenced by the size
of the baskets taken. Indeed, if the basket is too small all the
points in the trajectories will be taken, however if the baskets
are too big important points will be discarded. The size of the
basket will be greatly influenced by density and shape of the
thermo-mechanical cloud of points.

%Find Top Points of Cloud Trajectories

 f=figure
```

```
load('cone_data.mat')
points=cone_data;
dT=(max(points(:,2))- min(points(:,2)))/20;

dSTR=(max(points(:,3))- min(points(:,3)))/20;

TopPoints=[0 0 0];

lowT=min(points(:,2));
upT=lowT+dT;
lowSTR=0;
upSTR=0;
B=0;

for i=1:(max(points(:,2))- min(points(:,2)))/dT
 upT=lowT+dT;
 for j=1:(max(points(:,3))- min(points(:,3)))/dSTR
 lowSTR=0+dSTR*(j-1);
     upSTR=lowSTR+dSTR;
[r,c]=find(points(:,2)>=lowT & points(:,2)<=upT &
points(:,3)>=lowSTR & points(:,3)<=upSTR);
A=max(points(r,4));
if A ~= 0
[r2,c2]=find(points(r,4)==A);
B=points(r(r2),:);
if length(B(:,1))>1
r2=r2(1);
else
end
TopPoints(length(TopPoints(:,1))+1,:)=[points(r(r2),2)
points(r(r2),3) points(r(r2),4)];
else
end
  lowSTR=lowSTR+dSTR;
 end
lowT=lowT+dT;
end
TopPoints(1,:)=[];

scatter3(TopPoints(:,1),log10(TopPoints(:,2)),TopPoints(:,3),'fi
lled','MarkerEdgeColor','k','MarkerFaceColor','r');
hold on
set(gca,'FontSize',18)
set(f,'color','w')
```

5.2.4 Artificially Increase Number of Trajectory Points

```
%This code will take a thermos-mechanical points trajectories
%Then a curve will be fitted and divided into more points with
the final aim of multiplying initial set of points (multiplied by
a factor of 5 in the code below).

f=figure
set(gca,'FontSize',18)
set(f,'color','w')

load('cone_data')
initialpoints=cone_data;
numberofpoints=INSERT_NUMBER_DEPENDING_ON_DATA;  % INSERT NUMBER
DEPENDING ON HOW MANY POINTS IN THE FILE

scatter3(initialpoints(:,2),log10(initialpoints(:,3)),initialpoin
ts(:,4),30,'filled','MarkerEdgeColor','k','MarkerFaceColor','b')
hold on

cone_7_extended=[0 0 0 0];
a=1;
pointnum=[0];
for i=1:numberofpoints
    points=cone_7;
    [r,c]=find(points(:,1)==i);
% multiply the data in X column
x_extended = interp(points(r,2),5);
% multiply the data in Y column
y_extended = interp(points(r,3),5);
% multiply the data in Z column
z_extended = interp(points(r,4),5);
b=length(x_extended(:,1));
pointnum(1:(length(x_extended(:,1))),1)=i;
cone_7_extended(a:(a+b-1),:)=[pointnum x_extended  y_extended
z_extended]; % store points into new matrix

a=a+(length(x_extended(:,1)))-1;
end

% erase points with strain rate and strain less than 0.01
[r,c]=find(cone_7_extended(:,3)<0.01);
cone_7_extended(r,:)=[];
[r,c]=find(cone_7_extended(:,4)<0.01);
cone_7_extended(r,:)=[];

% new data containing multiplied points
cone_7_extended;
scatter3(cone_7_extended(:,2),  log10(cone_7_extended(:,3)),
cone_7_extended(:,4),60,'filled','MarkerEdgeColor','k','MarkerFac
eColor','r')
```

5.2.5. Curve fitting to find critical Strain Coefficients

```
%Load data variables
load('Variables\TopPoints_cone_data.mat')
load('Variables\cone_data.mat')
trajectories=cone_data;
Points=TopPoints_cone_data;

%Create Temp,StrainRate and Strain Variable for MATLAB CURVE
FITTING TOOL
Temperature=Points(:,2);
StrainRate=Points(:,3);
Strain=Points(:,4);

%Curve fitting- FITTYPE define the type of fit (custom equation)
while FIT nd fit finds the coefficients.
CSeq=fittype('k1.*((StrainRate.^m1).*exp(Q1./(8.314.*(Temperature
+273))))','independent',{'Temperature', 'StrainRate'});
C=fit([Temperature,StrainRate],Strain,CSeq);

%Copy Coefficients into new array

coefficientsvalues_cone_data=coeffvalues(C);
```

5.2.6. Plot Calibrated JMAK Surface

```
% Plot Calibrated Critical Strain curve against initial and top
point trajectories
f1=figure;
set(gca,'FontSize',18)
set(f1,'color','w')
hold on
grid on
axis([930 980 -2 -1 0 1.5])
hold on

load('Variables\TopPoints_cone_data.mat')
load('Variables\cone_data.mat')
load('Variables\CoefficientsValues_cone_data')
coefficients= coefficientsvalues_cone_data;
trajectories=cone_data;
TopPoints=TopPoints_cone_data;

Q1=coefficients(1);
k1=coefficients(2);
m1=coefficients(3);

[Temp, StRate]=meshgrid(linspace(900,1100,50),
linspace(0.001,10,500));
CriticalStrain=(k1.*((StRate.^m1).*exp(Q1./(8.314.*(Temp+273)))))
+0.1;%CriticalStrain
```

```
m=mesh(Temp,log10(StRate),CriticalStrain,'FaceColor','b','LineSty
le','none','FaceAlpha',0.5);
hold on


% Plotting a text box with Q1, m1 and k1
dim = [0.6 0.6 0.3 0.3];
str = {['\bf Q1=' num2str(Q1)],['m1= ' num2str(m1)],['k1='
num2str(k1)]};

annotation('textbox',dim,'String',str,'FitBoxToText','on','FontSi
ze',13);
hold on

% Plot Initial Points
scatter3( trajectories(:,2),log10(trajectories(:,3)),
trajectories(:,4),20,'filled','MarkerEdgeColor','k','MarkerFaceCo
lor','g')
hold on
% Plot Top Trajectory Poins
scatter3( TopPoints(:,2),log10(TopPoints(:,3)),
TopPoints(:,4),20,'filled','MarkerEdgeColor','k','MarkerFaceColor
','r')
hold on
```

5.2.7. Adjust Calibration Coefficients

```
% Adjust Calibrated Surface Parameters
f1=figure;
set(gca,'FontSize',18)
set(f1,'color','w')
hold on
grid on
axis([930 980 -2 -1 0 1.5])
hold on
xlabel('T[°C]') % x-axis label
ylabel('Strain Rate [Log(1/s)]') % y-axis label
zlabel('Strain') % y-axis label

load('Variables\TopPoints_cone_7.mat')
load('Variables\coefficientsvalues_cone_7.mat')
coefficients=coefficientsvalues_cone_7;
TopPoints=TopPoints_cone_7;

% Plot original surface
Q1=coefficients(1);
k1=coefficients(2);
m1=coefficients(3);
[Temp, StRate]=meshgrid(linspace(900,1100,50),
linspace(0.001,10,500));
CriticalStrain=(k1.*((StRate.^m1).*exp(Q1./(8.314.*(Temp+273)))))
;%CriticalStrain
m=mesh(Temp,log10(StRate),CriticalStrain,'FaceColor','b','LineSty
le','none','FaceAlpha',0.5);
hold on
```

```
% Plot surface with modified k1 20% increase
Q1=coefficients(1);
k1=coefficients(2)+(coefficients(2)*20/100)
m1=coefficients(3);
[Temp, StRate]=meshgrid(linspace(900,1100,50),
linspace(0.001,10,500));
CriticalStrain=(k1.*((StRate.^m1).*exp(Q1./(8.314.*(Temp+273)))))
;%CriticalStrain
m=mesh(Temp,log10(StRate),CriticalStrain,'FaceColor','y','LineSty
le','none','FaceAlpha',0.5);
hold on

% Plot surface with modified Q1 1.5% increase
Q1=coefficients(1)+(coefficients(1)*1.5/100)
k1=coefficients(2);
m1=coefficients(3);
[Temp, StRate]=meshgrid(linspace(900,1100,50),
linspace(0.001,10,500));
CriticalStrain=(k1.*((StRate.^m1).*exp(Q1./(8.314.*(Temp+273)))))
;%CriticalStrain
m=mesh(Temp,log10(StRate),CriticalStrain,'FaceColor','g','LineSty
le','none','FaceAlpha',0.5);
hold on

% Plot surface with modified m1 7.5% increase
Q1=coefficients(1);
k1=coefficients(2);
m1=coefficients(3)-(coefficients(3)*7.5/100)
[Temp, StRate]=meshgrid(linspace(900,1100,50),
linspace(0.001,10,500));
CriticalStrain=(k1.*((StRate.^m1).*exp(Q1./(8.314.*(Temp+273)))))
;%CriticalStrain
m=mesh(Temp,log10(StRate),CriticalStrain,'FaceColor','m','LineSty
le','none','FaceAlpha',0.5);
hold on


% Plot Top Trajectory Poins
scatter3( TopPoints(:,2),log10(TopPoints(:,3)),
TopPoints(:,4),20,'filled','MarkerEdgeColor','k','MarkerFaceColor
','r')
hold on
1)
```